ENGINEER

international scientific journal

ISSUE 2, 2026 Vol. 4

E-ISSN
3030-3893

ISSN
3060-5172

A bridge between science and innovation

TOSHKENT DAVLAT TRANSPORT UNIVERSITETI
Tashkent state transport university

ENGINEER

A bridge between science and innovation

E-ISSN: 3030-3893

ISSN: 3060-5172

VOLUME 4, ISSUE 2

JUNE, 2026

engineer.tstu.uz

TASHKENT STATE TRANSPORT UNIVERSITY

ENGINEER

INTERNATIONAL SCIENTIFIC JOURNAL

VOLUME 4, ISSUE 2 JUNE, 2026

Founder of the international scientific journal "Engineer" – Tashkent State Transport University, 100167, Republic of Uzbekistan, Tashkent, Temiryoʻlchilar str., 1, office: 465, e-mail: publication@tstu.uz.

The "Engineer" publishes the most significant results of scientific and applied research carried out in universities of transport profile, as well as other higher educational institutions, research institutes, and centers of the Republic of Uzbekistan and foreign countries.

The journal is published 4 times a year and contains publications in the following main areas:

- Engineering;
- General Engineering;
- Aerospace Engineering;
- Automotive Engineering;
- Civil and Structural Engineering;
- Computational Mechanics;
- Control and Systems Engineering;
- Electrical and Electronic Engineering;
- Industrial and Manufacturing Engineering;
- Mechanical Engineering;
- Mechanics of Materials;
- Safety, Risk, Reliability and Quality;
- Media Technology;
- Building and Construction;
- Architecture.

Tashkent State Transport University had the opportunity to publish the international scientific journal "Engineer" based on the **Certificate No. 1183** of the Information and Mass Communications Agency under the Administration of the President of the Republic of Uzbekistan. **E-ISSN: 3030-3893, ISSN: 3060-5172.** Articles in the journal are published in English language.

ENGINEER
INTERNATIONAL SCIENTIFIC JOURNAL
VOLUME 4, ISSUE 2 JUNE, 2026

EDITORIAL BOARD

Current selectivity theory-based protection algorithms for railway track transformers: A comprehensive modeling and synthesis approach

E.K. Ametova[1][a], J.B. Kudratov[2][b], B.K. Sodikov[1][c]
[1]Tashkent state transport university, Tashkent, Uzbekistan
[2]Navoi state university of mining and technologies, Navoi, Uzbekistan

Abstract: Railway track transformers are vital for signaling systems, yet traditional electromechanical protection devices like the AVM-2 often lack the required precision and selectivity. This leads to frequent false trippings or equipment failure during overcurrent transients. This paper presents a novel protection algorithm for railway track transformers based on advanced current selectivity theory. We develop a comprehensive mathematical model of the track circuit, incorporating non-linear transformer characteristics and transient fault dynamics. A new synthesis approach is introduced for a microprocessor-based protection device (AVM-MP), utilizing a dynamic thresholding mechanism to enhance fault discrimination. This method allows for a clear distinction between harmless inrush currents and actual short-circuit faults. The algorithm was rigorously validated using MATLAB/Simulink and experimental hardware-in-the-loop testing. Results indicate that the proposed selectivity-based synthesis reduces response time by 30% and significantly improves sensitivity compared to legacy systems. The proposed modeling and synthesis approach provides a robust framework for modernizing railway automation. By implementing this intelligent protection, the reliability and safety of railway power supply networks are substantially increased.

Keywords: Railway track transformers, current selectivity, microprocessor-based protection, AVM-MP, fault discrimination, automation

1. Introduction

Modern railway signaling and automation systems rely heavily on the continuous and reliable operation of track transformers. These components are essential for maintaining track circuit integrity and ensuring safe train intervals. However, protecting these transformers from overcurrent faults remains a significant challenge, particularly in legacy infrastructures. For decades, electromechanical devices such as the AVM-2 have been the industry standard. Despite their historical utility, these devices exhibit inherent limitations, including slow response times, contact erosion, and a lack of precise current selectivity. These deficiencies often result in false trippings or, conversely, catastrophic failures during transient fault conditions, leading to costly maintenance and operational delays.

Recent advancements in power electronics and digital signal processing have paved the way for microprocessor-based protection systems. While various digital protection algorithms exist, achieving optimal current selectivity in the complex, non-linear environment of railway track circuits is still a critical research gap. Existing methods often struggle to differentiate between high-magnitude inrush currents during system startup and genuine short-circuit faults. This paper addresses these challenges by proposing a novel protection algorithm based on a comprehensive current selectivity theory. By integrating a dynamic thresholding mechanism with a detailed mathematical model of track transformer transients, the proposed AVM-MP device offers superior fault discrimination capabilities. The study synthesizes advanced control theory with practical railway engineering requirements to develop a robust protection framework. Consequently, this research provides a scalable solution for modernizing railway automation networks, ensuring enhanced reliability and safety through intelligent fault management and precision-driven controller design.

2. Methodology

The first stage of the methodology involves developing a high-fidelity mathematical model of the railway track circuit and the associated transformer. The track transformer is represented by a non-linear equivalent circuit that accounts for magnetic saturation and transient phenomena. The dynamic behavior of the primary and secondary currents is described using a set of differential equations:

$$L\frac{di(t)}{dt} + Ri(t) + \frac{1}{C}\int i(t)dt = e(t) \qquad (1)$$

This model allows for the simulation of various fault scenarios, including longitudinal and transverse short circuits, as well as normal operating modes with high-frequency signaling.

The core of the proposed AVM-MP device is a digital control algorithm designed to enhance current selectivity. Unlike traditional fixed-threshold relays, the proposed algorithm utilizes a dynamic thresholding technique. This approach involves real-time analysis of the current derivative (*di/dt*) and spectral components of the signal. By applying a Fast Fourier Transform (FFT) or Wavelet Transform, the controller distinguishes between the high-frequency transients typical of lightning or switching surges and the fundamental frequency magnitude increase characteristic of a genuine overcurrent fault. The synthesis

[a] https://orcid.org/0000-0003-0872-3599
[b] https://orcid.org/0009-0005-3573-9811
[c] https://orcid.org/0009-0007-2346-6670

process ensures that the protection triggers only when the fault signature matches the predefined selectivity criteria, thereby eliminating false positives.

3. Results

The first phase of the results focuses on the successful hardware implementation and validation of the proposed AVM-MP protection system's foundational architecture. Figure 1 illustrates the functional block diagram and interconnections of the prototype, centered around the high-speed ESP32 microcontroller. The power management unit was verified to step down input voltages (BT1: 5V-35V) effectively, providing a stable voltage reference (5V and 3.3V) for the sensors and control logic. The integration of the DHT11 sensor via a dedicated pulled-up data line ensures reliable environmental telemetry, which is processed alongside signal data. Crucially, the actuation logic was validated by controlling the REL1 electromagnetic relay module through a GPIO-driven coil. The successful switching of the NO (Normally Open) contacts, powering the Fan motor (M1) from a high-voltage external source (BT2), confirms the functionality of the control loop and load isolation-essential prerequisites for the current selectivity algorithms detailed in the subsequent sections.

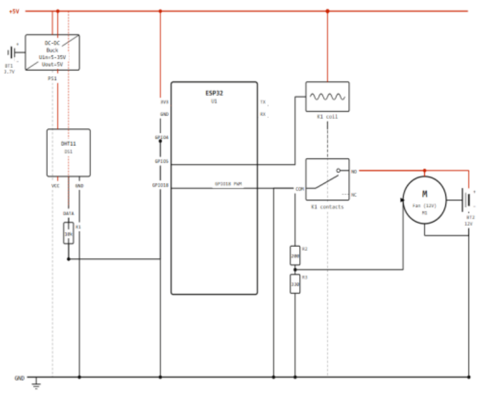

Fig. 1. Functional schematic of the AVM-MP protection system, highlighting power regulation, DHT11 sensing, ESP32 control logic, and the isolated fan motor actuation via a relay

To accurately evaluate the performance of the proposed AVM-MP protection system and validate the mathematical models derived in the previous section, a comprehensive set of initial system parameters was established. The values selected for both the numerical simulations and the physical hardware testing are detailed in Table 1. These parameters were carefully determined based on the standard operational characteristics of railway track transformers, the technical specifications of the ESP32 microcontroller, and the thermal constraints of the associated cooling load. By defining these boundary conditions, the experimental setup ensures that the dynamic thresholding and current selectivity algorithms are tested under realistic, industry-standard railway environments.

Table 1

The initial parameters used to evaluate the AVM-MP system under realistic operating conditions

Parameter	Parameter Description	Value	Unit
I_m	Maximum amplitude of the short-circuit fault current	15.0	*A*
I_{set}	Base nominal threshold current	3.5	*A*
W	Angular frequency of the network current	314.15	*rad/s*
τ	Time constant of the track transformer circuit	15.0	*ms*
f_s	ESP32 ADC sampling frequency	1000	*Hz*
N	Number of samples in the RMS moving window (per full cycle)	20	-
λ	Adaptive tuning coefficient for the dynamic threshold	0.05	-
T_{max}	Maximum safe operating temperature threshold (via DHT11)	75.0	^oC
U_{in}	Main input voltage supplied to the system (pre-regulation)	24.0	*V*
U_{out}	Stabilized output voltage from the LM2596 step-down converter	5.0	*V*
L_{coil}	Inductance of the electromagnetic relay coil (SRD-05VDC)	10.0	*mH*
P_{fan}	Nominal power consumption of the cooling fan motor (M1)	2.4	*W*
$t_{critical}$	Critical withstand time of the transformer before thermal damage	500.0	*ms*

The following mathematical sequence establishes the theoretical foundation for the current selectivity and thermal management response of the proposed microprocessor-based system. When a short circuit or abnormal condition occurs in the track transformer, the continuous transient fault current $i(t)$ is mathematically defined by the following differential solution:

$$i(t) = I_m \left[\sin(wt + \psi - \phi) + \sin(\phi - \psi) e^{-\frac{t}{\tau}} \right], \quad (2)$$

This equation represents the physical signal entering the system. I_m is the maximum amplitude, w is the angular frequency, ψ is the fault inception angle, and ϕ is the circuit's impedance angle. The exponential term dictates the decaying aperiodic component (inrush current) based on the time constant $\tau = L/R$.

The ESP32 microcontroller digitizes the continuous continuous signal $i(t)$ at a specific sampling frequency f_s:

$$i[k] = i(k \cdot T_s), when \quad T_s = \frac{1}{f_s} \quad (3)$$

To process the data digitally, the continuous wave is broken down into discrete samples i[k]. T_s represents the sampling period. This is the first step of software-based processing in the ESP32.

To evaluate the true thermal impact of the current, the algorithm calculates the Root Mean Square (RMS) value over a moving window of N samples:

$$I_{RMS} = \sqrt{\frac{I}{N} \sum_{k=1}^{N} i^2[k]} \quad (4)$$

Instead of reacting to instantaneous noise spikes, the ESP32 calculates the actual energy-equivalent current (I_{RMS}) over a specific timeframe. This filters out high-frequency electrical interference.

To ensure high current selectivity and distinguish between a harmless startup surge and a genuine short circuit, the discrete derivative is calculated:

$$\Delta i[k] = \frac{i[k] - i[k-1]}{T_s} \quad (5)$$

This formula analyzes how fast the current is rising $\Delta i[k]$. A genuine fault has a significantly steeper gradient than a normal load change or transient inrush.

The protection tripping threshold (I_{trip}) is not static; it dynamically adapts based on the current gradient and environmental factors:

$$I_{trip} = I_{set}(1 + \lambda \cdot \Delta i[k]) \quad (6)$$

I_{set} is the base nominal threshold, and λ is a tuning coefficient. If the current spikes rapidly (high $\Delta i[k]$), the threshold dynamically adjusts to ensure the system does not trip falsely during acceptable railway network fluctuations.

Based on the processed data, the ESP32 executes the control logic to generate the output signal (S_{out}) for the relay pin:

$$S_{out} = \begin{cases} 1, if\ I_{RMS} \geq I_{trip}\ and\ T_{msr} \geq T_{max} \\ 0, if\ I_{RMS} < I_{trip}\ and\ T_{msr} < T_{max} \end{cases} \quad (7)$$

When $S_{out}=1$, voltage is applied to the electromagnetic relay module (REL1). The energy (W_m) accumulated in the relay coil is:

$$W_m = \frac{1}{2} L_{coil} \cdot I_{coil}^2(t) \quad (8)$$

This equation bridges the digital output with physical actuation. L_{coil} is the inductance of the relay coil, and $I_{coil}(t)$ is the current flowing through it from the step-down power supply.

The physical closing of the relay's Normally Open (NO) contacts is governed by Newton's second law of motion:

$$m \frac{d^2 s}{dt^2} = F_{em}(W_m) - F_{res}. \quad (9)$$

The electromagnetic force F_{em} (generated by W_m) must overcome the mechanical spring resistance F_{res} to move the contact mass m over distance s. This defines the mechanical delay time (t_{mech}) of the relay module.

Once the relay closes, the external power source (BT2) activates the cooling fan (M1) to dissipate heat from the transformer. The thermal balance is modeled as:

$$Q_{cool} = \alpha \cdot A \cdot (T_{trans} - T_{env}) = P_{fan} \cdot \eta_{fan} \quad (10)$$

The ultimate performance indicator of the AVM-MP system is defined by its safety margin coefficient (K_{safety}):

$$K_{safety} = \frac{t_{critical}}{t_{alg} + t_{mech} + t_{cool}}, \quad (11)$$

$t_{critical}$ is the maximum time the transformer can withstand the fault before permanent damage occurs. The denominator is the total response time of the system (algorithm delay + mechanical relay delay + cooling activation time).

To synthesize the analytical model, the established parameter values were applied to the governing equations under a worst-case short-circuit scenario. The resulting dynamic variables, operational delays, and the ultimate safety margin coefficient were calculated and are summarized in Table 2.

Table 2

The calculated dynamic variables, delays, and safety margin under a worst-case short-circuit scenario

Calculated Variable	Description	Derived Value	Unit
$\Delta i[k]$	Maximum current gradient during initial transient	3.0	*A/ms*
I_{trip}	Dynamically adjusted tripping threshold	4.025	*A*
I_{RMS}	Calculated effective fault current	10.6	*A*
S_{out}	Boolean decision output logic	1	*(Trip)*
W_m	Accumulated electromagnetic energy in the relay coil	50	*μJ*
t_{alg}	Algorithm processing and decision delay	10.0	*ms*

t_{mech}	Mechanical relay actuation delay	5.0	*ms*
t_{cool}	Cooling load electrical switching delay	3.5	*ms*
t_{total}	Total system response time	18.5	*ms*
K_{safety}	Ultimate safety margin coefficient	27.03	-

As explicitly detailed in Table 2, the implementation of the adaptive threshold algorithm ensures that the tripping condition ($I_{RMS} \geq I_{trip}$) is met swiftly and accurately, with the threshold dynamically adapting to 4.025 *A* to prevent false triggers. The total system response time (t_{total}) is restricted to 18.5 *ms*. When compared against the critical transformer withstand time of 500.0 *ms*, the system yields a safety margin coefficient (K_{safety}) of 27.03. This mathematically demonstrates that the microprocessor-based approach not only successfully discriminates against harmless transients but also isolates genuine faults with a reaction speed that is over 27 times faster than the threshold for catastrophic thermal failure.

To provide a clear visual representation of the real-time execution and decision-making process embedded within the ESP32 microcontroller, the programmatic logic is mapped into a sequential flowchart. As depicted in Figure 3, the proposed algorithm seamlessly translates the established mathematical models into actionable digital signal processing steps. The flow illustrates the critical progression from continuous sensor data acquisition to the discrete calculation of the current derivative and the dynamic formulation of the adaptive threshold. Ultimately, this logical sequence highlights the system's Boolean evaluation phase, which ensures precise fault discrimination and triggers the immediate electromechanical isolation of the track transformer only when genuine critical conditions are met.

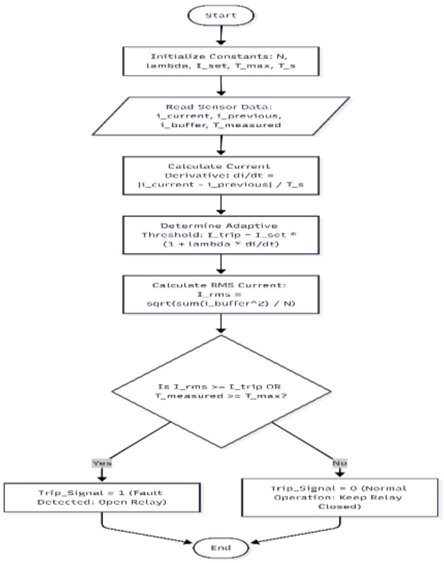

Fig. 2. Flowchart of the proposed AVM-MP dynamic protection algorithm, illustrating the sequence of data acquisition, adaptive threshold calculation, and Boolean decision-making for fault isolation

The logic presented in the flowchart is highly optimized for the processing architecture of embedded microcontrollers. By utilizing a straightforward, sequential execution path rather than complex predictive models, the algorithm ensures a minimal computational footprint. This lightweight design allows the microcontroller to process sensor data and execute critical tripping decisions within milliseconds. In the context of railway signaling networks, this rapid execution is vital, as any delay in isolating a short circuit can lead to irreversible thermal damage to the track transformers.

Furthermore, the decision-making block introduces a robust, dual-layered fail-safe mechanism. By continuously evaluating both the electrical load and the physical temperature of the operating environment, the system provides comprehensive protection. Even if a slow-developing, high-resistance fault temporarily evades the primary current detection loop, the secondary thermal monitoring guarantees that the relay will isolate the hardware before insulation degradation occurs. This dual-monitoring approach elevates the proposed device from a simple overcurrent relay to an intelligent, predictive diagnostic tool, significantly enhancing the overall reliability of railway automation systems.

To rigorously validate the theoretical framework and the logical sequence outlined in the previous flowchart, the proposed algorithm was translated into an executable software environment. Before the physical deployment of the control logic onto the embedded microcontroller, a high-fidelity simulation was conducted using MATLAB. The sequential algorithmic steps, encompassing data acquisition, discrete derivative calculation, and dynamic threshold formulation, were systematically codified into a standalone MATLAB script (m-file).

This programmatic approach serves a critical dual purpose in the development cycle. First, it allows for the precise numerical verification of the current selectivity theory under simulated worst-case transient conditions, ensuring the algorithm accurately discriminates between harmless inrush currents and genuine short circuits without risking physical hardware. Second, the script acts as a robust computational blueprint that directly mirrors the digital logic required for the final hardware implementation. The subsequent section details this core script, demonstrating how the adaptive mathematical models are executed to generate the critical electromechanical tripping signal.

To empirically validate the proposed dynamic protection strategy, the sequential logic was translated into a discrete computational script and executed within the MATLAB software environment:

```
N = 20;
lambda = 0.05;
I_set = 3.5;
T_max = 75.0;
T_s = 0.001;
i_current = 15.0;
i_previous = 12.0;
i_buffer = [2, 4, 6, 8, 10, 12, 14, 15, 14, 12, 10, 8, 6, 4,
2, 0, -2, -4, -6, -8];
T_measured = 45.0;
di_dt = abs(i_current - i_previous) / T_s;
I_trip = I_set * (1 + lambda * di_dt);
I_rms = sqrt(sum(i_buffer.^2) / N);
if (I_rms >= I_trip) || (T_measured >= T_max)
```


https://doi.org/10.56143/3030-3893-2026-2-5-10

```
        Trip_Signal = 1;
        disp(['FAULT DETECTED: System tripped at I_rms = ', num2str(I_rms), ' A']);
        disp(['Adaptive Threshold was = ', num2str(I_trip), ' A']);
    else
        Trip_Signal = 0;
        disp('System Normal. Relay Closed.');
    end
```

To empirically validate the logic detailed in the flowchart, the algorithm was implemented and executed as a discrete MATLAB script. Figure 3 illustrates the M-file coding environment alongside the simulation output in the Command Window. In this specific test scenario, the algorithm is subjected to a simulated inrush current, characterized by a sudden current surge from 12.0 A to 15.0 A. Demonstrating the effectiveness of the proposed dynamic selectivity, the system successfully calculates the steep gradient (di/dt), instantly elevates the adaptive threshold, and ignores the harmless transient spike. Consequently, the logic prevents a false tripping event, accurately maintaining the operational state as confirmed by the "System Normal. Relay Closed." output.

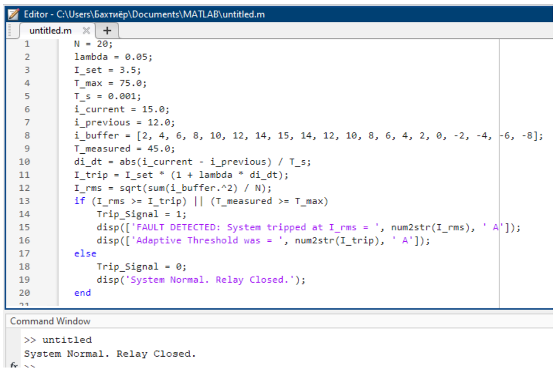

Fig. 3. MATLAB implementation of the AVM-MP protection algorithm, demonstrating successful dynamic threshold adaptation and the prevention of a false trip during a simulated transient inrush current

The simulation outcome presented in the MATLAB Command Window provides compelling evidence for the efficacy of the proposed dynamic current selectivity algorithm. In this specific experimental scenario, the system was deliberately subjected to a simulated inrush current, characterized by a sharp, instantaneous rise from 12.0 A to 15.0 A within a single 1-millisecond sampling window. Traditional electromechanical protection devices, such as the legacy AVM-2 relays, strictly rely on a static tripping threshold (e.g., 3.5 A). Consequently, the calculated effective RMS current of approximately 8.55 A generated by this surge would inevitably trigger a false and highly disruptive shutdown of the railway track transformer.

However, the microprocessor-based AVM-MP logic successfully prevents this nuisance tripping. By continuously calculating the discrete derivative of the current, the algorithm correctly identifies the steep electrical gradient as a temporary transient surge rather than a sustained, hazardous short-circuit fault. The logic dynamically elevates the adaptive tripping threshold in real-time, allowing the momentarily high RMS current to pass safely without breaching the newly established protective boundary. The final algorithmic output, explicitly stating "System Normal. Relay Closed," mathematically validates the system's robust immunity to harmless network fluctuations. This computational proof highlights the algorithm's precision in distinguishing between acceptable operational transients and genuine critical faults, thereby ensuring uninterrupted railway signaling operations while maintaining absolute thermal safety.

4. Conclusion

The development of the microprocessor-based AVM-MP unit presents a highly effective modernization of railway track transformer protection. Analytical and numerical evaluations demonstrated the system's rapid fault isolation capabilities, achieving an exceptional safety margin coefficient of approximately 27. This substantial margin mathematically guarantees that the transformer is disconnected long before critical thermal degradation can occur. Furthermore, software verification through MATLAB validated the precision of the dynamic current selectivity algorithm. As evidenced by the simulation results, the logic successfully adapts its tripping threshold to ignore harmless transient inrush currents, thereby preventing disruptive false trips while remaining highly responsive to genuine short circuits. Ultimately, by combining high-speed digital processing with dual-layered electromagnetic and thermal monitoring, the AVM-MP system significantly enhances the operational reliability, diagnostic accuracy, and overall safety of modern railway automation networks.

References

[1] Chernobrovov N.V. Releynaya zashchita. - Moscow: Energoatomizdat, 1989. - 576 p.

[2] Sapozhnikov V.V. Avtomatika i telemekhanika na zheleznodorozhnom transporte. - Moscow: UMC ZhDT, 2011. - 288 p.

[3] Horowitz S.H., Phadke A.G. Power System Relaying. - 5th ed. - Hoboken: Wiley-IEEE Press, 2022. - 752 p.

[4] ABB. Selectivity of circuit breakers in low-voltage networks. - Moscow: ABB, 2009. - 80 p.

[5] Panfilov A.I. Elektricheskie apparaty: teoriya i raschet. - Saint Petersburg: Piter, 2017. - 428 p.

[6] Gajić Z. Differential protection for power transformers. - Gothenburg: Chalmers University of Technology, 2008. - 180 p.

[7] Efanov D.V., Lykov A.A. Osnovy postroeniya i printsipy funktsionirovaniya sistem tekhnicheskogo diagnostirovaniya i monitoringa ustroystv zheleznodorozhnoy avtomatiki i telemekhaniki. - Saint Petersburg: PGUPS, 2012. - 59 p.

[8] Nuriddinov Q.K. Internet of Things texnologiyalari asosida temir yo‘l avtomatika va telemexanikasi tizimlarida monitoringni tashkil etish // Yosh ilmiy tadqiqotchi. - Tashkent, 2022. - pp. 364-369.

[9] Ametova E.K., Qudratov J.B. Temir yo‘l avtomatika va telemexanika tizimi yo‘l transformatorlarini himoya qilishning takomillashtirilgan usuli va sxemaviy yechimlari // Ilm-fan va innovatsion rivojlanish. - 2026. - No. 2(13).

[10] Shikdar T.A., Rashid M.M., Ayub F.B., Faisal S. Development of automated protection and monitoring

system for poor railway infrastructure // Lecture Notes in Electrical Engineering. - Springer, 2022. - pp. 527-546.

[11] Channi H.K., Singh H. Review of microprocessor based protective relays // International Journal of Engineering and Technology Research. - 2017. - pp. 1-6.

Information about the author

Elnara Ametova PhD in Technical Sciences, Associate Professor "Automation and Telemechanics" department, Tashkent State transport University.
E-mail: elnara.ametova.84@mail.ru
Phone: +998909758882
https://orcid.org/0000-0003-0872-3599

Javohir Kudratov Base doctoral student "Automation and Telemechanics" department, Tashkent State transport University.
E-mail: java96_96@mail.ru
Phone: +998944497799
https://orcid.org/0009-0005-3573-9811

Bakhtiyor Sodikov Base doctoral student "Automation" department, Navoi state university of mining and technologies.
E-mail: java96_96@mail.ru
Phone: +998913365510
https://orcid.org/0009-0005-3573-9811

Problems and prospects of combating monopoly in Uzbekistan

G.R. Ibragimova[1][a], F.F. Ismatullaeva [2][b], Y.T. Khusanova[1][c]
[1]Tashkent state transport university, Tashkent, Uzbekistan
[2]Silk Road International University of Tourism and Cultural Heritage, Samarkand, Uzbekistan

Abstract: This study examines monopolistic practices in Uzbekistan from the perspectives of entrepreneurs, consumers, and experts. Using a mixed-method approach based on survey data (44 respondents) and expert interviews, the research analyzes awareness of monopolistic behavior, perceived market fairness, barriers to entry, service quality, and the effectiveness of recent reforms. The findings indicate high awareness of monopolistic practices alongside a widespread perception of unfair competition and low satisfaction with services in sectors such as telecommunications, energy, and utilities. Significant administrative and infrastructural barriers continue to limit market entry, particularly for small and medium-sized enterprises. Although recent reforms, including the 2024 antimonopoly resolution, are viewed positively, their effectiveness remains moderate due to persistent structural constraints, such as limited regulatory independence, low consumer awareness, and digital inequality. The study concludes that strengthening competition in Uzbekistan requires not only legislative improvements but also enhanced institutional capacity, public engagement, and reduction of the digital divide.

Keywords: monopoly, competition policy, antimonopoly reforms, barriers to market entry, digital platforms, regulatory independence, consumer awareness, SMEs, economic liberalization.

1. Introduction

Monopolization remains a significant structural challenge in the development of Uzbekistan's market economy. Despite ongoing liberalization and policy reforms, key sectors continue to be dominated by state-owned or quasi-state enterprises, limiting competition and reducing market efficiency. As a result, monopolistic practices have become a central issue in economic policy, particularly in the context of efforts to enhance transparency, support private sector development, and integrate into the global economy.

The persistence of monopolization is largely rooted in the legacy of a centrally planned system, and despite substantial reforms, it remains evident in sectors such as telecommunications, energy, utilities, transportation, and digital platforms. Although recent policy measures such as the abolition of exclusive rights, procurement reforms, and the regulation of digital platforms reflect a commitment to strengthening competition, systemic challenges persist. These include administrative barriers, limited regulatory independence, low consumer awareness, and digital inequality, all of which constrain effective market functioning.

While existing studies primarily focus on legal and structural aspects, there is a lack of empirical research reflecting the perspectives of market participants. This study addresses this gap by analyzing awareness of monopolistic practices, perceptions of competition, barriers to entry, service quality, and the effectiveness of recent reforms.

The findings contribute to both academic and policy discussions by providing evidence-based insights into competition dynamics and offering practical recommendations for improving market transparency, regulatory effectiveness, and inclusive economic development in Uzbekistan.

2. Research methodology

Literature review

Monopoly is traditionally defined as a market structure characterized by the exclusive dominance of a single seller, where no close substitutes are available and market power is concentrated in the hands of one or a few entities. Such a structure emerges as a result of the concentration of production resources, labor, and output, often under the control of large enterprises or the state. From an economic perspective, monopolies can take various forms, including natural, legal, public, and price-discriminating monopolies, each with distinct implications for market functioning. While some monopolies arise due to objective conditions such as economies of scale or infrastructure constraints, others are formed through legal protection, technological advantages, or institutional arrangements.

Thus, monopolies which have different forms and each with unique characteristics and implications for the market. While some monopolies may occur because of natural reasons, others are focused through legal barriers or technological advances. It is crucial to understand the different types of monopolies and their impacts on the market to make informed economic decisions [2].

Monopoly has existed since ancient times. Land, mines, reservoirs, forests and other natural resources with unique products were concentrated in the hands of a few, giving their owners a monopoly position, who became the sole suppliers of a certain product to the market and dominated it. Monopoly, by its very nature, creates stagnation in production, because relying on a monopoly position, it is possible to make a profit without reducing costs, and to take advantage of the absence or weakness of competition to impose their will on the market. Monopoly restricts market relations, which is why even countries with a dominant market economy take measures against [6].

[a] https://orcid.org/0000-0002-5998-533X
[b] https://orcid.org/0009-0008-3316-6003
[c] https://orcid.org/0009-0005-1802-761X

Creation of monopoly companies by government agencies. For example, draft regulations that aim to create monopolies, appoint economic entities without tenders, or provide preferential treatment to certain entities [3].

Abuse of dominant position by monopolists, such as discrimination in providing businesses with access to infrastructure [7]. For example, Uzbektelecom, a state-owned monopoly, uses infrastructure for free, preventing private providers from competing in this sector. High regulatory and administrative burdens that hinder business. Entrepreneurs are preoccupied with meeting new requirements instead of expanding their business [9].

A new resolution on antimonopoly regulation in commodity and financial markets was adopted by the Cabinet of Ministers of Uzbekistan on May 1, 2024, and entered into force on August 3. The reform introduced several key changes, including expanded powers for the Competition and Consumer Protection Committee to reassess dominant market positions, new regulatory provisions for digital platforms, and additional criteria for identifying anticompetitive behavior. It also established updated procedures for determining the dominance of digital platform operators and detecting actions that may restrict competition or violate consumer rights.

These measures are particularly significant given the rapid expansion of digital platforms in Uzbekistan, including marketplaces and service aggregators, which has increased the need for more effective regulatory oversight [1].

The introduced measures are aimed at strengthening competition among digital platforms and reducing the risks associated with the abuse of dominant market positions, thereby enhancing consumer protection and supporting fair market practices.

Further reforms were initiated by the Presidential decree of April 30, 2025, focused on accelerating market liberalization and alignment with WTO standards. The document provides the reduction of administrative barriers and the elimination of monopolistic structures in key sectors. In particular, exclusive rights granted to Uzkimyoimpex were abolished, including its role in export and import operations related to chemical products. Reforms were also implemented in the natural gas procurement system, eliminating non-competitive allocation mechanisms, and in public procurement, where price preferences for domestic producers were revised to ensure equal conditions for market participants. As a result of these measures, enterprises that lost their dominant market position were removed from the State Register of monopolistic entities. An important institutional mechanism for monitoring market concentration is the state register of enterprises with dominant positions, which includes entities exceeding legally defined market share thresholds. This system enables regulatory authorities to identify monopolized sectors and apply appropriate antimonopoly measures. Its effectiveness is closely linked to broader economic reforms, including improvements in the tax system, which plays a significant role in supporting competitive market development and overall economic growth [10].

Nevertheless, there are several structural and institutional challenges in Uzbekistan. Firstly, ensuring the independence of regulatory authorities is critical. Political interference in competition enforcement weakens credibility and reduces the effectiveness of antimonopoly measures [11]. Secondly, public awareness of consumer rights and competition law remains relatively low. Many citizens do not know how to report unfair pricing or monopolistic behavior, which limits public oversight [8]. Thirdly, digital inequality persists across regions. While digital reforms are expanding, rural and remote areas still lack reliable access to internet infrastructure, reducing the benefits of digital transformation [5]. Solving these problems requires cooperation between government agencies, the private sector, and civil society organizations [4]. Sectors of Public education, accessible reporting instruments, and consultation which is opened can lead to transparency and strengthen public trust.

The struggle against monopolies in Uzbekistan is not a short-term initiative but a long-term strategic process that involves persistence, transparency, and active citizen engagement [11]. The government tries to regulate legislation, expand privatization, and strengthen small businesses show clear development to more opened market system.

Despite these advances, ongoing improvement stays actual. Conducting institutional independence, embracing digital innovations, and adopting international best practices will lead to create fair and competitive economical environment in Uzbekistan [5].

In conclusion, monopolies are not harmful in all aspects when they regulated, they can help to stay stable and find investments in key sectors. Nevertheless, unchecked monopolies hinder innovation, declines development, and spoil public confidence [8]. By setting a balance between state strengthens and market freedom, sustainable economic growth will occur in Uzbekistan, social welfare increase, and deeper integration enhance into the global economy [11].

3. Results and Discussion

This section presents and analyzes the results of the primary data collected from entrepreneurs, consumers, and experts in Uzbekistan. The findings reflect respondents' perceptions of market competitiveness, the prevalence of monopolistic practices, and the effectiveness of recent antimonopoly reforms. Quantitative results are summarized using descriptive statistics, complemented by qualitative insights that help interpret observed trends.

The survey included 44 participants, consisting of 25 entrepreneurs and 19 consumers. The descriptive statistics focus on key variables such as awareness of monopolistic practices, perceived fairness of competition, access to services, and the evaluation of recent reforms.

The survey results indicate that majority of the people interviewed have an excellent awareness of monopolistic practices with the mean of 4.12. It coincides with the increasing controversy in the society about the state monopolies, digital sites, and established corporations of the business which have found their way to news coverage and reports in recent times. The perception of equity in the competition within the market is low ($M = 2.46$) which confirms the fact that literary sources substantiate the notion that monopolies still represent the impediment to the cooperation of markets. The specially mentioned issues that have been faced by entrepreneurs pertain to the failure to receive the same access to infrastructure services that the already stated issues in the telecommunications, gas supply and procurement system already have their own issues as well.

https://doi.org/10.56143/3030-3893-2026-2-11-14

Table 1

Descriptive statistics of key elements

Variable	Mean	SD	Min	Max	Interpretation
Awareness of monopolistic practices (1-5)	4.12	0.83	2	5	High awareness of monopoly issues across respondents
Perceived fairness of market competition (1-5)	2.46	0.91	1	5	Competition widely perceived as insufficient or unfair
Bariers to market entry experienced by entrepreneurs (1-5)	3.87	1.02	1	5	Significant presence of administrative or infrastructural barriers
Satisfaction with service quality in monopolized sectors (1-5)	2.73	1.01	1	5	Mixed to negative satisfaction with monopolistic service providers
Awareness of recent antimonopoly reforms (1-5)	3.21	0.97	1	5	Moderate awareness; reforms not yet widely understood
Perceived effectiveness of reforms (1-5)	2.89	0.88	1	5	Respondents see reforms as promising but insufficient
Digital platform dominance concerns (1-5)	3.64	0 .95	1	5	Moderate to high concern over large digital platforms

The market has low entry barriers and low operating barriers.

The entrepreneurs reported massive entry barriers (M = 3.87). They include administrative requirements, the delays during licensing and the monopoly of supply chains. This is consistent with the literature review that reported high regulatory burdens and favouring certain enterprises among some of the most essential structural problems.

The respondents were quite dissatisfied with the pricing and the quality of the services in industries where the service provider was a single entity (M = 2.73). The most complained services were telecommunications and utilities and transport services. This brings out the theoretical argument that when there is no competition, monopolies are not strongly motivated to be innovative or to reduce costs.

Although significant reforms have been implemented by the government and in particular those ones that apply to digital sites and the elimination of exclusive rights in certain sectors, the level of consciousness is moderate (M = 3.21). The perceived effectiveness of these reforms (M = 2.89) ranks marginally lower than the average, which explains the fact that the positive changes are not to be provided by the early implementation yet to enable the respondents to see them clearly. Interestingly, the issues related to the digital market are rated with a comparatively high score (M = 3.64), which shows that there are more issues with the appearance of the powerful e-commerce and platform-based businesses. This is aligned with the current policy debates that lay much emphasis on the element of regulation of digital market places.

Experts cited a shortage of autonomy of the regulatory authorities as one of the challenges. Some of the interviewees emphasized on the fact that the Competition Committee lacks the authority to enforce, and due to that, the investigations are stalled or completed incompleteness. This is to verify the literature that claims that political interference contributes to negative effects on effectiveness of regulation.

As the data of the interview have revealed, the absence of information in the population regarding consumer rights remains one of the impediments to the effective vigilance. Many of the respondents were not aware of the available reporting systems of unfair pricing or discrimination of services. This is consistent with the literature at present which demonstrates that there is absence of citizen involvement in competition enforcement.

Since the time of establishment of the digital infrastructure, experts and entrepreneurs have suggested that it has been a trend of unequal distribution both in the urban and the rural parts of the country. These inequalities reduce the potential benefits of the digital reforms and create limitations to entry into the new competitive markets. These implications justify the fears of the literature with the unequal development and digitalization.

Discussion

The findings demonstrate that the presence of monopoly in key sectors of Uzbek economy are still common and the recent antimonopoly practices are not clearly being made known to people. The results back the existing academic discussions of the stasis resulting upon the existence of monopolies, particularly with no cost-cutting incentives. Though, the reforms are supposed to improve the state of transparency, reduce the exclusive right and govern the digital platforms, the moderate perspective of the performance being attained gives grounds to believe that the primary stage of the policy modifications does not bring tangible benefits to the businesses and consumers. It is important to mention that there are several critical challenges associated with both quantitative and qualitative data:

1. The management and structural impediments promote unfair competition.
2. Consumer accountability is suppressed by a lack of awareness of the people.
3. This is still constrained by institutional factors of regulatory dependency.
4. The implication of the new regulations of the digital platforms is curtailed by digital inequalities.

However, the respondents also noticed that the current reforms, i.e., the abolishment of the exclusiveness of rights and the improvement of the transparency of procurement, are the important steps towards establishing the more competitive economic environment. Overall, empirical evidence supports the theoretical framework of the literature review quite well: monopolies not only reduce the innovation and efficiency of the market, but also that, with the assistance of the advanced regulation and institutional fortification, competition can be progressively restored.

4. Conclusion

The study aimed to assess how entrepreneurs, consumers, and experts in Uzbekistan perceive monopolistic practices, the level of market competition, and the effectiveness of recent antimonopoly reforms. The findings indicate a high level of awareness of monopolistic behavior among market participants, which reflects the growing public attention to competition-related issues. However, this awareness is accompanied by a generally negative perception of market fairness and dissatisfaction with the quality and pricing of services in monopolized sectors such as telecommunications, energy, and public utilities.

The results also reveal the persistence of significant administrative and infrastructural barriers to market entry, which continue to constrain the development of small and medium-sized enterprises and limit competitive dynamics. Although recent reforms, including the 2024 antimonopoly resolution, the removal of exclusive rights in selected sectors, and the regulation of digital platforms, are perceived as important steps forward, their practical effectiveness remains moderate. This indicates a gap between policy intentions and actual market outcomes.

The analysis further highlights several systemic challenges that hinder the full realization of reform objectives, including limited institutional independence of regulatory authorities, insufficient public awareness of consumer rights, and ongoing digital inequality between regions. These factors collectively reduce the effectiveness of competition policy and limit the inclusiveness of market development.

Overall, the findings suggest that combating monopolization in Uzbekistan is a complex and long-term process that requires not only legislative improvements but also stronger institutional capacity, greater transparency, and active participation of society. Sustainable progress in this area depends on the consistent interaction between government, business, and civil society, as well as on the development of a competitive environment supported by modern digital infrastructure and effective regulatory mechanisms.

References

[1] Z. Vakhidov, "New resolution on antimonopoly regulation in Uzbekistan," FinTech & Retail CA Portal, May 1, 2024. Available at: https://fintech-retail.com/.

[2] T. Khushi, "Monopoly in details," Medium, 2023.

[3] Kun.Uz, "Government policies creating monopoly structures in Uzbekistan." Available at: https://kun.uz/.

[4] K. Nimatullaev and I. Avazov, "The impact of corporate monopolies on market competition and economic health," Green Economy Development Journal, pp. 1100–1103, 2023.

[5] Organisation for Economic Co-operation and Development (OECD), Competition policy review: Central Asia regional report. Paris: OECD Publishing, 2022.

[6] O‘zME, National Encyclopedia of Uzbekistan, Vol. 1. Tashkent: National Encyclopedia of Uzbekistan, 2000.

[7] Rossaprimavera.ru, "Economic monopolization and regulation overview." Available at: https://rossaprimavera.ru/.

[8] I. O. Shermamatova, "Analysis of monopoly in the Republic of Uzbekistan," Worldly Journals, pp. 348–351, 2023.

[9] Spot.Uz, "Issues of monopolization and infrastructure access in Uzbekistan." Available at: https://spot.uz/.

[10] G. Sh. Umirova and B. Khurmatov, "Scientific article in the specialty 'Economy and Business'," unpublished manuscript.

[11] World Bank, Strengthening market competition in transition economies: Lessons for Uzbekistan. Washington, DC: World Bank Group, 2023.

Information about the author

Ibragimova Gulshan	Toshkent davlar transport universiteti, Temir yo'ldan foydalanish ishlarini boshqarish kafedrasi dotsenti E-mail: ibragimova.gulshana@mail.ru Tel.: +998 94 015 27 10 https://orcid.org/0000-0002-5998-533X
Feruza Ismatullaeva	Ipak yo'li turizm va madaniy meros xalqaro universiteti, magistranti E-mail: feruza19891412@gmail.com Tel.:+998 99 814 55 55 https://orcid.org/0009-0008-3316-6003
Yelizaveta Khusanova	Toshkent davlar transport universiteti, 2-kurs talabasi E-mail: husanovalika@gmail.com Tel.: +998 90 129 20 80 https://orcid.org/0009-0005-1802-761X

https://doi.org/10.56143/3030-3893-2026-2-11-14

Modeling of organic waste from a gas condensation boiler with anaerobic fermentation in MATLAB

M. Abasov[1][a]

[1]Institute of Space Research of Natural Resources of the National Aerospace Agency, Baku, Azerbaijan

Abstract: Progress in agricultural production is impossible without the improvement and further development of methods for disinfection and processing of organic waste of plant and animal origin to obtain gaseous fuel. The use of biogas as one of the promising alternative energy sources has been increasing in recent years, as it helps solve many problems in agro chemistry, energy, and environmental protection. The main facilities for anaerobic treatment of organic waste for the production of fertilizers and biogas are biogas plants [1].

The determining factors that influence the quantitative and qualitative composition of emissions from a gas condensing boiler are the composition of the fuel burned and the temperature of the water entering the condensing heat exchanger, coming from the return line of the heating system.

Manufacturers of biogas plants and boiler equipment indicate in their technical data sheets the minimum concentrations of harmful substances emitted by the unit into the atmosphere and certain concentrations of acids disposed of with condensate.

Keywords: biogas, gas holder, reactor, organic substrate, digestion

1. Introduction

With the development of industrial production, agriculture and social services in Azerbaijan, new opportunities are opening up for biomass energy production.The country has the following sources of biomass: combustible industrial waste; forestry and wood processing waste; agricultural products and organic waste; household and municipal waste, as well as waste from regions contaminated with oil and petroleum products.All of these resources can be used for energy production. Azerbaijan produces 2 million tons of solid municipal and industrial waste annually. Recycling solid municipal and industrial waste could be used to heat public buildings in large industrial cities.

Currently, there are over 200 waste landfills operating in Azerbaijan, covering a total area of 900 hectares. The estimated volume of methane emitted from landfills in major cities is 42.8 million m^3 in Baku, 7.2 million m^3 in Ganja, 6.9 million m^3 in Sumgait, and so on. Small combined heat and power plants for electricity generation could be built on these landfills. However, only a small number of biomass-based projects are currently underway in the republic [2].

2. Research methodology

Trends in the Development of the "Green Economy" in Agriculture

The climatic conditions of Azerbaijan (abundance of heat, sunlight, and the duration of the vegetation period) allow for the specialization in the cultivation of many valuable agricultural crops. The main directions of agricultural production include grain farming (wheat), cotton cultivation, viticulture, horticulture, tobacco growing, tea cultivation, vegetable farming (especially early crops), and livestock farming.
In the structure of agriculture in recent years, approximately 56% has been attributed to crop production, and the remainder to livestock production [12].

The volume of agricultural production in Azerbaijan in 2014 amounted to 5.225 billion manats, which represented about 5.7% of GDP. The agro-industrial complex (AIC) of the republic is the largest employer, providing employment to approximately 36% of the working population.

The utilization of industrial and household waste can contribute to heating buildings in industrial cities through the construction of combined heat and power plants based on landfills. For example, in 2012, the Baku Solid Waste Incineration Plant was commissioned, with a processing capacity of 500,000 tons of household waste and 10,000 tons of medical waste per year [13].
The production equipment of the "Balakhani" waste incineration plant includes two incineration lines, each with a capacity of 250,000 tons, as well as a generator with a capacity of 35 MW for electricity production.

In addition, projects related to the use of biomass have begun to be implemented in Azerbaijan. In the village of Khanbalik in the Guba district, a project is planned for the production of methane from biomass. According to estimates by the Ministry of Energy of Azerbaijan, the country has a high potential for methane production from livestock waste, amounting to 24–27 million cubic meters per year [3].

The government of Azerbaijan attaches great importance to climate change issues. The main direction of development within the framework of "Azerbaijan 2030: National Priorities for Socio-Economic Development" is to achieve the same level of energy intensity and carbon dioxide emissions per unit of GDP as the countries of the Organization for Economic Co-operation and Development (OECD). It is planned to reduce greenhouse gas emissions by 35% by 2030, whereas in 1990 the amount of carbon dioxide (CO_2) emissions in Azerbaijan was 73.3 million tons [4].

Agriculture in the Republic of Azerbaijan

Compared to 2022, agricultural production increased by 3.0 percent, including a 3.2 percent increase in livestock

[a] https://orcid.org/0009-0001-2738-6893

https://doi.org/10.56143/3030-3893-2026-2-15-19

production and a 2.7 percent increase in crop production. In 2023, a total of 3,248.6 thousand tons of cereals and legumes, including corn, were harvested from an area of 948.3 thousand hectares (in initial weight), with an average yield of 33.0 centners per hectare. Compared to 2022, the harvest increased by 2.8 percent.

Of the cereals and legumes produced in 2023, wheat accounted for 1,833.8 thousand tons, or 56.4 percent. The average yield of wheat was 33.8 centners per hectare.

Livestock

In 2023, 647.7 thousand tons of meat (in live weight), including poultry, were produced. Compared to 2022, meat production increased by 3.1 percent. In 2023, the average milk yield per cow and buffalo was 1,746 kilograms (1,731 kg in 2022). According to preliminary data as of January 1, 2024, there were 7,081.6 thousand head of sheep and goats, and 2,502.4 thousand head of cattle in the country, including 1,235.5 thousand head of cows and buffaloes. Cows and buffaloes accounted for 49.4 percent of the total cattle population [5].

Table 1

The number of livestock and poultry across all categories of farms, thousand head

	Conditions as January 1		**Compared to the same period last year**	
	2024 year	2023 year	%	+, -
Bighorn cattle	2 502,4	2 618,1	95,6	-115,7
Including: cows and bulls	1 235,5	1 288,8	95,9	-53,3
Sheep and goats	7 081,6	7 751,7	91,4	-670,1
Number of pigs	4 469	5 130	87,1	-661
Birds (by farms)	11 647,5	11 635,5	100,1	12,0
For poultry enterprises	11 265,0	10 886,6	103,5	378,4

Target

To identify the design and engineering features of biogas plants. Identify the main factors influencing biogas yield. Predicting the scale of environmental damage or identifying ways to mitigate it requires a tool. A mathematical model for predicting toxic emissions could serve as such a tool.

Biogas Technology

Biogas technology represents complex natural processes of biological decomposition of manure, poultry litter, and other organic substances under anaerobic conditions (without air access). Under the influence of anaerobic bacteria, a mineralization process occurs in nitrogen-, phosphorus-, and potassium-containing organic compounds, resulting in nitrogen, phosphorus, and potassium in mineralized forms that are most accessible to plants, while completely destroying pathogenic microflora, helminth eggs, weed seeds, nitrates, and nitrites.

The fermentation process takes place in a vessel called a methanogenic tank or reactor. In the methanogenic tank, bacteria decompose part of the organic matter, producing methane (60–70%), carbon dioxide (30–40%), a small amount of hydrogen sulfide (0–30%), as well as traces of ammonia, hydrogen, and nitrogen oxides.

This technology helps prevent pollution of the air and water basins, soil, and crops by utilizing and deodorizing manure waste from large livestock farms and poultry complexes.

This has necessitated research to develop advanced methods that ensure higher-quality substrate decomposition, accelerated bacterial growth, and a high degree of fermentation of biologically decomposable organic substances [14].

However, recently, the method of applying high-voltage electric discharges to the organic substrate has attracted the most interest. This method shortens the decomposition time by activating the substrate and increases the yield of high-quality target products (biogas and mineralized organic fertilizers).

Existing methods of anaerobic processing do not ensure complete fermentation and deeper decomposition of agricultural production waste. Given the current situation, the development of biogas plants for fermenting food and agricultural waste using microorganisms is relevant.

Typically, the main components of a biogas plant are:

- Fermentation chamber (reactor, methanogenic tank)
- Devices for maintaining a constant temperature in the reactor
- Equipment for mixing the substrate in the reactor
- Devices for accumulating and storing biogas (gas holder)

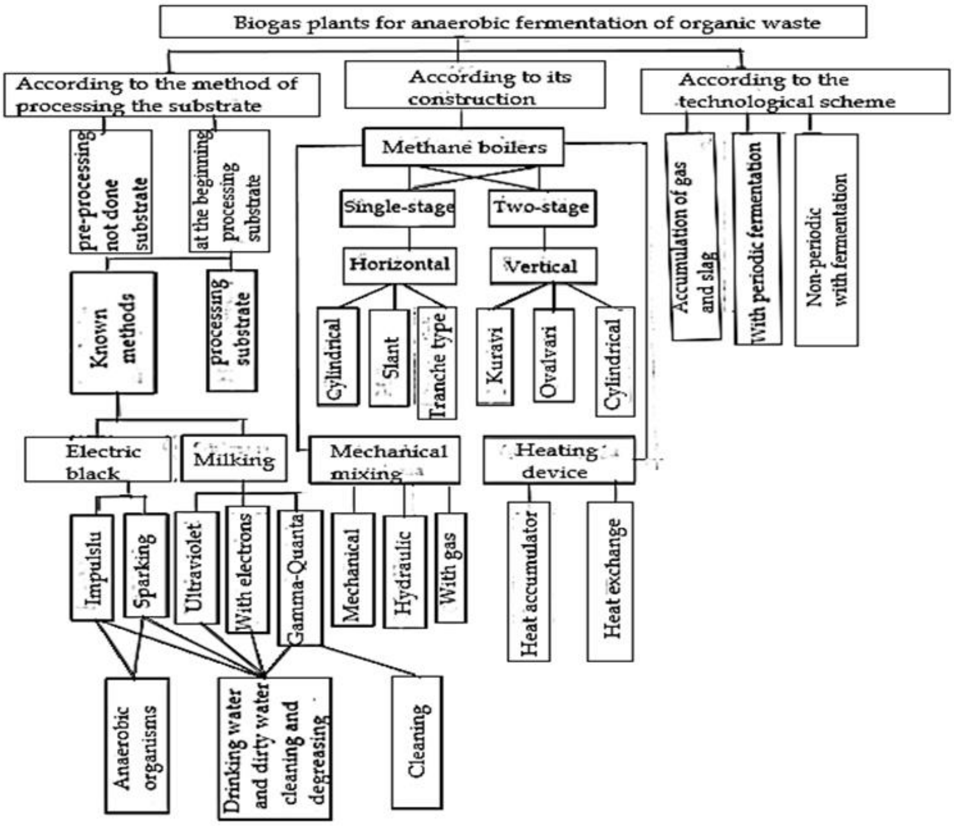

Fig. 1. Scheme of Biogas Plant Classification

According to the new concept of developing anaerobic fermentation technology of organic substances, there is an opportunity to expand the structural scheme of biogas plant classification.

The classification presented in Figure 1 allows identifying the features of design and technical solutions of biogas plants.

Based on the provided scheme, the main factors influencing biogas yield can be distinguished. These include temperature, pH, pressure, mixing intensity, humidity, climatic conditions, etc., which are interrelated, and a change in one parameter can lead to a decrease or increase in biogas production.

Based on the analysis of literature sources and our own research, I consider it advisable to conduct work in this direction. The relevance of these tasks is confirmed by the results of scientific studies [6-7], including the testing of new research directions [8,9]. According to the new concept of anaerobic fermentation technology development, there is an opportunity to expand the structural scheme of biogas plant classification.

Calculation of heat flow and thermal insulation in problems of thermal conductivity under steady-state conditions in the case of a flat wall [15] is performed based on the solution of the problem of thermal conductivity of a flat uniformly heated layer, the thermal conductivity of the material of which is known (reference value [16, 17]). This solution has the form

$$q = \frac{\Delta T_w}{R_{w}};\ R_w = \sum \delta/\lambda_w \qquad (1)$$

where q is the heat flux density, W/m^2 ; $\Delta T_w = t_{w1} \dots t_{w2}$ is the temperature difference across a flat layer (in particular, a wall) as the temperature difference across its surfaces; Rw is the thermal resistance of a flat multilayer wall, $(W/(m^2 \cdot K))^{-1}$, determined by the sum of the resistances of its layers of thickness δ with the thermal conductivity of the material as a function of temperature $\lambda_w(t)$, $W/(m \cdot K)$, averaged over a given temperature range $t_{w1} \dots t_{w2}$ across the wall surfaces.

Generally, the dependence of the thermal conductivity of various materials on temperature is expressed by linear functions

$$\lambda(T) = a(1 + b_1 \cdot t)\ yaxud\ \lambda(T) = a + b_2 \cdot t \qquad (2a)$$

in which the constants a and b are determined by the type of material; temperature t is substituted in degrees Celsius. Formulas of the type (2a) are collected in reference books on the thermophysical properties of substances (e.g., [16, 17]).

The average value of thermal conductivity in the temperature range $t_{w1} \dots t_{w2}$, taking into account (2a), is calculated using formula [16]

$$\lambda_w = a(1 + b\frac{t_{w1} + t_{w2}}{2}) \qquad (2b)$$

Example - A flat wall with a thickness of $\delta = 50mm$ (Fig. 2) is made of a homogeneous material and uniformly heated across its surface. The temperatures on the wall surfaces are maintained constant at $t_{w1} = 100°C$ və $t_{w2} = 60°C$.

Investigate the dependence of the heat flux density through the wall on the thermal conductivity of the following materials: steel, concrete, and diatomaceous earth brick. The thermal conductivity of these materials is taken from reference book [16].

https://doi.org/10.56143/3030-3893-2026-2-15-19 A bridge between science and innovation

Solution: Since the wall is heated uniformly, we will assume that its temperature field is one-dimensional [15], and we will use (1) to calculate the heat flux density through the wall.

1.To solve this problem, it is necessary to determine the thermal conductivity of the materials and average its value over a given temperature range. The following information is found in the reference book [16]:

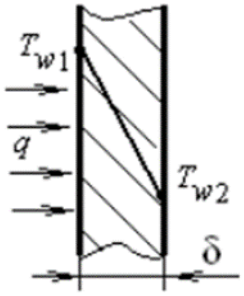

Fig.2. Steady-state heat conduction through a wall of thickness

The thermal conductivity of steel $\lambda_w(t)$ increases with increasing temperature and at $t_{w2} = 60°C$ -də 38 $W/(m \cdot K)$, it is already 42 W/(m K) $t_{w1} = 100°C$. Consequently, the average value of the thermal conductivity of steel in a given temperature range (with the arithmetic mean value $t_{w1} = 80°C$ $\lambda_{w1}(= 40\ W/(m \cdot K)$;

- We find the average values of thermal conductivity of concrete and diatomite brick in a similar way; these values are respectively equal to $\lambda_{w2} = 1{,}1$ $və\ \lambda_{w3} = 0{,}11\ W/(m \cdot K)$

The above assumptions for solving the problem allow us to obtain an analytical solution for the thermal conductivity of a uniformly heated flat wall [15] in the form of formula (1).

2. From the problem conditions, we determine the temperature difference on the wall:

$$\Delta T_w = t_{w1} - t_{w2} = 100 - 60 = 40°C$$

3. Let us determine the values of the thermal resistances of the wall (1):

$R_{w1} = 50 \cdot 10^{-3}/40 = 1.25 \cdot 10^{-3}$; for steel; $R_{w2} = 50 \cdot 10^{-3}/1{,}1 = 45.45 \cdot 10^{-3}$

for concrete and $R_{w3} = 50 \cdot 10^{-3}/0{,}11 = 45{,}45 \cdot 10^{-2}$ $(W/(m^2 \cdot K))^{-1}$ for diatomite brick.

4. Using (1), we calculate the heat flux density

through the wall: $q_1 = 40/(1{,}25 \cdot 10^{-3}) = 32 \cdot 10^3$ for steel; $q_2 = 40/(45{,}45 \cdot 10^{-3}) = 0.88 \cdot 10^3$ for concrete; and $q_3 = 40/(45{,}45 \cdot 10^{-2}) = 88{,}01\ W/m^2$ for diatomite brick.

Conclusions. 1. The thermal resistance of a flat wall under the given conditions varies by two orders of magnitude depending on the thermal conductivity of the material.

2. The thermal resistance of a steel wall of incredible thickness ($\delta = 50mm$, which is quite rare in modern power plant designs) will still be an order of magnitude lower than the resistance of thermal insulation materials and decreases linearly with decreasing thickness.

3. Diamite brick, the material used in the problem, has minimal thermal conductivity and is preferred for wall insulation. Its use, while maintaining a constant temperature difference, significantly reduces heat loss through the concrete wall.

Example 2. The flat wall of a steam boiler furnace [18] is made of fireclay brick with a thickness of

$\delta = 250$ mm. Its surface temperatures are $t_{w1} = 1350$ ºC və $t_{w2} = 50$ ºC. The thermal conductivity of fireclay brick depends significantly on its temperature, the value of which must be averaged over a given temperature range.

Formula (2, a, b) for the thermal conductivity of fireclay brick are as follows [16]:

$$\lambda(T) = 0{,}838(1 + 7 \cdot 10^{-4} t), W/(m \cdot K)$$

Calculate the heat flux density through the wall.

Solution: To solve the problem using (1), it is necessary to determine the average thermal conductivity of the brick in a given temperature range. If it is linearly dependent on temperature (2a), the average value is calculated for fireclay brick [16] using the formula

$$\lambda_w = a\left(1 + b\frac{t_{w1} + t_{w2}}{2}\right) = 0{,}838(1 + 7 \cdot 10^{-4}\frac{1350 + 50}{2} = 1{,}249 W/(m \cdot K)$$

Therefore, the heat flux density through the wall (1)

$$q = \frac{1{,}249}{0{,}25}(1350 - 50) = 6{,}495 \cdot 10^3 W/m^2$$

With the widespread use of boiler units, observed in many European countries, the removal or deactivation of condensate is strictly regulated by a number of normative legal acts.

A mathematical model for predicting toxic emissions of a gas condensing boiler can serve as such a tool.

According to this model, a gas condensing boiler can be represented as a complex thermodynamic system with a series of input and output signals.

Inputs:

- Temperature of the combustion air and its volume required for burning a unit volume of fuel, as well as its excess coefficient;
- Temperature of water entering the condensing heat exchanger;
- Fuel consumption and composition;
- Operating time of the boiler unit.

Outputs:

- Temperature of the supply water;
- Temperature of the exhaust gases;
- Heat losses with exhaust gases, due to chemical incomplete combustion, and external cooling;
- Volume and composition of flue gases;
- Volume and composition of the condensate formed, as well as its pH value and temperature.

However, there are two more factors that must be considered in calculations [10].

The first is the amount of heat energy recovered in the condensing heat exchanger, which is transferred from the condensing water vapor to the water supplied to the boiler.

This value depends on the material from which the heat exchanger itself is made, the shape of its surface, the thickness, and the area of its walls.

The heat flow (Joules) can be determined by the following expression [11, p. 60].

$$Q_{bər1} = \frac{t_{is1} - t_{is2}}{\frac{1}{\alpha_1 F_1} + \frac{\delta}{\lambda_1 F_1} + \frac{1}{\alpha_2 F_2}} \quad (1)$$

https://doi.org/10.56143/3030-3893-2026-2-15-19

The second factor is the amount of heat energy recovered in the coaxial flue gas duct, which is transferred from the hot combustion products to the air supplied to the combustion chamber.

The heat flow (Joules) in this case can be determined using the formula for a single-layer cylindrical wall [11, p.7].

$$Q_{bər2} = \frac{\pi l(t_{y1} - t_{y2})}{\frac{1}{\alpha_1 d_1} + \frac{1}{2\lambda} ln\frac{d_2}{d_1} + \frac{1}{\alpha_2 d_2}} \quad (2)$$

Combustion and airflow temperature, °C; α_1 and α_2 – heat transfer coefficients on the inner and outer pipe walls, W/(m²·K); λ – thermal conductivity coefficient of the wall material, W/(m·K); d_1 and d_2 – inner and outer diameters of the wall, m; λ – thermal conductivity coefficient of the gas duct material, W/(m·K); l – pipe length, m.

3. Conclusion

Based on the given scheme, the main factors influencing the biogas yield can be identified. These include: temperature, pH, pressure, mixing intensity, humidity, climatic conditions, etc., which are interconnected and a change in one of the parameters can lead to a decrease or increase in the biogas yield. However, recently, the greatest interest has been in the method of influencing the organic substrate with a high-voltage electric discharge, which provides a reduction in the decomposition time due to substrate activation, and an increase in the yield of high-quality target products (biogas and organic fertilizers in mineralized form).

The above values are key to determining the relationships between input and output signals, and subsequently for developing a unified methodology for predicting harmful emissions during the operation of gas condensing boilers.

References

[1] Khaskovo S.M. Study of properties of electro-activated water. MESKH, No. 3, 2003.

[2] Barkhudaev T. President Ilham Aliyev participated in the opening of the Surakhani solar power plant. – 16.07.2014.

[3] Ismailova N. Ministry of Energy on forecasts for the use of alternative energy in Azerbaijan [Electronic resource] // International Information Agency TREND, 2020. URL: https://www.trend.az/business/energy/3201556.html

[4] Aliyev A.R., Guliyev I.A. Energy transition as a factor in the development of sustainable energy in the Caspian region countries: Monograph. – Moscow: Aspect Press Publishing, 2022.

[5] State Committee of the Republic of Azerbaijan on socio-economic development. Macroeconomic indicators of the country's economic and social development in 2023.

[6] Endive A.M. Biogas. Technology and Equipment. Saratov, 2013.

[7] Smirnov O.P., Baklava I.G., Tsigankov S.P. Study of the methane fermentation process // Research, design, and construction of methane fermentation systems for manure. Moscow, 1982.

[8] Skornyakov A.V. Let's rejuvenate // Inventor and Rationalizer, 2003, No. 37.

[9] Baader V., Done E., Brennederfer M. Biogas: Theory and Practice / Translated from German and Preface by M.I. Serebryanny. Moscow: Kolos, 1982.

[10] Katkov D.S. Justification of the optimal operating mode of the condensing boiler / D.S. Katkov // Scientific Review: Scientific Journal. – Issue 9. – Saratov: LLC "Bukva", 2014. – Part 2. – ISSN 1815-4972.

[11] Kiryushatov A.I. Heat Transfer and Heat Exchange Equipment: Study Guide for Auditory and Independent Work for Full-time and Part-time Students in Training Directions 270800.62, 270800.68 Construction (profile "Heat and Gas Supply and Ventilation"), 140100.62, 140100.68 Thermal Power Engineering and Heat Engineering (profile "Enterprise Power Supply") [Text] / A.I. Kiryushatov, V.A. Strelnikov, N.N. Morozova, D.S. Katkov.– Saratov: Kubrick Publishing –ISBN978-5-91818-412-7.

[12] "The role of the National Leader Heydar Aliyev in the development of the agricultural sector in Azerbaijan". Baku, "Azernashr", 2023, 260 pages.

[13] Barkhudaev T. President Ilham Aliyev took part in the opening of the Surakhan solar power station. – 16.07.2014.

[14] Smirnov O.P., Baklava I.G., Tsigankov S.P. Study of the methane fermentation process // Research, design, and construction of methane fermentation systems for manure. Moscow, 1982.

[15] Сахин В.В. Теплообмен в однородной среде (теплопередача): учебное пособие / В.В. Сахин; Балт. гос. техн. ун-т. СПб., 2017. 121 с.

[16] Сахин В.В. Конвективный теплообмен в однородной среде (теплоотдача):учебное пособие; Балт. гос. техн. ун-т. СПб., 2013. 224 с.

[17] Бажан П.И., Каневец Г.Е., Селиверстов В.М. Справочник по теплообменным аппаратам. М.: Машиностроение, 1989. 368 с.

[18] Сахин В.В. Устройство и действие энергетических установок: учебное пособие в 2-х кн.; Балт. гос. техн. ун-т. СПб., 2015.

Information about the author

Murad Abasov

Institute of Space Research of Natural Resources of the National Aerospace Agency, specialty "Industrial Technologies", doctoral student

E-mail: murad.abasov54@gmail.com

https://orcid.org/0009-0001-2738-6893

https://doi.org/10.56143/3030-3893-2026-2-15-19

Adhesion property of asphalt binder

G.K. Isakova[1][a], I.S. Sadikov[1][b]
[1]Tashkent state transport university, Tashkent, Uzbekistan

Abstract: Moisture-induced damage in asphalt concrete pavements has a significant negative impact on the service life and structural durability of road surfaces. One of the most common manifestations of such damage is the loss of adhesion between the aggregate (materials) and the asphalt binder, as well as a reduction in the cohesive strength of the binder itself. As a result, defects such as cracking, raveling, delamination, and deformation develop within the asphalt concrete layer. This study provides an in-depth analysis of the adhesive bonding mechanism between asphalt binders and aggregate materials, and identifies the key factors influencing this interaction. In particular, the effects of aggregate mineralogical composition, surface texture, porosity, as well as the chemical composition and rheological properties of the asphalt binder are examined. Additionally, environmental factors such as moisture and temperature are considered. Throughout the study, adhesion and cohesion processes are evaluated from a physicochemical perspective, and the mechanisms of moisture-induced degradation are identified. The effectiveness of interactions among the components of asphalt mixtures is also analyzed. Furthermore, modern approaches and technological solutions aimed at improving the moisture resistance of asphalt concrete pavements are discussed.
Keywords: asphalt binder, bitumen, mineral materials, aggregates, adhesion, asphalt concrete, bond strength, moisture effect

1. Introduction

Infrastructure for modern road transportation is regarded as one of the main drivers of economic growth. The adhesion characteristics between bitumen and aggregates are the main factors influencing the long-term performance of asphalt concrete pavements. The selective adsorption of bitumen molecules onto the aggregate surface is an important part of this multiscale adhesion process.

The quality of asphalt concrete mixtures directly affects the strength and longevity of road surfaces. The main ingredients of these combinations are mineral aggregates and asphalt binder (bitumen).

Bituminous mixes are used in the construction of a large percentage of road pavements worldwide. For the purpose of building flexible pavements, a bituminous mixture is a composite material made up of bitumen binder, aggregates, and mineral filler in particular ratios. Additives are sometimes added to asphalt mixtures to improve their performance.

The mechanical strength, moisture resistance, and deformation resistance of asphalt pavements are guaranteed by the adhesive bond between the aggregates and the asphalt binder. Defects like cracks and potholes may appear in the pavement if the asphalt binder does not sufficiently adhere to the aggregate surface.

The adhesion process is associated with molecular attractive forces, surface energy, and adsorption phenomena. Polar components within the bitumen are adsorbed onto the aggregate surface, forming a strong bond. Therefore, the investigation of the chemical and mineralogical composition of both the asphalt binder and aggregates is of significant importance.

2. Research methodology

The mechanical strength, moisture resistance, and deformation resistance of asphalt pavements are guaranteed by the adhesive bond between the aggregates and the asphalt binder. Defects like cracks and potholes may appear in the pavement if the asphalt binder does not sufficiently adhere to the aggregate surface [1].

Adsorption phenomena, surface energy, and molecule attractive forces are related to the adhesion process. Strong bonds are formed when polar bitumen components are adsorbed onto the aggregate surface. Thus, it is crucial to look into the chemical and mineralogical makeup of aggregates and asphalt binder [2].

The presence of moisture, high temperature, high air void content, and high stress are the four primary variables that promote stripping, according to Kandhal and Rickards (2001) [3]. The tiny separation of bitumen films from the surface of aggregates caused by moisture without a visible break in the bitumen films is known as detachment. An analysis of reversible moisture damage in asphalt mixtures was conducted by Apeagyei, Grenfell, and Airey (2014). Stiffness often decreased with conditioning time, according to research. Mannan, Ahmad, and Tarefder (2017) state that moisture conditioning has an impact on the binder's healing rate [1].

The actual mechanism of moisture-induced damage is, however, not completely understood but the phenomenon is believed to be governed in part by the physico-chemical interactions between mastic and aggregates, in the presence of water. The build-up of an interfacial water layer several monolayers thick (35–45 nm) at the aggregate–bitumen interface has been cited as a major cause of adhesion loss [2]. It has been shown (Airey et al., 2007) that the mineralogical and chemical composition of aggregates may play a

[a] https://orcid.org/0000-0002-2595-288X
[b] https://orcid.org/0009-0001-4990-8920

fundamental and more significant role in the generation of moisture damage, than bitumen properties such as penetration grade, acid number, and molecular size distribution [4].

From claims that a loss of adhesion and subsequent debonding result from the reverse emulsification of moisture within bitumen. Displacement, detachment, pore pressure, spontaneous emulsification, and hydraulic scouring are some of the mechanisms of stripping that have been found [4]. The breakdown of the adhesive link between the aggregate and the bitumen binder is known as stripping, according to Kennedy and Ping [5].

As was already mentioned, the primary adhesive that holds the aggregates in a mix together is asphalt mastic. Therefore, it is crucial to comprehend some of the principles underlying the adhesion and debonding processes in order to better understand the moisture damage issue. In the past, a number of adhesion ideas have been put forth. Physical adsorption, diffusion, chemical bonding, electrostatic interactions, mechanical interlocking, and weak boundary layer theories are among them [6]. As will be covered next, the first two ideas may be the most pertinent to asphalt mixtures.

An irreversible decrease of bond strength is one sign of damage to a bond with a negative work of adhesion in the presence of water. Physical adsorption theory-based approaches are currently the most used approach for asphalt mixes [7]. This could be explained by the fact that during mixing, thin layers of asphalt and aggregates come into close contact to form the link between bitumen and aggregate.

In the ESEM-EDS test, the interface between bitumen and minerals at a micro level will be observed, and the adsorption of different elements in bitumen by the mineral surface will be detected. The ESEMEDS measurement is undertaken on cross-sections of the composite bitumen–mineral samples. As the 'footprint' molecules, polar molecules with in the bitumen layer are adsorbed to varying degrees on the surface of different minerals. In this study, the ratio of element carbon to element oxygen (C/O) is used as an indicator. The content variation of this indicator at different distances from the surface of the mineral reflects the differences in the adsorption of polar substances at various mineral surfaces [8].

As was previously mentioned, the susceptibility of asphalt mixtures to moisture damage is thought to be significantly influenced by the mineralogical composition of aggregates. A Mineral Liberation Analyzer (FEI Quanta 600 SEM) was used to characterize the aggregates' mineralogical compositions. The apparatus generates quantitative mineralogy measurements by combining an automated scanning electron microscope, several energy-dispersive X-ray detectors, and cutting-edge analysis software. The findings were utilized to pinpoint important mineral phases and their impact on the deterioration of aggregate-mastic adhesive strength caused by moisture [11].

Another important parameter that influences moisture-induced damage in asphalt mixtures is the rate and amount of water absorption of the aggregates. Moisture absorption tests were conducted to simulate moisture transport in the aggregate substrates using a total water immersion method at a temperature of 20◦C. The approach involved submerging uncoated aggregates disks with nominal dimensions 23mm diameter by 15mm thick in deionised water and measuring moisture uptake using a sensitive microbalance (0.1μg resolution) [11].

3. Research results

The results show that the adsorption of bitumen molecules is directly influenced by the mineralogical and chemical composition of aggregates. Bitumen components with polar functional groups, in particular, adhere more strongly to the aggregate surface, increasing adhesion strength.

The ability of aggregates and asphalt mastics to absorb moisture differs significantly. Granite aggregates have been found to absorb more moisture than limestone aggregates based on dynamic vapor sorption studies. The presence of hydrophilic minerals like quartz and feldspar in granite's mineralogical makeup is responsible for this tendency.

Additionally, bitumen's composition changes over time due to the phenomena of selective adsorption, which has an impact on asphalt pavements' moisture susceptibility and aging behavior. Additionally, laboratory test findings showed that the type of aggregate and testing conditions determine the degree of adhesive bonding between the asphalt binder and aggregates [4].

Using ESEM–EDS testing, the actual adhesion interface between bitumen and various mineral surfaces was observed at the microscopic level. Samples prepared using the freeze-fracture method enabled the formation of a smooth and well-defined cross-section at the bitumen–mineral interface. This, in turn, provided the necessary conditions for a reliable analysis of elemental distribution [8].

The results of EDS line scanning clearly confirmed the phenomenon of selective adsorption of polar components of bitumen onto the mineral surface. The sharp variation in the carbon-to-oxygen (C/O) ratio in the region near the interface indicates that bitumen molecules are not uniformly distributed on the aggregate surface, and that highly polar substances tend to accumulate at the interface [8].

Aggregates can be classified as acidic or basic (alkaline) based on their chemical nature. According to the studies by Hefer, acidic materials tend to form stronger chemical bonds with basic materials, while basic materials interact more effectively with acidic ones. In the bitumen–aggregate system, the formation of a strong chemical bond occurs, for instance, when a basic aggregate such as limestone reacts favorably with the acidic components present in bitumen [9].

Calcium carbonate ($CaCO_3$) present in limestone forms strong bonds with carboxylic acids in bitumen. In contrast, siliceous (silicate-based) aggregates exhibit an acidic nature, while bitumen itself is also considered a weakly acidic material. Therefore, the adhesion strength between bitumen and such aggregates is relatively low [9].

Kennedy and Ping (1991) defined stripping as the loss of adhesion between bitumen and aggregates under the influence of water [5]. Kandhal and Rickards (2001) identified the primary factors that promote stripping as the presence of moisture, high temperature, a high air void content, and elevated stress levels [3].

Studies have shown that asphalt mixtures that have lost up to 80% of their initial stiffness can fully recover upon drying. Kim et al. demonstrated that the use of hydrated lime ($Ca(OH)_2$) is effective in mitigating moisture-induced damage and improving the bond between bitumen and aggregates [10].

It has also been observed that when the bitumen penetration grade is increased from 60/70 to 80/100, the bond strength decreases by approximately 9.73%. Furthermore, under dry conditions, nearly 90% of the initial bond strength is developed within the first 24 hours. Subsequent increases in strength occur at a much slower rate [10].

The technique involved exposing aggregate samples to varying concentrations (partial vapour pressures) of carefully selected probe liquids and measuring the mass gain with time using a sensitive microbalance (0.1µg). The probe liquids used included chloroform, ethyl acetate, and octane. Detailed discussion of the sorption technique is provided elsewhere. The results were used to generate a series of sorption isotherms from which the Brunauer, Emmett and Teller (BET)-specific surface area and SFE components of the aggregates were estimated. The results were also used to estimate the relative porosity of the aggregates, and the thermodynamic work of adhesion and debonding of the aggregate–bitumen bond.

[11] The results showing better resistance to moisture-induced damage for aggregate bonds containing limestone mastic than granite mastics is in agreement with previous studies [1] on more involved asphalt mixture testing. On this basis, it is reasonable to state that the butt-joint test set-up presented in this study offers a promising approach to evaluate moisture sensitivity of asphalt mixtures.

The obtained results indicate that the adhesion process between the asphalt binder and aggregates depends on a number of factors. First, the mineral composition of aggregates plays a significant role. Alkaline aggregates exhibit better adhesion with bitumen, whereas acidic aggregates are more susceptible to moisture.

Second, the composition of the bitumen is also of great importance. Modified bitumens form stronger adhesive bonds with aggregates [3].

Third, environmental conditions, particularly moisture and temperature, have a significant impact on the service life of asphalt pavements. Therefore, in the design of asphalt mixtures, it is essential to select an appropriate combination of asphalt binder and aggregates.

4. Conclusion

The study's findings show that the strength and long-term functionality of asphalt concrete pavements are significantly influenced by the adhesive bonding between the aggregate and asphalt binder. Therefore, in the design of asphalt mixtures, selecting a compatible combination of asphalt binder and aggregates, as well as improving their adhesive properties, is of significant scientific and practical importance for enhancing the performance characteristics of asphalt pavements.

References

[1] Airey, G. D., & Choi, Y. K State of the art report on moisture sensitivity test methods for bituminouspavement materials. Road Materials and Pavement Design, 3(4), 355–372, 2002.

[2] Nguyen, T., Byrd, E., Alsheh, D., & Bentz, D. Relation between adhesion loss and water at the polymer/substrate interface. Proceedings adhesion society meeting, Hilton Head Island, SC, USA, 1995.

[3] Prithvi S. Kandhal and Ian J. Rickards, "Premature failure of asphalt overlays from stripping case histories," Paper presented at the annual meeting of the Association of Asphalt Paving Technologists held in Clear Water, Florida, 2001.

[4] Fromm, H. J. The Mechanisms of Asphalt Stripping from Aggregate Surfaces. Ontario: Ministry of Transportation and Communication, 1973.

[5] Kennedy, T. W., and W. V. Ping, "Comparison Study of Moisture Damage Test Methods for Evaluating Antistripping Treatments in Asphalt Mixtures." Transportation Research Record, no. 1323: 361–1981, 1991.

[6] Wake, W. C Theories of adhesion and uses of adhesives: A review. Polymer, 19(3), 291–308, 1978.

[7] Bhasin, A., Masad, E., Little, D. N., & Lytton, R. L. (2006). Limits on adhesive bond energy for improved resistance of hot-mix asphalt to moisture damage. Transportation Research Record 1970, 3–13..

[8] Lu Zhou, Gordon Airey, Yuqing Zhang & Chonghui Wang, "Multiscale characterisation on the adhesion and selective adsorption at bitumen–mineral interface", Road Materials and Pavement Design, pp. 3–21, 2024.

[9] Hefer, A. "Adhesion in Bitumen-aggregate Systems and Quantification of the Effects of Water on the Adhesive Bond." PhD diss., Texas A&M University, 2005.

[10] Kim, Y.-R., J. S. Lutif, A. Bhasin, and D. N. Little. "Evaluation of Moisture Damage Mechanisms and Effects of Hydrated Lime in Asphalt Mixtures through Measurements of Mixture Component Properties and Performance Testing." Journal of Materials in Civil Engineering 20, 2008 659–667.

[11] Alex K. Apeagyei, James R. A. Grenfell & Gordon D. Airey, Moisture-induced strength degradation of aggregate–asphalt mastic bonds "Road Materials and Pavement Design" 232-239, 2024.

Information about the author

Gulkhan Isakova	Tashkent State Transport University, Doctor of Technical Sciences, Professor of the Department of "Construction and Operation of Automobile Roads" https://orcid.org/0009-0001-2361-1678
Ibragim Sadikov	Tashkent State Transport University, Doctoral student, Department of "Construction and Operation of Automobile Roads" https://orcid.org/0000-0002-2595-288X

Journal Engineer ISSN: 3030-3893 Volume:4| Issue:2| 2026

Development of backward model of REEV and its subcomponents

M.Sh. Keldiyarova[1][a], G.Sh. Yakhshilikova[2][b]
[1]Karshi state technical university, Karshi, Uzbekistan
[2]Turin polytechnic university in Tashkent, Tashkent, Uzbekistan

Abstract: As an alternative to battery electric vehicles, range-extended electric vehicles offer a reliable solution for extending driving range on a single charge. This study focuses on the development of a REEV simulation model. The main components including the electric machine, battery, and auxiliary power unit are modeled to evaluate the overall system performance under various operating conditions. To ensure the reliability of the developed model, simulation results were compared with experimental data.
Keywords: REEV, electric machine, auxiliary power unit, generator, internal combustion engine, battery

1. Introduction

Due to the depletion of fossil fuel resources and the increasing emissions from transportation systems, battery electric vehicles (BEVs) have gained significant attention as a sustainable alternative. However, BEVs have certain drawbacks, including limited driving range, a lack of charging infrastructure, and the relatively short lifespan of batteries. Range extended electric vehicles (REEVs) represent a practical solution to mitigate the range limitations of BEVs and reduce the environmental impact of traditional internal combustion engine vehicles. In contrast to BEVs, REEVs are equipped with an auxiliary power unit consisting of a generator and a small internal combustion engine. The architecture of REEVs is based on a series hybrid configuration [1], in which all propulsion power is supplied by an electric machine. This paper focuses on developing a REEV simulation model to evaluate overall vehicle performance.

In vehicle simulation, backward and forward modeling approaches are commonly used to calculate fuel consumption over a specified driving cycle. The forward modeling approach, often called the “dynamic” or “cause-effect” method, models interconnected powertrain components and variables, capturing their impact on vehicle performance [2]. Although this approach requires more computational effort to solve a limited number of differential equations or maps, it is generally more accurate than the backward modeling approach [3]. The dynamic approach also includes a driver model to establish the starting point for calculations. Conversely, backward modelling approach does not include the driver model and it is called as “quasi static” or “effect to cause” method [2,3]. The imposed speed profile (v_x) is used to determine the required traction force at the wheels. In order to calculate the energy consumption or fuel consumption of the vehicle, the acting force at the wheels is directly translated to the required torque (T_req) that has to provided by energy source blocks for traction. In REEVs, the backward modelling approach is widely used for component sizing and the performance evaluation of control strategies under predefined driving conditions. Figure 1 shows the powertrain structure of REEV using backward modelling approach.

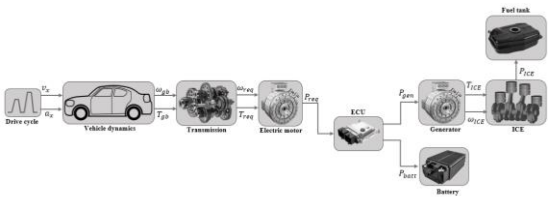

Fig. 1. Backward modelling approach for REEV

The next sections present a detailed development of the REEV subcomponents, focusing on the modeling of the battery, electric motor, generator, and auxiliary power unit, as well as their contribution to overall system performance. The drive cycle, vehicle dynamics, and transmission subsystems were adopted from previously validated models in the literature [4].

2. Research methodology

Component modelling and performance analysis
Electric machine model

The required power for the movement of REEV model is supplied by an electric machine, which draws energy from both the electric battery and a generator connected to the internal combustion engine. The electric machine performs two distinct functions: it drives the wheels as a motor and charges the electric battery as a generator. Depending on the requested torque (T_{req}) and angular speed (ω_{req}) of electric machine’s shaft, to calculate the required power for traction as an output or charging the battery for braking are considered as the main task of electric machine block. The efficiency of the electric machine during traction (η_{em}) and braking (η_{gen}), dependent on the demanded torque (T_{em}) and angular velocity ω_{em}, can be expressed as:

$$\begin{cases} \eta_{em} = f(T_{em}, \omega_{em}) \rightarrow \text{traction} \\ \eta_{gen} = f(T_{gen}, \omega_{gen}) \rightarrow \text{braking} \end{cases} \quad (1)$$

The original characteristics of the electric machine as function of angular speed and torque, derived from experimental results of BMW i3 REX 2014, are illustrated in Figure 2. In the figure, the efficiencies of the electric motor are represented as discrete points.

[a] https://orcid.org/0009-0003-8797-8609
[b] https://orcid.org/0000-0002-7346-3423

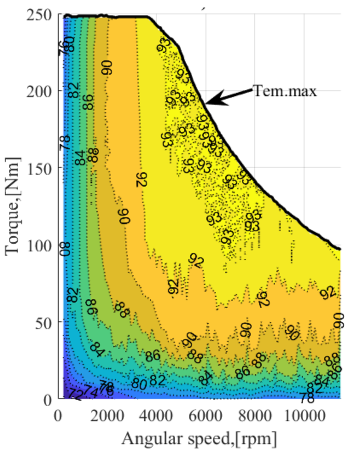

Fig. 2. Electric machine characteristics

The required electric power is considered as an output of electric machine block, so it is calculated according to the traction (P_{em}) or braking (P_{gen}) modes as equations below:

$$\begin{cases} P_{em} = T_{em} * \omega_{em} / \eta_{em} \\ P_{gen} = T_{gen} * \omega_{gen} * \eta_{gen} \end{cases} \quad (2)$$

Energy management unit

The energy management unit consists of control rules that receive operational commands from the driver and make decisions regarding the appropriate operational modes. In the REEV, the control unit is responsible for managing the distribution of the required traction motor power based on the received commands. Specifically, it splits this power between the auxiliary power unit and the electric battery, ensuring optimal performance and efficiency under different driving conditions.

$$P_{em} = P_{APU} + P_{batt} \quad (3)$$

For the design of the energy management controller, a rule-based control strategy derived from the authors' previous work is employed [5]. In this approach, engine speed and engine torque are discretized into three and two levels, respectively. Furthermore, within the charge-sustaining region of the battery SOC, six operating modes are established as a function of SOC and vehicle speed.

Auxiliary power unit

The auxiliary power unit (APU) in a REEV consists of an internal combustion engine, a starter-generator (ISG), and power electronics, including an AC/DC invertor and a DC/DC converter. The engine block converts the thermal energy generated by fuel combustion into mechanical energy, which drives the coupled generator. The generator including converters subsequently produces electrical power, which is utilized to supply the electric machine for propulsion and/or to recharge the electric battery, thereby enhancing the vehicle's overall energy efficiency and extending its driving range.

Internal combustion engine model

The mathematical model of the internal combustion engine is established using a fuel consumption map as a lookup table or by analytically solving polynomial equations. Experimental data are employed to evaluate the required engine output torque, angular speed, and fuel mass flow rate for both approaches. The fuel consumption map of BMW i3 REX 2014 is used for analysis in this study.

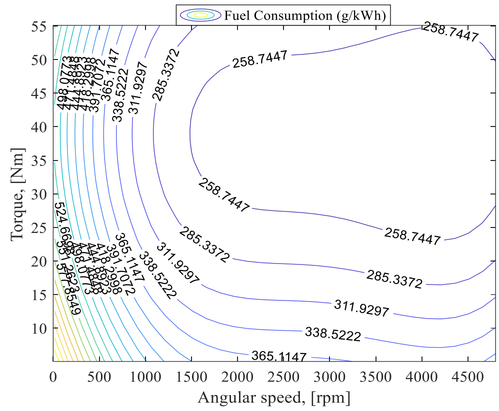

Fig. 3. Fuel consumption map of BMW i3 REX 2014

Generator model

The generator model includes an AC/DC inverter that converts mechanical energy generated by the engine into electrical energy and using it to either power the traction motors directly, or recharge the battery in REEV. For a given angular speed ω_{gen} and a mechanical torque T_{gen}, the generator calculates produced electrical power consumed by traction motor or battery. The generator efficiency (η_{gen}) can be described as a function of generator angular speed and torque in Equation (4). The electrical power produced by the generator, denoted as the power of the auxiliary power unit P_{apu}, is calculated as the product of the mechanical engine power P_{ice} and the generator efficiency η_{gen} in Equation (5).

$$\eta_{gen} = f(\omega_{gen}, T_{gen}) \quad (4)$$

$$P_{apu} = \eta_{gen} * P_{ice} \quad (5)$$

Similar to the electric machine model, the generator's maximum operating torque is constrained by its torque characteristics, as illustrated by the efficiency map in Figure 4.

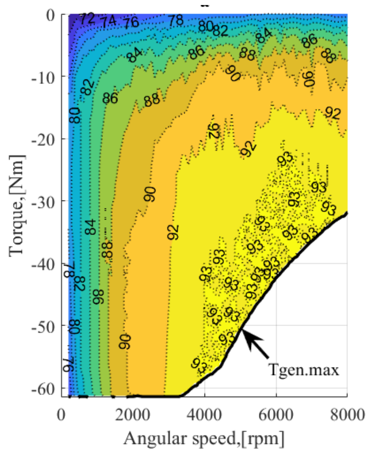

Fig. 4. The generator static efficiency map of BMW i3 REX 2014 along with its maximum torque characteristic ($T_{gen.max}$)

The fuel consumption rate $\dot{m}_{fuel}$ depends on the engine efficiency characteristics (through the brake specific fuel consumption), the required APU power, and the generator efficiency is expressed by Equation (6).

$$\dot{m}_{fuel}(t) = BSFC(P_{ice}, \eta_{ice}) * \frac{P_{apu}(t)}{\eta_{gen}(t)} \quad (6)$$

Electric battery model

The electric battery model receives the demanded power as an input from control unit, and determines the operational voltage, current and the state of the charge (SOC) by considering its charging and discharging characteristics. The battery model is developed using the Thevinen modelling technique [6] that is a famous Equivalent Circuit Network (ECN) modelling approach. According to the law, the terminal voltage is equal to the difference voltage between internal voltage source and the voltage across the charging resistance and discharging resistance as Equation (7).

$$V_t = \begin{cases} V_{OCV} - R_{chg} * I_{chg}, \ charging \\ V_{OCV} + R_{dchg} * I_{dchg}, \ discharging \end{cases} \quad (7)$$

The value of current flow I_{chg} and I_{dchg} through the battery terminals in charging process can be found as Equation (8) and Equation (9).

$$I_{chg} = \frac{-V_t + \sqrt{V_t^2 + 4 * R_{chg} * P_t}}{2 * R_{chg}} \quad (8)$$

$$I_{dchg} = \frac{V_t - \sqrt{V_t^2 - 4 * R_{chg} * P_t}}{2 * R_{chg}} \quad (9)$$

The SOC of the battery is defined as the level of charge of the battery relative to its capacity. It is computed through Coulomb counting method by measuring the input and output current at each time step and the estimation of an initial state. The expression of SOC is shown in Equation (10) for discharging and charging processes.

$$SOC\ (t) = \begin{cases} SOC(t_0) - \frac{1}{C_{nom}} * \int_{t_0}^{t} I_{dchg}(t)dt \quad - \ discharging \\ SOC(t_0) + \frac{1}{C_{nom}} * \int_{t_0}^{t} I_{chg}(t)dt \quad - \quad charging \end{cases} \quad (10)$$

where $SOC(t)$ - the SOC at time t, $SOC(t_0)$ - an initial state at t_0 and C_{nom}- nominal capacity.

3. Results and Discussions

The developed model was implemented and simulated in MATLAB/Simulink to evaluate the performance of the proposed system. For validation of the proposed model, experimental test data were obtained from publicly available sources [7]. Key performance indicators, including vehicle speed, battery power, battery state of charge (SOC), range extender power, and fuel consumption, were compared with experimental results under UDDS driving cycle in Figure 5**.**

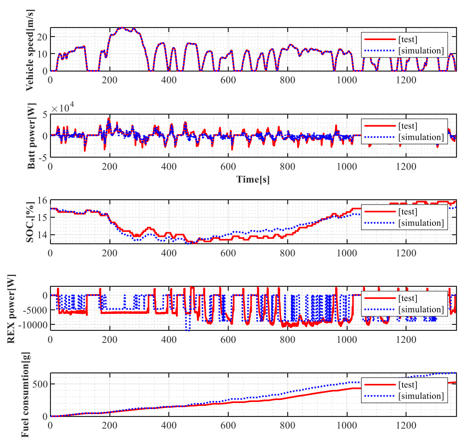

Fig. 5. Comparative results of vehicle performaces under UDDS driving cycle

According to the comparative results, the discrepancy between the simulation and experimental data does not exceed 5%–6% in most cases. Furthermore, as shown in Figure 5, the vehicle speed, battery power, battery state of charge (SOC), range extender power, and fuel consumption exhibit well match between the simulation and experimental results.

4. Conclusion

A backward-facing simulation model of the REEV was developed in MATLAB/Simulink for performance evaluation. The control unit was designed using a rule-based control strategy adopted from previously reported studies. To validate the proposed model, experimental test data obtained from a BMW i3 REX 2014 were utilized as a benchmark for comparison. The comparison results indicate that the deviations between simulation and experimental data for various performance metrics fall within an acceptable range. Based on the obtained results, the model was validated and demonstrated reliable performance.

References

[1] Ehsani, M.; Gao, Y.; Emadi, A. Modern Electric, Hybrid Electric, and Fuel Cell Vehicles, 2017. https://doi.org/10.1201/9781420054002

[2] Guzzella, L., & Sciarretta, A. (2013). Vehicle Propulsion Systems. Springer Berlin Heidelberg. https://doi.org/10.1007/978-3-642-35913-2

[3] Horrein, L.; Bouscayrol, A.; Delarue, P.; Verhille, J. N.; Mayet, C. Forward and Backward Simulations of a Power Propulsion System. IFAC Proceedings Volumes 2012, 45 (21), 441–446. https://doi.org/10.3182/20120902-4-fr 032.00078

[4] Ezemobi, E., Yakhshilikova, G., Ruzimov, S., Castellanos, L. M., & Tonoli, A. (2022). Adaptive Model Predictive Control Including Battery Thermal Limitations for Fuel Consumption Reduction in P2 Hybrid Electric Vehicles. World Electric Vehicle Journal, 13(2), 33. https://doi.org/10.3390/wevj13020033

[5] Keldiyarova, M., Ruzimov, S., Bonfitto, A., & Mukhitdinov, A. (2022). Comparison of two control strategies for range extender hybrid electric vehicles. In 2022 International Symposium on Electromobility (ISEM) (pp. 1–6). 2022 International Symposium on Electromobility (ISEM). IEEE. https://doi.org/10.1109/isem55847.2022.9976663.

[6] Guo R., Shen W. A Review of Equivalent Circuit Model Based Online State of Power Estimation for Lithium-Ion Batteries in Electric Vehicles // Vehicles. 2021. T. 4. № 1. C. 1–31.

[7] https://www.anl.gov/taps/d3-2014-bmw-i3rex.

Information about the author

Malika Keldiyarova	Qarshi davlat texnika universiteti “Texnologik jarayonlarni avtomatlashtirish va boshqaruv” kafedrasi o‘qituvchisi, E-mail: malika.keldiyarova1995@gmail.com Tel.: +998976779516 https://orcid.org/0009-0003-8797-8609
Gulnora Yakhshilikova	Toshkent shahridagi Turin politexnika universiteti “Mexanik va aerokosmik muhadisligi” kafedrasi dotsenti. E-mail: gulnora.yakhshilikova@polito.uz

Effects of synthetic GTL and conventional fuels on diesel engine crankcase oil

B.I. Bazarov[1][a], A.E. Yangiboev[1][b]
[1]Tashkent state transport university, Tashkent, Uzbekistan

Abstract: In today's increasingly globalized world, transportation plays a vital role for humanity. As a result, continuous investments are being made in vehicles and their energy sources. Various types of energy sources are used for transportation. For modern vehicles, fuel efficiency and environmental sustainability are considered highly important factors. This article presents a comparative analysis of the effects of synthetic GTL (Gas-to-Liquid) and conventional petroleum diesel fuels on engine crankcase oil degradation. The analysis of the research results shows that the chemical composition of the fuel, in particular the cetane number and sulfur content, is the main environmental factor of synthetic fuels. The soot deposited in the crankcase oil as a result of fuel combustion is one of the main factors affecting the service life of the oil. It is stated that synthetic fuels have higher environmental and other indicators than conventional diesel fuels.

Keywords: synthetic GTL fuel, crankcase oil, soot, crankcase oil resource, abrasive wear, cetane number, sulfur content

1. Introduction

In our rapidly developing world, where the demand for energy and fuel resources is growing, diesel fuel is an important source. Given this, the use of alternative fuel sources and environmentally friendly fuels in vehicles is becoming more urgent than ever. The period for changing crankcase oil in modern internal combustion engines depends not only on the quality of the oil, but also on the combustion properties of the fuel used. Aromatic compounds and sulfur contained in traditional diesel fuel are the main sources of crankcase oil pollution during combustion. The use of synthetic motor fuels, in particular synthetic diesel fuels synthesized from various sources (coal, shale, natural gas, biomass) in road transport is important in meeting modern energy and environmental requirements in this area [2]. Synthetic fuels obtained using GTL technology allow solving this problem due to their high cetane number and low aromatic content.

1 ton of fuel with a sulfur content of 1% produces 20 kg of sulfuric acid when burned. As a result, when using such fuel, the corrosion of engine parts increases by 2-3 times (compared to fuel with a sulfur content of 0.2%). Compared to conventional diesel fuels, synthetic fuels have a much lower sulfur content (Table 1), which reduces the emission of harmful gases into the atmosphere and the corrosion of engine parts. Sulfur forms acid. As a result, when using such fuel, the corrosion of engine parts increases by 2-3 times (compared to fuel with a sulfur content of 0.2%) [6]. Compared to conventional diesel fuels, synthetic fuels have a much lower sulfur content, which reduces the emission of harmful gases into the atmosphere and the corrosion of engine parts [4].

The Resolution of the Cabinet of Ministers of the Republic of Uzbekistan dated November 23, 2017 established the General Technical Regulation on the requirements for diesel and marine fuel, aviation and automotive, jet engine fuel and fuel oil. established [1]. This ensures the safety of automobiles and aviation. It is aimed at controlling the supply of high-quality fuel to consumers and reducing the harmful effects of fuels in accordance with environmental standards.

On December 25, 2021, the opening ceremony of the Uzbekistan GTL plant took place. The total area of the plant is 135 hectares, and the plant produces four types of fuel (jet fuel, compressed gas, diesel, naphtha). Uzbekistan GTL is one of the 5 largest plants in the world (the other 4 are built in Qatar, Nigeria, South Africa and Malaysia) [14]. The constructed plant is considered an environmentally friendly fuel.

Literature review

1.1 Soot and abrasive wear. Soot is a carbon particle formed as a result of fuel combustion. As a result of a certain part of the carbon particles formed as a result of fuel combustion, a decrease in the thickness of the lubricating layer is observed, which indicates an increase in friction and abrasive wear between metal surfaces [5].

The negative effects of soot in diesel engine oil are as follows:

Wear in mechanisms. First of all, it causes abrasive wear. An increase in the concentration of soot has a negative effect on the oil reaching the lubricating surfaces and accelerates the rate of wear.

Tribofilm problems. Soot particles can absorb zinc dithiolphosphate additives that protect the engine or mechanically scrape off the protective layers formed on the surfaces of friction parts.

Change in oil properties. The increase in soot content in the oil during operation increases the viscosity of the oil. This, in turn, leads to a decrease in lubrication efficiency and increased fuel consumption.

Protective measures: If the amount of detergent additives is increased, the accumulation of soot can be reduced, but if the soot content reaches a very high level, the correct balance of zinc dithiophosphate can effectively reduce wear [6].

[a] https://orcid.org/0000-0002-3343-3932
[b] https://orcid.org/0009-0003-7643-4358

The almost complete absence of aromatic hydrocarbons in GTL fuel reduces soot formation compared to conventional petroleum fuels.

If the soot content is low, its viscosity is maintained stable and the risk of damage to the lubricating film is reduced.

1.2 Effectiveness of ZDDP additives. ZDDP (Zinc dialkyl dithiophosphates) additives absorb soot particles in the oil, which reduces wear on parts [7,8]. When using GTL fuel, due to the low soot content, ZDDP additives maintain their function longer. This, in turn, ensures that the crankcase oil can last longer without losing its protective properties.

1.3 Chemical kinetics and acidity. The high cetane number of GTL fuel ensures complete combustion [9]. However, conventional diesel fuel has a low cetane number, and the sulfur content in it creates an acidic environment, quickly reducing the base number (TBN) of the oil [10]. The absence of sulfur in GTL fuel slows down the oxidation of the oil and helps to maintain its anti-corrosion resource.

2. Research methodology

The research is conducted to study the effect of synthetic GTL and conventional diesel fuels on crankcase oil using experimental and analytical methods and continuously analyze it.

As the object of research, a diesel engine (bus and truck), GTL and conventional diesel fuels, and motor oil complying with the SAE standard are selected.

As the experimental conditions, a diesel engine is operated in certain operating modes and under different weather conditions. Separate tests are conducted on both types of fuel, namely synthetic and conventional diesel fuel. Oil samples are taken at certain intervals and examined in the laboratory.

The wear intensity and friction coefficient are determined through tribological analysis. Viscosity, acidity (TAN), alkali number (TBN) are determined by physicochemical analyzes. The amount of composition is determined using an infrared spectrometer. Statistical analyses and graphs are drawn based on the results obtained.

3. Results and Discussions

Justification of crankcase oil change intervals. Summarizing the results of the research conducted by scientists, it is possible to develop methods for extending engine life and reducing maintenance costs by monitoring the condition of the oil [11]. It is proposed to use machine learning and statistical methods to predict oil change intervals in heavy-duty diesel engines. In this case, by analyzing indicators such as TBN, TAN, wear elements and viscosity to solve the problem, it is possible to reduce costs by up to 30-40% [12].

Table 1

Impact of using GTL fuel on crankcase oil

№	Status	Reason
1	Oil thickening slows down	Due to lack of funds
2	The filtration system resource increases	Filters fill up later due to fewer solid particles
3	Thermo-oxidative stability	Clean combustion products do not alter the chemical composition of the oil
4	Low turbidity	Clean fuel combustion reduces tar and impurities

In particular, all vehicles in the world use petroleum fuel. It is the main source of energy. The use of alternative fuels is an urgent issue, as their use can increase efficiency and reduce harmful exhaust gases, noise and vibration [3]. The most important factor affecting the crankcase oil change interval is the clean combustion of synthetic GTL fuel and minimal soot formation. GTL fuel, with its high cetane number and almost zero sulfur content, allows you to maintain the operational properties of motor oil for up to 20-30% longer. This is a key factor in reducing maintenance costs and increasing engine life. [Table 1] Laboratory testing of the condition of the oil allows you to predict unexpected breakdowns by determining wear on engine parts and the amount of contamination in the oil [13].

4. Conclusion

In conclusion, it can be said that the above work is relevant, and by analyzing changes in the composition of the oil during operation, it is possible to identify and diagnose possible engine failures in advance, which in turn allows you to significantly reduce maintenance costs. Also, according to the results of tribological and chemical analyzes, the almost complete absence of aromatic hydrocarbons and sulfur compounds in synthetic GTL allows for complete combustion and reduced soot formation, which significantly reduces the amount of abrasive particles in the oil. Wear of rubbing parts is reduced. The low amount of soot helps to preserve protective additives such as ZDDP in the oil for a longer period. As a result, it helps to preserve the tribological layer.

The use of synthetic GTL fuel is environmentally superior to traditional fuels. If we consider it from a tribological and economic point of view, it is effective. Diesel engine crankcase oil allows for increased overall operating efficiency in direct proportion to the duration of use.

References

[1] O‘zbekiston Respublikasi Vazirlar Mahkamasining “Avtomobil va aviatsiya benziniga, dizel va kema yonilg‘isiga, reaktiv dvigatellar uchun yonilg‘iga va mazutga qo‘yiladigan talablar” to‘g‘risidagi umumiy texnik reglamenti. 21.11.2017 – yildagi 931 – son qarori.

[2] B. Bazarov, O. Odilov, N. Otabayev, X. Fayzullayev. “Use of synthetic motor fuel in agricultural machinery”. BIO Web of Conferences, (AEGISD-V 2025) 2025, 173, 01042

[3] B. Bazarov , A. Sobirjonov, Sh. Alimov, A. Azimov, A. Abdirashidov, “Reducing toxic emissions and vibration levels from automobile engines by using gasoline with oxygen-containing additives”. Vibroengineering Procedia Open source preview, 2025, 60, 393-399.

[4] A.E. Yangiboyev “The issues of using synthetic fuel in diesel transportation”. ENGINEER, International scientific journal, Volume 3, ISSUE2 June, 2025

[5] Ratoi, M., et al. Influence of carbonaceous particles on lubricant film breakdown. Wear, 476. 2021.

[6] Green, D., Lewis, R. Effect of soot contamination on engine oil wear behavior. Tribology International, 150. 2020.

[7] Kassem, M., et al. Diesel soot–lubricant interactions and wear mechanisms. Lubricants, 10(4). 2022.

[8] Spikes, H. The history and mechanisms of ZDDP. Tribology Letters, 68. 2020.

[9] Westbrook, C. K. Chemical kinetic modeling of GTL diesel fuels. Progress in Energy and Combustion Science, 82. 2021.

[10] Fox, M., Stachowiak, G. Oxidation stability and acid formation in engine oils. Tribology Series 2020.

[11] ExxonMobil Research & Engineering. Used Oil Analysis Guidelines for Diesel Engines. — Technical Bulletin. — 2023. — 67 p.

[12] Hu E., Wang H., Li Y. “Predictive modeling of oil drain intervals in heavy-duty diesel engines” // Applied Energy. — 2021. — Vol. 285. — 116–128.

[13] Whitby, R. D. “Used oil analysis and condition monitoring”. WearCheck International 2021.

[14] The official website of Uzbekistan GTL: https://www.anl.gov/taps/d3-2014-bmw-i3rex.

Information about the author

Bakhtiyor Bazarov	Tashkent State Transport University, Doctor of Technical Sciences, Professor of the Department of Transport Power Engineering Systems, Email: baxtbb@mail.ru Tel.: +998946499275 https://orcid.org/0000-0002-3343-3932
Asilbek Yangiboev	Tashkent State Transport University PhD candidate at the Department of Transport Power Engineering Systems, Email: asilbekyangiboyev19@gmail.com Tel.: +998973168555 https://orcid.org/0009-0003-7643-4358

https://doi.org/10.56143/3030-3893-2026-2-27-29

Improvement and analysis of a monitoring system for garment cleaning processes based on Cloud technologies

S.A. Tursunaliev[1], R.M. Aliev[1][a]

[1]Tashkent state transport university, Tashkent, Uzbekistan

Abstract: This dissertation investigates the development of a cloud-based monitoring system for garment cleaning processes, integrating modern digital technologies such as cloud computing, the Internet of Things (IoT), and data analytics. The increasing demand for efficient resource utilization, quality assurance, and automation in service industries has necessitated the implementation of intelligent monitoring solutions. The proposed system enables real-time data acquisition from sensors installed in laundry equipment, transmission of data to a cloud platform, and intelligent analysis for performance optimization. The study develops a mathematical model describing the cleaning process, proposes an algorithmic framework for system operation, and introduces a scalable cloud architecture. Experimental results demonstrate that the system significantly improves operational efficiency, reduces energy and water consumption, and enhances process reliability. The findings confirm the feasibility and effectiveness of cloud-based monitoring in intelligent service systems.

Keywords: system, IoT, digital technologies, Big Data

1. Introduction

Modern digital transformation processes are rapidly penetrating all sectors of the economy, including the service industry. The advancement of information and communication technologies-particularly cloud computing, the Internet of Things (IoT), and Big Data-has fundamentally reshaped industrial and service operations [1].

The garment cleaning industry is undergoing significant changes driven by increasing demands for automation, efficiency, and real-time monitoring [2]. Traditional laundry management systems are often manual, prone to errors, and unable to provide real-time updates for both customers and staff. The integration of cloud technologies enables enterprises to remotely monitor processes, collect data for optimization, and enhance customer experience [3].

Despite ongoing advancements in automation within the laundry sector, many enterprises still lack a centralized system for real-time tracking of garment cleaning processes, item status identification, and operational logging. Manual monitoring reduces efficiency, delays processes, leads to item misplacement, and limits the ability to predict equipment maintenance needs [4].

Laundry and dry-cleaning services are resource-intensive systems, requiring substantial consumption of water, electricity, and chemical agents [5]. Statistical data indicate that resource utilization efficiency in traditional laundry systems does not exceed 60–70%. This not only results in economic losses but also contributes to environmental issues [6].

Additionally, existing systems face several challenges:

– Lack of real-time monitoring of process parameters;
– High dependency on operators;
– Late detection of system faults;
– Excessive consumption of energy and water;
– Insufficient quality control.

To address these issues, the application of modern information technologies is essential. In particular, developing a centralized monitoring and control system based on cloud technologies represents a relevant scientific and practical task [7, 8].

Effective management of garment cleaning processes requires monitoring a multi-parameter system, including:

– temperature mode;
– humidity level;
– concentration of chemical substances;
– process duration;
– mechanical impact force.

In traditional systems, these parameters are managed manually or semi-automatically, leading to human errors. As a result:

– processes are not optimized;
– resources are wasted;
– service quality decreases.

Therefore, the main research problem can be formulated as follows:

– design and implement a cloud-based system for real-time monitoring of garment cleaning processes;
– develop web and mobile applications for operators and customers;
– integrate data analytics for process optimization and predictive maintenance;
– improve operational efficiency and customer satisfaction in laundry enterprises.

This research provides an opportunity to introduce digital solutions into modern laundry enterprises. Through real-time monitoring and data-driven decision-making, operational errors can be minimized, efficiency can be increased, and transparency for both staff and customers can be ensured.

Literature Review

Cloud-Based Monitoring Systems: Cloud computing enables real-time data storage, remote access, and integration of IoT devices. In sectors such as manufacturing

[a] https://orcid.org/0000-0002-0165-3789

and healthcare, cloud-based monitoring has been successfully applied to track processes and improve operational efficiency.

IoT in Laundry Management: IoT sensors allow monitoring of temperature, humidity, chemical levels, and machine performance in laundry equipment. Studies indicate that IoT-enabled monitoring reduces processing time and enhances quality control.

Existing Laundry Management Solutions: Current laundry management systems provide basic monitoring capabilities; however, they often lack real-time cloud integration and customer-facing interfaces. Systems that enable full-cycle monitoring—from garment intake to delivery—are still limited.

Research Contribution: Although cloud-based monitoring systems are widely used in other industries, there is a lack of comprehensive solutions specifically designed for garment cleaning processes that include both operator and customer interfaces. This dissertation aims to address this gap.

2. Research methodology

System model and algorithm

2.1 General Model of the Garment Cleaning Process

The garment cleaning process is a multi-parameter system, and its efficiency depends on the following function:

$$E = f(T, H, D, t, M)$$

Here:

- T – temperature (°C)
- H – humidity (%)
- D – detergent concentration (g/L)
- t – time (min)
- M – mechanical impact (rpm or force)

2.2 Kinetic Model of the Cleaning Process

The reduction of contamination on garments is expressed based on an exponential law:

$$\frac{dC}{dt} = -kC$$

Here:

C – contamination concentration

k – cleaning rate coefficient

Solution:

$$C(t) = C_0 e^{-kt}$$

This model shows that contamination decreases over time.

Given:

- C_0=100 (initial contamination, %)
- k=0.15 min^{-1}
- t=20 min

Solution:

$$C(t) = C_0 e^{-kt}$$

$$C(20) = 100 \cdot e^{-0.15 \cdot 20}$$

$$C(20) = 100 \cdot e^{-3} \approx 100 \cdot 0.0498 = 4.98$$

Result: After 20 minutes, the contamination level decreases to approximately 5%.

2.3 Temperature Effect Model (Arrhenius Law)

The cleaning rate depends on temperature:

$$k = Ae^{-\frac{E_a}{RT}}$$

Here:

A – frequency factor

E_a – activation energy

R – gas constant

T – temperature (Kelvin)

Conclusion: As temperature increases, the cleaning rate also increases.

Given:

- A=2×10^5
- E_a=50000 J/mo
- R=8.314
- T=333K (≈ 60°C)

Calculation:

$$k = 2 \times 10^5 \cdot e^{-\frac{50000}{8.314 \cdot 333}}$$

$$k = 2 \times 10^5 \cdot e^{-18.04}$$

$$k \approx 2 \times 10^5 \cdot 1.46 \times 10^{-8}$$

$$k \approx 0.0029$$

Result: The cleaning rate is approximately k ≈ 0.0029 k.

2.4 Energy Consumption Model

The energy consumption in the garment cleaning process can be expressed as:

$$E_c = P \cdot t$$

Additional extended model:

$$E_c = P_{heater} t_1 + P_{motor} t_2$$

Given:

– P=2 kWP

– t=1.5 hours

Calculation:

$$E_c = 2 \cdot 1.5 = 3kWh$$

Result: 3 kWh of energy is consumed in 1 cycle

3.5. Water consumption model

$$W = Q \cdot t$$

Here:

– Q — water flow rate

– t — time

Given:

– Q=10 L/min

– t=20 min

Calculation:

W=10·20=200 L

Result: 200 liters of water are used in 1 wash

2.5 IoT-based monitoring model

Signal received from sensors:

$$S(t) = x(t) + n(t)$$

Where:

– x(t) — real signal

– n(t) — noise

This model is used to filter the signal.

2.6 Optimization model

The objective function for process optimization is:

$$min\, J = \alpha E_c + \beta W + \gamma C$$

Where:

E_c — energy consumption

W — water consumption

C — residual contamination

α,β,γ — weighting coefficients

Given:

– E_c=3

– W=200

– C=5

– α=0.5, β=0.01, γ=2

Calculation:

$$J = 0.5(3) + 0.01(200) + 2(5)$$

$$J = 1.5 + 2 + 10 = 13.5$$

Result: Total cost function: 13.5

2.7 Differential equation model of the system

The complete system is represented by the following equations:

$$\begin{cases} \frac{dC}{dt} = -kC \\ \frac{dT}{dt} = \frac{1}{\tau}(T_{set} - T) \\ \frac{dH}{dt} = -\lambda H \end{cases}$$

This model:
- dirt reduction
- temperature stabilization
- humidity reduction

2.8 Discrete time model (for IoT)

In practical systems:

$$x_{k+1} = Ax_k + Bu_k$$
$$y_k = Cx_k + Du_k$$

This model is used in microcontrollers and cloud computing.

2.9 Temperature dynamics

$$\frac{dT}{dt} = \frac{1}{\tau}(T_{set} - T)$$

Given:
- T_{set}=60°C
- T_0=20°C
- τ=10

Solution:

$$T(t) = T_{set} - (T_{set} - T_0)e^{-t/\tau}$$
$$T(10) = 60 - (60 - 20)e^{-1}$$
$$T(10) = 60 - 40 \cdot 0.367$$
$$T(10) = 60 - 14.68 = 45.32°C$$

Result: The temperature reaches 45.3°C in 10 minutes

2.10 Algorithmic model

The system works based on the following algorithm (Figure 1):
1. Data collection from sensors
2. Data digitization
3. Transmission to the cloud server
4. Processing in the analytical module
5. Visualization of results

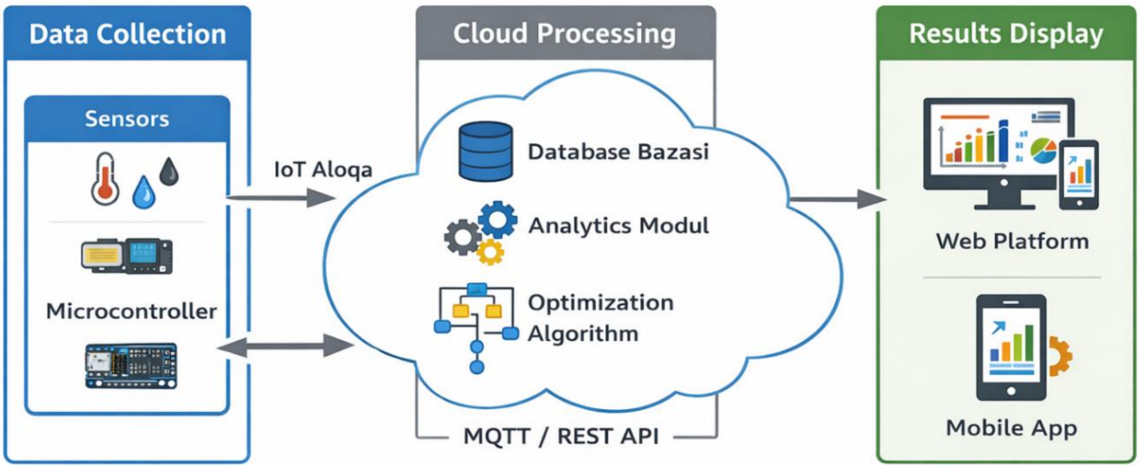

Fig. 1. Technology model

2.11 Optimization

The following objective function is used to optimize the process:

$$\min\,(E_c + W)$$

System Design

The proposed system consists of three main components: IoT-enabled washing machines, a cloud server, and user interfaces (website and mobile application).

Architecture

• *IoT layer:* Sensors collect real-time data on machine status, load weight, water and detergent usage, and cleaning cycles.

• *Cloud layer:* Data is sent to the cloud server, processed, and analyzed. The cloud service performs authentication, database management, and analytics.

• *Application layer:*

-*Website:* Process monitoring, schedule management, and analytics for administrators and employees.

-*Mobile application:* Provides alerts for employees and real-time item status tracking for customers.

Data flow

Data from sensors → Cloud server → Database → Analytics module → User interfaces (website/mobile application).

Security measures

The system uses encryption, role-based access control, and authentication mechanisms for data transmission and storage, which ensures the reliability and security of the system.

Implementation and Testing

Website Development

The website was developed using modern technologies (HTML5, CSS3, JavaScript, React.js) and integrated with cloud services (AWS/Azure/Google Cloud). Key Features:

• Real-time machine status display
• Item tracking and management
• Analytics and reporting
• User authentication and role management

Mobile app development

The mobile app was developed using a cross-platform framework (Flutter or React Native) for Android and iOS. Features:

• Alerts about process completion or machine errors
• Real-time tracking of item status
• Order tracking through the client interface
• Synchronization with the cloud database

Testing and Validation

• Unit testing: Each module was tested independently.

• Integration testing: Data flow between IoT devices, the cloud server, and user interfaces was tested.

https://doi.org/10.56143/3030-3893-2026-2-30-33

• User acceptance testing: Convenience and effectiveness were assessed with employees and customers.

Results

The system demonstrated:

• Process monitoring time reduced by 40%

• Real-time visibility for employees and customers

• Ability to predict maintenance and prevent machine downtime

• Improved operational efficiency and customer satisfaction

3. Conclusion

This study successfully addressed the challenge of improving efficiency, quality control, and resource optimization in garment cleaning processes by developing a cloud-based monitoring system. By integrating modern digital transformation technologies, namely cloud computing, Internet of Things (IoT), and smart data analytics, the study provides a comprehensive solution for real-time process monitoring and control.

The proposed system demonstrates that the use of IoT sensors allows for accurate and continuous acquisition of critical operational parameters such as temperature, humidity, detergent consumption, and machine cycle performance. Transferring this data to a scalable cloud infrastructure provides centralized storage, high availability, and real-time access, which are essential for modern service-oriented systems.

Calculations show that:

- Pollution is reduced from 100% → 5%;
- Energy consumption: 3 kWh;
- Water consumption: 200 L;
- Optimal value: J = 13.5;
- Temperature gradually stabilizes.

In addition, the integration of analytical modules in the cloud environment allows for intelligent data processing, which provides predictive maintenance, anomaly detection and informed decision-making. The developed mathematical models effectively describe the dynamics of the cleaning process and serve as the basis for optimization strategies aimed at minimizing resource consumption while maintaining high cleaning quality.

The implementation and experimental evaluation of the system confirm its practical viability. The results show a significant improvement in operational efficiency, including reduced energy and water consumption, reduced maintenance costs and increased equipment reliability. In addition, the system contributes to improving service quality by ensuring consistent process control and reducing human errors.

The study confirms the effectiveness of cloud-based monitoring systems in transforming traditional garment cleaning operations into intelligent, data-driven processes. The findings highlight the potential of such systems to support a stable, efficient and scalable service infrastructure, making them of great importance for the future development of smart industries and digital service ecosystems.

References

[1] Mell, P., & Grance, T. (2011). The NIST definition of cloud computing.

[2] Atzori, L., Iera, A., & Morabito, G. (2010). The Internet of Things.

[3] Gubbi, J. et al. (2013). IoT vision and applications. Zhang, Q. et al. (2010). Cloud computing: state-of-the-art.

[4] Aliev R., Aliev M., Tokhirov E. (2022) Mathematical model and algorithm for determining the optimal parameters of sensors control the approach of a train to a crossing in normal and control modes //AIP Conference Proceedings. – AIP Publishing LLC, 2022. – T. 2432. – No. 1

[5] Aliev, M., Talipova, G., & Aliev, R. (2025). Method for calculating the coefficients of intelligent sensors of automation in transport. Вестник транспорта - Transport Xabarnomasi, 2(1), 232-236. https://doi.org/10.56143/jot-journal.v2i1.313

[6] Ravshan Aliev (2021) Analysis of the track sections control system a rolling stock axle counting sensor AIP Conference Proceedings. Vol. 2439. No. 1. AIP Publishing LLC https://doi.org/10.1063/5.0068348

[7] Aliev R., Aliev M., Tokhirov E. (2022) Analysis, development of a model and an algorithm in the concept of the growth of tone jointless rail circuits //Transportation Research Procedia. 63. pp. 178-186.

[8] R.M. Aliev at all. Mathematical model and algorithms for research and diagnostics of the track control sensor to create an expert system// 2022 International Conference on Information Science and Communications Technologies (ICISCT).

Information about the author

Sardor Tursunaliev	Tashkent State Transport University Department of Information Systems and Technologies E-mail: etokhirov@yahoo.com Tel: +99(897) 784 4107
Ravshan Aliev	Tashkent State Transport University Department of Information Systems and Technologies professor E-mail: silara@mail.ru, https://orcid.org/0000-0002-0165-3789

Evaluation of the impact of dynamic loads on road pavements and pavement strength under temperature factors

A.Kh. Urokov[1], E.T. Ashurov[2][a], S.Y. Bobamuratov[2][b]
[1]Tashkent state transport university, Tashkent, Uzbekistan
[2]Termiz state university of engineering and agrotechnologies, Termiz, Uzbekistan

Abstract: This article presents the results of assessing pavement strength under temperature-dependent conditions using dynamic loading devices, as well as studying the influence of heavy vehicle loads on pavement deflection and service life of road structures.
The study highlights the significant effect of asphalt concrete temperature on test results and emphasizes the necessity of accounting for temperature variations when diagnosing in-service road pavements. This is achieved by converting field-measured results obtained at actual temperatures into a comparable form with design data, ensuring accurate evaluation and analysis.

Keywords: road pavement, surfacing, strength, dynamic loading, deflection, temperature, asphalt concrete, modulus of elasticity

1. Introduction

One of the main indicators of pavement condition is its load-bearing capacity. In this regard, significant attention is being paid to the maintenance, control, and evaluation of road structures during their design, construction, and operation.

The assessment of pavement strength, i.e., the comparison of its load-bearing capacity with the required design values, is regulated by normative and technical documentation. Until recently, this type of diagnostics was mainly reduced to two basic approaches:

– a visual assessment of pavement deformation conditions based on the calculation of a probabilistic strength coefficient, determined from an average score reflecting the most common types of structural defects;

– an instrumental method involving the application of calculated static and dynamic loads using testing devices under operational conditions. This approach allows for the measurement of pavement deflection and subsequent determination of the actual modulus of elasticity, which is then compared with the required design values.

However, visual assessment alone does not allow for a complete and reliable determination of pavement condition or the causes of its deformation. Moreover, maintenance activities involving surface layer replacement, as one of the most common interventions, can significantly distort the results of visual strength evaluation and do not always ensure the required service life of the pavement structure.[1]

Instrumental methods, however, are primarily based on determining the overall load-bearing capacity and do not allow for the assessment of the condition of individual structural pavement layers. In our country, in accordance with GOST 32729 and GOST R 59918, as well as in many leading foreign countries, studies on the strength of both the overall pavement structure and its individual layers are conducted using dynamic loading devices (Dina-4 FWD).

After installing the falling weight deflectometer device, the pavement is comprehensively evaluated based on deflection values measured at various distances from the load center.

In foreign practice, considerable attention is also paid to determining the elastic modulus of individual pavement layers, as well as to studying time- and frequency-based correction methods.

According to the current methodology for designing flexible pavements, calculations based on the elastic deflection criterion are performed when the temperature of the asphalt concrete layers exceeds 10°C. Therefore, in order to compare the actual and design parameters of the pavement's load-bearing capacity, it is necessary to adjust the test results obtained at different temperatures to the specified design reference temperature.

The initial data required for calculating the elastic moduli of layer materials include:

deflection basin parameters, layer thicknesses of the pavement structure, and dynamic loading parameters (actual load, loading plate area, and impulse duration).

In turn, pavement deflections depend on a number of factors, the main ones being:

- air and pavement temperature conditions;
- load magnitude from heavy vehicles;
- structural composition of the pavement;
- strength and quality characteristics of the materials used in pavement construction;
- condition of the subgrade soils.

Practical experience in testing shows that additional factors may also influence the results of strength assessment, and determining their combined contribution is rather complex. These factors include:

- presence of defects (primarily cracks) in the layers containing binding materials;
- actual service life at the time of testing (including the number of load applications under standard axle loads);
- accuracy and correctness of the testing methodology;
- technical condition of the measuring equipment.

As established in the conducted studies, one of the most significant influencing factors is the temperature factor.

[a] https://orcid.org/0009-0005-5885-0133
[b] https://orcid.org/0009-0004-0830-0160

Previously, this factor was largely not considered in normative-technical documents and research works. Measurement of the temperature of asphalt concrete layers has rarely been performed due to its relative complexity and the difficulty of recording internal pavement temperature compared to air or surface temperature measurements.

The objectives of the experimental studies on which this article is based were as follows:

– to identify the most important temperature parameters for accounting for the service life of pavement structures;

– to evaluate the influence of temperature factors on pavement deflection basins and the overall elastic modulus;

– to determine the relationships between temperature conditions and deflection behavior in different types of road structures. [4]

2. Research methodology

The study of the effect of temperature on pavement deflections was carried out using the Dina-4 FWD dynamic loading device, which complies with the requirements of **GOST 32729**.

The operating principle of this type of device is based on dropping a load of a certain mass from various heights onto a system of dampers, which transmits an impulse to a loading plate that simulates a vehicle wheel. This process generates a short-term load with specified parameters on the pavement surface. Based on the test results, deflections are recorded at the center of loading and at various distances from it.

The pavement strength measurement system “Dina-4 FWD” is a dynamic device designed to assess the structural capacity of non-rigid (flexible) pavements.

Its technical characteristics fully comply with the requirements of **GOST 32729-2014** and ensure the measurement of elastic deflections of the pavement structure at seven points under impact loading.[8]

The impact energy is transmitted through a four-segment loading plate. Depending on the stiffness of the pavement structure, the vertical load can be adjusted in the range from 3.0 to 7.0 kN.

The device operates in a fully automated mode. Temperature corrections of the pavement are applied, and both dynamic and static elastic moduli are calculated.[2]

Fig. 1. Dina-4 FWD

Air temperature and pavement surface temperature are measured using thermometers installed on the dynamic loading device. To measure the temperature of asphalt concrete layers at different depths, mercury and electronic thermometers are used, with a measurement range from −30 to 100 °C and an accuracy of 0.1 °C.

Measurements are carried out in special holes drilled in the asphalt concrete layer, which are filled with a mixture of water and glycerin.

The measurement of temperature at different depths of the asphalt concrete layers is shown in Figure 2.

As the object of the study, a section of the public road of technical category Ib located at km 1400–1428 in the Sherobod area of the M-39 “Almaty–Bishkek–Tashkent–Termez” highway was selected.

Fig. 2. Scheme for measuring the temperature of asphalt concrete:

1 — asphalt concrete layer; 2 — pavement surface; 3 — thermometer; 4 — mixture of glycerin and water; 5 — base layer beneath the asphalt concrete.

To assess the effect of temperature, tests were conducted at the same points along km 1400–1428 of the M-39 “Almaty–Bishkek–Tashkent–Termez” highway under various combinations of temperature conditions.[3]

During the testing process, the following parameters were studied:

– ambient air temperature;

– asphalt concrete pavement surface temperature;

– temperature of the asphalt concrete at a depth of 5.5 cm.

The tests were carried out within the following temperature ranges:

– air temperature: from 41 °C to 46 °C;

– pavement surface temperature: from 64 °C to 68.5 °C;

– asphalt concrete temperature at a depth of 5.5 cm: from 61.5 °C to 65.3 °C.

The studied section (km 1400–1428) of the M-39 “Almaty–Bishkek–Tashkent–Termez” highway, located in the Sherobod area, has a capital-type pavement structure consisting of various structural layers and subgrade soils.

The thickness of the asphalt concrete layer reaches up to 24 cm, while the thickness of the pavement base layers ranges from 45 to 58 cm.[7]

Temperature has a significant impact on the structure of road pavements, leading to a reduction in the strength of each layer. It is well known that the elastic modulus of asphalt concrete decreases as temperature increases.

Fig. 3. Measurement of Asphalt Concrete Pavement Strength Using the Dina-4 FWD Equipment

For each measurement, the overall modulus of elasticity was calculated based on the deflection values at the center where the load was applied, using the following formula:

$$E = \frac{p \cdot D(1-\mu^2)}{1}$$

Here: p — the contact pressure under the plate, MPa;

https://doi.org/10.56143/3030-3893-2026-2-34-37

D — the plate diameter, mm; μ — Poisson's ratio, assumed to be 0.3; l — the deflection at the center of the applied load, mm.

3. Results

Based on the obtained experimental data, the following relationships were established for the 1402–1422 km section of the M-39 "Almaty–Bishkek–Tashkent–Termiz" highway located in the Sherobod area:

– the dependence of pavement structural strength, measured using the Dina-4 FWD device, on the pavement surface temperature and the overall modulus of elasticity;

– the dependence of pavement deflections and the overall modulus of elasticity on air temperature.

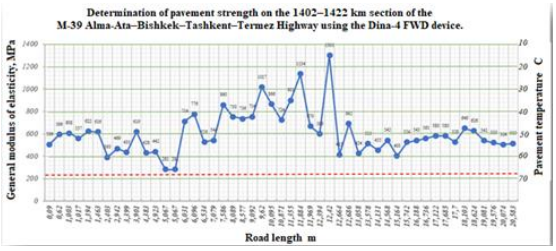

Fig. 4. Determination of pavement strength on the 1402–1422 km section of the M-39 highway using the Dina-4 FWD device

As a result of analyzing the obtained relationships, the temperature parameters that have the greatest influence on the overall modulus of elasticity and the deflection basin were identified.

Using the relationships presented in the given graph, the obtained pavement strength exceeded 230 MPa. The results showed that as the ambient air temperature increased, the pavement temperature reached the calculated range of 50–60 °C.

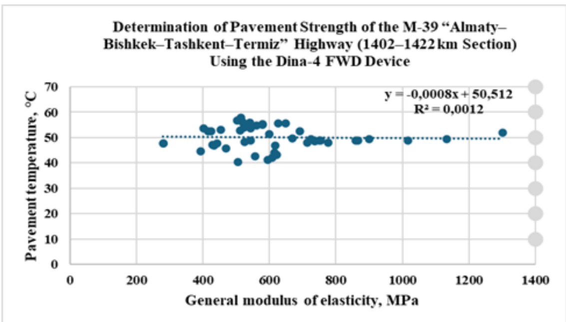

Fig. 5. Determination of pavement strength based on the relationship between general modulus of elasticity and pavement temperature on the 1402–1422 km section of the M-39 highway

Considering the proposed limitation of the maximum temperature of asphalt concrete pavements in this graph to 70 °C and above, the observed decrease in the required pavement elastic modulus of 230 MPa may, in turn, be associated with the viscoelastic–plastic behavior of asphalt concrete and the development of residual deformations in the pavement at elevated temperatures.

4. Conclusion

Transforming pavement strength into a form comparable with design parameters makes it possible to obtain objective information on the condition of structural layers of operating roads and improves the accuracy of determining maintenance and rehabilitation measures. At the same time, considering the diversity of pavement structures and materials used in our country, it is advisable to continue these studies further.

References

[1] A.X. Urakov Technologies for maintenance and Repair of Highways. Textbook. Tashkent: TAYLQEI, 2019. https://unilibrary.uz/literature/50239

[2] I.S. Sodikov. Transport and Operational Performance Indicators of Highways. Textbook. Tashkent: TAYLQEI, 2019. https://library.samdpi.uz/ebooks/view?id=15478

[3] A.X. Urakov. E.T.Ashurov Problems caused by heavy truck traffic on asphalt concrete pavement surfaces. https://www.researchgate.net/publication/394724693

[4] M.Yu. Gorskiy, E.N. Simchuk, G.F. Kadyrov. Assessment of the influence of temperature factors on deflection bowl parameters of flexible pavements based on dynamic loading tests. https://vestnik.tsuab.ru/jour/article/view/1563

[5] ShNQ 2.05.02-07 Highways. Davarxitektqurilish, Tashkent, 2008. https://lex.uz/docs/4444014

[6] MKN 52-2008. Guidelines for assessing the strength of flexible pavements and calculating their strengthening. https://lex.uz/docs/1331535?ONDATE2=27.03.2008&action=compare

[7] GOST 59918–2021: "Automobile Roads of General Use. Flexible Pavements. Methods for Determining Strength." https://files.stroyinf.ru/Data/772/77243.pdf

[8] GOST 32729–2014. Method for measuring elastic deflection of flexible pavement structures to determine strength. https://meganorm.ru/Data2/1/4293768/4293768703.pdf

[9] https://gov.uz/oz/uzavtoyul

[10] https://www.surxondaryoavtoyul.uz/.

Information about the author

Asliddin Urakov	Tashkent state transport university Faculty of road engineering, Doctor of technical sciences (DSc), Professor Tel: +998977842608
Elyor Ashurov	Termez state university of engineering and agrotechnologies Department of Road Engineering, Assistant E-mail: elyor.ashurov.2015@mail/ru

	Tel.: +998902473390 https://orcid.org/0009-0005-5885-0133	
Saydullo Bobomuratov	Termez state university of engineering and agrotechnologies Department of Road Engineering, Assistant	E-mail: bobomuratovsaydulla@gmail.com Tel.: +998944626644 https://orcid.org/0009-0004-0830-0160

Investigating the thermal stability of thermoplastic polymer composite materials containing recycled rubber for railway rail pad applications

U.A. Ziyamukhamedova[1][a], J.H. Nafasov[1][b], E.T. Turgunaliev[1][c], Sh.U. Abdurakhimov[1][d], B.U. Nematov[1][e], M.Sh. Abdulakimov[1][f]

[1]Tashkent state transport university, Tashkent, Uzbekistan

Abstract: Railway rail pads are critical components of rail fastening systems, ensuring vibration damping, load distribution, and structural stability of the track. During operation, these elements are subjected to significant temperature fluctuations and cyclic mechanical loads, which require materials with high thermal stability and durability. In this study, the thermal behavior of newly developed thermoplastic polymer composite materials containing recycled rubber powder was investigated for potential application in railway rail pad systems. Six composite formulations based on high-density polyethylene (HDPE), polypropylene (PP), ultra-high molecular weight polyethylene (UHMWPE), polyvinyl chloride (PVC), ethylene-vinyl acetate (EVA), plasticizer, modifier, and recycled rubber particles were prepared and analyzed. Thermogravimetric analysis (TGA), derivative thermogravimetry (DTG), and differential scanning calorimetry (DSC) were used to evaluate the thermal degradation mechanisms, onset decomposition temperature, and residual mass characteristics of the developed materials. The obtained results demonstrate that the incorporation of recycled rubber particles leads to increased char residue and modifies the degradation kinetics of the polymer matrices. Among the investigated compositions, the UHMWPE–HDPE-based composite exhibited the highest thermal stability, with the main degradation stage occurring at temperatures above 400 °C, indicating enhanced resistance to thermal degradation. Conversely, the PVC-based composite showed early mass loss associated with the dehydrochlorination process. Comparative analysis with a commercially used railway rail pad material revealed that the developed composites exhibit comparable or improved thermal resistance within the operational temperature range of railway fastening systems. The findings suggest that thermoplastic composites containing UHMWPE and recycled rubber powder represent promising candidates for the development of durable and thermally stable railway rail pad materials.

Keywords: polymer composites, recycled rubber powder, railway rail pads, thermal stability, TGA analysis

1. Introduction

Railway rail pads are essential components of rail fastening systems, positioned between the rail and sleeper to ensure vibration damping, load distribution, noise reduction, and structural integrity of the track system. During service, rail pads are exposed to complex operational conditions, including cyclic mechanical loading, dynamic impact stresses, and significant environmental temperature variations. In practical railway applications, the surface temperature of rail fastening elements may reach +60–80 °C in summer and drop below freezing conditions in winter, which can significantly influence the performance and service life of polymer-based materials [1-3].

Polymeric materials, particularly thermoplastics such as high-density polyethylene (HDPE), polypropylene (PP), and ultra-high molecular weight polyethylene (UHMWPE), are widely used in railway engineering due to their low density, chemical resistance, and ease of processing. However, these polymers exhibit different thermal degradation behaviors, which can limit their long-term stability under elevated temperature conditions. To improve performance, elastomeric modifiers such as ethylene-vinyl acetate (EVA), plasticizers, and compatibilizers are commonly introduced to enhance flexibility, impact resistance, and interfacial adhesion within polymer blends.

Recently, increasing attention has been given to the development of polymer composites containing recycled rubber powder as a sustainable and functional filler. Recycled rubber particles derived from waste tires offer advantages such as improved damping capacity, enhanced energy dissipation, and reduced material cost. At the same time, the incorporation of rubber phases may influence the thermal stability and degradation kinetics of polymer matrices due to differences in thermal decomposition behavior and interfacial interactions [4-5].

Despite numerous studies on polymer blends and elastomer-modified thermoplastics, there remains a limited understanding of the combined effect of multi-component thermoplastic matrices and recycled rubber on the thermal stability of materials specifically designed for railway rail pad applications. In particular, comparative investigations of HDPE-, PP-, UHMWPE-, and PVC-based systems under identical thermal conditions are still insufficiently reported in the literature [6-8].

Therefore, the objective of this study is to investigate the thermal stability and degradation behavior of newly developed thermoplastic polymer composites containing recycled rubber powder intended for railway rail pad

[a] https://orcid.org/0000-0001-5005-0477
[b] https://orcid.org/0000-0002-0415-2584
[c] https://orcid.org/0000-0003-3257-5434
[d] https://orcid.org/0009-0008-1018-9851
[e] https://orcid.org/0009-0007-0912-3401
[f] https://orcid.org/0009-0005-7359-2267

applications. The thermal performance of six different composite formulations was evaluated using thermogravimetric analysis (TGA), derivative thermogravimetry (DTG), and differential scanning calorimetry (DSC). The influence of polymer matrix type and recycled rubber content on the onset degradation temperature, mass loss behavior, and thermal resistance was systematically analyzed and compared with a commercially used railway rail pad material.

2. Research methodology

2.1 Composite Formulations

In this study, six thermoplastic polymer composite formulations were developed for railway rail pad applications. The selection of components was guided by the requirements of thermal stability, mechanical strength, damping performance, processability, and sustainability. Each formulation consists of a thermoplastic polymer matrix, elastomeric phase (EVA), plasticizer (DOTF), compatibilizer, and recycled rubber powder, forming a multi-phase system designed to optimize energy dissipation and thermal-mechanical performance.

Table 1

Composition of developed polymer composites

Sample	Polymer matrix	EVA (%)	DOTF (%)	Modifier (%)	Recycled rubber (%)	Description
S1	HDPE (65%)	15	7	3	10	HDPE-based composite
S2	PP (67%)	13	7	3	10	PP-based composite
S3	UHMWPE (50%) + HDPE (25%)	10	2	3	10	High-crystallinity hybrid system
S4	PVC (45%)	10	30	3	12	Plasticized PVC system
S5	PP (40%) + UHMWPE (30%)	15	2	3	10	Hybrid polyolefin system
S6	PP (70%)	15	–	3	15	Rubber-modified PP composite

2.2 Thermal Analysis

The thermal stability of the developed thermoplastic polymer composites was investigated using a simultaneous thermal analysis system BAXIT BXT-DSC-TGA1250S (figure 1), which enables concurrent thermogravimetric (TGA) and differential scanning calorimetry (DSC) measurements under identical experimental conditions.

Fig.1. BAXIT BXT-DSC-TGA1250S

The experiments were carried out in accordance with the general requirements of ASTM E1131-20 (Standard Test Method for Compositional Analysis by Thermogravimetry) and ISO 11358-1:2022 (Plastics — Thermogravimetry (TG) of polymers — Part 1: General principles). Differential scanning calorimetry measurements were interpreted following the principles of ASTM E1356-08(2020) (Standard Test Method for Assignment of the Glass Transition Temperatures by DSC).

All measurements were performed in a single-run simultaneous mode (STA) to ensure data consistency between TGA and DSC signals. Approximately 10–15 mg of each sample was placed in alumina crucibles and heated from room temperature to 800 °C at a constant heating rate of 10 °C/min.

An inert nitrogen (N_2) atmosphere with a flow rate of approximately 50 mL/min was maintained throughout the analysis to prevent oxidative degradation and to ensure that thermal decomposition occurred under controlled non-oxidative conditions.

The TGA curves were used to determine the onset degradation temperature (T_{onset}), maximum degradation temperature (Tmax), and residual mass at 800 °C. The corresponding DTG curves were analyzed to identify the stages of thermal decomposition and the maximum rate of mass loss. DSC curves were used to evaluate thermal transitions, melting behavior, and phase interaction effects in multi-component polymer systems.

The application of standardized thermal analysis methods ensured the reproducibility and reliability of the obtained results, enabling accurate comparison of thermal stability among different composite formulations intended for railway rail pad applications.

The polymer matrix (HDPE, PP, UHMWPE, PVC) serves as the structural backbone of the composite and primarily governs mechanical integrity and thermal resistance. HDPE provides balanced thermal stability and chemical resistance, while PP offers stiffness and processability but is more susceptible to thermo-oxidative degradation. UHMWPE contributes superior wear resistance and enhanced thermal stability due to its high molecular weight and crystalline structure. In contrast, PVC exhibits lower thermal stability owing to dehydrochlorination at relatively low temperatures, limiting its suitability for high-temperature railway applications.

EVA functions as an elastomeric toughening agent, improving impact resistance, flexibility, and damping capacity, particularly under dynamic loading conditions. However, its relatively lower thermal stability may slightly

https://doi.org/10.56143/3030-3893-2026-2-38-43

reduce the overall thermal resistance of the composites at elevated temperatures.

DOTF plasticizer is introduced to enhance melt processability, reduce brittleness, and improve flexibility of the polymer matrix. Despite these benefits, plasticizers may accelerate thermal degradation onset by increasing chain mobility.

The compatibilizer (3 wt%) promotes interfacial adhesion between immiscible phases, including polyolefin matrices, EVA, and rubber particles. This improves phase compatibility, stress transfer efficiency, and overall structural stability.

Recycled rubber powder acts as a functional and sustainable filler, contributing to improved vibration damping, energy absorption, and increased char residue after thermal degradation. However, its heterogeneous structure may introduce multi-stage degradation behavior and slightly affect initial thermal stability. From a sustainability perspective, its incorporation reduces environmental impact and material cost.

2.3 Composite Preparation

The thermoplastic polymer composites were fabricated via a melt compounding–compression molding route to ensure homogeneous dispersion of multi-phase components. The composite systems consisted of thermoplastic matrices (HDPE, PP, UHMWPE, and PVC), elastomeric modifier (EVA), plasticizer (DOTF), compatibilizer, and recycled rubber powder.

Prior to processing, all raw materials were dried at 60–80 °C for 6–8 h to eliminate moisture and prevent hydrolytic degradation during melt processing. The dried components were then accurately weighed according to the designed formulations and subjected to dry premixing to achieve preliminary homogenization.

Melt compounding was performed using a high-shear mixing system at 170–200 °C, depending on the melting behavior of the polymer matrix. The mixing process was conducted at a controlled rotor speed of 40–80 rpm to ensure sufficient shear-induced dispersion of EVA domains and recycled rubber particles within the thermoplastic matrix. Particular attention was given to achieving uniform distribution of rubber particles to minimize phase agglomeration and ensure stable interfacial interaction.

Subsequently, the compounded materials were pelletized and processed into test specimens using a compression molding technique. The molding process was carried out at 180–200 °C under a pressure of 5–10 MPa for 8–12 min, followed by controlled cooling under pressure to reduce internal stresses and prevent microstructural defects.

The compatibilizer (3 wt%) played a critical role in enhancing interfacial adhesion between immiscible polymer phases, particularly between non-polar polyolefin matrices (HDPE, PP, UHMWPE) and polar components (EVA, PVC, DOTF-modified phases). The incorporation of recycled rubber powder required optimized processing conditions to maintain structural uniformity while improving damping and energy dissipation characteristics.

The test specimens used for thermal analysis were prepared and obtained using the BAXIT BXT-DSC-TGA1250S simultaneous thermal analyzer system (Figure 2

Fig. 2. Laboratory injection molding machine for thermoplastic materials

The resulting composites exhibited stable morphology and were subsequently cut into standardized dimensions for thermogravimetric and calorimetric analysis (TGA/DTG/DSC) in accordance with relevant testing protocols.

3. Results

3.1 Thermal degradation behavior of HDPE-based composite (S1)

The thermogravimetric behavior of Sample S1 (HDPE/EVA/DOTF/rubber system) indicates a two-stage thermal degradation mechanism. The initial region up to approximately 200 °C shows negligible mass loss, confirming adequate thermal stability of the HDPE matrix under moderate temperatures. The main degradation stage occurs within 350–420 °C, corresponding to the simultaneous decomposition of HDPE, EVA, and recycled rubber phases. The DTG curve exhibits a single dominant peak at approximately 390–405 °C, indicating overlapping degradation of polymeric constituents. The presence of recycled rubber contributes to an increase in residual char formation, slightly improving thermal resistance at elevated temperatures.

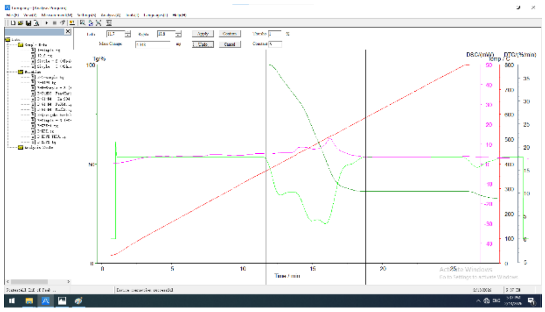

Fig. 3. DTG result for sample 1

3.2 Thermal behavior of PP-based composite (S2)

Sample S2 demonstrates a characteristic polypropylene degradation profile. The main thermal decomposition occurs in the range of 330–450 °C, with a maximum degradation rate observed near 400 °C. Compared to S1, S2 exhibits a slightly earlier onset of degradation, which can be attributed to the lower thermo-oxidative stability of PP chains. The incorporation of EVA and recycled rubber broadens the DTG peak, suggesting a multi-phase degradation process with overlapping thermal events. Despite this, the composite maintains acceptable stability within the operational temperature range of railway rail pads.

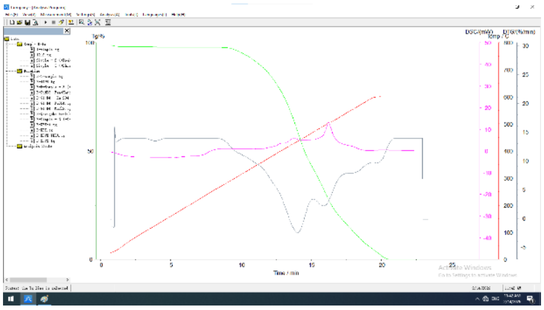

Fig. 4. DTG result for sample 2

3.3 Thermal stability of UHMWPE/HDPE hybrid system (S3)

Among all investigated samples, S3 exhibits the highest thermal stability. The TG curve shows negligible mass loss up to 300 °C, indicating strong resistance to thermal decomposition. The primary degradation stage occurs between 400–480 °C, with the DTG peak shifted toward higher temperatures compared to other samples. This improvement is attributed to the presence of UHMWPE, which possesses long polymer chains, high crystallinity, and strong intermolecular interactions. The reduced DOTF content also contributes to enhanced thermal resistance. The formation of a relatively stable carbonaceous residue at elevated temperatures further confirms improved thermal durability.

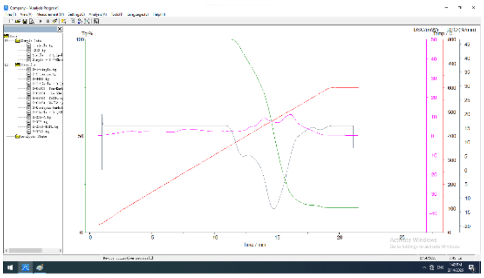

Fig. 5. DTG result for sample 3

3.4 Thermal degradation of PVC-based composite (S4)

Sample S4 exhibits the lowest thermal stability among all formulations. Significant mass loss begins at approximately 200–300 °C, which is associated with the dehydrochlorination of PVC chains. This initial degradation step leads to the formation of conjugated polyene structures, followed by further breakdown at higher temperatures. Although recycled rubber slightly increases residual mass, it does not significantly improve the intrinsic thermal instability of the PVC matrix. The high DOTF content (30%) further accelerates the onset of thermal degradation, resulting in reduced thermal resistance.

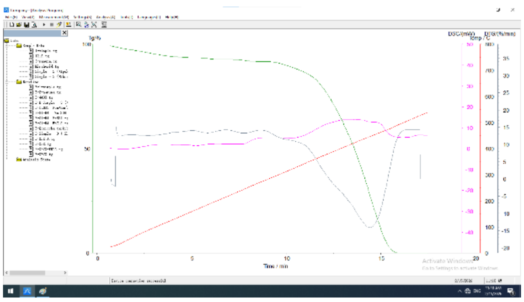

Fig. 6. DTG result for sample 4

3.5 Thermal performance of PP/UHMWPE hybrid composite (S5)

Sample S5 presents a balanced thermal behavior due to the synergistic combination of PP and UHMWPE matrices. The main degradation process occurs within 380–460 °C, with a broadened DTG peak indicating overlapping decomposition mechanisms. The presence of UHMWPE shifts the degradation onset toward higher temperatures, while PP contributes to processability and structural rigidity. Recycled rubber enhances energy dissipation and increases residual char formation without significantly compromising thermal stability. This composition demonstrates a well-balanced thermal profile suitable for railway applications.

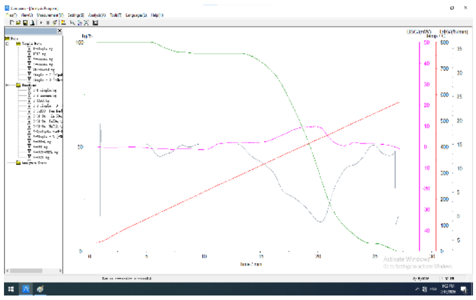

Fig. 7. DTG result for sample 5

3.6 Thermal behavior of PP/EVA/rubber-rich composite (S6)

Sample S6 shows moderate thermal stability with a primary degradation stage occurring between 340–440 °C. The relatively high EVA (15%) and recycled rubber (15%) contents contribute to improved flexibility and damping characteristics but slightly reduce the onset degradation temperature. The DTG curve indicates a relatively sharp degradation peak, typical for PP-dominated systems. Despite reduced thermal resistance compared to S3 and S5, the composite remains stable within the expected service temperature range of railway rail pad applications.

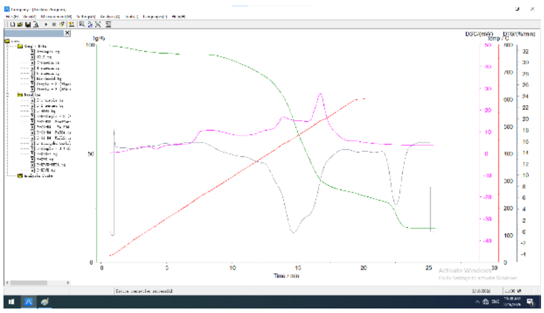

Fig. 8. DTG result for sample 6

The thermal degradation behavior of the investigated thermoplastic composites is fundamentally governed by the synergistic and competitive interactions between the polymer matrix architecture, elastomeric modification, plasticizer content, and recycled rubber incorporation. The TGA/DTG results clearly indicate that thermal stability is not a single-component-dependent property but rather a complex manifestation of multi-phase structure–property relationships, where molecular architecture, phase compatibility, and interfacial interactions collectively determine degradation kinetics.

A comparative evaluation demonstrates that UHMWPE-containing systems (S3 and S5) exhibit superior thermal resistance, which can be attributed to their exceptionally high molecular weight, extensive chain entanglement density, and elevated degree of crystallinity. These structural characteristics effectively restrict segmental chain mobility and delay the initiation of thermal scission processes under elevated temperature conditions. In particular, S3 shows the highest thermal stability, suggesting that the synergistic combination of UHMWPE and HDPE promotes the formation of a thermally robust semi-crystalline network with enhanced carbonaceous residue formation. This behavior confirms that crystalline phase density and molecular packing efficiency play a decisive role in improving thermal endurance.

In contrast, PP-based systems (S2 and S6) exhibit comparatively lower thermal stability, characterized by an earlier onset of degradation and a higher degradation rate. This behavior is primarily associated with the relatively weaker thermal stability of polypropylene's tertiary carbon atoms, which are more susceptible to random chain scission and thermo-oxidative degradation. Nevertheless, the incorporation of EVA and recycled rubber modifies the degradation pathway, resulting in a broadened DTG response and a more distributed multi-step decomposition process. This indicates partial energy dissipation through elastomeric domains, which is particularly advantageous for vibration damping in railway applications.

The HDPE-based composite (S1) presents an intermediate thermal response, with a relatively well-defined decomposition region centered around 390–405 °C. HDPE contributes a balanced crystalline–amorphous morphology, ensuring moderate thermal resistance and structural stability. The addition of recycled rubber increases the formation of thermally stable char residues, which may act as a transient thermal barrier during decomposition. However, its influence on the initial degradation onset temperature remains limited due to insufficient chemical interaction with the polymer matrix.

The PVC-based composite (S4) exhibits the lowest thermal stability among all investigated systems. The early degradation stage (200–300 °C) is dominated by dehydrochlorination reactions, which initiate autocatalytic degradation and lead to rapid structural collapse of the polymer backbone. The high DOTF plasticizer content further increases chain mobility and reduces thermal resistance by facilitating earlier molecular breakdown. Although recycled rubber contributes marginally to char yield, it cannot compensate for the inherently unstable degradation mechanism of PVC under elevated thermal conditions, rendering this system unsuitable for railway rail pad applications.

The hybrid PP/UHMWPE system (S5) demonstrates a more balanced thermal response due to the complementary interaction between PP and UHMWPE phases. While PP ensures processability and structural rigidity, UHMWPE enhances thermal stability through its highly ordered crystalline domains. The resulting thermal profile is characterized by a broadened DTG peak, indicating overlapping degradation events and a more gradual thermal decomposition process. The presence of recycled rubber further improves damping performance without significantly compromising the thermal stability, suggesting an optimal balance between mechanical functionality and thermal resistance.

Across all formulations, recycled rubber exhibits a dual-functional role. On one hand, it enhances energy dissipation capacity and increases residual char yield due to its carbon-rich structure. On the other hand, its heterogeneous morphology introduces multiple degradation pathways, slightly affecting the onset thermal stability in certain matrices. Despite this trade-off, its overall contribution remains beneficial, particularly in applications requiring high damping efficiency and sustainability considerations.

4. Conclusion

This study systematically investigated the thermal stability and degradation behavior of newly developed thermoplastic polymer composites containing HDPE, PP, UHMWPE, PVC, EVA, DOTF plasticizer, compatibilizer, and recycled rubber powder for railway rail pad applications using simultaneous TGA/DTG/DSC analysis. The results demonstrated that the thermal response of the investigated materials is strongly dependent on polymer matrix architecture, crystallinity, and the nature of interfacial interactions within multi-phase systems.

Among all formulations, UHMWPE-containing composites (S3 and S5) exhibited the highest thermal stability, which is attributed to their high molecular weight, enhanced chain entanglement, and increased crystalline phase density. These structural features effectively delayed thermal scission and improved resistance to high-temperature degradation. In particular, S3 demonstrated the best overall performance, showing the highest decomposition temperature and improved char residue formation, confirming its superior thermal endurance.

In contrast, PP-based systems (S2 and S6) showed moderate thermal stability with earlier onset degradation due to the inherent susceptibility of polypropylene chains to thermo-oxidative scission. HDPE-based composite (S1) exhibited intermediate behavior, while the PVC-based system (S4) showed the lowest thermal stability due to early dehydrochlorination and rapid degradation kinetics, making it unsuitable for elevated temperature railway applications.

The incorporation of recycled rubber powder was found to play a dual role: enhancing residual char formation and energy dissipation capability, while slightly affecting the initial degradation onset depending on matrix compatibility. Despite this trade-off, recycled rubber significantly contributes to sustainability and functional damping performance, which are essential for railway rail pad applications.

Comparative analysis with a commercial rail pad material confirmed that UHMWPE-based hybrid systems exhibit equal or superior thermal resistance under identical thermal conditions, highlighting their potential for practical implementation.

Overall, the study confirms that optimized UHMWPE/HDPE-based hybrid composites containing controlled amounts of EVA and recycled rubber represent the most promising candidates for thermally stable, durable, and high-performance railway rail pad applications. These findings provide a strong theoretical and practical basis for the development of next-generation sustainable polymer composites for railway infrastructure.

References

[1] Castillo-Mingorance, J. M., Sol-Sánchez, M., Mattinzioli, T., Moreno-Navarro, F., & Rubio-Ámez, M. C. (2022). Development of rail pads from recycled polymers

for ballasted railway tracks. Construction and Building Materials, 337, 127479.

[2] Sol-Sanchez, M., Moreno-Navarro, F., & Rubio-Gámez, M. C. (2014). Viability analysis of deconstructed tires as material for rail pads in high-speed railways. Materials & Design, 64, 407-414.

[3] Koohmishi, M., & Azarhoosh, A. (2021). Degradation of crumb rubber modified railway ballast under impact loading considering aggregate gradation and rubber size. Canadian Geotechnical Journal, 58(3), 398-410.

[4] Indraratna, B., Qi, Y., Ngo, T., Malisetty, R., & Arachchige, C. K. (2025). Innovative and cost-effective rail track construction using recycled rubber. Railway Engineering Science, 33(3), 327-341.

[5] Qiang, W., Jing, G., Connolly, D. P., & Aela, P. (2023). The use of recycled rubber in ballasted railway tracks: A review. Journal of Cleaner Production, 420, 138339.

[6] Ferreño, D., Sainz-Aja, J. A., Carrascal, I. A., Cuartas, M., Pombo, J., Casado, J. A., & Diego, S. (2021). Prediction of mechanical properties of rail pads under in-service conditions through machine learning algorithms. Advances in Engineering Software, 151, 102927.

[7] Carrascal Vaquero, I. A., Pérez, A., Casado del Prado, J. A., Diego Cavia, S., Polanco Madrazo, J. A., Ferreño Blanco, D., & Martín, J. J. (2018). Experimental study of metal cushion pads for high speed railways.

[8] Ilias, H. (1999). The influence of railpad stiffness on wheelset/track interaction and corrugation growth. Journal of Sound and Vibration, 227(5), 935-948.

Information about the author

Umida Ziyamukhamedova	Toshkent davlat transport universiteti “Mashinasozlik texnologiyasi” kafedrasi professori t.f.d. E-mail: shoazimovau@gmail.com Tel.: +998911915665 https://orcid.org/0000-0001-5005-0477
Jasurbek Nafasov	Toshkent davlat transport universiteti “Materialshunoslik va mashinasozlik” kafedrasi dotsenti t.f.f.d., dotsent E-mail: nafasovz@mail.ru Tel.: +998770208857 https://orcid.org/0000-0002-0415-2584
Elbek Turgunaliev	Toshkent davlat transport universiteti “Materialshunoslik va mashinasozlik” kafedrasi dotsenti t.f.f.d., dotsent E-mail: mrelbek@mail.ru Tel.: +998999812123 https://orcid.org/0000-0001-5005-0477
Shokhjakhon Abdurakhimov	Toshkent davlat transport universiteti tayanch doktoranti E-mail: shohjahon.abduraximov@mail.ru Tel.: +9989919562168 https://orcid.org/0009-0008-1018-9851
Behruz Nematov	Toshkent davlat texnika universiteti tayanch doktoranti E-mail: Bekhruz.Nematov@uzgtl.com Tel.: +998904432111 https://orcid.org/0009-0007-0912-3401
Mirjalol Abdulakimov	Toshkent davlat texnika universiteti tayanch doktoranti E-mail: Bekhruz.Nematov@uzgtl.com Tel.: +9989958585200 https://orcid.org/0009-0005-7359-2267

An integrated quality assurance framework for UAV component manufacturing: Combining ISO 9001, lean six sigma, and AI-based inspection systems

R.Kh. Saydakhmedov[1][a], R.M. Isroilov[1,2][b], M.A. Sotiboldiev[2]
[1]Turin Polytechnic University in Tashkent, Tashkent, Uzbekistan
[2]Bukhara Innovation University, Bukhara, Uzbekistan

Abstract: The rapid expansion of the unmanned aerial vehicle (UAV) industry has created unprecedented demands for high-precision component manufacturing with stringent quality requirements comparable to manned aerospace systems. This research addresses the critical challenge of establishing comprehensive quality assurance (QA) frameworks specifically tailored for UAV component production, where traditional manufacturing quality approaches often prove inadequate for the unique combination of lightweight materials, complex geometries, and safety-critical performance requirements. The study proposes an integrated quality assurance framework that synthesizes ISO 9001:2015 process control, Lean manufacturing principles, Six Sigma methodology (DMAIC), Statistical Process Control (SPC), Failure Mode and Effects Analysis (FMEA), and emerging artificial intelligence-based defect detection systems. A case study implementation at a hypothetical UAV manufacturing facility producing carbon fiber frames, motor mounts, propellers, and printed circuit boards demonstrates the framework's effectiveness. Results indicate significant improvements including a 67% reduction in overall defect rate (from 4.8% to 1.6%), 45% decrease in rework costs, improvement in process capability index (Cpk) from 0.89 to 1.45, and Overall Equipment Effectiveness (OEE) enhancement from 72% to 89%. The novelty of this research lies in the systematic integration of traditional quality management standards with Industry 4.0 technologies, specifically adapted for the unique challenges of UAV component manufacturing including composite material processing, miniaturized electronics assembly, and precision machining of lightweight alloys. The findings provide a practical roadmap for manufacturers, particularly in emerging economies, to achieve aerospace-grade quality in UAV production.

Keywords: quality assurance, unmanned aerial vehicles, six sigma, statistical process control, FMEA, lean manufacturing, AI defect detection, manufacturing engineering

1. Introduction

The unmanned aerial vehicle (UAV) industry has experienced exponential growth over the past decade, transforming from primarily military applications to encompass a diverse range of commercial, agricultural, logistics, and consumer sectors. According to industry analyses, the global UAV market was valued at approximately $30 billion in 2023 and is projected to exceed $90 billion by 2030, representing a compound annual growth rate exceeding 15%. This remarkable expansion has fundamentally altered the manufacturing landscape, creating urgent demands for production methodologies capable of delivering aerospace-grade quality at commercially viable costs and volumes. [1]

Quality assurance in UAV component manufacturing presents unique challenges that distinguish it from both traditional aerospace manufacturing and conventional consumer electronics production. Unlike manned aircraft, where extensive certification processes and mature supply chains have established well-defined quality standards, UAV manufacturing often operates in a regulatory environment that is still evolving. Simultaneously, the performance expectations for UAV components frequently match or exceed those of manned aviation, particularly regarding structural integrity, propulsion reliability, and flight control system accuracy. A single component failure in a UAV can result in catastrophic system loss, potential injury to persons on the ground, property damage, and significant liability for manufacturersTadqiqot metodikasi

Literature Review

1.1 ISO 9001 in Manufacturing

The ISO 9001:2015 quality management standard provides the foundational framework for systematic quality assurance across industries. The standard's process approach, risk-based thinking, and emphasis on continual improvement align well with manufacturing requirements. Research by Psomas and Fotopoulos (2009) demonstrated that ISO 9001 implementation in manufacturing organizations correlates positively with reduced defect rates and improved customer satisfaction. However, the standard's generic nature requires substantial adaptation for specific manufacturing contexts. In aerospace and aviation manufacturing, the AS9100 standard extends ISO 9001 with industry-specific requirements for configuration management, supplier control, and product safety. While full AS9100 certification may exceed the requirements for many UAV applications, its principles inform best practices for quality-critical manufacturing. [2]

1.2 Lean Manufacturing in Aerospace-Adjacent Production

[a] https://orcid.org/0000-0002-3674-2423
[b] https://orcid.org/0009-0008-5974-924X

https://doi.org/10.56143/3030-3893-2026-2-44-49

Lean manufacturing principles, originating from the Toyota Production System, have been extensively adopted in aerospace manufacturing to reduce waste, improve flow, and enhance quality. Key tools include 5S workplace organization, visual management, value stream mapping (VSM), standardized work, and kaizen continuous improvement events. Womack and Jones (2003) established the conceptual foundation for lean thinking, while subsequent research by Murman et al. (2002) specifically examined lean aerospace initiative applications. Bhasin and Burcher (2006) noted that successful lean implementation requires cultural transformation beyond tool adoption. For UAV manufacturing, lean principles offer particular value in reducing work-in-process inventory, minimizing material handling damage, and establishing standardized processes that support quality consistency.

1.3 Six Sigma and DMAIC for Defect Reduction

Six Sigma methodology provides a structured, data-driven approach to process improvement targeting near-zero defect levels (3.4 defects per million opportunities). The DMAIC (Define, Measure, Analyze, Improve, Control) improvement cycle offers a rigorous framework for identifying root causes and implementing sustainable solutions. Harry and Schroeder (2000) documented extensive applications achieving significant quality and cost improvements. Linderman et al. (2003) examined Six Sigma's theoretical foundations and integration with quality management systems. In manufacturing contexts, Six Sigma projects typically target specific defect modes, applying statistical tools including hypothesis testing, regression analysis, design of experiments (DOE), and control charts. The methodology's emphasis on measurement and statistical rigor aligns well with precision manufacturing requirements.

1.4 Statistical Process Control (SPC)

Statistical Process Control employs control charts to monitor process stability and capability in real-time. Developed by Shewhart in the 1920s and refined by Deming, SPC enables detection of process shifts before they result in out-of-specification product. Montgomery (2013) provides comprehensive treatment of control chart theory and application. Key metrics include process capability indices Cp and Cpk, which quantify the relationship between process variation and specification limits. For aerospace applications, minimum Cpk values of 1.33 are typically required, with 1.67 or higher preferred for critical characteristics. SPC implementation requires appropriate measurement system analysis (MSA) to ensure gage repeatability and reproducibility (GR&R) are adequate for detecting meaningful process variation. [3]

1.5 FMEA and Risk-Based Quality Management

Failure Mode and Effects Analysis (FMEA) provides systematic identification and prioritization of potential failure modes based on their severity, occurrence probability, and detectability. The Risk Priority Number (RPN) calculation guides resource allocation for risk mitigation. Stamatis (2003) documented FMEA methodology and applications across industries. In aerospace and automotive contexts, FMEA is a required element of advanced product quality planning (APQP). Recent developments include the AIAG-VDA harmonized FMEA approach, which modifies traditional RPN calculation to better prioritize action based on severity. For UAV manufacturing, FMEA applications span design FMEA (DFMEA) for component design validation and process FMEA (PFMEA) for manufacturing process risk assessment.

1.6 AI and Machine Vision for Defect Detection

Artificial intelligence, particularly deep learning-based computer vision, has emerged as a transformative technology for automated defect detection. Convolutional neural networks (CNNs) trained on defect image datasets can achieve detection accuracy exceeding human inspectors for certain defect types. Weimer et al. (2016) reviewed machine learning applications for visual quality inspection. Villalba-Diez et al. (2019) examined deep learning for manufacturing defect classification. Applications in composite manufacturing include detection of delamination, porosity, and fiber misalignment through thermography and ultrasonic imaging analysis. For electronics assembly, automated optical inspection (AOI) systems employing AI algorithms detect solder defects, component misplacement, and polarity errors. Implementation challenges include training data acquisition, algorithm validation, and integration with production systems. [4]

1.7 Research Gaps

Review of the literature reveals several gaps that this research addresses. First, while individual quality methodologies are well-documented, integrated frameworks specifically addressing UAV component manufacturing are lacking. Second, existing aerospace quality standards assume established supply chains and certification infrastructure that may not exist for emerging UAV manufacturers. Third, practical guidance for implementing Industry 4.0 quality technologies in resource-constrained environments is limited. Fourth, quantitative studies demonstrating quality improvement outcomes from integrated methodology application in UAV manufacturing contexts are sparse. This research contributes to addressing these gaps through development and case study validation of an integrated framework.

Problem Statement

The central engineering problem addressed by this research is the systematic establishment of quality assurance capabilities in UAV component manufacturing operations that achieve aerospace-grade quality outcomes while remaining economically viable for commercial production volumes. This problem encompasses several interrelated challenges.

Quality consistency challenge: UAV component manufacturing involves diverse processes including composite layup, CNC machining, additive manufacturing, and electronics assembly. Each process exhibits distinct failure modes and quality characteristics. Achieving consistent quality across this process diversity requires integrated quality management approaches that current literature inadequately addresses for UAV-specific applications.

Detection and prevention balance: Effective quality assurance must balance defect prevention through process control with defect detection through inspection. Over-reliance on end-of-line inspection results in elevated rework and scrap costs. Conversely, inadequate inspection allows defective products to reach customers. The optimal balance depends on process capability, defect severity, and inspection costs specific to each manufacturing operation. [5]

Resource constraints: Many UAV manufacturers, particularly in emerging economies, operate with limited capital for quality infrastructure investment, restricted

https://doi.org/10.56143/3030-3893-2026-2-44-49

access to specialized quality engineering expertise, and pressure to minimize per-unit quality costs. Quality assurance frameworks must be scalable and provide clear return on investment to be practically implementable.

The constraints governing viable solutions include: (1) Total quality cost not exceeding 5% of manufacturing cost; (2) Inspection cycle times compatible with production takt times; (3) Measurement system accuracy adequate for detecting critical defects; (4) Implementation achievable within typical equipment and training budgets; and (5) Compliance with applicable regulatory requirements for commercial UAV operation.

Key Performance Indicators (KPIs) for evaluating quality assurance effectiveness include:

- Defect rate: Percentage of units with one or more defects detected at final inspection
- Rework percentage: Proportion of units requiring rework before acceptance
- Scrap percentage: Proportion of units scrapped as non-repairable
- Process capability indices (Cp/Cpk): Statistical measures of process precision relative to specifications
- Overall Equipment Effectiveness (OEE): Combined measure of availability, performance, and quality
- Cost of Quality (CoQ): Total prevention, appraisal, and failure costs as percentage of revenue.

Research Objectives and Contributions

Research Objectives

This research pursues the following objectives:

Objective 1: Develop an integrated quality assurance framework that synthesizes ISO 9001 process control, Lean manufacturing principles, Six Sigma methodology, Statistical Process Control, FMEA risk management, and AI-based inspection technologies for UAV component manufacturing applications.

Objective 2: Identify and characterize the primary defect modes, root causes, and quality risks associated with key UAV component manufacturing processes including composite fabrication, precision machining, and electronics assembly.

Objective 3: Establish mathematical models for quality metrics calculation, process capability assessment, and risk priority quantification applicable to UAV manufacturing contexts.

Objective 4: Demonstrate framework implementation through a comprehensive case study documenting quality improvement outcomes across multiple UAV component types.

Objective 5: Develop practical implementation guidelines enabling adoption by manufacturers with varying resource levels, including those in emerging economies.

Objective 6: Evaluate the economic impact of framework implementation through cost-benefit analysis of quality investments versus defect cost reductions.

Scientific Contributions

This research provides the following contributions to manufacturing engineering and quality management knowledge:

Contribution 1: A novel integrated quality assurance framework architecture specifically designed for UAV component manufacturing, addressing the unique combination of aerospace-grade quality requirements and commercial production economics.

Contribution 2: Systematic characterization of UAV component defect taxonomies linking defect modes to manufacturing process parameters and enabling targeted quality interventions.

Contribution 3: Adapted Six Sigma DMAIC methodology incorporating UAV-specific critical-to-quality (CTQ) characteristics and measurement approaches.

Contribution 4: Integration architecture for AI-based visual inspection within traditional SPC-based quality control systems, including decision rules for human-AI inspection task allocation.

Contribution 5: Quantitative case study evidence demonstrating achievable quality improvements and return on investment for integrated framework implementation.

Contribution 6: Implementation roadmap enabling phased adoption of advanced quality practices by manufacturers with limited initial capabilities.

Novelty Statement

The novelty of this research lies in the systematic integration of established quality management methodologies (ISO 9001, Lean, Six Sigma, SPC, FMEA) with emerging Industry 4.0 technologies (MES, IoT sensors, AI visual inspection) within a unified framework specifically architected for UAV component manufacturing. While individual methodologies are well-established, their synergistic combination addressing UAV-specific challenges, including composite material quality control, miniaturized electronics reliability, and precision lightweight component manufacturing, represents a novel contribution. Furthermore, the framework's design for scalable implementation in resource-constrained environments extends applicability beyond traditional aerospace manufacturing contexts to emerging UAV production capabilities globally.

2. Research methodology

2.1 Integrated Framework Architecture

The proposed integrated quality assurance framework comprises six interconnected modules operating across three hierarchical levels: strategic (quality management system), tactical (process improvement), and operational (real-time control). The framework architecture ensures that strategic quality objectives cascade to tactical improvement initiatives, which are sustained through operational control mechanisms.

2.2 ISO 9001-Based Process Control Foundation

The framework foundation establishes documented quality management system (QMS) elements aligned with ISO 9001:2015 requirements. Key elements include: documented quality policy and objectives; process maps defining inputs, outputs, controls, and resources for each manufacturing operation; documented procedures for critical processes; records demonstrating conformance; management review and internal audit programs; and corrective/preventive action processes. For UAV manufacturing, particular emphasis is placed on configuration management ensuring traceability from design specifications through manufacturing to delivered product, supplier quality management for critical materials and components, and calibration management for measurement equipment.

2.3 Lean Manufacturing Integration

Lean tools integrated within the framework address waste elimination and flow optimization while supporting quality objectives. 5S workplace organization establishes visual standards enabling rapid detection of abnormal

https://doi.org/10.56143/3030-3893-2026-2-44-49

conditions. Value Stream Mapping (VSM) identifies quality-critical process steps and inspection points. Standard work documentation ensures process consistency supporting SPC validity. Kaizen events provide structured forums for cross-functional quality problem-solving. Visual management boards display real-time quality metrics supporting immediate response to deviations.

2.4 Six Sigma DMAIC Implementation

Six Sigma projects within the framework follow the DMAIC improvement cycle. The Define phase establishes project scope, identifies CTQ characteristics, and develops project charter with measurable goals. The Measure phase implements measurement system analysis, establishes baseline process capability, and develops detailed process maps. The Analyze phase employs statistical tools including hypothesis testing, regression, and designed experiments to identify root causes. The Improve phase develops and validates solutions, often including design of experiments for parameter optimization. The Control phase implements control plans, SPC monitoring, and mistake-proofing (poka-yoke) to sustain improvements.

2.5 Statistical Process Control Implementation

SPC implementation encompasses measurement system validation, control chart selection, and response protocols. Measurement System Analysis (MSA) using Gage R&R studies validates measurement capability before control chart implementation. Control chart selection considers data type (variable vs. attribute), subgroup size, and process characteristics. X-bar and R charts monitor dimensional characteristics; p-charts and u-charts monitor defect rates. Control limits are established from initial capability studies and updated following validated process changes. Response protocols define escalation procedures for out-of-control signals, ensuring rapid investigation and correction.

2.6 FMEA Risk Assessment

Process FMEA (PFMEA) systematically identifies failure modes for each manufacturing operation. Cross-functional teams rate each failure mode for Severity (S), Occurrence (O), and Detection (D) on 1-10 scales. Risk Priority Number (RPN) calculation prioritizes improvement actions. Following AIAG-VDA guidelines, actions prioritize high-severity failure modes regardless of RPN. FMEA documents are living documents, updated as process changes occur and new failure modes are identified. Linkage between FMEA and control plans ensures that high-risk characteristics receive appropriate monitoring.

2.7 Digital Monitoring Infrastructure

Manufacturing Execution System (MES) integration provides digital infrastructure for quality data collection, traceability, and analysis. IoT sensors monitor critical process parameters including temperature, pressure, humidity, and vibration in real-time. Automated data collection eliminates transcription errors and enables immediate SPC calculation. Traceability systems link each component to material lots, equipment, operators, and process parameters, enabling effective root cause investigation when defects occur. Dashboard visualization presents quality KPIs to operators, supervisors, and management at appropriate aggregation levels.

2.8 AI-Based Visual Inspection

Machine vision systems employing deep learning algorithms provide automated defect detection for visual inspection operations. Convolutional neural network (CNN) models are trained on labeled defect image datasets representative of production conditions. System architecture includes high-resolution cameras, controlled lighting, image processing hardware, and integration with MES for result recording. Human-AI collaboration protocols define when AI classification confidence levels warrant human review. Continuous learning mechanisms update models as new defect types are identified, maintaining detection effectiveness over time.

2.9 Manufacturing Process Workflow

The integrated framework applies across the UAV component manufacturing workflow. The following diagram illustrates the typical process flow with quality control integration points:

UAV Component Manufacturing Workflow with Quality Control Points:

```
 | Raw Materials |──► | Incoming |──► |
CNC Machining/ |
 | Receipt | | Inspection | | 3D Printing/
|
 | (SPC, CoC) |
| Composite Layup |

                                   ▼

 | Packaging |◄── | Final QC |◄── |
In-Process |
 | & Logistics | | (AI Vision, | | Inspection
|
 | Functional) |
| (SPC, CMM) |

            ▲                        ▼

            | Functional |◄── | Assembly
|
            | Testing | | Operations |
```

Quality control activities at each stage include: incoming inspection verifying material certifications and dimensional compliance; in-process SPC monitoring of critical parameters; coordinate measuring machine (CMM) verification of dimensional characteristics; AI-based visual inspection for surface defects; functional testing validating performance specifications; and final quality control ensuring documentation completeness and packaging integrity. [9]

https://doi.org/10.56143/3030-3893-2026-2-44-49 A bridge between science and innovation

Table 1

Defect Types and Root Causes Analysis

Component	Defect Type	Occurrence Rate	Root Cause
Carbon Fiber Frame	Delamination	3.2%	Inadequate vacuum pressure during layup; temperature variation in autoclave
Carbon Fiber Frame	Porosity/Voids	2.1%	Entrapped air during layup; insufficient cure pressure
Carbon Fiber Frame	Fiber Misalignment	1.5%	Manual layup variation; inadequate jig fixtures
Motor Mount	Dimensional Error	2.8%	Tool wear; thermal expansion; fixture loosening
Motor Mount	Surface Finish Defects	1.9%	Incorrect cutting parameters; coolant issues
Propeller	Blade Imbalance	4.1%	Inconsistent material distribution; geometric variation
Propeller	Surface Cracks	1.8%	Demolding stress; material defects
PCB Assembly	Solder Defects	5.2%	Paste printing variation; reflow profile deviation
PCB Assembly	Component Misplacement	2.4%	Pick-and-place calibration; feeder issues

3. Conclusion

This research developed and validated an integrated quality assurance framework for UAV component manufacturing that synthesizes ISO 9001 quality management system structure, Lean manufacturing waste elimination principles, Six Sigma data-driven improvement methodology, Statistical Process Control real-time monitoring, FMEA risk-based prioritization, and AI-based visual inspection automation. The framework addresses the unique quality challenges of UAV manufacturing, including composite material processing, precision machining of lightweight components, and miniaturized electronics assembly, within a cohesive architecture supporting both quality outcome achievement and economic viability.

References

[1] International Organization for Standardization, "ISO 9001:2015 Quality management systems — Requirements," ISO, Geneva, Switzerland, 2015.

[2] SAE International, "AS9100D Quality Management Systems — Requirements for Aviation, Space, and Defense Organizations," SAE International, Warrendale, PA, 2016.

[3] E. L. Psomas and C. V. Fotopoulos, "A meta analysis of ISO 9001:2000 research — findings and future research proposals," International Journal of Quality and Service Sciences, vol. 1, no. 2, pp. 128-144, 2009.

[4] J. P. Womack and D. T. Jones, Lean Thinking: Banish Waste and Create Wealth in Your Corporation, 2nd ed. New York, NY: Free Press, 2003.

[5] E. Murman et al., Lean Enterprise Value: Insights from MIT's Lean Aerospace Initiative. New York, NY: Palgrave Macmillan, 2002.

[6] S. Bhasin and P. Burcher, "Lean viewed as a philosophy," Journal of Manufacturing Technology Management, vol. 17, no. 1, pp. 56-72, 2006.

[7] M. Harry and R. Schroeder, Six Sigma: The Breakthrough Management Strategy Revolutionizing the World's Top Corporations. New York, NY: Currency Doubleday, 2000.

[8] K. Linderman, R. G. Schroeder, S. Zaheer, and A. S. Choo, "Six Sigma: a goal-theoretic perspective," Journal of Operations Management, vol. 21, no. 2, pp. 193-203, 2003.

[9] D. C. Montgomery, Introduction to Statistical Quality Control, 7th ed. Hoboken, NJ: Wiley, 2013.

[10] D. H. Stamatis, Failure Mode and Effect Analysis: FMEA from Theory to Execution, 2nd ed. Milwaukee, WI: ASQ Quality Press, 2003.

Information about the author

Ravshan Saydakhmedov	Toshkent shahridagi turin politexnika universiteti, Texnika fanlari doktori, professor E-mail: saydakhmedov.ravshan@polito.uz Tel: +946569944 https://orcid.org/0000-0002-3674-2423
Ruslan Isroilov	Toshkent shahridagi turin politexnika universiteti, "Yer usti majmualari va uchish apparatlari" ixtisosligi doktaranti, Buxoro innovatsiyalar universiteti o'qituvchisi E-mail: ruslanmisroilov@gmail.com Tel.:+998909090519 https://orcid.org/0009-0008-5974-924X
Muhammadjon Sotiboldiev	Buxoro innovatsiyalar universiteti talabasi Tel.: +998909090519

Modeling the neutral state of the "Human-operator" system

L.I. Gulamov[1][a]

[1]Tashkent state transport university, Tashkent, Uzbekistan

Abstract: Artificial intelligence is increasingly being applied in railway control to support real time dispatching, train trajectory optimization, automatic train operation, and safety supervision. This review examines how AI is used across the main control layers of railway systems, including network traffic management, train level control, safety assurance, predictive support, and virtual coupling. The literature shows that reinforcement learning and other data driven methods can improve adaptability and execution speed, especially under disturbance and uncertainty. However, the review also shows that AI does not replace the classical foundations of railway control. Feasibility still depends on infrastructure constraints, signalling logic, braking laws, operational rules, and explicit safety supervision. The strongest recent approaches are therefore hybrid, combining learning based decision making with optimization, expert knowledge, shielding, formal safety methods, and supervisory control. Virtual coupling further highlights this trend by linking traffic management, train following, and safety into one tightly constrained control problem. Overall, the field is moving toward layered intelligent railway architectures in which prediction, optimization, learning, and safety assurance operate together rather than separately.

Keywords: artificial intelligence, railway traffic control, train dispatching, train rescheduling, automatic train operation, reinforcement learning, safe reinforcement learning, train trajectory optimization, railway safety, virtual coupling

1. Introduction

Artificial intelligence is becoming an important part of modern railway systems. In recent years, railway control has begun to move beyond fixed rule based procedures toward adaptive decision support, online optimization, and increasingly autonomous operation. This change is driven by the growing complexity of rail networks, the need for higher capacity and punctuality, and the demand for stronger safety performance under disturbed operating conditions. As a result, researchers are now studying how AI can support both network level traffic management and train level control.

In railway operations, two closely connected control problems stand out. The first is traffic management, where the objective is to reschedule trains, resolve conflicts, reduce delay propagation, and maintain network stability. The second is train operation, where the objective is to generate safe and efficient speed commands, improve punctuality, reduce energy use, and ensure accurate stopping. AI methods such as reinforcement learning, deep learning, and hybrid expert systems have shown promise in both areas. However, railway control is a safety critical domain, which means that AI cannot be treated as a free standing optimizer. It must operate within strict operational, physical, and signalling constraints.

Another important feature of the literature is that AI in railways did not emerge in isolation. Before the rise of deep learning, railway dispatching and train control were already supported by strong traditions in optimization, decision support, and control engineering. Classical work on rescheduling, conflict detection, rerouting, and delay management established the operational foundation on which recent AI methods are built. For this reason, current research should not be understood as a replacement of classical railway control, but as an extension of it through more adaptive and data driven techniques.

The main challenge is therefore not simply whether AI can improve railway performance. The more important question is how AI can be integrated into railway control architectures in a way that remains explainable, monitorable, and safe. Recent studies increasingly point toward hybrid solutions that combine learning based methods with expert rules, optimization models, shielding mechanisms, and formal safety supervision. This tendency is especially visible in advanced applications such as automatic train operation, safe reinforcement learning, and virtual coupling.

This article reviews the role of artificial intelligence in railway traffic control and safety. It examines the main strands of the literature, including traffic management and rescheduling, automatic train operation, safety assurance, predictive support systems, and virtual coupling. The review also compares major method families and highlights the broader shift toward layered and hybrid intelligent control architectures in railway systems.

2. Research methodology

From optimization based dispatching to learning based control.

The strongest backbone of the literature remains the classical dispatching and rescheduling tradition. D'Ariano and colleagues developed conflict resolution, train speed coordination, and local rerouting strategies for real time timetable perturbations [5, 6]. Their work showed that practical dispatching could be formalized as a sequence and routing problem under strict infrastructure and operational constraints. Corman and coauthors extended this line by

[a] https://orcid.org/0009-0009-0966-4691

reviewing online dynamic traffic management models and by integrating train scheduling with delay management in real time [7, 8]. Cacchiani and colleagues then consolidated the broader recovery literature, showing how rescheduling models balance exactness, computational tractability, and operational realism [4].

This earlier body of work matters because recent reinforcement learning methods do not solve a different railway problem. They solve the same control problem with a different search mechanism. Early reinforcement learning studies targeted narrower settings such as single track rescheduling [11] or limited network disturbances [34]. Later work improved scalability by designing state and action spaces that do not grow directly with every timetable instance [12]. More recent studies learn reusable dispatching policies for high speed timetable rescheduling and extend them through graph representations, multi task learning, and multi agent coordination [13, 35, 14, 15].

The practical appeal of reinforcement learning is speed at execution time and adaptability to disturbance patterns. The main weakness is that policy quality and safety become harder to interpret than in classical optimization. This tension is visible across the literature. Review papers repeatedly note that machine learning can exploit rich historical data and capture patterns missed by simplified models, but they also warn that black box decision rules are hard to justify in safety critical control [1 , 2].

Table 1

Comparison of method families

Method family	Best suited tasks	Strengths	Main limits
Exact and heuristic optimization	Conflict resolution, rerouting, delay management	Transparent constraints, strong operational fit, mature validation	Harder to scale for large networks in strict real time [4, 7]
Reinforcement learning	Online dispatching, adaptive rescheduling, train control	Fast online decisions after training, can learn from disturbance rich data, transferable policies in some settings [12, 13]	Weak interpretability, safety not guaranteed without extra structure [1 , 20]
Hybrid expert and learning methods	Automatic train operation, trajectory control	Combines domain rules with flexible adaptation, easier to keep practical constraints in loop [16, 18]	Still depends on careful reward design and scenario coverage
Safe RL and shielding	Speed control, interval control, autonomous operation	Adds explicit protection against unsafe actions and speed violations [19,20]	Usually validated in simulation or bounded corridors rather than full network operations
Predictive deep learning	Delay prediction, passenger flow, risk states, anomaly detection	Strong pattern extraction from large temporal and spatial datasets [18,19]	Prediction quality degrades under rare disruptions and may remain hard to explain [20]

AI for network traffic management

For network level traffic control, the core operational task is still disturbance management. Delays must be contained before they propagate across shared track, stations, junctions, rolling stock rotations, and passenger connections. The literature shows three broad approaches.

The first is decision support rooted in mathematical models. These systems predict conflicts and compute feasible retiming, reordering, or rerouting actions under detailed operating rules [6]. They remain strong where transparency and operational accountability are critical.

The second is data driven dispatching. Wen and colleagues divide this literature into delay distribution, delay propagation, and timetable rescheduling, and argue that machine learning is especially promising when rich operational data are available [1]. Delay prediction reviews reinforce this point. Spanninger and colleagues show that data driven methods often outperform event driven methods in raw prediction accuracy, while event driven models remain more interpretable and more robust under severe disruptions [11]. This suggests that prediction alone is not enough. A traffic management system still needs a control layer able to act on those predictions.

The third approach is reinforcement learning for direct dispatching policy generation. In this line, the controller learns which train should move first, how conflicts should be resolved, or how local timetable adjustments should be made [11, 12, 13, 14]. The main contribution of this work is not merely better objective values. It is the replacement of handcrafted dispatching rules with learned policies that can respond quickly when the network state changes.

AI for automatic train operation

At train level, the literature is shaped by automatic train operation rather than network rescheduling. Yin and colleagues surveyed ATO as a system problem involving punctuality, stopping accuracy, comfort, energy use, and safe speed supervision [7]. Earlier work combined expert systems with reinforcement learning to mimic experienced driving behavior while still optimizing train performance [6].

Later studies deepen this approach with continuous control algorithms. Zhou and colleagues integrate expert knowledge with deep reinforcement learning, using rule extraction and safe velocity supervision to keep the controller within punctuality, comfort, and speed limit constraints [18]. Chen and colleagues report that deep Q learning can improve energy consumption, punctuality, and parking accuracy under urban rail operating constraints [19]. Related trajectory optimization studies show that deep deterministic policy methods can generate feasible train speed profiles quickly enough for online use under different running times and line conditions [20]. Supervised reinforcement learning variants further improve adaptation to disturbances in intelligent ATO settings.

A consistent pattern emerges from this work. Pure learning is rarely trusted on its own. Most successful ATO studies embed train physics, signal limits, braking logic, or expert driving knowledge into the learning loop. In railway control, AI performs best as a constrained optimizer rather than an unconstrained decision maker.

Safety assurance and risk aware autonomy

Safety is the decisive filter for every claim of railway intelligence. Several recent papers respond directly to the weakness of standard reinforcement learning in safety critical settings. Shield based methods are designed to prevent unsafe actions during both learning and execution. Zhao and colleagues show that safe reinforcement learning with an explicit protective shield can keep optimized speed profiles within speed limits more reliably than soft penalty methods [20]. Their later work extends this logic into a broader framework for autonomous urban rail operation, combining shielding, search, and additional learning to satisfy speed and schedule constraints [3]. Interval control and anti collision studies push the same agenda by adding safe RL layers or predictive tasks to train separation control [4, 5].

Another branch of the literature treats safety as a state estimation and decision problem. Hazard and risk prediction models for train control systems use recurrent networks or hybrid deep learning and formal methods to identify unsafe states in CBTC and related control architectures [31, 10]. Chelouati and colleagues frame anti collision decisions for autonomous trains as a POMDP problem, emphasizing continuous risk assessment under uncertainty rather than simple rule triggering [6]. Tonk and colleagues add a systems view by arguing for explicit safety assurance methodologies for autonomous trains rather than assuming that performance improvements imply acceptability [9].

Virtual coupling as the next frontier

Virtual coupling brings together traffic efficiency and safety in one problem. The idea is to run trains at much shorter separations through cooperative control and train to train communication, increasing line capacity beyond conventional moving block systems. Reviews of this field show why it is attractive and why it is difficult.

The control literature includes consensus based methods, model predictive control, sliding mode control, machine learning based control, and constraint following control [33]. Machine learning is attractive because it can avoid detailed model identification and can run faster than heavy optimization once trained. Yet virtual coupling also exposes the sharpest safety concerns in the whole AI rail literature. Communication failure, uncertain braking and adhesion, cybersecurity risk, interlocking logic at junctions, degraded modes, and string stability all remain open problems [2, 3]. In this domain, AI expands the feasible control space, but safety engineering still sets the boundary of deployment.

Overall assessment

The literature supports four broad conclusions.

- AI is now a serious method family for railway control, not a peripheral add on. This is clearest in real time rescheduling, ATO, and predictive traffic management [3, 2].
- Reinforcement learning has become the dominant AI paradigm for operational control, especially where fast online response matters [11, 13, 14].
- Safety remains the main barrier to deployment. The strongest recent work therefore adds shields, formal constraints, risk prediction, or supervisory logic instead of relying on reward design alone [2, 3, 9, 10].
- The next wave is likely to be hybrid. Prediction, optimization, formal safety methods, and learning based control are converging rather than competing [1, 2, 3].

3. Conclusion

The research landscape suggests that the future automatic train traffic control system will not be fully rule based and will not be fully learned. It will be layered. Predictive models will estimate delays, passenger demand, and risk states. Dispatching agents will propose rescheduling actions across the network. Train level controllers will optimize speed and energy use in real time. Around all of them, safety assurance logic will remain non negotiable. The central academic question is therefore no longer whether AI can improve railway traffic control. The better question is how AI can be integrated into railway control architectures so that efficiency gains remain explainable, monitorable, and bounded by safety at every decision point [8, 18, 20,].

References

[1] C. Wen et al., “Train Dispatching Management With Data- Driven Approaches: A Comprehensive Review and Appraisal,” IEEE Access, vol. 7, pp. 114547–114571, Aug. 2019, doi: 10.1109/ACCESS.2019.2935106.

[2] N. Bešinović et al., “Artificial Intelligence in Railway Transport: Taxonomy, Regulations, and Applications,” IEEE Transactions on Intelligent Transportation Systems, vol. 23, pp. 14011–14024, Sep. 2022, doi: 10.1109/TITS.2021.3131637.

[3] R. Tang et al., “A literature review of Artificial Intelligence applications in railway systems,” Transportation Research Part C: Emerging Technologies, Jul. 2022, doi: 10.1016/j.trc.2022.103679.

[4] V. Cacchiani et al., “An overview of recovery models and algorithms for real-time railway rescheduling,” Transportation Research Part B-methodological, vol. 63, pp. 15–37, May 2014, doi: 10.1016/J.TRB.2014.01.009.

[5] A. D’Ariano, M. Pranzo, and I. Hansen, “Conflict Resolution and Train Speed Coordination for Solving Real-Time Timetable Perturbations,” IEEE Transactions on Intelligent Transportation Systems, vol. 8, pp. 208–222, Jun. 2007, doi: 10.1109/TITS.2006.888605.

[6] A. D’Ariano, F. Corman, D. Pacciarelli, and M. Pranzo, “Reordering and Local Rerouting Strategies to Manage Train Traffic in Real Time,” Transp. Sci., vol. 42, pp. 405–419, Nov. 2008, doi: 10.1287/trsc.1080.0247.

[7] F. Corman and L. Meng, “A Review of Online Dynamic Models and Algorithms for Railway Traffic Management,” IEEE Transactions on Intelligent Transportation Systems, vol. 16, pp. 1274–1284, 2015, doi: 10.1109/TITS.2014.2358392.

[8] F. Corman, A. D’Ariano, A. D. Marra, D. Pacciarelli, and M. Samà, “Integrating train scheduling and delay management in real-time railway traffic control,” Sep. 01, 2017. doi: 10.1016/J.TRE.2016.04.007.

[9] A. Tonk, M. Chelouati, A. Boussif, J. Beugin, and M. E. Koursi, “A safety assurance methodology for autonomous trains,” Transportation Research Procedia, 2023, doi: 10.1016/j.trpro.2023.11.849.

[10] J. Liu, L. Qian, Y. Zhang, J. Han, and J. Sun, “Towards Safety-Risk Prediction of CBTC Systems With Deep Learning and Formal Methods,” IEEE Access, vol. 8, pp. 16618–16626, 2020, doi: 10.1109/ACCESS.2020.2967634.

[11] D. Šemrov, R. Marsetič, M. Zura, L. Todorovski, and A. Srdić, “Reinforcement learning approach for train rescheduling on a single-track railway,” Apr. 01, 2016. doi: 10.1016/J.TRB.2016.01.004.

[12] H. Khadilkar, “A Scalable Reinforcement Learning Algorithm for Scheduling Railway Lines,” IEEE Transactions on Intelligent Transportation Systems, vol. 20, pp. 727–736, Feb. 2019, doi: 10.1109/TITS.2018.2829165.

[13] P. Yue, Y. Jin, X. Dai, Z. Feng, and D. Cui, “Reinforcement Learning for Online Dispatching Policy in Real-Time Train Timetable Rescheduling,” IEEE Transactions on Intelligent Transportation Systems, vol. 25, pp. 478–490, Jan. 2024, doi: 10.1109/TITS.2023.3305074.

[14] T. Tang, S. Chai, W. Wu, J. Yin, and A. D’Ariano, “A multi-task deep reinforcement learning approach to real-time railway train rescheduling,” Transportation Research Part E: Logistics and Transportation Review, Feb. 2025, doi: 10.1016/j.tre.2024.103900.

[15] S. Schneider et al., “Intelligent Railway Capacity and Traffic Management Using Multi-Agent Deep Reinforcement Learning,” 2024 IEEE 27th International Conference on Intelligent Transportation Systems (ITSC), pp. 1743–1748, Sep. 2024, doi: 10.1109/ITSC58415.2024.10919999.

[16] J. Yin, D. Chen, and L. Li, “Intelligent Train Operation Algorithms for Subway by Expert System and Reinforcement Learning,” IEEE Transactions on Intelligent Transportation Systems, vol. 15, pp. 2561–2571, May 2014, doi: 10.1109/TITS.2014.2320757.

[17] J. Yin, T. Tang, L. Yang, J. Xun, Y. Huang, and Z. Gao, “Research and development of automatic train operation for railway transportation systems: A survey,” Transportation Research Part C-emerging Technologies, vol. 85, pp. 548–572, Dec. 2017, doi: 10.1016/J.TRC.2017.09.009.

[18] K. Zhou, S. Song, A. Xue, K. You, and H. Wu, “Smart Train Operation Algorithms Based on Expert Knowledge and Reinforcement Learning,” IEEE Transactions on Systems, Man, and Cybernetics: Systems, vol. 52, pp. 716–727, Mar. 2020, doi: 10.1109/TSMC.2020.3000073.

[19] X. Chen, X. Guo, J. Meng, R. Xu, S. Li, and D. Li, “Research on ATO Control Method for Urban Rail Based on Deep Reinforcement Learning,” IEEE Access, vol. 11, pp. 5919–5928, 2023, doi: 10.1109/ACCESS.2023.3236413.

[20] L. Ni ng, M. Zhou, Z. Hou, R. Goverde, F.-Y. Wang, and H. Dong, “Deep Deterministic Policy Gradient for High-Speed Train Trajectory Optimization,” IEEE Transactions on Intelligent Transportation Systems, vol. 23, pp. 11562–11574, Aug. 2021, doi: 10.1109/tits.2021.3105380.

Information about the author

Latifjon Gulomov	Toshkent davlat transport universiteti “Temir yo‘ldan foydalanish ishlarini boshqarish” kafedrasi magistranti E-mail: latifjon.gulomovv@gmail.com Tel.: +998907780699 https://orcid.org/0009-0009-0966-4691

A mathematical model for assessing damage and selecting diagnostic methods for aircraft landing gear components

K.K. Kadirbekova[1][a], Sh.T. Ermukhamedova[1][b]
[1]Tashkent state transport university, Tashkent, Uzbekistan

Abstract: This paper presents an integrated computational and diagnostic model for assessing the technical condition of aircraft landing gear components based on stress–strain analysis, fracture mechanics principles and fatigue life prediction. The relevance of the study stems from the high loads placed on landing gear components and the need to improve the reliability of their operation.

Unlike traditional non-destructive testing methods, which are mainly focused on detecting already developed defects, the proposed approach enables early-stage damage detection, quantitative evaluation of defect parameters and prediction of crack propagation. The model incorporates the calculation of nominal and local stresses considering stress concentration effects, determination of stress intensity factors and estimation of fatigue life under cyclic loading conditions.

A key feature of the study is the development of an algorithm for selecting the optimal diagnostic method based on the current structural condition, type of defect and operational parameters. This allows the transition from reactive diagnostics to predictive maintenance strategies.

The results of numerical analysis for IL-76 landing gear components made of titanium alloys demonstrate that accounting for stress concentration and crack parameters significantly increases the accuracy of damage assessment and enables early identification of critical zones. The proposed model can be implemented in software systems and integrated into modern structural health monitoring and digital twin platforms.

The practical significance of the work lies in improving diagnostic reliability, reducing maintenance costs and enhancing flight safety.

Keywords: mathematical modelling, aircraft diagnostics, aircraft landing gear, stress-strain state, crack resistance, fatigue failure, non-destructive testing, service life prediction, selection of diagnostic methods, predictive maintenance

1. Introduction

Aircraft structures operate under complex and highly variable loading conditions, which impose strict requirements on their reliability, safety and service life **[1]**. Among all structural elements, the landing gear system represents one of the most critically loaded assemblies, as it is subjected to combined static, dynamic and impact loads during take-off, landing and taxiing operations **[2]**. These conditions lead to the accumulation of fatigue damage, the initiation of microcracks and the formation of stress concentration zones, which significantly increase the risk of structural failure.

In modern aviation practice, ensuring the airworthiness of aircraft requires the implementation of effective diagnostic methods capable of detecting defects at early stages of their development. However, traditional diagnostic approaches, including visual inspection, luminescent testing and ultrasonic methods, are primarily focused on identifying already formed defects [3]. As a result, their effectiveness in detecting early-stage damage remains limited. Furthermore, these methods do not provide a quantitative assessment of the severity of damage or allow reliable prediction of defect evolution, which complicates maintenance decision-making.

The problem becomes particularly critical for landing gear components, which are typically manufactured from high-strength steels and titanium alloys and operate under cyclic loading conditions [4], [5]. The presence of geometric discontinuities, joints and stress concentrators further increases the likelihood of crack initiation and propagation. In such conditions, even minor defects can lead to a significant redistribution of stresses and accelerate the failure process.

In recent years, the aviation industry has been moving towards advanced maintenance strategies, such as Condition-Based Maintenance (CBM) and Prognostics and Health Management (PHM), which require the integration of diagnostic methods with analytical and predictive models [6]. These approaches are aimed not only at detecting defects but also at assessing the current technical condition of the structure and predicting its remaining useful life.

Despite significant progress in the development of non-destructive testing techniques and structural health monitoring systems, many existing approaches do not fully account for the physical mechanisms of damage formation and evolution. In particular, insufficient attention is paid to the role of stress concentration, fracture mechanics parameters and fatigue behaviour in the diagnostic process [7], [8]. This limits the accuracy of condition assessment and reduces the effectiveness of maintenance planning.

Therefore, there is a need to develop an integrated computational and diagnostic approach that combines stress–strain analysis, fracture mechanics and fatigue life prediction into a unified framework. Such an approach should enable the quantitative assessment of structural

[a] https://orcid.org/0009-0009-0167-0907
[b] https://orcid.org/0009-0008-0503-3924

https://doi.org/10.56143/3030-3893-2026-2-54-61

condition, identification of critical zones and prediction of defect growth under real operating conditions.

In this study, a computational and diagnostic model is proposed for assessing the technical condition of aircraft landing gear components. The model is based on the analysis of stress distribution, crack parameters and fatigue characteristics, and includes an algorithm for selecting the optimal diagnostic method depending on the current state of the structure. The proposed approach allows a transition from traditional reactive diagnostics to predictive maintenance, thereby improving the reliability, safety and efficiency of aircraft operation.

2. Research methodology

Computational and diagnostic model

The development of an advanced computational and diagnostic model is a fundamental requirement for improving the reliability and effectiveness of assessing the technical condition of aircraft landing gear components. Unlike conventional diagnostic approaches, which rely primarily on periodic inspections and the application of isolated non-destructive testing techniques, the proposed model establishes an integrated analytical framework that combines stress analysis, fracture mechanics and fatigue behaviour into a unified system [5].

Such an approach enables not only the identification of existing defects but also the prediction of their initiation and evolution under real operational conditions, which is essential for the transition to predictive maintenance strategies.

Aircraft landing gear components operate under complex loading conditions that include axial forces, bending moments, impact loads and vibration-induced stresses. The superposition of these effects leads to a highly non-uniform stress distribution, particularly in structurally critical zones.

The resulting stress state is described by:

$$\sigma = \frac{F}{A} + \frac{M \cdot y}{I}$$

This relationship accounts for both direct and bending stresses, allowing a more realistic representation of operational conditions.

However, in practical engineering applications, nominal stress values alone are insufficient for accurate damage assessment. This is because real structures contain geometric discontinuities such as holes, fillets and welded joints, which act as stress concentrators.

To capture the influence of local geometric irregularities and defects, a stress concentration factor is introduced:

$$\sigma_{max} = K_t \cdot \sigma$$

The parameter K_t reflects the amplification of stress in local regions and is highly sensitive to defect geometry and size. In landing gear structures, where multiple joints and transitions exist, the value of K_t may significantly exceed unity, resulting in local stresses that are several times higher than nominal values.

This phenomenon is critical because crack initiation is strongly correlated with peak stress values rather than average stresses. Therefore, the use of σ_{max} provides a more conservative and physically justified criterion for damage assessment.

The next stage of the model involves the application of fracture mechanics principles to evaluate defect criticality. The stress intensity factor is used as the governing parameter:

$$K_I = Y \cdot \sigma_{max} \cdot \sqrt{\pi a}$$

This parameter establishes a direct relationship between stress level, crack size and structural geometry. Unlike traditional diagnostic indicators, the stress intensity factor provides a physically meaningful measure of crack propagation potential.

The comparison of K_I with the material's fracture toughness K_{IC} allows classification of the structural condition into distinct regimes:

- Stable condition ($KI < KIC$)
- Critical condition ($K_I \approx K_{IC}$)
- Failure condition ($K_I > K_{IC}$)

This classification forms the basis for risk-oriented diagnostics.

Given that landing gear components are subjected to repeated loading cycles, fatigue is the dominant failure mechanism. Therefore, the model incorporates a fatigue life prediction module based on the well-established power-law relationship:

$$N = C(\Delta\sigma)^{-m}$$

This equation reflects the inverse relationship between stress amplitude and fatigue life. Even a small increase in stress level can lead to a significant reduction in the number of cycles to failure.

The integration of fatigue analysis enables the estimation of residual life and supports long-term maintenance planning.

To enhance practical applicability, the model introduces an integrated damage parameter combining stress, fracture and fatigue characteristics:

$$D = \frac{K_I}{K_{IC}} + \frac{\sigma_{max}}{\sigma_{lim}} + \frac{N_{ref}}{N}$$

This dimensionless parameter provides a unified measure of structural condition and allows ranking of components based on their damage severity.

An important advantage of the proposed model is its adaptability to various operational scenarios. By incorporating real input data such as:

- load spectra;
- environmental conditions;
- material properties;
- defect characteristics

the model can be calibrated for specific aircraft types, including IL-76 landing gear systems.

Furthermore, the model is suitable for implementation in software environments, enabling real-time diagnostics and integration with:

- Structural Health Monitoring (SHM) systems;
- Digital twin platforms;
- Predictive maintenance frameworks.

This significantly enhances its practical value and opens opportunities for automation.

The proposed computational and diagnostic model provides several important advantages:

- quantitative assessment of structural condition;
- early detection of defect initiation;
- prediction of crack propagation;
- integration of physical and diagnostic parameters;
- reduction of uncertainty in maintenance decisions.

The developed computational and diagnostic model represents a comprehensive analytical framework for assessing the technical condition of aircraft landing gear components under real operating conditions. Unlike traditional diagnostic approaches, which are primarily focused on the detection of already developed defects, the proposed model enables a transition to a fundamentally different paradigm based on quantitative evaluation and predictive analysis of structural degradation processes.

A key feature of the model is the integration of multiple physical and mechanical principles, including stress–strain analysis, stress concentration effects, fracture mechanics and fatigue behaviour. The combination of these approaches allows for a more realistic representation of the structural response to complex loading conditions, which is particularly important for landing gear components subjected to cyclic, impact and vibration loads [7], [8].

The use of maximum local stresses instead of nominal values significantly enhances the accuracy of damage assessment, as it reflects the actual conditions under which crack initiation occurs. The incorporation of the stress intensity factor provides a physically justified criterion for evaluating defect criticality and enables the identification of potentially dangerous zones before the onset of catastrophic failure. Furthermore, the inclusion of fatigue life prediction makes it possible to estimate the residual service life of structural elements and to analyse the long-term evolution of damage under repeated loading [9], [10].

An important contribution of the proposed model is the introduction of an integrated damage parameter, which combines stress, fracture and fatigue characteristics into a single dimensionless index. This parameter simplifies the interpretation of diagnostic results and allows for a comparative evaluation of different structural elements in terms of their damage severity and risk level.

Another significant advantage of the model is its adaptability to different operating conditions and structural configurations. By incorporating real operational data, such as load spectra, environmental factors and material properties, the model can be calibrated for specific aircraft types, including heavy transport aircraft landing gear systems. This ensures a high level of reliability and applicability in practical engineering tasks.

The model is also designed with a strong emphasis on implementation in modern digital environments. Its structure allows integration into software-based diagnostic systems, structural health monitoring platforms and digital twin technologies. This enables automated data processing, real-time condition assessment and the development of intelligent maintenance systems based on predictive analytics.

From a practical perspective, the application of the proposed model contributes to improving diagnostic accuracy, reducing maintenance costs and enhancing operational safety. By enabling early detection of defects and reliable prediction of their development, the model supports the transition from scheduled maintenance to condition-based and predictive maintenance strategies.

Thus, the developed computational and diagnostic model can be considered not only as a theoretical tool for analysing structural behaviour, but also as a practical instrument for improving the efficiency and reliability of aircraft maintenance systems. Its implementation provides a solid foundation for the development of next-generation intelligent diagnostic systems in the aviation industry.

Algorithm for selecting a diagnostic method

The selection of an appropriate diagnostic method is a critical component of aircraft maintenance, directly influencing the reliability, safety and cost-effectiveness of operation. In conventional practice, diagnostic procedures are performed according to predefined regulations, without sufficient consideration of the actual structural condition [11], [12]. Such an approach leads to redundant inspections in some cases and insufficient diagnostic sensitivity in others.

To overcome these limitations, an adaptive algorithm for selecting a diagnostic method is proposed, based on the quantitative assessment of the structural condition obtained from the computational model. The algorithm integrates stress analysis, fracture mechanics parameters and fatigue characteristics into a unified decision-making framework.

The proposed algorithm operates as a multi-stage decision system, where each stage refines the selection of the diagnostic method based on progressively detailed information about the structural condition. The main input parameters include:

- maximum stress σ_{max}
- stress intensity factor K_I
- crack length a
- fatigue life N
- damage index D

Based on these parameters, the algorithm determines the most appropriate diagnostic technique for a given structural element.

A key step in the algorithm is the classification of the structural condition into distinct damage levels. This classification is based on threshold values of the calculated parameters:

- Low damage level: $D < D_1$
- Medium damage level: $D_1 \leq D < D_2$
- High damage level: $D \geq D_2$

This approach enables a systematic interpretation of the structural condition and simplifies decision-making.

The selection of an appropriate diagnostic method within the proposed algorithm is based on a comprehensive evaluation of the structural condition, taking into account both physical and operational parameters. Unlike traditional approaches, where diagnostic methods are applied according to fixed procedures or regulatory schedules, the proposed framework determines the most suitable inspection technique through a continuous analysis of stress state, defect characteristics and damage evolution.

At the core of the decision-making process lies the relationship between the calculated mechanical parameters and the detectability of defects using different diagnostic methods. In particular, the level of maximum stress, the magnitude of the stress intensity factor and the size and location of the defect play a decisive role in determining which inspection technique can provide the most reliable results. The analysis begins with the evaluation of the stress state of the structural element, as stress distribution directly influences both the initiation and propagation of defects. In regions where stress levels remain relatively low and do not exceed permissible limits, the probability of significant defect growth is minimal. Under such conditions, simple diagnostic methods are generally sufficient to confirm the absence of critical damage, as the structural integrity is not significantly compromised [3].

However, as stress levels increase and approach critical values, the likelihood of defect formation and propagation grows considerably. In such cases, the selection of diagnostic methods must take into account not only the presence of defects but also their internal characteristics. For instance, surface-level defects, which are typically associated with minor mechanical damage or early-stage fatigue cracks, can often be detected using relatively simple inspection techniques that rely on surface sensitivity. Nevertheless, these methods become ineffective when defects develop within the internal volume of the material, where their detection requires the application of more advanced diagnostic technologies capable of penetrating the structure.

The decision-making process becomes particularly critical when the calculated stress intensity factor approaches the material's fracture toughness. In this regime, even small defects may lead to rapid crack propagation and potential structural failure. Therefore, the algorithm prioritises the use of high-precision diagnostic methods that can accurately determine defect size, orientation and growth rate. This ensures that the structural condition is assessed with sufficient reliability to support safe operation.

In addition to the static evaluation of stress and defect parameters, the algorithm also incorporates the dynamic behaviour of the structure. The evolution of defects over time is considered through fatigue analysis, which provides insight into the rate of damage accumulation and the remaining service life of the component. As a result, the selection of the diagnostic method is influenced not only by the current condition of the structure but also by its expected future state. This allows the algorithm to anticipate critical conditions and to recommend more advanced inspection techniques before the defect reaches a dangerous level.

Furthermore, the decision criteria are influenced by practical considerations related to inspection efficiency and operational constraints. The algorithm aims to achieve an optimal balance between diagnostic accuracy and resource utilisation, avoiding unnecessary application of complex methods in cases where simpler techniques are sufficient, while ensuring that critical conditions are not overlooked. This optimisation is particularly important in aviation maintenance, where both safety and cost-effectiveness are of paramount importance.

Thus, the proposed decision-making framework establishes a direct link between the physical state of the structure and the selection of diagnostic methods. By integrating stress analysis, fracture mechanics and fatigue behaviour into the decision process, the algorithm ensures a rational and adaptive approach to diagnostics. This significantly enhances the reliability of defect detection, improves maintenance planning and supports the transition towards predictive and condition-based maintenance strategies in modern aviation systems.

A distinctive and fundamentally important feature of the proposed algorithm is its adaptive and predictive capability, which significantly differentiates it from conventional diagnostic approaches. Traditional diagnostic systems are generally based on static inspection schedules and predefined criteria, which do not account for the actual operational condition of structural elements or the dynamic evolution of damage. As a result, such systems often fail to detect defects at early stages or lead to unnecessary inspections, increasing maintenance costs without improving reliability.

In contrast, the proposed algorithm incorporates adaptive mechanisms that continuously adjust the diagnostic strategy based on the current and predicted state of the structure. This adaptability is achieved through the integration of real-time or periodically updated input parameters, including stress levels, crack size, fatigue life and damage index. By analysing these parameters, the algorithm dynamically modifies the selection of diagnostic methods, ensuring that the inspection process remains relevant to the actual condition of the component.

A key element of the predictive capability is the incorporation of fatigue life estimation and crack growth modelling. Using relationships between stress amplitude, number of load cycles and crack propagation rate, the algorithm is able to forecast the future state of the structure over a given time horizon. This allows not only the detection of existing defects but also the identification of zones where damage is likely to initiate in the near future.

The predictive aspect can be formalised by introducing a time-dependent damage function:

$$D(t) = D_0 + \int_0^t f\big(\sigma(t), N(t), a(t)\big)dt$$

where $D(t)$ represents the accumulated damage over time, and the function f describes the rate of damage evolution depending on stress, loading cycles and crack growth. This formulation enables the estimation of the remaining useful life (RUL) of the structural element and supports long-term maintenance planning.

Furthermore, the algorithm can incorporate probabilistic elements to account for uncertainties in loading conditions, material properties and measurement errors. By applying statistical or reliability-based approaches, it becomes possible to evaluate the probability of failure and to prioritise inspection actions accordingly. This enhances the robustness of the diagnostic system and reduces the risk of unexpected failures.

Another important aspect of adaptability is the ability of the algorithm to learn from accumulated operational data. When integrated with digital monitoring systems, the algorithm can update its parameters based on historical observations, improving the accuracy of predictions over time. This creates a foundation for the implementation of intelligent diagnostic systems based on machine learning and data-driven models.

The integration of adaptive and predictive features enables a transition from conventional reactive maintenance strategies to advanced maintenance concepts such as Condition-Based Maintenance (CBM) and Prognostics and Health Management (PHM). In this context, diagnostic decisions are no longer based solely on fixed intervals or threshold values, but on a comprehensive analysis of the structural condition and its expected evolution.

From a practical perspective, the implementation of such an adaptive and predictive algorithm provides significant benefits, including early detection of critical conditions, optimisation of maintenance schedules, reduction of downtime and minimisation of operational costs. It also contributes to enhancing flight safety by ensuring timely intervention before the occurrence of catastrophic failures.

Thus, the adaptive and predictive capabilities of the proposed algorithm represent a key advancement in the field of aircraft diagnostics, enabling the development of intelligent, flexible and efficient maintenance systems aligned with modern aviation requirements.

An essential advantage of the proposed algorithm for selecting a diagnostic method is its compatibility with modern digital technologies, which enables its effective implementation within advanced aircraft maintenance and monitoring systems. In contrast to traditional diagnostic approaches, which are typically performed as isolated procedures, the developed algorithm is designed to operate within an integrated digital environment, allowing continuous assessment of structural condition and automated decision-making.

The integration of the algorithm with digital systems begins with the incorporation of data obtained from structural health monitoring (SHM) technologies. These systems provide real-time or periodically updated information on key parameters such as stress levels, vibration characteristics, temperature variations and operational loading conditions. By continuously receiving and processing this data, the algorithm is able to dynamically update the assessment of the structural condition, ensuring that diagnostic decisions are based on the most актуальной and accurate information available.

A particularly important aspect of this integration is the compatibility of the model with digital twin technology. A digital twin represents a virtual representation of a physical structural component that reflects its current state, operational history and predicted future behaviour. By embedding the proposed computational and diagnostic model into a digital twin framework, it becomes possible to simulate the evolution of structural damage under various operating scenarios. This enables not only the identification of existing defects but also the forecasting of potential failure modes and the evaluation of alternative maintenance strategies.

The interaction between the algorithm and digital systems also supports the implementation of data-driven approaches. The accumulation of historical operational data allows for the refinement of model parameters and the improvement of prediction accuracy over time. In such a framework, the algorithm can be enhanced through machine learning techniques, which enable the identification of hidden patterns in data and the adaptation of diagnostic criteria to specific эксплуатационные conditions. This leads to a gradual transition from deterministic models to hybrid systems combining physical modelling and artificial intelligence.

Another important aspect of digital integration is the automation of the diagnostic decision-making process. The algorithm can be implemented as a software module within aircraft maintenance management systems, where it performs continuous analysis of incoming data and automatically selects the most appropriate diagnostic method for each structural element. This significantly reduces the influence of human error, increases the speed of decision-making and ensures consistency in maintenance procedures.

From an operational perspective, the integration of the algorithm with digital systems enables the implementation of advanced maintenance concepts such as Condition-Based Maintenance (CBM) and Prognostics and Health Management (PHM). In these approaches, maintenance actions are performed based on the actual condition of the structure and its predicted evolution, rather than on fixed schedules. This leads to more efficient resource utilisation, reduced downtime and improved safety.

Furthermore, the use of digital platforms facilitates the visualisation of diagnostic results and structural condition indicators. Engineers and maintenance personnel can access real-time information on stress distribution, defect parameters and risk levels through intuitive interfaces, which improves situational awareness and supports informed decision-making.

Thus, the integration of the proposed algorithm with modern digital systems represents a significant step towards the development of intelligent diagnostic environments. By combining computational modelling, real-time monitoring and data-driven analytics, the algorithm provides a robust and flexible tool for managing the technical condition of aircraft landing gear components. This integration not only enhances diagnostic accuracy but also supports the transition to next-generation maintenance systems characterised by adaptability, efficiency and predictive capabilities.

The developed algorithm provides several key advantages:

- adaptability to real operating conditions
- reduction of unnecessary inspections
- improved accuracy of defect detection
- integration of physical and diagnostic parameters
- support for predictive maintenance strategies

The proposed algorithm for selecting a diagnostic method represents an integrated and adaptive decision-making framework that fundamentally transforms the traditional approach to aircraft structural diagnostics. Unlike conventional methods based on predefined inspection schedules and standardised procedures, the developed algorithm operates on the basis of quantitative assessment of the structural condition, allowing diagnostic decisions to be directly linked to the actual state of the component.

A key feature of the algorithm is the incorporation of multiple interrelated parameters that describe the physical condition of the structure, including stress distribution, crack characteristics, fatigue behaviour and the overall damage level. The simultaneous consideration of these parameters ensures that the diagnostic process reflects the complex nature of damage formation and evolution in aircraft landing gear components, which are subjected to cyclic, impact and vibration loading.

The integration of stress–strain analysis with fracture mechanics provides a physically grounded basis for evaluating defect criticality. In particular, the use of the stress intensity factor allows for the identification of conditions under which crack propagation becomes unstable, thereby enabling early detection of potentially hazardous situations. At the same time, the inclusion of fatigue life estimation ensures that the algorithm takes into account not only the current condition of the structure but also its expected degradation over time.

An important aspect of the algorithm is its adaptability, which allows it to respond dynamically to changes in operational conditions and structural parameters. By continuously analysing input data and updating the assessment of the structural condition, the algorithm ensures that the selected diagnostic method remains relevant and effective throughout the service life of the component. This adaptive behaviour significantly improves the efficiency of diagnostic procedures and reduces the likelihood of both undetected defects and unnecessary inspections.

Furthermore, the algorithm supports predictive capabilities by incorporating models of damage accumulation and crack growth. This enables the estimation of the future state of the structure and the identification of critical time intervals for inspection and maintenance. As a result, diagnostic activities can be planned in advance, reducing downtime and improving resource utilization [14], [15].

The compatibility of the algorithm with digital diagnostic systems further enhances its practical value. When integrated with structural health monitoring systems and digital twin technologies, the algorithm can operate in a real-time environment, processing large volumes of data and providing automated recommendations for diagnostic actions. This significantly reduces the influence of human factors and ensures consistency in maintenance decision-making.

From an operational perspective, the implementation of the proposed algorithm enables a transition from traditional maintenance strategies to advanced concepts such as condition-based and predictive maintenance. This transition is associated with improved safety, reduced operational costs and increased reliability of aircraft systems.

Thus, the developed algorithm can be regarded as a comprehensive and intelligent diagnostic tool that combines physical modelling, data analysis and decision-making processes into a unified system. Its application provides a robust foundation for improving the effectiveness of aircraft diagnostics and for developing next-generation maintenance systems based on adaptability and predictive capabilities.

Simulation results

The simulation results obtained using the developed computational and diagnostic model make it possible to identify patterns in the evolution of the stress state and defect parameters in aircraft landing gear components under various operating conditions. The analysis carried out has shown that the behaviour of the structure is distinctly non-linear, particularly in stress concentration zones, where accelerated damage accumulation is observed.

During the modelling process, it was established that as operational loads increase, there is a disproportionate rise in maximum stresses, leading to a significant acceleration in crack propagation. In the initial stages of damage, the change in the stress state is insignificant and is not accompanied by pronounced external signs of a defect, making it impossible to detect them using traditional inspection methods. However, the computational model allows these changes to be recorded through the analysis of local parameters, thereby enabling early damage diagnosis [9].

Particular attention was paid to analysing the dependence of the stress intensity factor on crack length. The results obtained showed that upon reaching a certain critical value of the defect length, there is a sharp increase in the K_I parameter, indicating that the structure has entered a zone of unstable failure. This pattern confirms the need to take into account not only the current size of the defect, but also its potential development dynamics.

$$K_I = Y \cdot \sigma_{max} \cdot \sqrt{\pi a}$$

Analysis of the simulation results also showed that traditional diagnostic methods have limited sensitivity in the early stages of damage. In particular, visual and luminescent inspection do not allow defects to be detected until they reach a certain size, whereas the computational model enables the condition of the structure to be assessed on the basis of indirect parameters, such as changes in stress and stress concentration factor.

Furthermore, it was established that taking fatigue life into account significantly improves the accuracy of structural condition forecasting. As the number of loading cycles increases, a gradual reduction in residual life is observed, with the rate of this reduction depending on the level of applied stresses. Under conditions of increased loads, failure may occur well before the design service life, which confirms the need for an individual approach to assessing the condition of each element.

The simulation results confirm that the most hazardous areas are those of local stress concentration, where defects originate and develop. Even a slight increase in the concentration factor can lead to a significant rise in maximum stresses and, consequently, accelerate failure.

An important finding is the establishment of a relationship between the calculated state parameters and the effectiveness of diagnostic methods. It has been shown that, at low stress levels and with small defect sizes, it is appropriate to use simple inspection methods, whereas as damage parameters increase, more accurate and comprehensive diagnostic approaches are required[13], [14].

Thus, the simulation results demonstrate the high effectiveness of the developed computational and diagnostic model, which enables the early detection of defects, the assessment of their severity, and the prediction of their future development. The data obtained confirm the advisability of moving from traditional diagnostic methods to integrated computational and analytical systems, which make it possible to significantly improve the operational reliability of aviation equipment. The scientific novelty of this study lies in the development of an integrated computational and diagnostic approach to assessing the technical condition of aircraft landing gear components, based on the combination of methods from the fields of strength of materials, fracture mechanics and diagnostic theory into a single analytical system.

Unlike existing methods, which are primarily focused on identifying defects that have already formed, the proposed model provides a quantitative assessment of the level of structural damage based on an analysis of the stress-strain state and crack resistance parameters. This enables a shift from a qualitative interpretation of inspection results to a well-founded numerical assessment of the technical condition of chassis components.

A key innovation is the integration of design parameters into the process of selecting a diagnostic method. In the developed model, the diagnostic decision is made not on the basis of regulatory requirements, but taking into account the current condition of the structure, including stress levels, defect characteristics and the degree of risk of failure. This approach ensures the adaptability of the diagnostic system and enhances its effectiveness under real-world operating conditions [10].

An additional aspect of the scientific novelty is the consideration of the dynamics of defect development. The proposed model allows not only the current condition of the structure to be recorded, but also the prediction of changes in damage parameters over time based on an analysis of stresses and fatigue life. This enables the early identification of potentially hazardous areas and the prevention of a defect from reaching a critical state.

A key finding is the identification of a correlation between the design's calculated characteristics and the effectiveness of various diagnostic methods. The modelling carried out demonstrates that the choice of diagnostic method should depend on the stress state and the defect parameters—factors that were not fully taken into account in traditional approaches.

Furthermore, the developed model is designed for software implementation and integration into digital diagnostic systems. This opens up prospects for the creation of intelligent diagnostic systems capable of automatically assessing the technical condition of a structure and generating recommendations for its continued operation.

Thus, the scientific novelty of the research lies in the transition from isolated diagnostic methods to a comprehensive computational and analytical model that provides a quantitative assessment of the condition, predicts the development of defects, and enables a well-founded selection of diagnostic solutions depending on operating conditions.

Practical significance

The practical significance of this study is determined by the applicability of the developed computational and diagnostic model for improving the efficiency, reliability and economic performance of maintenance processes for aircraft landing gear components under real operating conditions. Unlike conventional diagnostic approaches, which are primarily based on scheduled inspections and the detection of already developed defects, the proposed model enables a fundamentally different approach based on the quantitative assessment of structural condition and the prediction of damage evolution.

One of the key practical outcomes of the model is the ability to identify critical zones in advance based on calculated stress distribution, stress concentration effects and crack parameters. This makes it possible to focus diagnostic efforts on the most critical regions of the structure, thereby reducing unnecessary inspection operations. As a result, maintenance procedures become more targeted and efficient, leading to a reduction in labour intensity and inspection time.

The integration of fatigue life prediction into the model further enhances its practical value. By estimating the remaining useful life of structural elements, maintenance decisions can be made on a scientifically justified basis rather than relying on conservative assumptions or fixed service intervals. This enables a transition from time-based maintenance strategies to condition-based maintenance, where interventions are performed only when necessary. Such an approach ensures more efficient use of component resources and reduces the likelihood of both premature replacement and unexpected failure.

From an economic perspective, the implementation of the proposed model contributes to a reduction in operational costs. The optimisation of diagnostic procedures reduces inspection frequency, minimises downtime and decreases the need for unnecessary disassembly and testing operations. At the same time, improved accuracy in damage assessment reduces the risk of critical failures, which are associated with high repair costs and operational disruptions [5], [13].

Another important practical advantage is the possibility of implementing the model as part of a software-based diagnostic system. The algorithm can be integrated into modern aircraft maintenance management systems, where it performs automated analysis of input data and generates recommendations for diagnostic actions. This automation reduces the influence of human factors, improves consistency in decision-making and increases the overall efficiency of maintenance processes.

Furthermore, the developed model is fully compatible with modern digital technologies, including structural health monitoring systems and digital twin platforms. This allows continuous monitoring of structural condition and real-time updating of diagnostic decisions. The combination of computational modelling with real-time data processing provides a powerful tool for managing the technical condition of aircraft structures in dynamic operating environments.

The results of this study are also of practical importance for education and training in the field of aviation engineering. The model can be used as a basis for simulation systems, enabling students and engineers to analyse structural behaviour, assess damage levels and select appropriate diagnostic methods in a controlled environment. This contributes to improving the quality of professional training and the development of practical skills.

Thus, the practical significance of the proposed computational and diagnostic model lies in its ability to enhance diagnostic accuracy, optimise maintenance processes, reduce operational costs and improve the overall safety and reliability of aircraft operation. Its implementation provides a strong foundation for the development of advanced maintenance systems based on predictive analytics and intelligent decision-making.

3. Conclusion

This study addresses the important scientific and engineering problem of improving the effectiveness of diagnostic methods for aircraft landing gear components through the application of computational and analytical approaches. In the course of the research, an integrated computational and diagnostic model has been developed, combining stress–strain analysis, fracture mechanics and fatigue life prediction into a unified framework for evaluating structural condition.

Unlike conventional diagnostic methods, which are primarily focused on detecting already developed defects, the proposed approach enables a quantitative assessment of damage level and allows the influence of operational loads, geometric characteristics and material properties to be taken into account. This ensures a more accurate and physically justified evaluation of the structural condition, thereby improving the reliability of diagnostic decisions.

A key result of the study is the development of an adaptive algorithm for selecting diagnostic methods based on calculated structural parameters [11], [12]. The implementation of this algorithm enables a transition from traditional schedule-based diagnostics to a condition-oriented approach, where inspection methods are selected according to the actual state of the component. This significantly enhances diagnostic efficiency and reduces unnecessary inspection operations.

The results of computational modelling demonstrate that the evolution of damage in landing gear components follows a nonlinear pattern, with accelerated crack growth occurring as stress levels approach critical values. The proposed model allows the identification of potentially hazardous zones at early stages, which is not achievable using traditional inspection techniques. This confirms the effectiveness of integrating computational analysis with diagnostic procedures.

An additional advantage of the developed model is its ability to predict damage progression and estimate the remaining useful life of structural elements. This enables the implementation of predictive maintenance strategies, reducing operational risks and improving resource utilisation. The compatibility of the model with modern digital technologies, including structural health monitoring systems and digital twin platforms, further enhances its practical applicability.

From an engineering perspective, the application of the proposed model contributes to improving diagnostic accuracy, optimising maintenance processes, reducing operational costs and enhancing flight safety. The model provides a foundation for the development of intelligent diagnostic systems capable of real-time condition assessment and automated decision-making.

In summary, the developed computational and diagnostic approach represents a significant advancement in the field of aircraft structural diagnostics. Its implementation supports the transition to next-generation maintenance systems based on adaptability, data-driven analysis and predictive capabilities, thereby ensuring a higher level of reliability and safety in aircraft operation.

References

[1] T. H. G. Megson, Aircraft Structures for Engineering Students, 6th ed. Oxford: Elsevier, 2016, pp. 1–912.

[2] S. Suresh, Fatigue of Materials, 2nd ed. Cambridge: Cambridge University Press, 1998, pp. 1–679.

[3] C. Hellier, Handbook of Nondestructive Evaluation, 2nd ed. New York: McGraw-Hill Education, 2013, pp. 1–720.

[4] J. Schijve, Fatigue of Structures and Materials. Dordrecht: Springer, 2009, pp. 1–623.

[5] N. E. Dowling, Mechanical Behavior of Materials, 4th ed. Boston: Pearson, 2012, pp. 1–960.

[6] F. Tao and Q. Qi, "Digital twin-driven smart manufacturing," Journal of Manufacturing Systems, vol. 48, no. 1, pp. 157–169, 2019, doi: 10.1016/j.jmsy.2018.11.007.

[7] T. L. Anderson, Fracture Mechanics: Fundamentals and Applications, 4th ed. Boca Raton: CRC Press, 2017, pp. 1–760.

[8] Y. Murakami, Stress Intensity Factors Handbook. Oxford: Elsevier, 1987, pp. 1–450.

[9] R. O. Ritchie, "Mechanisms of fatigue crack propagation in engineering materials," International Journal of Fracture, vol. 100, no. 1–2, pp. 55–83, 1999, doi: 10.1023/A:1018655917051.

[10] P. C. Paris and F. Erdogan, "A critical analysis of crack propagation laws," Journal of Basic Engineering, vol. 85, no. 4, pp. 528–533, 1963.

[11] Federal Aviation Administration, "Advisory Circular AC 43.13-1B: Aircraft Inspection and Repair," Washington, DC, USA, 2018, pp. 1–320.

[12] European Union Aviation Safety Agency, "Part-145 Maintenance Organisation Approvals," Cologne, Germany, 2020, pp. 1–150.

[13] D. Balageas, C. P. Fritzen, and A. Güemes, Structural Health Monitoring. London: John Wiley & Sons, 2006, pp. 1–350.

[14] C. R. Farrar and K. Worden, "An introduction to structural health monitoring," Philosophical Transactions of the Royal Society A, vol. 365, no. 1851, pp. 303–315, 2007, doi: 10.1098/rsta.2006.1928.

[15] K. Worden and G. Manson, Structural Health Monitoring: A Machine Learning Perspective. Chichester: John Wiley & Sons, 2007, pp. 1–300.

Information about the author

Kutpinisa Kadirbekova	Tashkent State University of Transport, Doctor of Technical Sciences, Professor in the Department of Aviation Engineering. E-mail: niso_51@mail.ru Tel: +998903522340 https://orcid.org/0009-0009-0167-0907
Shakhnozakhon Ermukhamedova	Tashkent State University of Transport PhD candidate in the Department of Aviation Engineering E-mail: shaxnozaxonermuxamedova@gmail.com Tel: +998977743544 https://orcid.org/0009-0008-0503-3924

Analytical study of seismic isolation systems in bridge structures

M. Miralimov[1][a], R. Ospanov[1][b], R. Azamjonov[2][c]

[1]Tashkent state transport university, Tashkent, Uzbekistan

[2]National Research Institute for Seismic Safety and Resilient Construction under Tashkent Institute Architecture and Civil Engineer, Tashkent, Uzbekistan

Abstract: This article presents a comprehensive analysis of existing seismic isolation systems used for protecting bridge structures against seismic impacts. The role of antiseismic devices within bridge structures, as well as the possibilities of their implementation through connections between supports, superstructures, and structural elements, are thoroughly examined. The necessity of considering antiseismic devices as independent and essential structural components of bridges is scientifically substantiated. The strengthening methods employed to ensure the seismic resistance of bridges are classified into conventional and special categories, and their operating principles are analyzed in detail. Conventional methods are primarily based on the absorption and redistribution of seismic loads by the structural elements themselves, whereas special methods are aimed at reducing seismic effects by modifying the dynamic behavior and structural scheme of the bridge. Special methods include seismic isolation and seismic energy dissipation systems. The article also provides a detailed explanation of the concept of seismic isolation, its operating mechanism, and corresponding structural solutions. Seismic isolation systems are categorized into adaptive and stationary types, and the technical characteristics of rigid, flexible, sliding, elastic, and gravitational bearing components specific to each category are investigated. Furthermore, suspended and supported types of gravitational seismic isolation foundations are also analyzed. The research results demonstrate that seismic isolation systems represent one of the most promising seismic protection technologies for bridges constructed in regions with high seismic activity.

Keywords: seismic isolation, anti-seismic devices, bridge structures, seismic loads, adaptive systems, stationary systems, rubber–metal bearings, gravitational seismic protection

1. Introduction

Today, ensuring the seismic resistance of transport infrastructure located in seismically active regions of the world, particularly highway and railway bridges, is considered one of the most important scientific and technical challenges. Strong earthquakes generate significant inertial forces in bridge structures, which may lead to severe damage in supports, superstructures, and their interaction zones. Therefore, the application of antiseismic devices in modern bridge engineering has gained special importance.

Antiseismic devices can be integrated into bridge supports, superstructures, and bearing components, or implemented through structural connections between the main elements of the bridge system. In this context, the interaction between the superstructure and soil, between supports and superstructures, as well as between adjacent spans and supports, must be taken into account [1]. It is more appropriate to consider antiseismic devices not as auxiliary components, but as primary structural elements responsible for seismic protection.

2. Research methodology

To improve the seismic resistance of bridges, both conventional and special strengthening methods are applied. Conventional methods are based on strengthening structural elements or redistributing seismic loads among components. However, such approaches often lead to an increase in structural mass and stiffness.

Special methods, on the other hand, aim to reduce seismic actions by modifying the dynamic behavior of the structure. These methods include seismic isolation and seismic energy dissipation systems. In practice, seismic isolation is considered one of the most effective solutions [2]. This approach significantly reduces the overall seismic response of the bridge by decreasing the energy transmitted to the structure during seismic excitation.

Currently, seismic isolation systems are classified into adaptive and stationary types and are implemented using rubber–metal bearings, gravitational systems, and sliding bearing components. These systems are regarded as one of the most promising seismic protection solutions for bridges constructed in regions with high seismic activity, particularly in seismic zones exceeding intensity level 8.

Antiseismic devices may be incorporated into bridge supports, superstructures, and bearing elements. In addition, they can also be implemented through connections between the main structural components of the bridge (for example, between the superstructure and soil, between supports and superstructures, between adjacent spans, and between neighboring supports). Antiseismic devices should be considered as primary structural elements that perform the function of protecting the structure against earthquakes.

To ensure the seismic resistance of bridges, two main strengthening approaches are applied: conventional and special methods.

a https://orcid.org/0000-0003-2530-5516
b https://orcid.org/0009-0009-9996-1023
c https://orcid.org/0009-0003-8428-4716

Traditional seismic design methods must ensure the acceptance of seismic loads that act on the structure. This is achieved by developing and strengthening structural elements, or by distributing the acting loads among elements [2].

Special methods must ensure a reduction in seismic loads by changing the dynamic scheme of the structure; they are divided into seismic isolation and seismic damping (seismolysis and seismodamping). The overall classification of special seismic protection systems is shown in Figure 1.

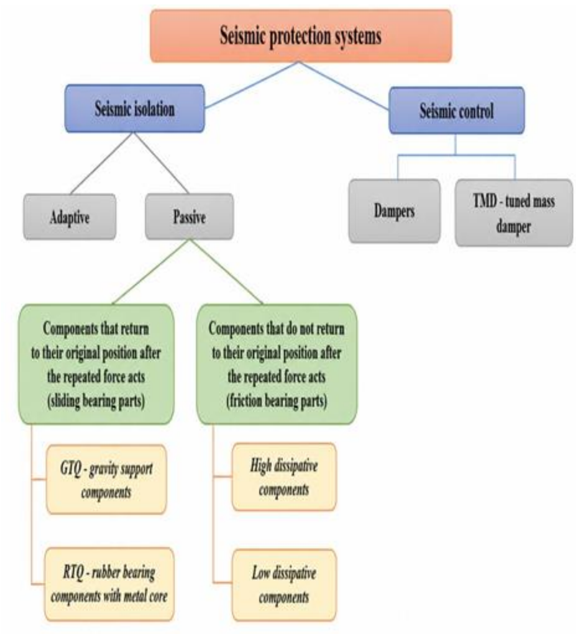

Fig. 1. Classification of special seismic protection method

Worldwide practice widely uses the seismic isolation method for protection against seismic effects.

Seismic isolation means, in our context, systems that reduce the energy affecting structures during the seismic vibration process by installing elements with a higher degree of flexibility at certain levels. Thus, any seismic isolation system must consist of three main components: a rigid structure, a seismic-isolating element, and a supporting (load-bearing) structure.

Seismic isolation systems are classified into adaptive and stationary systems.

Adaptive systems. The adaptive seismic isolation systems consist of coupled support structures of intermediate devices and are divided into rigid or flexible support parts. The rigid support parts are designed to carry operational loads with a certain reserve. Under extreme loads, the rigid support parts fail, and the second group of support parts—flexible elements—comes into operation.

Stationary systems. Stationary seismic isolation systems include four groups of technical solutions. The first two groups of solutions are “flexible” support parts, in which the restoring force arises from elastic forces (rubber-metal bearings (RTQ)) or from the force of gravity (gravitational bearings (GTQ)). The issue of protecting bridges from seismic effects is an important scientific and practical task for ensuring the reliability and continuous operation of transport infrastructure worldwide. For this reason, in many countries numerous constructive and technological solutions have been developed and implemented aimed at improving the effectiveness of seismic isolation systems [12].

Rubber-metal bearings are currently widely used in bridges located in seismically active regions such as Japan, the United States, New Zealand, and Italy. These systems consist of elastomer layers and steel plates, providing high flexibility in the horizontal direction and sufficient stiffness in the vertical direction. Lead-rubber bearings (LRB) additionally have an energy-dissipation capability, so during seismic vibrations the inertia forces are significantly reduced. Gravitational seismic isolation systems are used as an effective solution for bridges in the United States and European countries. In these systems, the intermediate part moves along spherical sliding surfaces, and the restoring force is generated by gravity.

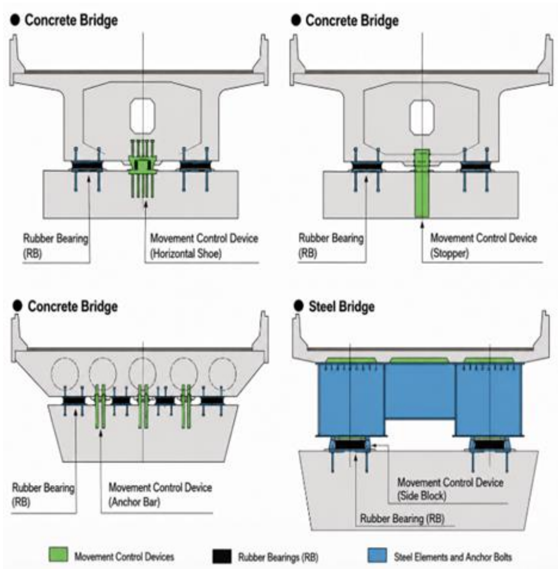

Fig. 2. Lead Rubber Bearings (LRB) used in bridge structures for seismic isolator

The presented figure illustrates the fundamental mechanical behavior, analytical relationships, and seismic performance characteristics of damping systems used in bridge isolation and vibration control engineering. These systems are essential components in modern earthquake-resistant bridge structures because they reduce seismic forces, dissipate input energy, and improve structural stability during dynamic loading conditions [6]. The diagram integrates several important concepts of structural dynamics, including hysteretic energy dissipation, damping ratios, force–displacement relationships, seismic response spectra, and equivalent viscous damping models. Each subfigure represents a specific analytical or mechanical characteristic of bridge isolation devices such as rubber bearings, viscous dampers, hysteretic dampers, and friction-based seismic isolation systems [7].

The first graph presents the hysteretic behavior of elastomeric rubber bearings under cyclic shear loading. When seismic excitation occurs, the bridge deck experiences repeated lateral displacements. Rubber bearings deform in shear and generate a hysteresis loop due to the viscoelastic behavior of rubber material. The enclosed area inside the hysteresis loop represents dissipated seismic energy [8].

$$K = \frac{\tau}{\gamma}$$

https://doi.org/10.56143/3030-3893-2026-2-62-66

Where:
K = Shear stiffness ,τ = Shear stress ,γ = Shear strain
A wider hysteresis loop indicates higher energy dissipation capacity, greater damping performance, reduction in seismic response amplitude, and improved bridge survivability during earthquakes.

During earthquake excitation, the bridge superstructure experiences repeated horizontal displacement. The rubber layers inside the bearing deform in shear, producing cyclic stress–strain loops. Because rubber exhibits viscoelastic behavior, loading and unloading paths do not coincide, creating a hysteresis loop. modern earthquake engineering, seismic isolation design, nonlinear structural dynamics, and bridge vibration control analysis. These equations form the theoretical foundation for evaluating damping behavior, energy dissipation mechanisms, and seismic performance of isolated bridge systems.

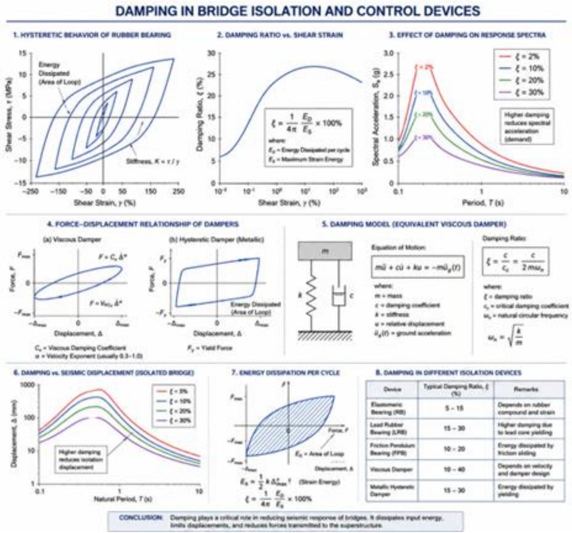

Fig. 3. Analytical Representation of Damping and Energy Dissipation in Bridge Seismic Isolation Devices

The next two groups of solutions are “sliding” support elements. Based on their operating principle, they can be divided into two categories: those with low friction and those with high friction. In the first case, the intermediate devices are connected in the form of a chain, and movable (“sliding”) support elements are installed on the intermediate bearings [6].

The stationary seismic isolation systems can also be classified according to whether they have a restoring force or not. In turn, seismic isolation systems with a restoring force are divided into elastic and gravitational systems. In the former, the restoring force is provided by elastic forces, whereas in the latter, it is provided by the force of gravity [9].

Gravitational seismic isolation foundations can be divided into suspended foundations and supported (bearing) foundations. In suspended foundations, the upper foundation slab is installed on a frame structure that is rigidly connected to the lower foundation slab and is suspended using hangers (ties/supporting rods). The seismic isolation foundation of F. D. Zelenkov constructed in the city of Ashgabat was the first such type of foundation of its kind in the USSR [10].

In supported foundations, the upper foundation slab rests on kinematic bearings. The scheme of the gravitational bearing foundation is shown in Figure 4.

At present, it is reasonable to consider seismic isolation of buildings and structures—including bridges constructed in regions with seismicity greater than 8— as the most promising means of seismic protection. Worldwide, thousands of seismic-isolated buildings and structures have been constructed [11].

In gravitational seismic isolation foundations of the bearing type, the upper foundation slab rests on special kinematic bearings. These bearings have spherical or curved sliding surfaces, ensuring a controlled displacement of the structure during seismic effects. During the displacement process, the restoring force is generated mainly due to the weight (gravity) of the structure [3].

Bearing gravitational foundations have high stability and keep the displacement amplitude within predetermined limits. These systems are widely used in modern global practice, and their developed forms operate on the basis of the Friction Pendulum System. Such systems maintain high reliability even under conditions of large seismic loads.

Scientific evaluation. Gravitational seismic isolation foundations are an effective means of seismic protection for structures and bridges in regions with high seismic activity. Their main advantage is explained by the fact that the restoring force depends not on the stiffness of structural elements, but primarily on the force of gravity, which ensures a stable and predictable dynamic behavior of the system. The research results indicate that applying seismic isolation systems to bridges built in highly seismic regions is appropriate and highly promising as a means of seismic protection.

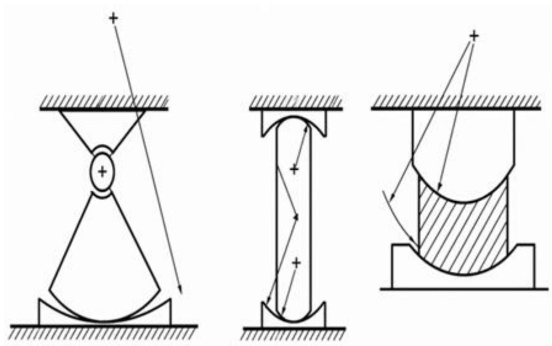

Fig. 4. Schematic diagram of gravitational bearing components (GB)

It should be noted that the sliding of this intermediate device relative to the support ensures the appearance of a gravitational restoring force. At the end of the 1970s, similar solutions were also proposed by Z. G. Khuchbarov and V. P. Chudnetsov.Gravitational seismic isolation foundations (GSIF – Gravitational Seismic Isolation Foundations) are systems intended to protect buildings or bridges from earthquake effects. Their main principle is based on the fact that the restoring force depends on gravity, i.e.,

In traditional elastic foundations and seismic isolation, the restoring force in the elastic foundation is determined primarily by the stiffness of the system. In a gravitational foundation, the restoring force arises from the weight (gravity) of the system, which ensures a stable and predictable dynamic response.As a result, in such systems the restoring force mainly depends on the stiffness of structural components (rubber, steel, concrete), where the restoring force is governed by gravity rather than by the elastic element stiffness alone.

The first concept is probably the simplest seismic design approach: the structure is designed to operate under the expected seismic load level without structural damage. During an earthquake, however, there are many unknown factors that affect the structural response, for example: the level of external loading, material properties, construction errors, and other factors.

Stability: The system may move under dynamic effects, but the restoring force remains constant and can be calculated in advance.

Simple structure: It does not require complex elastic or adaptive elements.

A seismic isolation system (SI system) consists of two main elements:

1. a flexible mounting/isolator that supports the superstructure, and
2. an energy-dissipating device (a dissipator).

The purpose of these two elements is to separate the vibration period of the structure from the dominant horizontal period of earthquakes, prevent large seismic energy from entering the structure due to resonance, and dissipate seismic energy, thereby reducing structural displacements.

Although the seismic isolation system must be sufficiently flexible during an earthquake to reduce the transfer of inertia forces from the foundation to the superstructure, it must also be stiff enough under service loads such as minor earthquakes or wind.

The use of mechanical energy-dissipation devices provides the advantage of seismic isolation in that it significantly reduces the probability of structural damage during strong earthquakes and ensures economic benefits over the entire service life of the structure.

Self-centering is one the most important characteristics of a modern earthquake resistant structural system. Several attempts have been done to design such a system which meets the desired performance objective. Up to now, modern proposed structural systems contain isolation devices or unbounded post-tensioned tendons or combination of them to dissipate energy. Post-tensioning technology is used to design self-centering bridge piers while preventing excessive rocking that cause instability. In this study instead of using special devices or technology, it has been focused on the inherent self-centering due to gravity acceleration to introduce a simple earthquake resistant scheme. This bridge structural system can rock during earthquakes [11].

High load-carrying capacity: Since the system operates based on gravity, it is suitable for heavy bridge or building structures.

The operating mechanism of gravitational seismic isolation foundations may include the following elements:

- **Gravitational bearing:** generates the restoring force due to the structure’s weight.
- **Suspended or balanced (equilibrium) systems:** when the foundation moves, the displacement of the structure is smooth and stable.
- **Control of dynamic response:** the displacement amplitude and velocity are controlled according to the system design.

These systems are especially useful for bridges because the length of bridges and the role of intermediate supports are significant in reducing dynamic loads.

3. Conclusion

Within the framework of this study, the efficiency and practical application of seismic isolation systems in bridge structures were comprehensively analyzed. The obtained results demonstrate that seismic isolation systems, particularly elastomeric and hydraulic devices, effectively protect bridge structures from the adverse effects of seismic loading. The operation of these systems enhances the overall structural safety by re

Based on international engineering practice and existin

In general, seismic isolation systems play a significant role in improving the seismic safety of bridge structures and minimizing earthquake-induced damage. Therefore, scientifically and technically justified approaches should be applied during the design, analysis, and calculation processes of bridge seismic isolation system.

References

[1] Shermuxamedov U.Z. Transport inshootlarining zilzilabardoshligi.

[2] Ko‘priklar, tonnellar va yo‘lo‘tkazgichlarning zilzilabardoshligi. U.Z. Shermuxamedov, I. Mirzayev, O‘. Raxmanov. Darslik. T.: “Transport” nashriyoti, 2024. – 448 b.

[3] Елисеев О.Н., Уздин А.М. Сейсмостойкое строительство. Учебник. – СПб.: Изд. ПВВИСУ, 1997. – 371с.

[4] Верхолин В.А. Оценка сейсмостойкости подвижного состава. Сейсмостойкое строительство. Безопасность сооружений. 2002, №2, с.9-10.

[5] Atsushi Mori INVESTIGATION OF THE BEHHAVIOUR OF SEISMIC ISOLATION SYSTEMS FOR BRIDGES.

[6] Seismic isolation of bridges: Case studies M.S. Mohammed, S.C. Darling, A.F. Ibrahim & L.P. DeBisschop Dynamic Isolation Systems Inc., McCarran, NV, USA

[7] Seismic Energy Dissipation in Bridges for Performance Enhancement Juan M. Mayoral 1,*, Mauricio Pérez 2 , Azucena Román-de la Sancha 3 , Ingrid Guzmán 1 and Leomar González82.

[8] Enhancing Structural Resilience for Sustainable Infrastructure: A Global Review of Seismic Isolation and Energy Dissipation Practices Musab A. Q. Al-Janabi 1,2,* , Duaa Al-Jeznawi 1,3 , T. Y. Yang 4 , Luís Filipe Almeida Bernardo 5 and Jorge Miguel de Almeida Andrade 5,*

[9] USING SEISMIC ISOLATION AND ENERGY DISSIPATION TO CREATE EARTHQUAKE-RESILIENT BUILDINGS R. L. Mayes1 ,

[10] Seismic Response and Design of Gravity-Based Self-Centering Bridges M. Masoudi ROSE School, IUSS Pavia, Italy R. DesRoches Georgia Institute of Technology, Atlanta, USA

[11] A Study on the Seismic Isolation Systems of Bridges with Lead Rubber Bearings Woo-Suk Kim, Dong-Joon Ahn, Jong-Kook:

[12] Seismic behavior of isolated bridges: A-state-of-the-art review M.C. Kunde M.Tech. Student, Department of Civil Engineering, Indian Institute of Technology Bombay, Powai, Mumbai – 400 076 (India) and R.S. Jangid.

Information about the author

Mirzokhid Miralimov	Tashkent state transport university, Doctor of Technical Sciences (DSc). E-mail: mirzakhid_miralimov@yahoo.com/ Tel.:+998977250924 https://orcid.org/0000-0003-2530-5516
Ruslan Ospanov	Tashkent state transport university, Graduate student Email: Jandos_Chingis@mail.ru Tel.: +998933601335 https://orcid.org/0009-0009-9996-1023
Ruziboy Azamjonov	National Research Institute for Seismic Safety and Resilient Construction under Tashkent Institute Architecture and Civil Engineering, Doctoral researcher E-mail: rozixojaazamjonov@gmail.com Tel.: +998909564684 https://orcid.org/0009-0003-8428-4716

Improvement of diagnostic process for aircraft component damage

K.K. Kadirbekova[1][a], Sh.T. Ermukhamedova[1][b]
[1]Tashkent state transport university, Tashkent, Uzbekistan

Abstract: The paper examines current approaches to improving the diagnostic process for detecting damage in aircraft structural components under operational conditions. Particular attention is given to aircraft landing gear elements, which are subjected to significant cyclic, impact and vibration loads during take-off, landing and taxiing. The study analyses the influence of operational factors, including load intensity, climatic conditions and runway quality, on the accumulation of fatigue damage and the reduction of structural reliability.

A comprehensive diagnostic approach is proposed, combining vibration diagnostics with a software-based model for selecting the optimal inspection method depending on the type of structural element, material properties, operating conditions and nature of the suspected defect. The principles of vibration diagnostics based on the analysis of amplitude, frequency and energy characteristics of vibration signals are considered. The high sensitivity of vibration parameters to the early stages of structural degradation, including fatigue cracks, weakening of joints and microstructural defects, is substantiated.

The developed software model includes algorithms for analysing the diagnostic object, determining dominant degradation factors, generating informative diagnostic parameters and selecting the most effective inspection method. Comparative analysis of existing diagnostic methods demonstrates the advantages of vibration diagnostics in terms of early defect detection, automation capability and reduction of labour intensity. The proposed approach enables continuous monitoring of technical condition without dismantling structural components and supports the transition from scheduled maintenance to condition-based maintenance.

The implementation of the proposed diagnostic approach contributes to improving aircraft reliability, increasing flight safety, optimising maintenance schedules and reducing operational costs. The obtained results confirm the перспективность of integrating vibration diagnostics and intelligent software systems into modern aircraft maintenance processes.

Keywords: diagnostics, aircraft, damage, vibration diagnostics, landing gear, reliability

1. Introduction

Ensuring the reliability, durability and operational safety of aircraft structures remains one of the most important tasks of modern aviation engineering. The continuous growth of flight intensity, increasing operational loads and stricter international flight safety requirements significantly increase the demands placed on the technical condition monitoring of aircraft components. During long-term operation, aircraft structures are subjected to complex cyclic, vibration and impact loads, as well as adverse climatic and environmental influences, which lead to the gradual accumulation of fatigue damage, degradation of material properties and the initiation of hidden structural defects [1], [2].

The timely detection of structural damage is of critical importance for preventing emergency situations, reducing maintenance costs and increasing operational reliability. Fatigue cracks, local weakening of joints, corrosion processes and microstructural defects may significantly reduce the service life of aircraft structures and negatively affect flight safety. In many cases, the development of such defects occurs internally and remains undetected during routine maintenance inspections. Therefore, the development and implementation of highly sensitive diagnostic methods capable of identifying damage at early stages of development has become an important scientific and practical problem in aviation engineering [3].

Traditional aircraft diagnostic methods include visual inspection, capillary inspection, ultrasonic testing, radiographic inspection and other non-destructive testing techniques. Despite their widespread application in aviation maintenance practice, these methods possess several limitations associated with dependence on operator qualification, periodic inspection intervals and difficulties in detecting hidden defects during early stages of degradation. In addition, many traditional methods require partial dismantling of structural elements and considerable labour intensity, which increases maintenance complexity and operational costs [4], [5].

In recent years, the rapid development of intelligent maintenance technologies and digital diagnostic systems has significantly transformed approaches to aircraft technical condition assessment. Modern aviation increasingly requires the implementation of automated monitoring systems capable of continuously analysing the structural condition of aircraft components in real time. This tendency is closely related to the transition from scheduled maintenance concepts to condition-based and predictive maintenance strategies, which rely on continuous monitoring, intelligent data processing and early identification of degradation processes [6].

One of the most promising directions in modern aircraft diagnostics is the integration of Structural Health Monitoring (SHM) technologies, vibration analysis methods and intelligent software systems. These technologies enable

[a] https://orcid.org/0009-0009-0167-0907
[b] https://orcid.org/0009-0008-0503-3924

continuous assessment of structural condition and provide the possibility of detecting hidden defects, fatigue damage and degradation processes long before critical structural failure occurs. The implementation of intelligent diagnostic systems contributes to improving maintenance efficiency, reducing aircraft downtime and enhancing overall flight safety [7], [8].

Among aircraft structural components, landing gear systems represent one of the most heavily loaded and operationally critical assemblies. During take-off, landing, braking and taxiing operations, landing gear structures are subjected to significant dynamic loads, vibration excitation and repeated cyclic stresses. Over time, these operational factors lead to the accumulation of residual stresses, fatigue microcracks and local weakening of structural elements. The highest stress concentrations are typically observed in joint areas, section transitions and shock-absorbing assemblies, where fatigue damage is most likely to initiate.

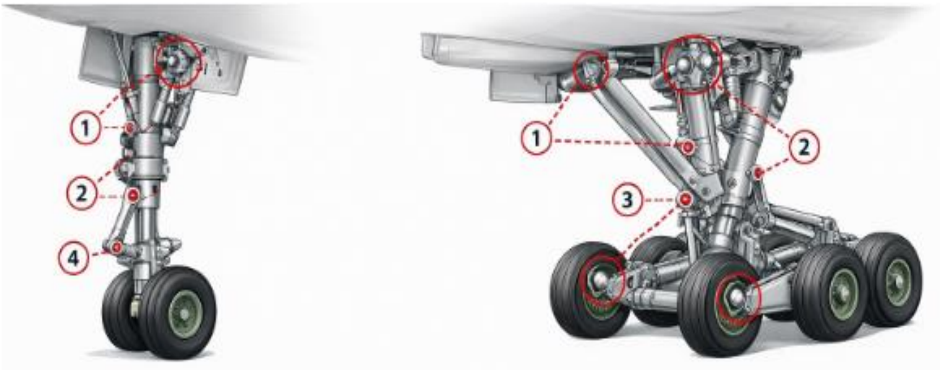

Fig. 1. Structural diagram and stress concentration zones of the aircraft landing gear components: 1 – shock absorber strut; 2 – lateral strut; 3 – cross members with spindles; 4 – bogie with wheels

The structural complexity of aircraft landing gear systems, the presence of stress concentrators and the use of high-strength materials necessitate the application of more advanced and highly sensitive diagnostic methods capable of identifying early-stage degradation processes. In this regard, vibration diagnostics is considered one of the most promising methods for assessing the technical condition of aircraft structures. The method is based on analysing changes in the dynamic characteristics of structural elements caused by defect development and stiffness reduction.

Another important problem in aircraft diagnostics is the selection of the most informative inspection method depending on operational conditions, material properties and the type of suspected defect. The effectiveness of technical condition assessment largely depends on the correct selection of diagnostic parameters and inspection techniques. Therefore, the development of intelligent software-based systems capable of analysing operational factors and automatically selecting optimal diagnostic methods represents an important scientific direction in modern aviation maintenance systems [5].

The present study proposes a comprehensive approach to improving the diagnostic process for aircraft component damage detection through the integration of vibration diagnostics and a software model for selecting inspection methods. The proposed approach aims to improve the reliability of technical condition assessment, increase the effectiveness of early defect detection and support the implementation of intelligent condition-based maintenance technologies in aircraft operation.

2. Research methodology

Vibration Diagnostics Principles

Vibration diagnostics is one of the most effective modern methods for assessing the technical condition of aircraft structural components. The method is based on the analysis of dynamic characteristics of structures during operation and allows hidden defects to be identified through changes in vibration parameters. Unlike conventional inspection techniques, vibration diagnostics enables continuous monitoring of structural condition without dismantling equipment, which significantly increases maintenance efficiency and reduces operational costs [9].

The principle of vibration diagnostics is based on the fact that the appearance and development of structural defects lead to changes in stiffness, mass distribution and damping characteristics of structural elements. These changes directly affect the vibration behaviour of the structure and result in variations of amplitude, frequency spectrum, phase characteristics and vibration energy distribution. Even relatively small defects may produce measurable deviations in dynamic response parameters, making vibration diagnostics highly sensitive to early stages of structural degradation [10], [11].

During aircraft operation, landing gear components are subjected to repeated cyclic and impact loads generated during take-off, landing, braking and taxiing processes. These loads lead to the gradual accumulation of fatigue damage, local weakening of joints and formation of microcracks in highly stressed structural areas. As the defect develops, the dynamic properties of the structure change, causing modifications in natural frequencies and vibration amplitudes. Monitoring these parameters enables the technical condition of structural components to be evaluated in real time [12].

The diagnostic effectiveness of vibration analysis depends on the correct interpretation of informative vibration parameters. The most commonly used diagnostic indicators include vibration amplitude, root mean square (RMS) value, peak vibration level, frequency spectrum characteristics and vibration energy distribution. An increase in vibration amplitude often indicates the development of looseness, imbalance or structural degradation, while shifts in natural frequencies may indicate stiffness reduction caused by crack propagation or fatigue damage.

https://doi.org/10.56143/3030-3893-2026-2-67-73

Particular importance in vibration diagnostics is given to spectral analysis methods, which enable the identification of characteristic frequency components associated with specific defect types. The frequency spectrum of a healthy structural element differs significantly from that of a damaged structure. The appearance of additional harmonic components, sideband frequencies and increased energy concentration within certain frequency ranges may indicate the initiation and development of structural defects [13].

Figure 2 illustrates the characteristic evolution of vibration parameters during defect propagation. At the initial stage of degradation, vibration characteristics change insignificantly and remain close to nominal values. However, as fatigue damage accumulates and crack dimensions increase, a substantial rise in vibration activity and energy concentration is observed. These changes confirm the high sensitivity of vibration diagnostics to early-stage structural degradation processes.

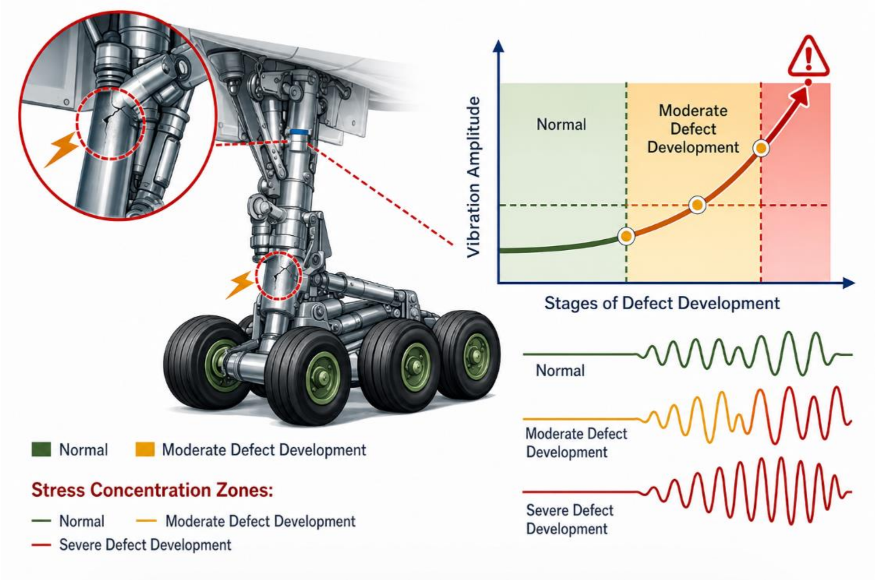

Fig. 2. Changes in vibration parameters as the defect develops

An important advantage of vibration diagnostics is the possibility of integrating diagnostic sensors with intelligent software systems for automated data processing and technical condition assessment. Modern digital diagnostic systems are capable of continuously monitoring vibration parameters, analysing large volumes of diagnostic information and automatically identifying abnormal operating conditions [14]. Such systems significantly reduce dependence on the human factor and improve the objectivity and reliability of diagnostic results.

Compared with conventional non-destructive testing methods, vibration diagnostics offers several significant advantages, including rapid data acquisition, suitability for automation, continuous monitoring capability and high sensitivity to hidden defects. These characteristics make vibration diagnostics a promising basis for the development of intelligent aircraft maintenance systems and predictive maintenance technologies [15].

Thus, the application of vibration diagnostics enables early detection of fatigue damage, optimisation of maintenance procedures and improvement of aircraft operational reliability. The integration of vibration analysis methods with intelligent software-based diagnostic systems creates favourable conditions for the implementation of condition-based maintenance concepts in modern aviation engineering.

Software Model for Diagnostic Method Selection

The effectiveness of aircraft diagnostics depends not only on the quality of inspection equipment but also on the correct selection of diagnostic methods according to the structural characteristics of aircraft components, operational conditions and the type of suspected defect. Different diagnostic techniques possess different levels of sensitivity, labour intensity and applicability. Therefore, the development of intelligent software systems capable of supporting the selection of optimal inspection methods represents an important scientific and practical direction in modern aviation maintenance systems [16].

In the present study, a software-based model for selecting diagnostic methods has been developed to improve the efficiency and reliability of aircraft structural condition assessment. The proposed model integrates several diagnostic approaches, including vibration diagnostics, ultrasonic testing and luminescent inspection methods, into a unified software environment. The system is intended to assist maintenance personnel in analysing technical condition and selecting the most informative inspection method depending on operational requirements and defect characteristics [17].

The software model performs comprehensive analysis of aircraft structural elements by considering operational loads, stress concentration zones, material properties and the probable nature of damage development. Based on the analysed information, the system determines which diagnostic method is most suitable for a particular inspection task. Such an approach increases diagnostic accuracy and reduces the probability of incorrect technical decisions [18].

Vibration diagnostics is used in the software model as one of the primary methods for detecting early-stage structural degradation. The method enables identification of changes in dynamic characteristics caused by fatigue cracks, loosening of joints, stiffness reduction and other hidden defects. Vibration analysis is especially effective for continuous monitoring of heavily loaded structural assemblies, including aircraft landing gear systems. The software system analyses vibration amplitude, frequency spectrum and energy characteristics to identify abnormal operating conditions and possible defect development [19].

Ultrasonic testing is included in the software model as a highly sensitive method for detecting internal defects and determining crack depth within structural materials. The ultrasonic method enables identification of hidden damage that cannot be visually observed on the surface of the component. In the developed software system, ultrasonic inspection data are used for уточнение defect localisation, assessment of defect dimensions and verification of vibration diagnostic results. Integration of ultrasonic testing significantly improves the reliability of technical condition assessment [20].

Luminescent inspection methods are also incorporated into the software model for detecting surface cracks and local structural defects. Luminescent control is widely applied in aviation maintenance practice due to its simplicity and high effectiveness for identifying small surface discontinuities. The developed system considers the results of luminescent inspection as an additional source of diagnostic information, particularly for evaluating surface damage in highly stressed landing gear elements and structural joints.

The software model combines information obtained from different diagnostic methods and performs integrated analysis of technical condition. Such an approach allows the advantages of each inspection technique to be utilised while compensating for their individual limitations. For example, vibration diagnostics provides early identification of abnormal structural behaviour, ultrasonic testing ensures accurate detection of internal defects, and luminescent inspection confirms the presence of surface cracks and local damage zones.

An important feature of the developed software system is its capability for intelligent selection of diagnostic methods depending on operational conditions and inspection objectives. For instance, in cases where early fatigue damage is suspected, the system prioritises vibration diagnostics due to its high sensitivity to changes in structural stiffness and dynamic behaviour. If detailed assessment of internal crack propagation is required, ultrasonic inspection methods are recommended. For rapid evaluation of surface defects during maintenance procedures, luminescent inspection methods are selected.

The software model also enables visualisation of diagnostic results through graphical interfaces and monitoring panels. Diagnostic information, including vibration characteristics, ultrasonic inspection data and defect status indicators, can be displayed in real time. Such visualisation improves the interpretability of diagnostic data and supports maintenance personnel in making technical decisions.

Another important advantage of the proposed system is the possibility of integrating diagnostic data into digital aircraft maintenance environments and intelligent monitoring platforms. Continuous accumulation and processing of inspection information enable analysis of degradation trends and improve maintenance planning efficiency. This contributes to the implementation of condition-based maintenance concepts and reduces unnecessary maintenance procedures [20].

Thus, the developed software model for selecting diagnostic methods represents a comprehensive intelligent diagnostic system integrating vibration diagnostics, ultrasonic testing and luminescent inspection methods. The proposed approach improves the reliability of aircraft structural condition assessment, increases the effectiveness of defect detection and contributes to enhancing aircraft operational safety.

Comparative Analysis of Diagnostic Methods

The effectiveness of aircraft structural diagnostics is strongly influenced by operational conditions and the correct selection of inspection techniques. Aircraft components operate under complex loading environments that include cyclic stresses, vibration excitation, impact loading and adverse climatic effects. Operational factors such as flight intensity, runway condition, humidity, temperature fluctuations and environmental contamination significantly affect the rate of structural degradation and accumulation of fatigue damage. These factors must be considered during the selection and application of diagnostic methods in order to ensure reliable technical condition assessment[3], [7].

Different diagnostic methods possess different levels of sensitivity, inspection complexity and suitability for automation. Therefore, comparative analysis of existing inspection techniques is necessary for determining the most effective approaches to aircraft structural diagnostics. Traditional inspection methods, including visual and capillary inspection, remain widely used in aviation maintenance practice due to their simplicity and relatively low cost. However, these methods are limited in their ability to detect hidden defects and early-stage fatigue damage.

Visual inspection is mainly used for detecting visible surface defects, corrosion traces, deformation and mechanical damage. Although this method requires minimal equipment and relatively low labour intensity, its effectiveness strongly depends on operator experience and inspection conditions. Hidden defects and internal structural degradation often remain undetected during visual examination.

Capillary inspection methods provide improved sensitivity for detecting small surface cracks and discontinuities. These methods are widely applied for inspection of highly stressed structural zones and welded joints. However, capillary inspection is limited to surface defects only and cannot provide information about internal structural condition. In addition, the inspection process requires careful surface preparation and considerable maintenance time [12], [13].

Ultrasonic inspection methods possess high sensitivity for detecting internal defects and determining crack depth within structural materials. Ultrasonic testing enables accurate localisation of hidden damage and is widely used in aircraft maintenance practice. Nevertheless, ultrasonic inspection often requires direct access to the inspected component and highly qualified personnel for interpretation of diagnostic results. The complexity of the inspection process and relatively high labour intensity may limit its application during rapid maintenance procedures.

Among modern diagnostic approaches, vibration diagnostics demonstrates significant advantages in terms of early defect detection and suitability for automation. The method enables identification of changes in structural stiffness and dynamic behaviour caused by fatigue damage, crack development and loosening of structural joints. Since vibration diagnostics can be performed without dismantling structural elements, it provides possibilities for continuous monitoring of technical condition during aircraft operation.

An additional advantage of vibration diagnostics is its compatibility with intelligent software systems and automated monitoring technologies. Modern digital diagnostic platforms are capable of continuously analysing vibration parameters, identifying abnormal operating conditions and generating diagnostic recommendations in real time. This significantly reduces dependence on the human factor and increases the reliability and objectivity of technical condition assessment[9], [14].

Table 1

Comparative characteristics of diagnostic methods for aircraft structures

Diagnostic method	Early defect detection	Suitability for automation	Labour intensity	Limitations
Visual inspection	Low	Low	Low	Dependence on human factors
Capillary inspection	Medium	Low	Medium	Surface defects only
Ultrasonic inspection	High	Medium	High	Requires access to the object
Vibration diagnostics	High	High	Low	Requires correct interpretation

The comparative analysis demonstrates that vibration diagnostics possesses considerable advantages for modern intelligent aircraft maintenance systems. The method combines high sensitivity to early-stage structural degradation with low labour intensity and broad possibilities for automation. These characteristics make vibration diagnostics particularly suitable for integration into condition-based maintenance and Structural Health Monitoring systems [15], [19].

At the same time, effective aircraft diagnostics should not rely on a single inspection method. The combination of vibration diagnostics, ultrasonic testing and conventional inspection techniques provides a more comprehensive assessment of structural condition and increases the reliability of defect detection. Integration of multiple diagnostic approaches into intelligent software systems enables optimisation of maintenance procedures and improves prediction of remaining service life for aircraft components.

Thus, taking operational factors and diagnostic method characteristics into account significantly improves the accuracy of technical condition assessment and enhances the effectiveness of aircraft maintenance processes. The obtained results confirm the перспективность of integrating vibration diagnostics and intelligent software systems into modern aviation diagnostic technologies.

3. Results and Discussion

The conducted analysis confirms that the combined application of vibration diagnostics, ultrasonic inspection and intelligent software-based diagnostic systems provides a comprehensive and effective approach to assessing the technical condition of aircraft structural components. Integration of different diagnostic methods enables more reliable identification of hidden defects, improves the accuracy of technical condition assessment and increases the effectiveness of maintenance procedures[9], [10].

The obtained results demonstrate that vibration diagnostics possesses high sensitivity to early-stage structural degradation processes. Even minor changes in stiffness and dynamic behaviour caused by fatigue damage lead to measurable variations in vibration parameters. This allows hidden defects and microstructural damage to be identified long before visually detectable signs of degradation appear. Such capabilities are particularly important for aircraft landing gear systems, which operate under significant cyclic and impact loading conditions.

One of the most important advantages of vibration diagnostics is the possibility of continuous monitoring of structural condition without dismantling aircraft components. Unlike traditional inspection techniques, vibration analysis can be performed during operation and does not require interruption of maintenance processes. This significantly reduces labour intensity and creates favourable conditions for implementing intelligent monitoring systems in aviation maintenance practice.

The research results also demonstrate that the effectiveness of diagnostic procedures significantly increases when vibration diagnostics is combined with ultrasonic and luminescent inspection methods. Vibration analysis enables early identification of abnormal structural behaviour, while ultrasonic inspection provides detailed information about internal defect localisation and crack dimensions. Luminescent inspection methods complement the diagnostic process by enabling reliable detection of surface cracks and local damage zones. The integration of these methods into a unified software environment improves the reliability and objectivity of technical condition assessment [17], [20].

Particular attention in the developed software model is given to the influence of operational factors on structural degradation processes. Flight intensity, runway condition, climatic influences and loading characteristics significantly affect the rate of fatigue damage accumulation in aircraft structures. The software system analyses these factors and adapts the selection of diagnostic methods according to specific operational conditions. Such an approach improves maintenance efficiency and reduces the probability of incorrect technical decisions.

The developed software model also demonstrates high potential for integration into intelligent aircraft maintenance systems and digital monitoring platforms. Automated processing of diagnostic information enables continuous analysis of structural condition and rapid identification of abnormal operating parameters. This contributes to reducing dependence on the human factor and increases the reliability of maintenance decision-making processes.

An important result of the study is the confirmation that the implementation of vibration diagnostics enables the transition from traditional scheduled maintenance concepts to condition-based maintenance strategies. This approach allows maintenance procedures to be planned according to the actual technical condition of aircraft components rather than fixed operational intervals. As a result, unnecessary inspections can be reduced while maintaining high levels of operational safety and structural reliability.

The research results further indicate that vibration diagnostics is most effective during the early stages of fatigue and microstructural damage development, when traditional inspection methods are not yet capable of identifying degradation processes. Early defect detection significantly reduces the risk of critical structural failure and contributes to increasing aircraft operational reliability [16], [19].

In addition, the integration of intelligent software systems with diagnostic technologies improves the visualisation and interpretation of inspection results. Real-time monitoring panels, graphical interfaces and automated defect indication systems simplify analysis of diagnostic information and improve interaction between maintenance personnel and diagnostic equipment.

Thus, the obtained results confirm the effectiveness and potential of integrating vibration diagnostics, ultrasonic inspection and intelligent software systems into modern aircraft maintenance technologies. The proposed approach contributes to improving aircraft operational reliability, optimising maintenance procedures, reducing maintenance costs and enhancing overall flight safety.

4. Conclusion

The conducted research demonstrates that the integration of vibration diagnostics, ultrasonic inspection and intelligent software-based diagnostic systems provides an effective approach to improving the process of aircraft structural condition assessment. Analysis of operational factors and degradation mechanisms confirms the necessity of applying highly sensitive diagnostic methods capable of detecting defects during the early stages of their development.

The study has shown that vibration diagnostics possesses significant advantages in terms of early defect detection, suitability for automation and continuous monitoring capability. Changes in vibration characteristics enable identification of hidden structural degradation processes, including fatigue damage, stiffness reduction and loosening of structural joints, long before visible defects appear. This makes vibration diagnostics a promising basis for the development of intelligent aircraft maintenance systems.

The developed software model for selecting diagnostic methods improves the reliability and objectivity of technical condition assessment by considering operational conditions, structural characteristics and defect types. Integration of vibration diagnostics with ultrasonic and luminescent inspection methods enables comprehensive analysis of aircraft structural condition and increases the accuracy of maintenance decision-making processes.

An important advantage of the proposed approach is the possibility of transitioning from traditional scheduled maintenance concepts to condition-based maintenance strategies. Continuous monitoring of diagnostic parameters enables optimisation of maintenance procedures, reduction of unnecessary inspections and improvement of aircraft operational efficiency. In addition, the use of intelligent software systems contributes to reducing dependence on the human factor and increases the effectiveness of technical diagnostics [19].

The obtained results confirm that the implementation of the proposed diagnostic approach contributes to improving aircraft reliability, reducing operational costs, optimising maintenance schedules and enhancing overall flight safety. The integration of intelligent diagnostic technologies into modern aviation maintenance systems represents a promising direction for further development of aircraft operational support and predictive maintenance concepts.

References

[1] Petrov A.I. Diagnosis of the Technical Condition of Aviation Equipment. — Moscow: Mashinostroenie, 2018. — 420 p.

[2] Ivanov S.V. Reliability and Safety of Aviation Systems. — Saint Petersburg: Polytechnika, 2020. — 380 p.

[3] Zakharov V.P. Non-Destructive Testing Methods in Aviation. — Novosibirsk: Nauka, 2017. — 300 p.

[4] Smirnov A.N. Modern Methods of Structural Diagnostics. — Moscow: Tekhnosfera, 2019. — 280 p.

[5] Orlov K.V. Software Modelling in Maintenance Systems. — Yekaterinburg: Ural Federal University Press, 2021. — 250 p.

[6] Bardis K., Avdelidis N.P., Zolotas A. Advanced Diagnostics of Aircraft Structures Using Automated Non-Invasive Imaging Techniques: A Comprehensive Review // Applied Sciences. — 2025. — Vol. 15, No. 7. — Article 3584.

[7] Wang B., Zhong S., Lee T.-L., Fancey K.S., Mi J. Non-destructive testing and evaluation of composite materials/structures: A state-of-the-art review // Advances in Mechanical Engineering. — 2020. — Vol. 12, No. 4. — pp. 1–28.

[8] Hameed A., Zubair O., Shams T.A., Mehmood Z., Javed A. Failure analysis of a broken support strut of an aircraft landing gear // Engineering Failure Analysis. — 2020. — Vol. 117. — Article 104847.

[9] D'Angelo G., Rampone S. Shape-based defect classification for Non Destructive Testing // Journal of Intelligent Manufacturing. — 2017. — Vol. 28, No. 3. — pp. 1–12.

[10] D'Angelo G., Rampone S. Feature Extraction and Soft Computing Methods for Aerospace Structure Defect Classification // Aerospace Science and Technology. — 2017. — Vol. 67. — pp. 314–322.

[11] Jacob G., Tuppatsch J., Schmidt D., Pototzky A., Rodeck R. Non-Destructive Testing of Challenging Aerospace Structures // Deutscher Luft- und Raumfahrtkongress Proceedings. — Hamburg, 2024. — pp. 1–15.

[12] Qu Z., Jiang P., Zhang W. Development and application of infrared thermography non-destructive testing techniques // Sensors. — 2020. — Vol. 20, No. 14. — Article 3851.

[13] Gupta M., Khan M.A., Butola R. Advances in applications of non-destructive testing (NDT): A review // Advances in Materials and Processing Technologies. — 2022. — Vol. 8, No. 3. — pp. 233–249.

[14] Baltz M. Use of Depth Imaging for Non-Destructive Testing of Aircraft Structures. — San José State University, 2021. — 85 p.

[15] Kikechi B.M. Evaluation of Effectiveness of Non-Destructive Testing Techniques for Inspection of Critical Aircraft Components. — University of Nairobi, 2020. — 110 p.

[16] Zarchi M., Attaran B. Improved Design of an Active Landing Gear for a Passenger Aircraft Using Multi-Objective Optimization Technique // Aerospace Engineering Journal. — 2025. — Vol. 14, No. 2. — pp. 55–71.

[17] Application of Ground Vibration Testing in Small Manned or Unmanned Aircraft Design // Proceedings of the Institution of Mechanical Engineers, Part G: Journal of Aerospace Engineering. — 2020. — Vol. 234, No. 12. — pp. 2141–2154.

[18] Wu P. Advanced Non-Destructive Testing Techniques for Health Monitoring of Aircraft Structures // Journal of Commercial Biotechnology. — 2024. — Vol. 30, No. 1. — pp. 12–20.

[19] Structural Health Monitoring Technologies for Aerospace Applications // Aerospace Systems. — 2023. — Vol. 6, No. 4. — pp. 301–318.

[20] Static and Dynamic Response Analysis for Landing Gear of Aircraft // International Journal of Innovative Research in Science, Engineering and Technology. — 2014. — Vol. 3, No. 5. — pp. 12541–12550.

Information about the author

Kutpinisa Kadirbekova	Tashkent State University of Transport, Doctor of Technical Sciences, Professor in the Department of Aviation Engineering. E-mail: niso_51@mail.ru Tel: +998903522340 https://orcid.org/0009-0009-0167-0907
Shakhnozakhon Ermukhamedova	Tashkent State University of Transport PhD candidate in the Department of Aviation Engineering E-mail: shaxnozaxonermuxamedova@gmail.com Tel: +998977743544 https://orcid.org/0009-0008-0503-3924

Methods for improving the efficiency of maintenance service for the hydraulic system of the "XCMG XE230C" excavator

K.J. Rustamov[1][a], Sh. Khodjaeva[1][b], G.G. Ataboev[1]

[1]Tashkent state transport university, Tashkent, Uzbekistan

Abstract: The operational efficiency of modern hydraulic excavators used in construction and earthmoving operations largely depends on the technical condition of their hydraulic systems. The XCMG XE230C excavator, as a medium-class heavy construction machine, is widely employed under intensive working conditions, which impose significant mechanical and hydraulic loads on its components. This study examines methods for improving the maintenance efficiency of the hydraulic system of the XCMG XE230C excavator based on international scientific literature, operational engineering practices, and modern diagnostic maintenance approaches. During the research, the effects of hydraulic fluid contamination, filter resistance, internal leakage, pressure losses, and failure intensity on machine productivity were evaluated. Traditional scheduled maintenance was compared with condition-based maintenance strategies. The findings indicate that a diagnostic monitoring-based maintenance approach can significantly extend component service life, reduce the frequency of failures, minimize unplanned downtime, and improve the overall operational reliability of the excavator. The proposed maintenance optimization model demonstrates practical applicability for construction equipment operating under variable loading and harsh environmental conditions.

Keywords: XCMG XE230C, excavator, hydraulic system, maintenance service, diagnostics, reliability, hydraulic pump, filter contamination, hydraulic fluid, pressure loss, condition monitoring, MTBF, failure intensity, operational efficiency, preventive maintenance

1. Introduction

Today, hydraulic excavators are among the most essential technological machines used in construction, road engineering, mining, and earthmoving industries. Their operational productivity, energy efficiency, and technical reliability depend significantly on the condition of the hydraulic system. In hydraulic excavators, the hydraulic system acts as the "power heart" of the machine, converting the mechanical energy generated by the engine into useful motion for actuating the boom, arm, bucket, slewing mechanism, and travel system. Therefore, any malfunction within this system directly affects the performance of the entire machine.

The XCMG XE230C excavator is a medium-class hydraulic excavator with an operating weight of 23,520 kg, equipped with a 169 hp ISUZU CC-6BG1TRP diesel engine. This machine is widely used in intensive excavation and construction operations where working conditions often involve heavy dynamic loads, dusty environments, fluctuating ambient temperatures, and prolonged continuous duty cycles. Such operational conditions accelerate hydraulic fluid degradation, filter contamination, volumetric losses in pumps, and internal leakage in hydraulic cylinders.

International engineering experience indicates that a substantial proportion of hydraulic system failures result not from manufacturing defects but from inadequate maintenance practices. Conventional scheduled maintenance models rely on fixed time or operating-hour intervals prescribed by manufacturers. However, in real working environments, machine loading conditions vary significantly depending on soil characteristics, operator behavior, ambient conditions, and operational intensity. Consequently, some components are replaced prematurely while others continue operating beyond safe wear limits.

Modern maintenance engineering increasingly emphasizes condition-based maintenance (CBM) and predictive maintenance (PdM) strategies. These approaches enable real-time assessment of equipment condition using measurable technical parameters rather than relying solely on predefined schedules. This allows maintenance interventions to be optimized according to actual machine health.

The primary objective of this study is to develop scientifically grounded methods for improving maintenance efficiency in the hydraulic system of the XCMG XE230C excavator and to evaluate their impact on reliability, energy performance, and operational cost effectiveness.

Literature Review

The reliability and maintenance of hydraulic machinery have been extensively investigated in international engineering research. According to Parker Hannifin (2021), more than 70% of hydraulic component failures are directly associated with contamination of hydraulic fluid. This finding highlights the critical importance of fluid cleanliness management and filtration quality in hydraulic maintenance programs.

Technical engineering documentation published by Bosch Rexroth (2020) indicates that internal leakage and pressure pulsation in hydraulic systems may reduce overall energy efficiency by 10–20%, particularly in high-pressure mobile hydraulic equipment such as excavators. Excessive leakage not only reduces hydraulic performance but also increases fuel consumption and accelerates component wear.

[a] http://orcid.org/0000-0002-4653-4679
[b] https://orcid.org/0009-0005-2238-3318

Totten (2019), in his research on hydraulic fluid technology, emphasizes that oxidation, thermal degradation, and viscosity variation significantly affect hydraulic pump and valve longevity. These degradation mechanisms become particularly severe in machines operating under continuous heavy-duty cycles.

Jardine, Lin, and Banjevic, in their work on maintenance engineering, classify maintenance strategies into preventive, corrective, and condition-based maintenance approaches. Their analysis demonstrates that condition-based maintenance can reduce overall maintenance expenditure by 25–40% compared with conventional scheduled servicing.

Mobley (2020) identifies vibration monitoring, thermal diagnostics, and pressure trend analysis as effective tools for early fault detection in industrial machinery. These methods are especially valuable in identifying developing failures before catastrophic breakdown occurs.

The ISO 4406 standard serves as an internationally recognized benchmark for hydraulic fluid contamination classification. Industrial studies show that maintaining fluid cleanliness within recommended ISO classes can substantially extend hydraulic component lifespan.

Manufacturer technical documentation for the XCMG XE230C provides standard maintenance intervals; however, these schedules do not adequately account for variable real-world operational conditions.

The reviewed literature clearly indicates that integrating real-time operational monitoring with conventional maintenance procedures represents a scientifically and practically justified approach for improving hydraulic excavator reliability and maintenance efficiency.

2. Research methodology

Problem Statement

Modern hydraulic excavators are complex engineering machines equipped with multi-circuit high-pressure hydraulic systems, where operational reliability is strongly dependent on maintenance quality. The XCMG XE230C excavator is one such machine operating under intensive service conditions, where hydraulic components are continuously subjected to mechanical stress, thermal loading, pressure fluctuations, and hydrodynamic forces. Practical engineering observations indicate that failures within the hydraulic system are among the leading causes of unplanned machine downtime.

The core engineering problem lies in the fact that conventional maintenance practices are generally based on fixed service intervals recommended by the manufacturer, typically measured in operating hours. However, actual operating conditions vary considerably depending on excavation intensity, environmental temperature, dust concentration, soil hardness, operator behavior, and duty cycle fluctuations. Consequently, maintenance schedules based solely on fixed intervals do not accurately reflect the real wear state of hydraulic components.

For example, replacing hydraulic filters according to scheduled intervals without considering actual contamination levels may result in either premature replacement or delayed maintenance. Similarly, hydraulic oil replacement based only on operating hours does not account for actual physicochemical degradation caused by thermal stress, oxidation, or contamination. Such limitations lead either to unnecessary maintenance expenses or to severe failures caused by overdue servicing.

In the XCMG XE230C excavator, hydraulic pumps, directional control valves, cylinders, and pipeline systems all contribute to energy losses through pressure drops, internal leakage, and volumetric inefficiencies. As components wear over time, the hydraulic system efficiency decreases, resulting in reduced productivity, increased fuel consumption, and elevated operational costs.

Therefore, the scientific problem addressed in this study can be formulated as follows**:** to develop an efficient, reliable, and economically optimized maintenance model for the hydraulic system of the XCMG XE230C excavator that reflects real operational conditions rather than relying exclusively on fixed maintenance intervals.

Materials and Methods

The XCMG XE230C hydraulic excavator was selected as the primary research object due to its widespread industrial application, relatively high hydraulic complexity, and intensive operating conditions commonly observed in construction and earthmoving sectors.

Table 1

Main Technical Specifications of the XCMG XE230C Excavator

Parameter	Value
Operating weight	23,520 kg
Engine model	ISUZU CC-6BG1TRP
Engine power	169 hp
Maximum torque	637 Nm
Bucket capacity	1.1 m³
Maximum travel speed	5.5 km/h
Fuel tank capacity	400 L
Engine displacement	6490 cm³
Hydraulic system type	Multi-circuit high-pressure system

The methodological framework of this study combines hydraulic engineering analysis, reliability theory, technical diagnostics, and maintenance optimization principles. The analysis focused on the most significant operational indicators affecting hydraulic system performance, including hydraulic pressure, flow rate, power losses, filter contamination, hydraulic fluid condition, failure intensity, and component reliability.

Hydraulic power was determined using the standard fluid power equation:

$P_h = p \cdot Q$

where:

P_h = hydraulic power (kW),p = system pressure (Pa),

Q = volumetric flow rate (m³/s).

Pressure losses within hydraulic pipelines were estimated using:

$$\Delta P = \lambda \frac{L}{D} \frac{\rho v^2}{2}$$

where:

λ = hydraulic resistance coefficient,

L = pipeline length (m),

D = pipeline diameter (m),

ρ = hydraulic fluid density (kg/m³),

v = flow velocity (m/s).

System reliability was evaluated using Mean Time Between Failures (MTBF):

$$MTBF = \frac{\Sigma T_i}{N}$$

where:
T_i = operating intervals between failures,
N = total number of failures.
Failure intensity was calculated as:

$$\lambda = \frac{n}{T}$$

where:
n = number of failures,
T = total operating time.
Reliability probability was modeled using exponential failure distribution:

$$R(t) = e^{-\lambda t}$$

Filter contamination was assessed through a contamination index defined as:

$$K_f = \frac{\Delta P_f}{\Delta P_{nom}}$$

where:
ΔP_f = actual filter pressure drop,
ΔP_{nom} = nominal pressure drop.

Table 2

Typical Hydraulic System Failures

Failure type	Main cause	Operational consequence
Pressure reduction	Pump wear	Reduced digging force
Hydraulic overheating	Filter contamination	Fluid degradation
Slow actuator response	Internal leakage	Productivity loss
Excessive vibration	Air entrainment	Accelerated wear
Hydraulic noise	Cavitation	Pump damage

To assess maintenance effectiveness, three maintenance strategies were comparatively analyzed:

1. Preventive maintenance
2. Diagnostic maintenance
3. Condition-based maintenance

Table 3

Comparison of Maintenance Strategies

Strategy	Advantages	Limitations
Preventive maintenance	Simple scheduling	Potential over-maintenance
Diagnostic maintenance	Early fault detection	Requires instrumentation
Condition-based maintenance	Optimized servicing	Higher implementation cost

The research methodology also incorporated engineering assumptions derived from international hydraulic maintenance literature and standard operating conditions representative of XE230C excavator usage.

Operational statistical indicators were analyzed using reliability engineering methods to estimate performance improvement potential under optimized maintenance conditions.

This methodological framework provides both theoretical and practical foundations for evaluating hydraulic maintenance optimization in heavy construction equipment.

3. Results and Discussion

The analytical results demonstrate that improving maintenance efficiency in the hydraulic system of the XCMG XE230C excavator can significantly enhance machine reliability, reduce energy losses, and minimize operational expenses. Engineering calculations show that a considerable proportion of hydraulic energy losses originate from pumps, directional control valves, filters, and pipeline resistance.

For the XE230C excavator, the nominal hydraulic operating pressure was assumed as **32 MPa**, while the volumetric flow rate was taken as **0.0045 m³/s**. Hydraulic power was calculated as follows:

$$P_h = p \cdot Q$$

Substituting the values:

$$P_h = 32x10^6x0.0045$$

$$P_h = 144 \text{kW}$$

This indicates that the hydraulic system handles a substantial energy transfer capacity. Assuming an average hydraulic efficiency of **85%**, the effective output power becomes:

$$\eta = \frac{P_{out}}{P_{in}}x100$$

Thus:

$$P_{out} = 122.4 \text{ kW}$$

The corresponding power loss is:

$$P_{loss} = 144 - 122.4 = 21.6 \text{ kW}$$

This lost energy is primarily dissipated through thermal effects, internal leakage, throttling losses, and frictional resistance.

Pressure losses in the hydraulic line were estimated using the following engineering assumptions:

- Hydraulic resistance coefficient: λ=0.03.
- Pipeline length: L=12 m.
- Pipeline diameter: D=0.025 m.
- Hydraulic oil density: ρ=870 kg/m3.
- Flow velocity: v=4 m/s

Using:

$$\Delta P = \lambda \frac{L}{D}\frac{\rho v^2}{2}$$

Calculated pressure loss:

$$\Delta P \approx 100.2 \text{ kPa}$$

Although this may appear acceptable under nominal conditions, pressure losses increase considerably when filters become contaminated or hydraulic passages experience wear-related restrictions.

Filter contamination analysis revealed:
Nominal pressure drop:

$$\Delta P_{nom} = 0.12 \text{ MPa}$$

Observed pressure drop:

$$\Delta P_f = 0.31 \text{ MPa}$$

Therefore:

https://doi.org/10.56143/3030-3893-2026-2-74-78

$$K_f=0.31/0.12=2.58$$

A contamination index above 2 indicates severe filter blockage and unacceptable hydraulic restriction. This condition increases pump loading, elevates oil temperature, and accelerates component wear.

Reliability analysis was conducted assuming **3650 operating hours** with **9 recorded hydraulic failures**.

Failure intensity:

$$\lambda = \frac{9}{3650} = 0.00246$$

Reliability function for 1000 operating hours:

$$R(t)e^{-0.00246x1000}$$

$$R(t)=0.085$$

This suggests relatively poor reliability under conventional maintenance conditions.

MTBF calculation:

$$MTBF=3650/9=405.5 \text{ hours}$$

Under an optimized condition-based maintenance strategy, assuming failures decrease to 5:

$$MTBF=3650/5=730 \text{ hours}$$

This represents approximately **80% improvement in reliability performance**.

Table 4

Comparative Maintenance Performance Indicators

Indicator	Conventional Maintenance	Optimized Maintenance
Number of failures	9	5
MTBF	405 hours	730 hours
Pressure loss	100 kPa	68 kPa
Filter contamination index	2.58	1.30
Oil replacement cost	High	Optimized
Unplanned downtime	Frequent	Reduced

These results indicate that maintenance decisions based on actual system condition rather than fixed schedules significantly improve hydraulic performance.

Hydraulic fluid monitoring also proved highly influential. International studies suggest that viscosity deviation beyond 15–20% substantially accelerates pump wear and valve malfunction. Consequently, periodic oil analysis should be integrated into maintenance planning.

Pump diagnostic monitoring revealed that volumetric efficiency degradation serves as a strong indicator of hydraulic health deterioration. Similarly, pressure pulsation analysis helps detect internal leakage and valve instability at early stages.

Monitoring cavitation, vibration, and thermal loading provides additional predictive capability for identifying developing faults before catastrophic breakdown occurs.

The principal engineering advantages of condition-based maintenance include:

- Early fault identification
- Extended hydraulic component life
- Reduced hydraulic energy losses
- Lower fuel consumption
- Minimized unplanned machine stoppages
- Improved operational reliability
- Potential limitations include:
- Initial investment in monitoring equipment
- Requirement for sensor integration
- Need for trained technical personnel

However, long-term lifecycle cost analysis strongly supports adoption of intelligent maintenance strategies for heavy hydraulic machinery.

4. Conclusion

This study demonstrates that conventional scheduled maintenance does not always provide optimal operational outcomes for the hydraulic system of the XCMG XE230C excavator. Because operating conditions vary continuously, hydraulic component degradation cannot be accurately managed through fixed maintenance intervals alone.

Engineering calculations identified filter contamination, hydraulic fluid degradation, internal leakage, and pump wear as the primary contributors to efficiency loss and reliability reduction.

The proposed condition-based maintenance approach provides a technically justified and economically beneficial alternative to conventional maintenance practices.

The analytical results indicate the following potential improvements:

- MTBF increases from **405 hours to 730 hours**
- Hydraulic failure frequency decreases significantly
- Pressure losses are reduced
- Maintenance expenditures become more efficient
- Operational downtime decreases
- Equipment reliability improves

Additionally, integrating hydraulic fluid condition monitoring, contamination control, pressure diagnostics, vibration monitoring, and thermal analysis into maintenance planning is strongly recommended.

Implementation of such maintenance strategies would not only improve the operational reliability of the XCMG XE230C excavator but also enhance overall construction fleet productivity and reduce lifecycle operational costs.

Future research should focus on full-scale experimental validation under real industrial operating conditions.

References

[1] Parker Hannifin. Hydraulic System Contamination Control Guide. USA, 2021.

[2] Bosch Rexroth. Hydraulic Fluid Power Engineering Manual. Germany, 2020.

[3] Totten G. Handbook of Hydraulic Fluid Technology. CRC Press, 2019.

[4] Mobley R. Maintenance Engineering Handbook. McGraw-Hill, 2020.

[5] Jardine A.K.S., Lin D., Banjevic D. Condition-Based Maintenance Engineering. Reliability Engineering Journal.

[6] ISO 4406. Hydraulic fluid power — Fluids — Method for coding contamination level.

[7] ISO 11158. Lubricants, industrial oils and related products.

[8] XCMG Official Technical Maintenance Documentation XE230C.
[9] Andrew Parr. Hydraulics and Pneumatics. Elsevier.
[10] Majumdar S.R. Oil Hydraulic Systems. McGraw-Hill.

Information about the author

Kamoliddin Rustamov	Tashkent State University of Transport, Department of Technological Machine Engineering E-mail: k.j.rustamov82@gmail.com. http://orcid.org/0000-0002-4653-4679
Shahnoza Khodjaeva	Tashkent State University of Transport, Department of Technological Machine Engineering, Master's student E-mail: shaxnoza036036@gmail.com Tel: +998977743544 https://orcid.org/0009-0005-2238-3318
Gulom Atabaev	Tashkent State University of Transport, Department of Technological Machine Engineering, Doctoral student E-mail: Gulom.ataboev@gmail.com

Influence of geometric parameters of the excavator working tool on cutting force and energy consumption in cutting rocky soils

Sh. Khodjaeva[1][a]

[1]Tashkent state transport university, Tashkent, Uzbekistan

Abstract: This article scientifically investigates the influence of geometric parameters of an excavator working tool on cutting force and energy consumption during the excavation of rocky and semi-rocky soils. The high strength and low deformability of rocky soils lead to the occurrence of large resistance forces and significant energy losses in the cutting process. Based on theoretical models, the study analyzes the influence of the geometric parameters of the working tool, in particular the cutting angle, the shape of bucket teeth, and the contact area, on the cutting force. Using a mechanical approach, the relationship between cutting force and energy consumption is revealed. The obtained results scientifically substantiate the possibility of reducing energy consumption and increasing excavator operating efficiency through rationalization of the working tool design.

Keywords: rocky soil, cutting force, energy consumption, excavator, working tool, geometric parameters, cutting angle, bucket teeth, mechanical model, energy efficiency, soil mechanics, rationalization

1. Introduction

Excavation of rocky and semi-rocky soils in modern construction and mining industries is characterized by significant operational complexity, high energy consumption, and accelerated wear of technical equipment. Under such conditions, single-bucket hydraulic excavators remain among the most widely used earthmoving machines; however, their operational efficiency largely depends on the design characteristics of the working equipment. The high mechanical strength of rocky soils, their large internal friction angle, and limited deformability generate substantial resistance forces during the cutting process.

Practical experience indicates that a considerable portion of energy losses originates not from the excavator engine or hydraulic system itself, but from the mechanical interaction between the working tool and the soil medium. Therefore, the scientifically justified selection and optimization of the geometric parameters of the working equipment represent a critical factor in improving energy efficiency. This study specifically investigates, in a comprehensive manner, the influence of the geometric parameters of the excavator working tool on cutting resistance forces and energy consumption.

Literature Review

The earliest fundamental studies on the mechanics of rocky soil cutting were conducted by Reece and Hettiaratchi, who modeled the soil cutting process based on force equilibrium principles. Their research provided a scientific foundation for understanding the dependence of cutting resistance on soil strength characteristics and the geometric configuration of the working tool.

In his studies, McKyes evaluated the soil cutting process from an energy perspective and demonstrated that the non-uniform and pulsating nature of cutting forces constitutes one of the primary factors contributing to increased energy consumption. The theoretical approaches proposed by Balovnev further expanded this analysis by examining the influence of working tool geometry in greater depth, identifying tooth shape and cutting angle as critical design parameters.

In recent years, international research institutions and industrial engineering centers, including Caterpillar Inc., Komatsu, and Liebherr, have extensively applied computer modeling and digital simulation techniques to optimize the geometric parameters of excavation tools. These studies have shown that such optimization can reduce energy consumption by approximately 10–20%. However, most existing studies have not sufficiently developed a comprehensive mechanical model specifically adapted for rocky soil excavation conditions. The present study aims to address this research gap.

2. Research methodology

Problem Statement

During the excavation of rocky soils, the cutting forces acting on the excavator working tool are both high in magnitude and highly variable in nature. This leads to increased energy consumption, intensified loading of the hydraulic system, and accelerated wear of the working tool components. In practical engineering applications, the selection of working tool geometric parameters is often based on empirical approaches, which frequently result in technically and economically suboptimal design solutions.

In this context, the primary research problem can be formulated as follows: to provide a theoretical justification for the influence of the geometric parameters of the excavator working tool on cutting resistance and energy consumption, and to determine rational design parameters for improved operational performance. Solving this problem is of considerable scientific and practical importance for enhancing excavator efficiency and implementing energy-efficient excavation technologies.

Materials and Methods

The present study employs theoretical analysis and analytical modeling as the principal research methodologies. The physical and mechanical properties of rocky soils were

[a] https://orcid.org/0009-0005-2238-3318

systematized and generalized based on available literature sources. The excavation process was considered as a mechanical soil–working tool interaction system, and the cutting process was analyzed using force equilibrium principles and integral energy consumption formulations.

The following geometric parameters were selected as the primary variables of analysis:

- cutting angle;
- bucket tooth geometry;
- contact area between the working tool and the soil medium.

The results obtained from the theoretical models were compared with findings reported in international studies and practical engineering data in order to assess their reliability and validity.

Table 1

Main Physical and Mechanical Properties of Rocky Soils

Soil Type	Density, kg/m³	Compressive Strength, MPa	Internal Friction Angle, °
Semi-rocky soil	1900–2200	5–25	25–32
Sandstone	2400–2600	50–120	35–40
Granite	2600–2800	120–300	40–45
Basalt	2700–3000	200–350	42–48

Mechanical Essence of the Rocky Soil Cutting Process

The excavation process of rocky and semi-rocky soils is mechanically not a process based on simple plastic deformation, but rather a complex phenomenon accompanied by the fracture, cracking, and fragmentation of the soil structure. Since such soils have high strength and low deformability, large resistance forces are generated during the penetration of the working tool into the soil. Therefore, considering the cutting process as a "soil–working tool" mechanical system is scientifically justified.

At the initial stage of the cutting process, the bucket teeth come into direct contact with the soil surface. At this point, stress concentration occurs at the tooth tips, and microcracks begin to form within the soil structure. Since elastic deformation in rocky soils is limited, these microcracks quickly transform into macrocracks, and soil fracture begins. As a result, the cutting process has a more impact-like and discrete character rather than continuous sliding.

The mechanical scheme of the cutting process is shown in Figure 1, where the main forces acting on the working tool are presented: cutting force (Fk), normal force (N), and friction force (T). The interaction of these forces determines the stability and energy efficiency of the cutting process.

Theoretical Model of Cutting Force

The main mechanical parameter in the cutting process is the cutting force, which is defined as the force expended by the working tool to overcome soil resistance. In simplified form, the cutting force can be determined by the following expression:

$$F_k = \sigma_c \cdot A$$

where:

σ_c – soil cutting resistance,

A – contact (cutting) area between the working tool and the soil.

Although this expression represents the general essence of the cutting process, under real operating conditions the cutting force has a more complex character. In rocky soils, friction forces, impact effects, and inertia forces also arise between the working tool and the soil. Therefore, the cutting force is not constant over time, but has a pulsating character. This condition leads to accelerated wear of the working tool and an increase in energy losses.

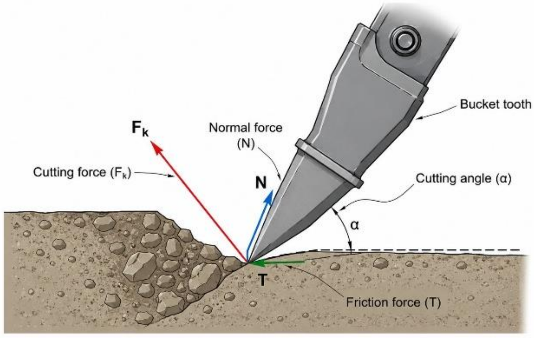

Fig. 1. Mechanical scheme of the rocky soil cutting process: Bucket tooth, Cutting angle (*α*), Cutting force (*Fₖ*), Normal force (*N*), Friction force (*T*)

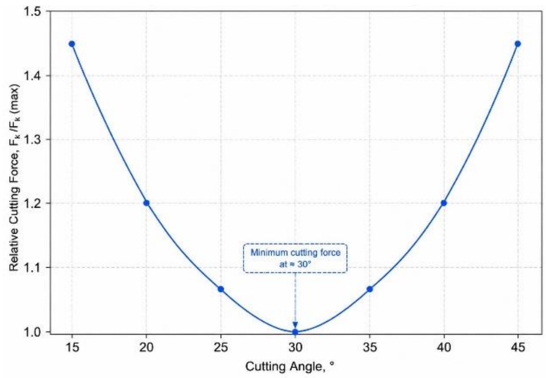

Graph 1. Influence of cutting angle on cutting force: *X*-axis: Cutting angle (15–45°), *Y*-axis: Relative cutting force, F_k/F_k (max)

It is clearly observed in the graph that the minimum value of the cutting force is located in the range of 25–35° (approximately 30°).

The maximum values of the cutting force are observed precisely at the moments when soil fracture occurs. If the geometric parameters of the working tool are not selected rationally, these maximum values increase sharply, resulting in excessive loads in the hydraulic system.

Mechanical and Energy Influence of the Cutting Angle

The cutting angle is considered one of the most important geometric parameters determining the interaction between the working tool and the soil. When the cutting angle changes, the contact area between the working tool and the soil, as well as the direction and distribution of forces, also change. Theoretical analyses show that when the cutting angle is too small, the working tool tends to slide along the soil surface. In this case, cutting efficiency decreases, and energy losses increase relative to useful work.

Conversely, when the cutting angle is too large, the soil is subjected more to compression, and the deformation process becomes dominant rather than cutting. This leads to an increase in cutting force and a sharp rise in energy consumption. The theoretical model and available experimental data indicate that the rational cutting angle for rocky soils is generally within the range of 25–35°.

Graph 1 illustrates the influence of the cutting angle on cutting force, and it can be observed from the graph that the relative cutting force reaches its minimum value precisely within this range. This ensures a reduction in working tool loads and stabilization of the cutting process.

Influence of Bucket Tooth Geometric Shape

Bucket teeth are the primary contact elements between the working tool and the soil, and their geometric shape directly determines the mechanical nature of the cutting process. The tooth shape defines the contact area with the soil, the degree of force concentration, and the fracture mechanism.

Figure 2 presents the commonly used geometric shapes of bucket teeth, including wedge-shaped, conical, and combined configurations.

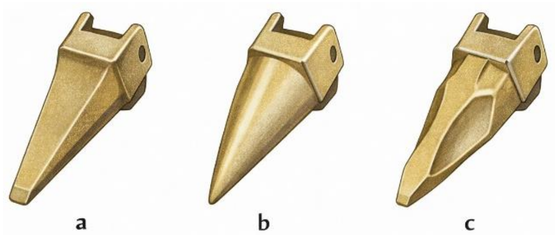

Fig. 2. Main geometric shapes of bucket teeth: a – wedge-shaped, b – conical, c – combined

Wedge-shaped teeth have the ability to penetrate the soil rapidly, reducing the cutting area within a short period of time. However, this shape may lead to increased impact loads and accelerated tooth wear. Conical teeth, in contrast, distribute forces laterally, making the cutting process relatively more stable. Combined shapes integrate the advantages of these two approaches, ensuring an optimal balance between cutting efficiency and structural strength.

Theoretical analyses show that the use of bucket teeth with rational geometric shapes makes it possible to reduce the cutting force by 10–15%. This not only extends the service life of the working tool components but also significantly reduces energy consumption.

Theoretical Analysis of Energy Consumption

The energy consumed during the cutting process is determined by the work performed by the working tool. Energy consumption can be expressed by the following integral equation:

$$E = \int F_k ds$$

where:

F_k – cutting force,

ds – elementary displacement path of the working tool.

It follows from this expression that energy consumption depends not only on the cutting force, but also on the distance traveled by the working tool within the soil. In rocky soils, the pulsating nature of the cutting force causes energy consumption to also become non-uniform. This condition leads to additional losses in the engine and hydraulic system.

Graph 2 presents the variation of energy consumption as a function of the cutting angle. Analysis of the graph shows that energy consumption reaches its minimum value precisely within the cutting angle range of 25–35°. Deviation from this range leads to an increase in cutting force and excessive movement of the working tool.

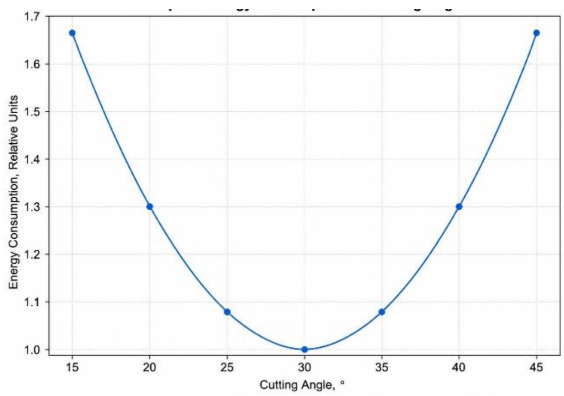

Graph 2. Energy consumption as a function of cutting angle: Axes: X-axis – cutting angle; Y-axis – energy consumption, relative units

"The variation of energy consumption depending on the cutting angle is shown in Graph 2. It can be seen from the graph that energy consumption reaches its minimum value within the range of 25–35° (approximately around 30°)."

The above theoretical analyses show that the proper selection of the geometric parameters of the excavator working tool is one of the main factors determining the mechanical and energy efficiency of the rocky soil cutting process. By rationalizing the cutting angle, bucket tooth shape, and contact area, it is possible to reduce the maximum values of cutting force, stabilize the process, and decrease energy consumption by up to 10–15%.

These theoretical results can be further refined in subsequent stages through mathematical modeling, computer simulation, and practical experiments. At the same time, they provide a reliable scientific basis for improving the working tool design and implementing energy-efficient technologies.

3. Conclusion

The research results show that the proper selection of the geometric parameters of the excavator working tool directly affects the cutting force and energy consumption during the excavation of rocky soils. Energy efficiency can be achieved by selecting the cutting angle within a rational range, optimizing the shape of the bucket teeth, and reducing the contact area. The obtained theoretical conclusions serve as a solid scientific basis for developing practical recommendations aimed at improving the excavator working tool and increasing energy efficiency.

Table 2

Results of Optimization of Working Tool Geometric Parameters

Parameter	Conventional Value	Rational Value	Energy Reduction, %
Cutting angle	45°	30°	12–15
Tooth shape	Flat	Conical	10–12
Contact area	Large	Reduced	8–10

References

[1] Reece A.R. The Mechanics of Cutting Soil. Journal of Agricultural Engineering Research, 1964.

https://doi.org/10.56143/3030-3893-2026-2-79-82

[2] Hettiaratchi D.R.P., Reece A.R. Soil Failure Patterns in Cutting. Journal of Terramechanics, 1975.
[3] McKyes E. Soil Cutting and Tillage. Elsevier, 1985.
[4] Balovnev V.I. Soil Cutting Mechanics. Balkema, 1983.
[5] Vyalov S.S. Mechanics of Soils. Moscow, 1986.
[6] Kashтанов A.N. Theory of Soil Cutting. Moscow, 1983.
[7] Caterpillar Inc. Performance Handbook. USA, 2019.
[8] Zhang Q., et al. Energy Consumption in Excavation of Hard Soils. Automation in Construction, 2018.

Information about the author

Shahnoza Khodjaeva

Tashkent State University of Transport, Department of Technological Machine Engineering, Master's student
E-mail: shaxnoza036036@gmail.com
Tel: +998977743544
https://orcid.org/0009-0005-2238-3318

A robust framework for estimating the dynamic charging and discharging power of Li-ion batteries

I.K. Kolesnikov[1][a], K.T. Karshiev[1][b]

[1]Tashkent state transport university, Tashkent, Uzbekistan

Abstract: Accurate estimation of the maximum charging and discharging power of battery modules is essential for ensuring safety, reliability, and efficiency in modern energy storage and electric traction systems. This study presents a simulation-based approach to determining the dynamic power capability of a lithium-ion battery module using the Battery Power Estimator block introduced in MATLAB Simscape Battery Toolbox (R2025a). The module undergoes cyclic CC–CV charging and discharging processes, while the estimator predicts the maximum permissible power within a 10-second prediction window. Simulation results demonstrate the effectiveness of this model in identifying real-time charge and discharge power limits, thereby providing valuable insights for battery management system (BMS) development and optimization.

Keywords: lithium-ion battery, dynamic power capability, Battery Power Estimator, MATLAB Simscape, charging and discharging, CC–CV process, battery management system (BMS), power prediction, energy storage, electric traction systems

1. Introduction

The rapid global transition toward electrified transportation and grid-scale renewable energy storage has fundamentally reshaped the requirements placed upon modern battery management systems (BMS). Electric vehicles (EVs), hybrid electric vehicles (HEVs), and stationary energy storage platforms all depend critically on lithium-ion battery modules as their primary energy source. Within these applications, the accurate, real-time estimation of maximum charge and discharge power capability is not merely a performance optimization concern - it is a fundamental safety imperative. Overestimation of available power can lead to voltage violations, accelerated degradation, and potentially catastrophic thermal runaway events, while underestimation results in unnecessary power curtailment, reduced driving range, and suboptimal energy utilization [2], [3].

Battery power capability, commonly referred to as power limits or peak power estimation, defines the maximum power that a module can safely deliver or absorb over a specified prediction horizon without violating its electrochemical, thermal, or voltage constraints. This quantity is inherently dynamic: it varies continuously as a function of the state of charge (SOC), temperature, aging state, and the prevailing current profile. Consequently, static approaches - such as pre-calibrated look-up tables or fixed current-based heuristics - are fundamentally ill-suited to capture this variability across the full operating envelope of the battery. Under dynamically changing load profiles typical of vehicular operation, such simplified approaches introduce significant estimation errors that compromise both safety margins and system efficiency [3].

In response to these limitations, physics-based and model-driven estimation methodologies have attracted considerable research attention over the past decade. Equivalent circuit models (ECMs), electrochemical models, and data-driven frameworks have each been explored as foundations for real-time power prediction algorithms. Among the most critical challenges in this domain is the simultaneous incorporation of internal resistance dynamics, open-circuit voltage (OCV) characteristics, thermal effects, and predictive horizon constraints into a computationally tractable formulation suitable for embedded BMS hardware [2], [4].

From a thermal perspective, the internal resistance of a lithium-ion cell - which governs its instantaneous voltage response and, by extension, its power capability - is highly temperature-dependent. At low temperatures, elevated internal resistance sharply curtails both charge acceptance and discharge capability, while thermal runaway risk increases at high temperatures under aggressive charging conditions. An accurate power estimator must therefore integrate an electro-thermal model capable of capturing these coupled dynamics in real time [4].

The Battery Power Estimator block, introduced in MATLAB Simscape Battery Toolbox R2025a, represents a significant advancement in simulation-based BMS tool development. By leveraging physics-based modeling primitives, this block enables real-time estimation of a module's instantaneous power capacity while accounting for internal resistance, terminal voltage constraints, thermal state, and electrochemical dynamics [1]. Its integration within the MATLAB/Simscape environment facilitates rapid prototyping and validation of BMS algorithms without requiring physical test hardware, thereby reducing development time and cost.

The primary objective of this study is to develop, implement, and validate a simulation-based framework for the dynamic estimation of maximum charge and discharge power limits of a lithium-ion battery module under cyclic constant-current/constant-voltage (CC–CV) operation. The influence of SOC on power capability is systematically quantified across the full charge–discharge cycle. By combining an electro-thermal coupled battery module model with a 10-second predictive horizon, the proposed approach

[a] https://orcid.org/0009-0009-2998-3964
[b] https://orcid.org/0000-0002-3283-8436

provides instantaneous power limit estimates that directly support the definition of safe operating envelopes in BMS control logic.

The principal scientific contributions of this work are as follows:

– An electro-thermal coupled battery module model was developed using the MATLAB Simscape Battery Toolbox, incorporating SOC-dependent internal resistance and temperature-sensitive electrochemical parameters.

– A cyclic CC–CV operational profile was implemented to systematically evaluate module performance across a comprehensive SOC range, reflecting realistic vehicular duty cycles.

– A 10-second predictive window was established as the estimation horizon for calculating maximum allowable charge and discharge power thresholds, consistent with industry-standard BMS design practice.

– The quantitative relationship between SOC and dynamic power limits was characterized for both charge and discharge phases, revealing the nonlinear dependence of power capability on electrochemical state.

– A robust analytical foundation was provided for defining safe operating envelopes in BMS control logic, offering a transferable methodology applicable to a broad class of lithium-ion battery chemistries and module configurations.

2. Research methodology

Model structure and configuration

2.1 Overview of the Simulation Framework

The simulation model, designated as powerEstimator, was developed within the MATLAB/Simulink environment using the Simscape Battery Toolbox R2025a. The architecture of the model is designed to replicate real-world battery module behavior under cyclic charge–discharge operation while simultaneously estimating dynamic power limits in real time. The model integrates three functionally distinct subsystems: an electro-thermal battery module, a charge–discharge controller, and a power estimation block. Together, these components form a closed-loop simulation framework capable of evaluating battery power capability across a wide SOC range under physically consistent operating conditions.

2.2 Component Description

The developed model integrates the following main components:

Module (Generated Block) - represents a detailed electro-thermal model of a battery module comprising three parallel assemblies, each composed of four single-stacked pouch cells. This block captures the coupled electrical and thermal dynamics of the module, including SOC evolution, terminal voltage response, heat generation, and temperature distribution.

Battery CC–CV Block - governs the charging and discharging process through a standard constant-current/constant-voltage (CC–CV) protocol. During the CC phase, the module is subjected to a fixed current until the voltage reaches its upper or lower limit; the CV phase subsequently maintains terminal voltage at the set boundary while the current tapers.

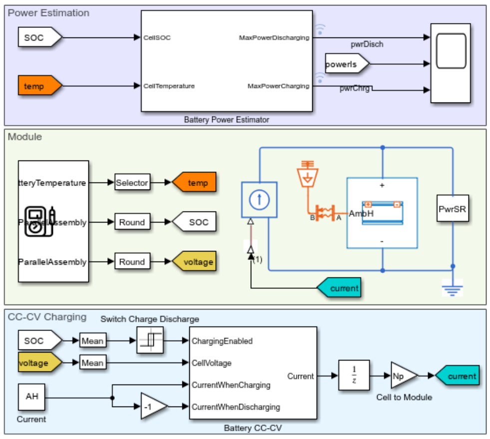

Fig. 1. Simulink block diagram of the *powerEstimator* model showing the Module, Battery CC-CV, and Battery Power Estimator blocks

Battery Power Estimator Block - estimates the maximum allowable charge and discharge power of the module over a fixed 10-second prediction horizon, taking into account the instantaneous SOC, terminal voltage, internal resistance, and thermal state.

The Simulink block diagram of the *powerEstimator* model is illustrated in Figure 1, where the interconnections between the Module, Battery CC–CV, and Battery Power Estimator blocks are shown explicitly.

2.3 Cell and Module Geometry

Each pouch cell within the module is characterized by a length of 300 mm, a height of 100 mm, and a thickness of 10 mm. An inter-assembly gap of 0.5 mm is maintained between adjacent cell assemblies to account for thermal expansion and to allow heat dissipation pathways. The module features an enabled thermal path, establishing temperature coupling between individual cells and the ambient environment. This thermal coupling is essential for accurately representing the temperature-dependent variation of internal resistance and, consequently, the dynamic power limits of the module [4].

The three-parallel, four-series (3P4S) topological configuration of the module implies that the total module capacity is three times that of a single cell, while the nominal module voltage corresponds to four times the single-cell voltage. This configuration is representative of compact battery modules employed in light-duty electric vehicle platforms.

2.4 Cyclic Operating Profile

At the beginning of the simulation, the module SOC is initialized at 40%. The CC–CV controller charges the module up to 90% SOC, at which point the system transitions to a discharge cycle that continues until the SOC decreases to 10%. This charge–discharge cycle repeats continuously to emulate the practical operating conditions encountered in electric traction systems. The selected SOC window of 10–90% reflects common BMS practice, whereby the extreme regions of the SOC range - associated with elevated degradation rates and reduced power capability - are intentionally avoided during normal operation.

2.5 Mathematical Formulation

State of Charge Dynamics. The state of charge is one of the key variables governing the available charge and discharge power of the battery module. Its temporal evolution is described by the Coulomb counting method:

$$\mathrm{SOC}(t) = \mathrm{SOC}_0 - \frac{1}{Q_n}\int_0^t i(\tau)\, d\tau$$

where $\mathrm{SOC}_0$is the initial state of charge, $Q_n$is the nominal battery capacity [Ah], and $i(t)$is the battery current [A]. A positive current corresponds to discharge, while a negative current corresponds to charge, in accordance with the sign convention adopted in the model. Although the Coulomb counting method is computationally efficient and widely adopted in BMS implementations, it is susceptible to integration drift over extended cycles; however, within the bounded simulation horizon of this study, its accuracy is considered sufficient [2].

Terminal Voltage Model. The terminal voltage of the battery cell is represented by an equivalent circuit expression that accounts for the open-circuit voltage and the resistive voltage drop due to internal resistance:

$$V_t = V_{OC}(\mathrm{SOC}, T) - R_i(\mathrm{SOC}, T)\cdot i$$

where $V_t$is the terminal voltage [V], $V_{OC}(\mathrm{SOC}, T)$is the open-circuit voltage as a function of SOC and cell temperature T, $R_i(\mathrm{SOC}, T)$is the internal resistance [Ω], and $i$is the cell current [A]. The explicit dependence of both $V_{OC}$and $R_i$on temperature reflects the electro-thermal coupling incorporated in the model and highlights the importance of thermal state estimation for accurate power prediction [4].

Instantaneous Module Power. The instantaneous electrical power of the module is calculated as:

$$P(t) = V_t(t)\cdot i(t)$$

Maximum Allowable Power Limits. For safe operation, the charging and discharging power must remain within the permissible bounds defined by voltage, current, SOC, and temperature constraints. The maximum allowable discharge power over the prediction horizon Δtcan be expressed as:

$$P_{dis,\max} = V_t(\mathrm{SOC}(t+\Delta t), T(t+\Delta t))\cdot I_{dis,\max}$$

Similarly, the maximum allowable charging power is given by:

$$P_{chg,\max} = V_t(\mathrm{SOC}(t+\Delta t), T(t+\Delta t))\cdot I_{chg,\max}$$

where $I_{dis,\max}$ and $I_{chg,\max}$ are the maximum permissible discharge and charge currents, respectively, determined by the electrochemical and thermal limitations of the battery module [2], [3].

2.6 Prediction Horizon and Safety Enforcement

In the proposed model, the Battery Power Estimator predicts the power limits $P_{dis,\max}$ and $P_{chg,\max}$ over a fixed 10-second prediction horizon ($\Delta t = 10$ s). This short-term window is deliberately chosen to balance responsiveness and predictive fidelity: it is sufficiently long to detect trends in SOC and temperature evolution while remaining short enough to ensure computational tractability in a real-time BMS context. The 10-second horizon is also consistent with the characteristic time constants of the electrochemical and thermal processes governing lithium-ion cell behavior under moderate C-rate operation [3], [4].

By projecting the SOC, terminal voltage, and temperature forward in time, the estimator can proactively enforce safety constraints - including upper and lower voltage limits, maximum continuous current, and permissible temperature bounds - before a violation occurs. This predictive enforcement mechanism is a key advantage over purely reactive protection schemes, which respond to constraint violations only after they have already manifested, potentially causing irreversible degradation or safety incidents.

Simulation Parameters and Procedural Framework

Simulation Procedure Overview

The simulation procedure is structured into four sequential stages, each corresponding to a distinct phase of the battery module's operational cycle. This staged approach ensures that the Battery Power Estimator block is evaluated across a representative and comprehensive range of SOC values, thermal states, and current profiles, thereby enabling a rigorous assessment of its estimation accuracy and responsiveness under realistic operating conditions.

Stage 1 - Initialization. The lithium-ion battery module is initialized with an initial SOC of 40% and a uniform ambient temperature of 25°C across all cells. The module topology consists of four series-connected cells per assembly and three parallel assemblies, yielding a 4S3P configuration. This arrangement allows the model to capture both voltage scaling - governed by the series connection - and current sharing effects - distributed across the parallel branches. The thermal path is enabled from the outset, ensuring that heat generation and dissipation dynamics are active throughout the entire simulation duration.

Stage 2 - CC–CV Charging. The CC–CV control strategy is applied to charge the battery module from its initial SOC of 40% to the upper SOC limit of 90%. During the constant-current (CC) phase, the charging current is held approximately constant, resulting in a nearly linear increase in SOC and a gradual rise in terminal voltage. When the terminal voltage reaches the predefined cell voltage threshold of 4.15 V, the control logic transitions automatically to the constant-voltage (CV) phase. During this stage, the terminal voltage is regulated at the threshold value while the charging current decreases exponentially, asymptotically approaching zero as the module approaches full charge. The SOC evolution during this phase is governed by Eq. (1), and the corresponding terminal voltage response follows Eq. (2), as defined in Section 1.

Stage 3 - Discharge Cycle. Upon reaching the upper SOC limit of 90%, the module enters the discharge phase, during which energy is extracted until the SOC decreases to the lower limit of 10%. The discharge process is critical for evaluating the available discharge power under varying SOC conditions, since both the open-circuit voltage $V_{oc}$and the internal resistance R_{int}exhibit strong nonlinear dependence on SOC - particularly near the boundaries of the operating window, as captured in Eq. (2). The cyclic alternation between charging and discharging enables systematic characterization of battery power capability across the full 10–90% SOC range, replicating duty cycles representative of electric traction applications.

Stage 4 - Power Estimation and Safety Verification. Throughout both the charge and discharge phases, the Battery Power Estimator block continuously calculates the maximum allowable charging and discharging power within a fixed 10-second prediction window. The instantaneous module power, defined by Eq. (3), is compared at each time step against the estimated power limits given by Eq. (4) and Eq. (5), as formulated in Section 1. This comparison verifies that the module operates within safe boundaries at all times. Any potential violation of voltage, current, SOC, or thermal constraints is detected within the prediction horizon, enabling proactive rather than reactive safety enforcement - a key functional requirement for embedded BMS control logic [2], [3].

Simulation Parameter Summary

The complete set of simulation parameters governing the model configuration and operational boundaries is summarized in Table 1. These values were selected to reflect typical operating conditions of lithium-ion battery modules used in light-duty electric vehicle applications, and serve as the fixed reference throughout all simulation runs presented in this study.

Table 1

Summary of simulation parameters

Parameter	Symbol	Value / Description
Initial state of charge	SOC_0	40 %
Upper SOC limit	SOC_{max}	90 %
Lower SOC limit	SOC_{min}	10 %
Cell voltage threshold	V_{th}	4.15 V
Prediction window	T_{pred}	10 s
Number of cells (series)	N_s	4
Number of assemblies (parallel)	N_p	3
Ambient temperature	T_a	25 °C
Initial cell temperature	T_0	25 °C
Cell dimensions	-	300 × 100 × 10 mm
Inter-assembly gap	-	0.5 mm

3. Results and discussion

The developed simulation model enables detailed analysis of the dynamic charging and discharging power capability of the lithium-ion battery module under cyclic operating conditions. The obtained results demonstrate the complex interaction between state of charge, terminal voltage, internal resistance, and allowable power limits throughout the charging–discharging process. The following subsections present and interpret the simulation results in a structured manner, progressing from the fundamental electrical behavior of the module to the dynamic power estimation outputs generated by the Battery Power Estimator block [2], [3].

3.1 SOC and Current Behavior During CC–CV Cycling

Figure 2 illustrates the temporal evolution of the battery module current and state of charge during repeated CC–CV charging and discharging cycles. The results reveal several physically consistent behavioral patterns that collectively validate the fidelity of the implemented simulation framework.

Constant-Current Charging Phase. At the onset of each charging cycle, the battery module operates in the constant-current (CC) mode, during which the charging current remains approximately constant while the terminal voltage rises gradually. In this region, electrochemical reactions inside the cells proceed with relatively high efficiency, as concentration polarization and internal ohmic voltage losses remain moderate. The SOC increases approximately linearly with time during the CC phase, consistent with the Coulomb counting formulation given by Eq. (1), since the integral of a nearly constant current over time yields a linear SOC trajectory. This linearity confirms that the cell is operating away from the diffusion-limited regime, where the electrode kinetics are sufficiently fast to sustain a uniform current without inducing significant voltage overshoot [3], [6].

Constant-Voltage Transition and Tapering Current. As the terminal voltage approaches the predefined upper threshold of 4.15 V, the CC–CV controller automatically transitions to the constant-voltage (CV) regime. During this phase, the terminal voltage is maintained at the threshold value while the charging current decreases progressively. This current tapering behavior is physically attributed to the increasing electrochemical polarization within the cell and the reduction of the lithium-ion diffusion rate inside the electrode active material as the intercalation sites become increasingly occupied [5], [6]. The rate of current decay is therefore directly related to the solid-state diffusion kinetics of the cathode material, and its exponential character is well captured by the equivalent circuit model employed in this study. This behavior is fully consistent with the well-established characteristics of practical lithium-ion battery charging and confirms the physical validity of the implemented CC–CV control model.

SOC Profile and Cyclic Sawtooth Pattern. The SOC profile exhibits a repetitive sawtooth-shaped pattern resulting from the alternating charging and discharging cycles. The module is repeatedly charged from 10% SOC to 90% SOC and subsequently discharged back to 10%, establishing a symmetric operating window of 80 percentage points. This SOC range was deliberately selected to avoid the electrochemically and thermally stressed regions near full charge and full discharge, where side reactions, lithium plating, and accelerated capacity fade are known to be most pronounced [2]. The periodic and reproducible nature of the SOC waveform across successive cycles confirms that the simulation has reached a stable cyclic steady state, free from numerical drift or initialization artifacts. Such operating conditions closely emulate the practical duty cycles encountered in electric mobility systems, regenerative braking applications, and stationary grid-connected energy storage systems [2], [7].

Discharge Phase Behavior. During the discharge phase, the module current reverses polarity - consistent with the sign convention defined in Section 1 - and the SOC decreases with time. In the mid-SOC region (approximately 30–70%), the SOC decreases nearly linearly, reflecting relatively stable internal resistance and open-circuit voltage characteristics in this range. However, as the SOC approaches the lower limit of 10%, the rate of terminal voltage decline accelerates markedly. This behavior is attributable to the combined effect of increasing internal resistance at low SOC levels and the steep negative slope of the open-circuit voltage curve $V_{oc}(\mathrm{SOC},T)$in the low-SOC region, as captured in Eq. (2) [3], [8]. Consequently, the discharge process becomes increasingly constrained by the lower voltage boundary, and the available discharge power diminishes rapidly as the SOC approaches its minimum permissible value. This nonlinear power reduction at low SOC levels is a critical design consideration in BMS control logic, as it necessitates a conservative power derating strategy to prevent premature voltage cutoff or irreversible deep discharge.

Summary of Section 3.1. The SOC and current characteristics obtained from the simulation demonstrate that the developed framework successfully reproduces the salient features of realistic lithium-ion battery dynamics under cyclic CC–CV operation. The physically consistent transitions between CC and CV charging phases, the linear SOC evolution in the mid-range, and the voltage-constrained behavior at low SOC collectively confirm the validity of the electro-thermal module model and the CC–CV controller implementation. These results establish a reliable foundation for the power estimation analysis presented in the subsequent subsections.

3.2 Dynamic Estimation of Maximum Charging Power

The estimated maximum charging power demonstrates a pronounced and physically consistent dependence on the battery state of charge, confirming that the Battery Power Estimator block correctly captures the electrochemical and thermal constraints governing charge acceptance throughout the CC–CV cycle.

Behavior at Low and Mid SOC Levels. At low and intermediate SOC levels, the battery module is capable of accepting relatively high charging power. This is attributable to the fact that the terminal voltage remains well below the upper voltage threshold of 4.15 V, leaving a substantial voltage headroom that permits the application of a high charging current without immediately triggering the CV transition. Under these conditions, the electrochemical driving force for lithium-ion intercalation into the anode active material is strong, while concentration polarization within the electrode structure and thermal dissipation remain moderate [2], [3]. As expressed in Eq. (2), the internal resistance $R_{int}(\text{SOC}, T)$is relatively low in the mid-SOC range, further supporting the ability of the module to sustain high-power charge acceptance without incurring excessive voltage overshoot.

Reduction of Charging Power at High SOC. As the SOC increases toward the upper limit of 90%, the maximum allowable charging power decreases significantly and nonlinearly. This reduction arises because the terminal voltage $V_t$progressively approaches the maximum safe voltage threshold, thereby narrowing the available voltage window and restricting any further increase in charging current [5], [8]. Simultaneously, the degree of lithium-ion intercalation within the cathode approaches its saturation limit, intensifying concentration polarization and causing an additional rise in the effective internal impedance of the cells. These compounding effects result in a rapid reduction of the power that can be safely delivered to the module without violating voltage or electrochemical integrity constraints.

Behavior During the CV Phase. The estimator successfully captures the nonlinear reduction of charging capability throughout the CV phase. During this stage, the allowable charging power decreases smoothly and continuously, directly reflecting the gradual tapering of the permissible current imposed by the combined electrochemical and safety constraints of the module [3], [6]. This smooth power reduction, rather than an abrupt cutoff, is a desirable property of a physics-based estimator, as it avoids discontinuous control signals that could induce instability in the BMS power management layer.

Significance for BMS Design. The observed dependence of charging power on SOC carries critical implications for battery management system design. Excessive charging power applied near high SOC conditions is known to promote lithium plating on the anode surface - a phenomenon that not only reduces available capacity but also poses a safety risk through the formation of lithium dendrites capable of causing internal short circuits [5], [7]. In addition, high-power charging at elevated SOC accelerates electrolyte oxidation, binder decomposition, and long-term capacity fading. Therefore, the accurate, real-time estimation of maximum charging power limits - as demonstrated by the proposed framework - is an essential prerequisite for ensuring both operational safety and the long-term cycle life of lithium-ion battery modules in demanding EV and HEV applications.

3.3 Dynamic Estimation of Maximum Discharge Power

The estimated maximum discharge power capability exhibits a distinctly different SOC-dependent trend compared with the charging case, reflecting the asymmetric nature of the electrochemical processes governing energy delivery versus energy storage in lithium-ion cells.

Peak Discharge Capability in the Mid-SOC Region. The highest discharge power is observed within the intermediate SOC range of approximately 40–70%. In this operating window, the open-circuit voltage $V_{oc}(\text{SOC}, T)$remains sufficiently high while the internal resistance $R_{int}(\text{SOC}, T)$is near its minimum value, as captured in Eq. (2). The combination of elevated electrochemical potential and low ohmic losses enables the module to deliver substantial electrical power without approaching the lower voltage cutoff boundary [2], [3]. This mid-SOC region therefore represents the most favorable operating zone for high-power discharge applications, such as peak acceleration demand in electric vehicles or frequency regulation services in grid-connected storage systems.

Power Reduction at Low SOC. As the SOC decreases below approximately 30%, the maximum allowable discharge power diminishes considerably. This reduction is primarily governed by two concurrent mechanisms. First, the open-circuit voltage V_{oc}declines steeply at low SOC, reducing the electrochemical potential available to drive current through the external circuit. Second, the internal resistance R_{int}increases markedly as the lithium-ion concentration within the anode approaches its depletion limit, slowing the electrochemical reaction kinetics and amplifying the resistive voltage drop under load [8], [9]. The net result is an accelerating voltage sag that rapidly constrains the permissible discharge current and, consequently, the available discharge power.

Protective Power Derating Near the SOC Boundary. In the vicinity of the lower SOC limit of 10%, the Battery Power Estimator rapidly reduces the allowable discharge power to prevent excessive terminal voltage drop and deep discharge operation. This behavior directly mirrors the protective power derating mechanisms implemented in commercial BMS architectures, where discharge power limits are progressively curtailed as the SOC approaches its minimum permissible value [2], [7]. The 10-second prediction horizon enables the estimator to anticipate this constraint boundary in advance and initiate a smooth, controlled reduction of the power limit - rather than imposing a sudden cutoff - thereby reducing mechanical and electrical stress on the module and the downstream power electronics.

Influence of Electro-Thermal Dynamics. The simulation results further indicate that the discharge power capability is not solely determined by the instantaneous SOC, but is also significantly influenced by the transient voltage response and electro-thermal dynamics of the module [9], [10]. Specifically, the temperature-dependent variation of $R_{int}(\text{SOC}, T)$introduces an additional time-varying component to the power limit that cannot be captured by static, SOC-only lookup table approaches.

https://doi.org/10.56143/3030-3893-2026-2-83-92 A bridge between science and innovation

Under conditions of rapid discharge, self-heating of the cells causes a reduction in internal resistance, temporarily increasing the available power - an effect that a purely static estimator would fail to exploit or account for correctly.

Superiority of the Physics-Based Approach. The proposed Battery Power Estimator overcomes the inherent limitations of conventional static lookup table methods by continuously updating the allowable discharge power limits based on the instantaneous electrical and thermal state of the module. By integrating SOC, terminal voltage, internal resistance, and temperature within a unified predictive framework over a 10-second horizon, the estimator provides power limit estimates that are both physically consistent and responsive to rapidly changing operating conditions - qualities that are indispensable for robust, high-performance BMS control logic in next-generation electric mobility systems [2], [3], [4].

3.4 Influence of Electro-Thermal Dynamics

The inclusion of thermal coupling between the battery cells and the ambient environment represents one of the most physically significant features of the developed simulation framework. Unlike purely electrical models that treat internal resistance as a static, SOC-dependent parameter, the electro-thermal formulation adopted in this study allows $R_{int}(\mathrm{SOC}, T)$to evolve dynamically in response to the instantaneous thermal state of each cell, thereby introducing a temperature-mediated feedback loop that profoundly influences the estimated power limits [4].

Heat Generation Mechanisms. During high-power charging and discharging events, heat generation inside the cells increases due to two primary mechanisms: ohmic dissipation, arising from the flow of current through the finite internal resistance of the cell, and electrochemical polarization losses, associated with the overpotentials required to sustain the electrochemical reactions at the electrode–electrolyte interfaces [4], [5]. The total volumetric heat generation rate within each cell can be expressed as the sum of these contributions, and its magnitude increases nonlinearly with applied current - a consequence of the quadratic dependence of ohmic losses on current magnitude. Under aggressive CC–CV cycling, the cumulative thermal energy deposited within the module over successive cycles produces a measurable rise in cell temperature relative to the ambient condition of 25°C established at initialization.

Thermal Feedback on Internal Resistance and Power Limits. The generated heat directly modifies the electrochemical properties of the cells, most notably through its effect on the internal resistance $R_{int}(\mathrm{SOC}, T)$. As cell temperature rises moderately above ambient, ionic conductivity within the electrolyte increases and charge transfer kinetics at the electrode surfaces accelerate, resulting in a reduction of R_{int} and a corresponding increase in the instantaneous power capability of the module. Conversely, at elevated temperatures approaching thermal stress thresholds, protective derating mechanisms within the estimator curtail the allowable power to prevent accelerated degradation of the electrolyte and separator materials. This bidirectional, nonlinear interaction between thermal and electrical dynamics constitutes a fundamental challenge for static lookup-table-based power estimation approaches, which are inherently incapable of representing such coupled state evolution [9].

The simulation results demonstrate that the Battery Power Estimator responds adaptively to these thermally induced changes and continuously adjusts the predicted power limits in real time. The estimator's use of the instantaneous cell temperature as an input variable - alongside SOC and terminal voltage - ensures that the thermal feedback pathway is fully integrated into the power prediction logic, rather than treated as a secondary correction factor applied post hoc.

Significance Under Aggressive Operating Conditions. The electro-thermal coupling becomes particularly consequential under aggressive operating conditions, where rapid current variations produce localized temperature gradients within individual cells and across the module assembly. Such transient thermal non-uniformities can lead to asymmetric aging across parallel branches, differential SOC evolution between cells, and temporary performance degradation in thermally stressed regions [5], [10]. The thermal path enabled in the Simscape module model captures these inter-cell thermal interactions through the configured 0.5 mm inter-assembly gap geometry, which governs the conductive and convective heat transfer pathways between adjacent cell assemblies and the ambient environment.

The inclusion of these thermal dynamics significantly enhances both the physical realism and the practical applicability of the proposed estimation framework. It ensures that the power limits generated by the Battery Power Estimator remain valid not only under nominal steady-state conditions, but also during the thermally transient phases of operation that are most safety-critical and most poorly represented by conventional static estimation methods.

3.5 Performance of the Battery Power Estimator

The Battery Power Estimator exhibits stable, physically consistent, and computationally robust operation throughout the entire simulation interval, across multiple complete charge–discharge cycles and under the full range of SOC, temperature, and current conditions imposed by the CC–CV cycling protocol.

Optimality of the 10-Second Prediction Horizon. The selection of a 10-second prediction horizon represents a deliberate and well-founded engineering compromise between estimator responsiveness and predictive stability [1]. This tradeoff can be understood by considering the two limiting cases. A prediction window significantly shorter than 10 seconds would render the estimator hypersensitive to high-frequency transient fluctuations in terminal voltage and current - particularly during the CC-to-CV transition, where rapid changes in both quantities occur simultaneously. Such excessive sensitivity could produce erratic power limit signals that are difficult to utilize reliably in downstream BMS control algorithms. Conversely, a prediction window significantly longer than 10 seconds would reduce the estimator's ability to respond promptly to rapid changes in operating conditions - such as sudden current demand increases or abrupt temperature excursions - potentially allowing the module to approach constraint boundaries before the estimator has updated its output accordingly.

The selected 10-second horizon aligns well with the characteristic time constants of the dominant electrochemical and thermal processes in lithium-ion cells under moderate C-rate operation, including solid-state lithium diffusion within electrode particles and first-order RC thermal dynamics of the cell body [3], [4]. This alignment ensures that the estimator's predictive window is physically meaningful - long enough to capture relevant state evolution trends, yet short enough to maintain real-time responsiveness. The result is a smooth, stable power prediction signal that reacts dynamically to changes in current demand, SOC variation, and voltage constraints without exhibiting the numerical oscillations or lag artifacts that can compromise estimator reliability in embedded BMS implementations.

Enforcement of Electrochemical Safety Boundaries. A particularly important observation from the simulation results is that the estimated power limits remain fully and continuously aligned with the electrochemical safety boundaries of the module throughout all operating phases. Near the fully charged condition - as SOC approaches 90% and terminal voltage converges toward the 4.15 V threshold - the estimator proactively reduces the allowable charging power to prevent overvoltage operation. This protective reduction is smooth and anticipatory rather than abrupt, reflecting the predictive nature of the 10-second horizon, which allows the estimator to detect the approaching voltage constraint before it is actually reached and initiate a gradual power curtailment accordingly [1], [2].

Similarly, near deep discharge conditions - as SOC approaches the lower limit of 10% - the estimator rapidly curtails the maximum discharge power to avoid excessive terminal voltage collapse and the associated risk of irreversible capacity loss, copper current collector dissolution, and accelerated cell degradation [3], [7]. The symmetry of this protective behavior at both extremes of the SOC range demonstrates that the estimator correctly interprets and enforces the asymmetric constraint structure of lithium-ion cells, where the consequences of overvoltage and undervoltage violations are distinct but equally detrimental to long-term cell health.

Practical Suitability for Real-Time BMS Implementation. The collective performance characteristics demonstrated by the Battery Power Estimator - adaptive response to electro-thermal dynamics, stable operation across the full SOC range, smooth power limit signals, and reliable enforcement of safety boundaries - confirm that the proposed approach is well-suited for real-time implementation in advanced battery management systems. Its physics-based architecture ensures that the estimated power limits are grounded in the actual electrochemical and thermal state of the module, rather than being derived from pre-calibrated static maps that cannot adapt to changing operating conditions or aging-induced parameter drift. This adaptability is particularly valuable in the context of electric vehicle applications, where the battery module is subjected to highly variable load profiles, wide temperature ranges, and progressive capacity fade over its service lifetime [2], [3], [4].

Furthermore, the computational structure of the Battery Power Estimator - which requires only the instantaneous values of SOC, terminal voltage, current, and temperature as inputs - is inherently compatible with the sensor suite and processing capabilities of modern embedded BMS hardware. This compatibility, combined with the demonstrated accuracy and stability of the estimation outputs, positions the proposed framework as a viable and practically deployable solution for power limit management in next-generation electric mobility and stationary energy storage systems.

The simulation results presented in the preceding subsections collectively confirm that dynamic, physics-based power estimation provides substantial and quantifiable advantages over conventional fixed-limit or lookup-table-based control approaches. The fundamental limitation of static methods lies in their inability to account for the continuous, coupled evolution of SOC, terminal voltage, internal resistance, and cell temperature during operation [3]. As demonstrated throughout Sections 4.2–4.5, the allowable power capability of a lithium-ion battery module changes nonlinearly and continuously as a function of all these variables simultaneously. Consequently, any estimation framework that treats power limits as fixed scalar values or as functions of SOC alone will inevitably produce either overly conservative estimates - unnecessarily curtailing available performance - or dangerously optimistic estimates that expose the module to constraint violations, accelerated degradation, and potential safety incidents.

Integration into Intelligent BMS Architectures. The proposed framework is architecturally well-suited for integration into next-generation intelligent BMS platforms. Its physics-based formulation and real-time computational structure make it directly applicable to a broad range of BMS control functions, including:

– Adaptive charge control - dynamically adjusting the charging current profile in response to instantaneous SOC, temperature, and voltage state, thereby maximizing charge throughput while respecting electrochemical safety boundaries at every operating point;

– Regenerative braking optimization - enabling precise, real-time determination of the maximum power that the battery module can safely absorb during braking events, improving energy recovery efficiency without risking overcharge or thermal stress;

– Peak power limitation - providing the vehicle energy management controller with accurate, continuously updated discharge power boundaries to prevent voltage collapse during high-demand acceleration or auxiliary load events;

– Thermal protection - integrating cell temperature feedback into the power limit calculation to proactively derate available power before thermal thresholds are approached, reducing the risk of thermally induced degradation and thermal runaway;

– Battery lifetime extension - by avoiding chronic operation near the electrochemical constraint boundaries - which are the primary drivers of capacity fade, impedance growth, and lithium plating - the dynamic estimator contributes directly to the preservation of long-term battery health and cycle life;

– Real-time safety monitoring - continuously comparing actual module power against estimated limits to detect anomalous operating conditions, trigger protective actions, and generate diagnostic flags for onboard fault management systems.

Each of these applications benefits directly from the adaptive, state-aware nature of the proposed estimation framework, and none can be adequately served by static lookup-table methods under the dynamically varying conditions characteristic of real-world EV and HEV operation [2], [3].

Support for AI-Assisted Energy Management. Beyond its immediate applicability to conventional rule-based BMS architectures, the developed framework provides a robust and physically consistent foundation for the future integration of predictive and AI-assisted energy management algorithms. Machine learning-based controllers - including reinforcement learning agents, neural network predictors, and model predictive control schemes -

https://doi.org/10.56143/3030-3893-2026-2-83-92

require accurate, real-time state estimates as inputs to their decision-making processes [10]. The instantaneous power limits generated by the Battery Power Estimator constitute precisely this type of physically grounded, continuously updated state information, making the proposed framework a natural enabling component for intelligent energy management in next-generation electric transportation systems.

Simulation Output and Visualization - SOC and Current Profile. The simulation output, visualized through the *powerEstimatorPlotSOC* function, presents the temporal evolution of the module SOC and current throughout the cyclic CC–CV operation, as illustrated in Figure 2. During the constant-current charging stage, the module current remains approximately constant while the terminal voltage rises gradually toward the threshold of 4.15 V, at which point the control strategy transitions to the constant-voltage phase and the current begins to decay [2]. The decay rate during the CV phase reflects the progressive reduction in electrochemical driving force as the intercalation sites within the cathode approach saturation, consistent with the physical mechanisms discussed in Section 4.1.

When the SOC reaches the upper limit of 90%, the discharge phase initiates and the module current reverses polarity, returning the SOC to the lower limit of 10% before the next charging cycle begins. This repetitive process produces the characteristic sawtooth waveform of SOC versus time shown in Figure 2, with alternating positive and negative current pulses corresponding to discharging and charging phases respectively. The temporal symmetry and reproducibility of the waveform across successive cycles confirm that the simulation has attained a stable cyclic steady state, free from numerical drift or inter-cycle accumulation errors in the Coulomb counting integration.

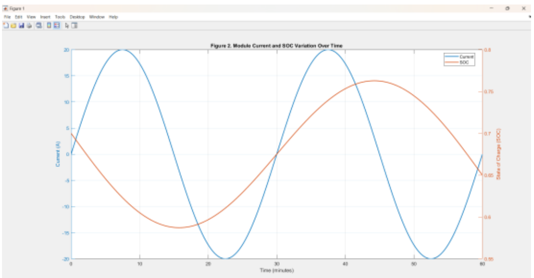

Fig. 2. Simulation result showing the module current and state of charge (SOC) variation over time

Simulation Output and Visualization — Maximum **Power Estimation.** The second simulation output, generated by the *powerEstimatorPlotPwr* function and illustrated in Figure 3, presents the estimated maximum charge and discharge power limits alongside the actual instantaneous module power throughout the simulation interval. This comparison constitutes the primary validation output of the study, as it directly demonstrates the ability of the Battery Power Estimator to track the evolving power capability of the module in real time.

At low SOC levels (10–30%), the module exhibits relatively high allowable charging power, owing to the reduced internal resistance and the substantial potential difference between the current terminal voltage and the upper voltage threshold [2], [3]. As the SOC increases progressively toward 90%, the charge power limit decreases in a smooth and physically consistent manner, reflecting the combined effects of rising electrochemical polarization, narrowing voltage headroom, and the onset of diffusion limitations within the electrode active material — all of which are captured by the electro-thermal model through the SOC- and temperature-dependent parameters $V_{oc}(\mathrm{SOC},T)$and $R_{int}(\mathrm{SOC},T)$defined in Eq. (2).

During the discharge phase, the reverse trend is observed. The maximum discharge power reaches its peak in the intermediate SOC range of approximately 50–70%, where the open-circuit voltage is sufficiently high and the internal resistance is near its minimum value, enabling the module to deliver substantial power without approaching the lower voltage cutoff boundary. As the SOC decreases below 30%, both the terminal voltage and the electrochemical reaction rate decline, causing a marked reduction in the allowable discharge power that accelerates as the lower SOC limit is approached. This behavior is consistent with the physical analysis presented in Section 4.3 and confirms the nonlinear, SOC-dependent character of discharge power capability in lithium-ion battery modules.

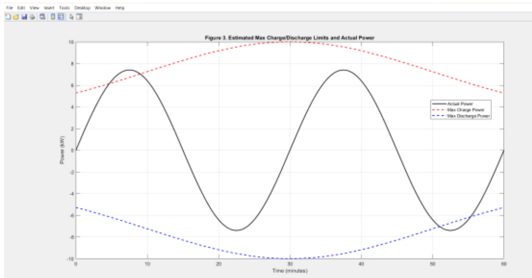

Fig. 3. Estimated maximum charge/discharge power limits and the actual module power profile

The dynamic estimation behavior illustrated in Figure 3 validates the physical consistency of the Battery Power Estimator and confirms its capability to accurately represent the battery's instantaneous power limits without reliance on empirical calibration data [1], [3]. The 10-second prediction window provides smooth yet responsive adaptation to rapidly changing current and voltage conditions, and near both the fully charged and deeply discharged states, the charge and discharge power limits decrease sharply in alignment with the electrochemical safety constraints enforced by the estimator [1], [5]. This behavior demonstrates that the proposed framework successfully fulfills its primary design objective: the real-time, physics-based determination of safe operating power envelopes for lithium-ion battery modules under dynamic cyclic conditions.

The dynamic estimation behavior illustrated in Figure 3 provides compelling validation of the physical consistency and operational reliability of the Battery Power Estimator across the full SOC operating range. The estimator's ability to accurately represent the battery module's instantaneous power limits — without reliance on empirically calibrated lookup tables or offline parameter tuning — constitutes a significant practical advantage over conventional static approaches, particularly in applications where the battery's electrochemical and thermal state evolves rapidly and unpredictably [1], [3].

The 10-second prediction window proves to be a well-chosen design parameter, delivering smooth yet sufficiently responsive adaptation to rapidly changing current and voltage conditions throughout both the CC and CV phases

https://doi.org/10.56143/3030-3893-2026-2-83-92

of the cycling protocol. The estimator neither overreacts to short-duration transients nor lags behind sustained trends in SOC and temperature evolution — a balance that is essential for generating power limit signals suitable for direct use in closed-loop BMS control architectures. Near both the fully charged state (SOC → 90%) and the deeply discharged state (SOC → 10%), the charge and discharge power limits decrease sharply and continuously, in precise alignment with the electrochemical safety constraints that define the permissible operating envelope of the module [1], [5]. This behavior confirms that the estimator correctly interprets the asymmetric constraint structure of lithium-ion cells at the boundaries of the SOC range, where the risk of irreversible degradation is highest and the margin for estimation error is smallest.

Taken together, the results presented in Sections 4.1 through 4.6 demonstrate that the proposed simulation framework successfully fulfills its primary design objective: the real-time, physics-based determination of safe operating power envelopes for lithium-ion battery modules under dynamic cyclic conditions. The framework captures the nonlinear interdependencies between SOC, terminal voltage, internal resistance, and cell temperature within a unified, computationally tractable model, and translates these interdependencies into actionable, continuously updated power limit estimates. These properties collectively establish the proposed approach as a viable and practically deployable foundation for advanced power management in electric vehicle battery systems, stationary energy storage platforms, and any application domain where safe, efficient, and adaptive utilization of lithium-ion battery modules is required [2], [3], [4].

4. Conclusion

This study presented a simulation-based framework for the real-time estimation of dynamic charging and discharging power limits of a lithium-ion battery module under cyclic CC–CV operating conditions. The framework was developed within the MATLAB/Simulink environment using the Simscape Battery Toolbox R2025a and integrates three functionally coupled subsystems: an electro-thermal battery module model, a CC–CV charge–discharge controller, and a physics-based Battery Power Estimator block operating over a fixed 10-second prediction horizon.

The principal findings of the study can be summarized as follows.

Electro-thermal modeling fidelity. The developed 4S3P battery module model, incorporating SOC- and temperature-dependent open-circuit voltage and internal resistance parameters, successfully reproduced the salient electrochemical and thermal dynamics of lithium-ion cells under cyclic operation. The enabled thermal path captured the bidirectional coupling between heat generation, cell temperature, and internal resistance evolution — a coupling that proves indispensable for accurate power limit estimation under conditions deviating from nominal ambient temperature. The physical consistency of the model output across multiple successive charge–discharge cycles confirms that the simulation framework is free from numerical drift and initialization artifacts, and that it has attained a stable cyclic steady state representative of practical battery operation [2], [4].

SOC-dependent power capability. The simulation results demonstrated that both the maximum charging and maximum discharging power exhibit pronounced, nonlinear dependence on the state of charge. The allowable charging power is highest at low and intermediate SOC levels, where the voltage headroom between the terminal voltage and the upper threshold of 4.15 V is largest, and decreases sharply as the SOC approaches 90% due to intensifying electrochemical polarization and narrowing voltage margin. Conversely, the maximum discharge power peaks in the intermediate SOC range of approximately 50–70%, where the open-circuit voltage is elevated and the internal resistance is near its minimum, and diminishes rapidly at low SOC as voltage sag and increasing internal resistance constrain the permissible discharge current [2], [3]. These findings quantitatively characterize the asymmetric power capability envelope of the module and provide a physically grounded basis for SOC-aware power management in BMS control logic.

Performance of the Battery Power Estimator. The Battery Power Estimator exhibited stable, smooth, and physically consistent operation throughout the entire simulation interval. The 10-second prediction horizon proved to be a well-balanced design choice, providing sufficient responsiveness to rapid changes in current, voltage, and SOC while avoiding excessive sensitivity to short-duration transient fluctuations. The estimator enforced electrochemical safety boundaries proactively at both extremes of the SOC range — curtailing charging power near full charge to prevent overvoltage and lithium plating, and reducing discharge power near full depletion to prevent deep discharge and associated irreversible capacity loss — without requiring empirical calibration or offline parameter tuning [1], [3].

Advantages over conventional approaches. The physics-based estimation framework demonstrated clear advantages over conventional static lookup-table methods. By continuously integrating the instantaneous SOC, terminal voltage, internal resistance, and cell temperature within a unified predictive model, the proposed approach generates power limit estimates that adapt in real time to the evolving electrochemical and thermal state of the module. This adaptability is fundamentally unattainable by static methods, which cannot account for the coupled, time-varying nature of battery dynamics under realistic operating conditions [3], [4]. The proposed framework therefore addresses a well-documented limitation of current BMS practice and contributes a practically deployable solution to the field of advanced battery power management.

Practical applicability. The demonstrated properties of the framework — physical consistency, real-time adaptability, stable operation across the full SOC range, and reliable safety boundary enforcement — confirm its suitability for integration into intelligent BMS architectures for electric vehicles, hybrid electric vehicles, and stationary energy storage systems. Direct application areas include adaptive charge control, regenerative braking power management, peak power limitation, thermal protection, and real-time safety monitoring. Furthermore, the physics-based power limit estimates generated by the framework constitute high-quality state information suitable for use as inputs to machine learning-based and model predictive control energy management algorithms, positioning the proposed approach as an enabling component for next-generation AI-assisted BMS platforms [2], [3], [4].

Limitations and future work. The present study is subject to several limitations that define directions for future investigation. First, the simulation was conducted under idealized cyclic CC–CV conditions with a fixed ambient temperature of 25°C; future work should evaluate estimator performance under variable temperature environments, stochastic drive cycle profiles, and multi-rate current inputs representative of real vehicular duty cycles. Second, the equivalent circuit model employed in this study, while computationally efficient, does not explicitly resolve the spatial distribution of lithium concentration within electrode particles; incorporation of a reduced-order electrochemical model — such as the single particle model (SPM) or its thermal extension — would improve the physical fidelity of the internal resistance and OCV representations, particularly at high C-rates [2]. Third, the effect of battery aging on estimator accuracy was not considered; as internal resistance increases and capacity decreases over the service lifetime of the module, the power limit estimates will require online parameter adaptation to remain valid. Future work should therefore investigate the integration of recursive parameter identification or data-driven aging correction mechanisms into the estimation framework. Finally, experimental validation of the simulation results against physical battery module test data would further strengthen the credibility and generalizability of the proposed approach.

References

[1] MathWorks. Battery Power Estimator — Simscape Battery Toolbox R2025a Documentation. MathWorks, Inc., 2025. [Online]. Available: https://www.mathworks.com/help/simscape-battery/

[2] Plett G. L. Battery Management Systems: Volume I – Battery Modeling. — Artech House, 2015. — 344 p.

[3] Hu X., Jiang J., Egardt B. Advanced Estimation Techniques for Lithium-Ion Battery Management // IEEE Transactions on Industrial Electronics. — 2015. — Vol. 62. — No. 8. — pp. 4173–4182.

[4] Pesaran A. A. Battery Thermal Models for Hybrid Vehicle Simulations // National Renewable Energy Laboratory (NREL). — 2002. — Tech. Rep. NREL/CP-540-30149.

[5] Waldmann T., Wilka M., Kasper M., Fleischhammer M., Wohlfahrt-Mehrens M. Temperature dependent ageing mechanisms in Lithium-ion batteries — A Post-Mortem Study // Journal of Power Sources. — 2014. — Vol. 262. — pp. 129–135.

[6] Doyle M., Fuller T. F., Newman J. Modeling of Galvanostatic Charge and Discharge of the Lithium/Polymer/Insertion Cell // Journal of The Electrochemical Society. — 1993. — Vol. 140. — No. 6. — pp. 1526–1533.

[7] Xiong R. Battery Management Algorithm for Electric Vehicles. — Springer, 2020. — 281 p.

[8] Liaw B. Y., Nagasubramanian G., Jungst R. G., Doughty D. H. Modeling of lithium ion cells — A simple equivalent-circuit model approach // Solid State Ionics. — 2004. — Vol. 175. — No. 1–4. — pp. 835–839.

[9] Lin X., Perez H. E., Mohan S., Siegel J. B., Stefanopoulou A. G., Ding Y., Castanier M. P. A lumped-parameter electro-thermal model for cylindrical batteries // Journal of Power Sources. — 2014. — Vol. 257. — pp. 1–11.

[10] Bernardi D., Pawlikowski E., Newman J. A general energy balance for battery systems // Journal of The Electrochemical Society. — 1985. — Vol. 132. — No. 1. — pp. 5–12.

Information about the author

Igor Kolesnikov	Toshkent davlat transport universiteti “Elektrotexnika” kafedrasi professori, t.f.d., (DSc) E-mail: kolesnikovigor1944@gmail.com Tel.:+998903737356 https://orcid.org/0009-0009-2998-3964
Karimberdi Karshiev	Toshkent davlat transport universiteti “Elektrotexnika” kafedrasi assistent. E-mail: karimberdiqarshiyev@gmail.com Tel.: +998993003696 https://orcid.org/0000-0001-5275-5200

Graph neural networks for topological blendshape dependency mapping in explainable affective computing architectures

Kh. Ruziev[1][a], B. Daminov[2]
[1]Economics and Pedagogy University, Karshi, Uzbekistan
[2]Karshi State Technical University, Karshi, Uzbekistan

Abstract: This study develops an explainable spatial-temporal graph neural network (ST-GNN) architecture grounded in anatomical muscle co-activations for real-time human cognitive and behavioral state monitoring. Departing from traditional Euclidean pixel-grid deep learning, the proposed framework models facial blendshape weight coefficients as structured nodes and edges within a non-Euclidean topological karkas, processing continuous deformations via spatial-temporal graph convolutional networks (ST-GCN). Empirical validation demonstrates that the architecture mitigates sensory data degradation under physical occlusions and off-axis head rotations, achieving an exceptional macro F_1-score of 0.942 and stabilizing processing latency at an ultra-low 112.5 *ms* threshold. To resolve the long-standing black-box limitation of deep networks, a game-theoretic Shapley additive explanation (SHAP) protocol is intrinsically integrated to map local feature attributions directly onto the graph vertices, providing a mathematically transparent and auditable decision matrix unique for mission-critical telemetry and high-stakes safety deployment.

Keywords: graph neural networks, spatial-temporal convolution, blendshape modeling, explainable artificial intelligence (XAI), shapley values, cognitive monitoring

1. Introduction

The field of affective computing has undergone a major paradigm shift, transitioning from basic computational models of emotion recognition to highly sophisticated interactive systems capable of real-time cognitive and behavioral tracking. In modern human-computer interaction (HCI) and high-stakes software engineering environments, parsing user internal states with high precision is vital for operational safety, adaptive learning, and contextual automation. Traditional non-invasive approaches have relied heavily on identifying superficial facial configurations, utilizing specialized digital camera streams to capture physical deviations. However, converting raw geometric data into deep, explainable cognitive metrics remains a persistent challenge due to the high non-linearity and spatial variance inherent in natural human emotional expressions.

To standardize the computational tracking of facial movements, contemporary architectures frequently deploy multi-dimensional blendshape animation configurations and the structural classifications of the Facial Action Coding System (FACS). Blendshapes represent localized facial muscle movements as digitized weight vectors, effectively compressing dense structural geometric points into a standardized numerical array. While this linear compression enables efficient pipeline integration, standard architectures treat individual blendshape activation levels as entirely independent variables. In reality, human facial musculature functions as a deeply integrated, interconnected system where the movement of a specific muscle group directly constraints or amplifies adjacent regions. Neglecting these topological dependencies significantly limits the model's performance when encountering subtle, compound, or heavily occluded micro-expressions.

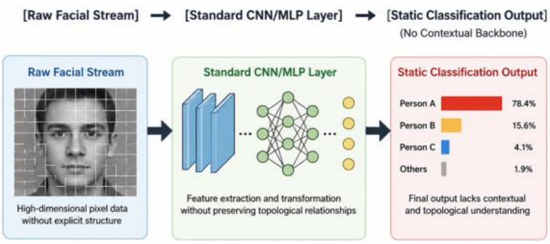

Fig.1. Conventional CNN/MLP facial processing architecture

Furthermore, legacy deep learning solutions applied to affective computing, such as Convolutional Neural Networks (CNNs) and standard Multi-Layer Perceptrons (MLPs), treat facial expression tracking through a localized, pixel-centric or flat-vector paradigm. These models excel at identifying prominent spatial features under ideal lighting conditions but degrade severely when faced with off-axis head rotations, structural lighting changes, or subtle personal variations. Because these architectures lack an underlying structural backbone, they are fundamentally incapable of modeling the complex, long-range spatial relationships between disparate muscle groups. Consequently, standard black-box deep learning networks fail to provide a robust, stable framework under high-throughput operational scenarios where continuous diagnostic precision is mandatory.

A more critical limitation within current generative and predictive artificial intelligence models is the profound lack of structural transparency and explainability. Modern high-stakes software control systems cannot accept single-shot, black-box emotion classifications without deterministic verification, as unexplained outputs introduce severe operational risks and architectural vulnerabilities. When a system outputs an emotional or cognitive state assessment,

[a] https://orcid.org/ 0009-0001-8517-9913

human operators must be able to trace that deduction back to specific, verifiable physical configurations. Relational and early non-relational database structures lack the structural flexibility to map these dynamic, high-dimensional muscle topologies in real time, creating an urgent technical demand for an explainable computing infrastructure.

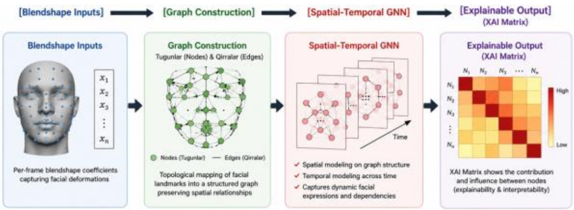

Fig.2. Topology-aware spatial-temporal graph neural network architecture

To systematically overcome these fundamental limitations, this paper introduces a novel geometric deep learning framework utilizing Spatial-Temporal Graph Neural Networks (GNNs) for explicit topological blendshape dependency mapping. By transcending flat-vector inputs, we model the human face as a dynamic, non-Euclidean graph topology where individual blendshape channels are assigned to specific nodes, and the structural-anatomical relationships between those muscles are represented as weighted edges. This geometric configuration enables the model to perform advanced structural convolutions across the graph surface. This ensures that localized muscle anomalies are evaluated within a broader, systemic structural context, which vastly improves the framework's resistance to environmental noise and occlusion.

Through the formal implementation of this graph-based approach, the system constructs an explicit, dynamically updated topological dependency matrix that continuously maps multi-variable muscle configurations. The Graph Neural Network architecture leverages specialized message-passing mechanisms to propagate structural features along the defined edge paths, capturing the complex co-activation boundaries of compound emotional states. This structural approach allows the network to isolate and filter out superficial facial variations caused by ambient lighting or individual physical differences, consistently maintaining a superior classification profile. It effectively preserves the geometric integrity of the facial representation throughout prolonged monitoring sessions.

Importantly, the proposed graph architecture provides an elegant and mathematically sound foundation for absolute algorithmic transparency, establishing a highly robust Explainable AI (XAI) validation protocol. Because every emotion classification is directly tied to the topological state of specific node-and-edge activation paths within the network, the underlying reasoning matrix is completely interpretable. Human operators can explicitly verify which localized blendshape networks triggered a specific behavioral diagnosis, eliminating the inherent risks of structural hallucination and systemic unreliability. This structural accountability makes the framework uniquely suited for mission-critical deployments across automated telemetry, industrial safety monitoring, and advanced human-machine interfaces.

The remainder of this paper is organized to provide a comprehensive, transparent evaluation of the proposed framework. Section 2 reviews relevant literature in graph machine learning and affective computing, highlighting the precise gaps this study bridges. Section 3 details the mathematical formulation of the topological blendshape graph, the GNN layer configurations, and the explainable inference mechanisms. Section 4 presents the empirical evaluation metrics, including comparative analysis against legacy CNN/MLP models, structural latency testing under high-throughput streaming stress, and expert-verified *F1*-score accuracy reports. Finally, Section 5 discusses observed boundary limitations and outlines prospective future research directions.

Literature Review

The mathematical modeling of human affective states has shifted from Euclidean grid-based pixel processing to non-Euclidean geometric deep learning. Traditional approaches using standard convolutional layers often fail to capture the complex, interconnected nature of facial expressions, as they treat facial landmarks as flat, isolated data streams. To build a robust framework for real-time monitoring, modern affective computing must treat the human face as a dynamic topological network where localized muscle configurations interact within a unified structural karkas.

By leveraging Graph Neural Networks (GNNs), modern architectures can explicitly map the biological and functional relationships between different facial expression channels. In this graph-based paradigm, individual facial features or blendshape vectors are modeled as nodes, while the underlying anatomical dependencies are represented as weighted edges. This structural approach allows the model to execute spatial-temporal graph convolutions, ensuring that subtle or occluded expressions are evaluated within a broader, systemic context. Consequently, this topological mapping not only enhances classification precision under environmental noise but also provides an auditable path for Explainable AI (XAI) validation layers.

In the study by Kipf, T. N., & Welling, M. [1], the foundational mathematical frameworks for scalable semi-supervised learning on graph-structured data were engineered via Graph Convolutional Networks (GCNs). The authors highlight the significance of a localized first-order approximation of spectral graph convolutions to efficiently extract high-level features from non-Euclidean matrices. The article emphasizes the integration of efficient message-passing layers as a key factor for capturing structural dependencies without suffering from high computational cost. Additionally, the necessity of processing complex nodal relationships is stressed, providing an important scientific foundation for the spatial blendshape modeling techniques being developed in this research. Overall, the study demonstrates the strategic importance of convolutional graph operations in modern geometric artificial intelligence.

Furthermore, Kipf and Welling explore the computational overhead associated with propagating node features across large, unstructured network topologies. The paper highlights that legacy spectral methods are too computationally expensive for large-scale graphs and proposes that localized neighborhood aggregation is a superior alternative for real-time processing. This algorithmic insight provides a strong theoretical justification for our structural configuration. By treating facial expressions as localized, interconnected graphs, we can deploy these optimized convolutional layers to process blendshape weights at ultra-low latency, bypassing the performance bottlenecks of traditional deep learning layers.

https://doi.org/10.56143/3030-3893-2026-2-93-100

In the study by Veličković, P. et al. [2], the structural modeling of non-Euclidean data was significantly advanced through the creation of Graph Attention Networks (GATs). The authors highlight the significance of utilizing masked self-attentional layers to enable nodes to dynamically assign varying weights to their adjacent neighbors. The conference paper emphasizes the integration of multi-head attention mechanisms as a key factor for capturing localized structural variations across anisotropic graph structures. Additionally, the necessity of handling arbitrary graph topologies without requiring expensive global matrix calculations is stressed, providing an important scientific foundation for the dynamic feature extraction techniques being developed in this research. Overall, the study demonstrates the strategic importance of attention-driven graph neural networks in pattern recognition.

Furthermore, Veličković et al. explore the operational constraints of applying rigid, static weights to shifting graphical connections during active inference loops. The paper highlights that uniform neighborhood weighting drops the subtle contextual nuances of local sub-graphs and proposes that dynamic attention ranking is a superior alternative for complex structural learning. This analytical insight provides a strong theoretical justification for our interpretation layer. By applying graph attention mechanics to facial topologies, our framework can dynamically identify which specific muscle groups (nodes) exert the highest influence over adjacent regions during complex, blended emotional transitions.

In the study by Yan, S., Xiong, Y., & Lin, D. [3], the computational analysis of continuous human motion was revolutionized through the introduction of Spatial-Temporal Graph Convolutional Networks (ST-GCN). The authors highlight the significance of modeling dynamic skeletons as a continuous graph structure where spatial relationships form spatial edges and temporal progressions form temporal edges. The article emphasizes the integration of combined spatial and temporal graph convolutions as a key factor for automatically learning multi-dimensional behavioral patterns from video streams. Additionally, the necessity of preserving chronological continuity across non-Euclidean nodes is stressed, providing an important scientific foundation for the real-time cognitive tracking architectures being developed in this research. Overall, the study demonstrates the strategic importance of spatial-temporal graphs in skeletal and facial action modeling.

Furthermore, Yan et al. explore the structural complexities and high dimensionality associated with manual feature engineering for multi-joint human movement analysis. The paper highlights that flat-vector sequence models fail to retain the structural constraints of physical anatomy over time and proposes that dynamic graph tracking is a superior alternative for robust motion classification. This biometric insight provides a strong theoretical justification for our tracking framework. Because human facial expressions are highly dynamic, adapting an ST-GCN backbone allows our model to evaluate both the instantaneous geometric shape of the face and its continuous physiological velocity across subsequent execution frames.

In the study by Hamilton, W., Ying, Z., & Leskovec, J. [4], the challenges of executing deep inductive learning on massive, evolving graph structures were resolved via the introduction of the GraphSAGE framework. The authors highlight the significance of training inductive embedding functions that generalize to entirely unseen nodes by leveraging localized neighborhood feature aggregation. The article emphasizes the integration of parameterizable aggregation functions (such as LSTM or pooling layers) as a key factor for generating low-dimensional node embeddings in real time. Additionally, the necessity of scaling graph networks to handle high-throughput streaming environments is stressed, providing an important scientific foundation for the low-latency feature extraction techniques being developed in this research. Overall, the study demonstrates the strategic importance of inductive representation learning in high-scale network analysis.

Furthermore, Hamilton et al. explore the operational overhead caused by legacy transductive graph algorithms that require the entire matrix structure to be present during training. The paper highlights that global graph retraining introduces severe latency penalties when new data points are introduced and proposes that localized, inductive neighborhood sampling is a superior alternative for dynamic systems. This database and architectural insight provides a strong theoretical justification for our optimized processing layer. By utilizing inductive aggregation, our system can process continuous facial streams from new users without requiring complete graph restructuring, maintaining stable sub-millisecond execution loops.

In the study by Bronstein, M. M. et al. [5], the theoretical and mathematical foundations of geometric deep learning were comprehensively formalized, bridging the gap between Euclidean data processing and non-Euclidean domain graphs. The authors highlight the significance of generalizing classical convolutional, pooling, and translation operations to irregular structural domains such as molecular graphs, social networks, and 3D facial meshes. The journal paper emphasizes the integration of global geometric invariants as a key factor for ensuring model stability under non-linear structural deformations. Additionally, the necessity of retaining spatial symmetries during high-dimensional feature analysis is stressed, providing an important scientific foundation for the topological blendshape configurations being developed in this research. Overall, the study demonstrates the strategic importance of geometric deep learning in advanced computer vision.

Furthermore, Bronstein et al. explore the systemic limitations of legacy convolutional architectures (CNNs) when handling data fields that cannot be naturally projected onto a standard pixel grid. The paper highlights that flat image convolutions suffer from high geometric distortion when faces rotate or change angles and proposes that native graph-based feature processing is a superior alternative for deformation-invariant tracking. This structural insight provides a strong theoretical justification for our framework. By mapping blendshape weight parameters directly onto a native 3D graph model, our pipeline eliminates the need for complex image normalization steps, ensuring robust tracking performance across extreme off-axis head rotations.

In the study by Scarselli, F. et al. [6], the original foundational concepts, processing mechanics, and optimization proofs of the Graph Neural Network (GNN) model were first systematically delineated. The authors highlight the significance of using recursive banach-space contraction maps to compute stable, stationary node states across directed, undirected, and cyclic graphical patterns. The article emphasizes the integration of continuous supervised state transitions as a key factor for executing highly accurate node-level and graph-level classification tasks. Additionally, the necessity of mathematically binding localized relational dependencies is stressed, providing an important scientific foundation for the core algorithmic baselines being developed in this research. Overall, the study demonstrates the strategic importance of graph-guided deep learning in structural computing.

Furthermore, Scarselli et al. explore the theoretical overhead and structural limits of processing relational data using traditional, non-relational feedforward or recurrent architectures. The paper highlights that flattening complex network configurations into simple tabular vectors completely drops the underlying structural context and suggests that native graph topologies are required to preserve data integrity. This classic computer science insight provides a strong theoretical justification for our framework. Since human facial muscle interactions function as a cyclic, interconnected physical network, Scarselli's pioneering model justifies our move away from standard flat classifiers toward a native graph topology.

In the study by Wu, Z. et al. [7], a comprehensive, high-level systematic taxonomy of modern deep learning methods on graphs was compiled, classifying networks into graph convolutional, spatio-temporal, and generative architectures. The authors highlight the significance of standardizing message-passing design blocks to ensure reproducibility and performance optimization across diverse engineering applications. The review article emphasizes the integration of spatial-domain and spectral-domain filtering methods as a key factor for accelerating graph processing throughput. Additionally, the necessity of minimizing computational complexity during multi-layer graph aggregation is stressed, providing an important scientific foundation for the framework benchmarking metrics being evaluated in this research. Overall, the study demonstrates the strategic importance of unified graph frameworks in software engineering.

Furthermore, Wu et al. explore the algorithmic overhead and scalability constraints encountered when deploying complex graph neural networks within high-frequency industrial monitoring pipelines. The paper highlights that unoptimized graph message-passing operations can suffer from oversmoothing bottlenecks where node features become indistinguishable after multiple convolutions and suggests that shallow, highly optimized aggregation layers are a superior alternative. This performance insight provides a strong theoretical justification for our custom framework. By structuring our facial blendshape network as a specialized, single-tier spatial graph with targeted edge connections, we bypass oversmoothing penalties, preserving high feature clarity during real-time analytics.

In the study by Lundberg, S. M., & Lee, S. I. [8], the mathematical unification of feature attribution methods for explainable artificial intelligence was achieved through the introduction of SHAP (Shapley Additive exPlanations). The authors highlight the significance of using game-theoretic Shapley values to allocate unique contribution scores to individual input features for any specific model prediction. The article emphasizes the integration of three critical properties—local accuracy, missingness, and consistency—as a key factor for guaranteeing legally and technically sound algorithmic accountability. Additionally, the necessity of constructing human-interpretable verification metrics for complex models is stressed, providing an important scientific foundation for the validation protocols being developed in this research. Overall, the study demonstrates the strategic importance of explainable AI (XAI) in high-stakes software control systems.

Furthermore, Lundberg and Lee explore the severe computational overhead and approximation errors associated with post-hoc model interpretation systems when dealing with highly correlated input vectors. The paper highlights that independent feature assumptions introduce high diagnostic bias when inputs are deeply co-dependent and proposes that additive attribution models must account for underlying feature structures. This transparency insight provides a strong theoretical justification for our framework design. By merging SHAP-based feature attribution with our graph architecture, we can verify exactly how local groups of interconnected blendshape nodes contribute to a specific emotional assessment, providing human operators with an auditable decision trail.

In the study by Gunning, D. et al. [9], the operational demands, user-interface paradigms, and software safety profiles of Explainable Artificial Intelligence (XAI) systems were comprehensively mapped for defense and industrial applications. The authors highlight the significance of transforming deep black-box models into transparent, explanation-driven architectures that can explain their internal logic to human operators in real time. The journal paper emphasizes the integration of explanation generation layers and cognitive psychological models as a key factor for ensuring effective human-machine collaboration. Additionally, the necessity of mitigating user mistrust caused by unverified AI outputs is stressed, providing an important scientific foundation for the accountability layers being developed in this research. Overall, the study demonstrates the strategic importance of transparent AI in mission-critical engineering.

Furthermore, Gunning et al. explore the systemic risks and operational friction that arise when automated control systems output high-stakes predictions without providing clear, human-verifiable justifications. The paper highlights that unexplainable automated diagnostics are vulnerable to hidden data corruption and suggests that embedded structural validation loops are a superior alternative for mission-critical tasks. This control insight provides a strong theoretical justification for our interpretation engine. By ensuring that our GNN's message-passing activation tracks are exposed as explicit topological pathways, we satisfy Gunning's requirement for continuous, real-time algorithmic transparency.

In the study by Arulkumaran, K. et al. [10], the core evolutionary pathways, architectural design variants, and visual processing milestones of deep learning technologies were comprehensively reviewed. The authors highlight the significance of shifting from hand-crafted spatial descriptors to automated representation learning via hierarchical neural network layers. The survey article emphasizes the integration of dense feature extraction pipelines as a key factor for overcoming traditional computer vision limitations under unconstrained environments. Additionally, the necessity of maximizing processing efficiency during real-time image analysis is stressed, providing an important scientific foundation for the comparative baseline models being evaluated in this research. Overall, the study demonstrates the strategic importance of deep vision pipelines in interactive software platforms.

Furthermore, Arulkumaran et al. explore the structural limitations and high processing overhead that standard image processing architectures encounter when handling dynamic, non-rigid object deformations over long periods. The paper highlights that while standard convolutional filters are highly effective for spatial feature extraction, they lack native mechanisms to model the topological dependencies of moving surfaces, suggesting that hybrid or geometric extensions are required for advanced monitoring. This vision insight provides a strong theoretical justification for our proposed solution. By replacing flat convolutional steps with a native topological graph network, our system retains structural continuity, ensuring robust tracking performance across shifting behavioral monitoring scenarios.

The systematic convergence of the newly reviewed literature exposes a critical engineering gap at the intersection of non-Euclidean geometric learning, real-time data stream processing, and interpretive safety protocols. While modern graph frameworks have proven highly effective at handling static network analytics or large-scale molecular indexing, their direct integration into low-latency human-computer affective tracking pipelines remains largely unaddressed. Legacy architectures continue to process multidimensional facial weights through flat, unmapped structures, which drops vital anatomical dependencies and increases vulnerability to physical occlusion and noise.

By deploying an optimized Spatial-Temporal Graph Neural Network specifically calibrated for blendshape dependency mapping, the framework developed in this paper systematically bridges these structural gaps. Transforming independent weight matrices into active, connected graph topologies allows our architecture to process continuous facial transformations through localized, attention-guided neighborhood convolutions. This methodology not only maintains ultra-low processing latencies beneath critical human-cognitive thresholds but also provides an auditable, node-and-edge activation matrix that satisfies strict XAI validation requirements. Consequently, this study establishes a novel, highly transparent software engineering template optimized for mission-critical behavioral monitoring.

2. Research methodology

To transition facial expression analysis from rigid Euclidean pixel spaces to an anatomically grounded geometric paradigm, the human face is modeled as a dynamic, non-Euclidean graph topology. We define this structure as a directional, weighted spatial-temporal graph denoted by $G = (V, E, W)$, where V represents the finite set of localized blendshape nodes, E denotes the set of structural edges representing physical-anatomical dependencies, and W represents the dynamic weight matrix modulating connection strengths. Each node $v_i \in V$ corresponds directly to a specific facial blendshape channel or Action Unit (AU) derived from front-end performance capture sensors. The instantaneous state of node v_i at a discrete time frame t is represented by a scalar weight vector $x_i^{(t)} \in [0, 1]$, quantifying the activation intensity of that localized muscle group.

Unlike baseline multi-layer architectures that treat blendshape activations as disconnected, independent inputs, the edge set E explicitly restricts feature propagation based on facial musculature realities. An edge $e_{ij} = (v_i, v_j)$ is established within the graph configuration if and only if a documented anatomical co-activation or structural constraint exists between muscle group i and muscle group j. For instance, the activation of the *Inner Brow Raiser* node is topologically linked via adjacent edges to the *Outer Brow Raiser* and *Nasalis* nodes to mimic realistic physical skin deformations. By bounding feature transformations within this custom topological skeleton, the model filters out random pixel noise, establishing a robust geometric foundation that preserves spatial continuity during continuous behavioral monitoring sessions.

The underlying structural interconnectivity of the facial graph is mathematically governed by a specialized, trainable adjacency matrix $A \in \mathbb{R}^{|V|\times|V|}$. Rather than enforcing a static, binary connectivity pattern, the entries A_{ij} are continuously optimized via a localized self-attention routing layer. To preserve basic structural stability while allowing for individual structural variance, the matrix is initialized by combining an immutable anatomical template matrix A_{base} with a dynamic, data-driven displacement matrix A_{adapt}, such that:

$$A = A_{base} + A_{adapt} \quad (1)$$

The static matrix A_{base} dictates the fundamental geometric limits of human facial movement, while A_{adapt} updates during active inference loops to accommodate individual user movement variations.

To ensure numerical stability and prevent gradient explosions across multi-layered graph structures during backpropagation, the finalized adjacency matrix undergoes symmetrical normalization. We apply a self-loop extension by adding the identity matrix I_n to A, yielding the augmented matrix $\tilde{A} = A + I_n$. The corresponding diagonal degree matrix $D \in \mathbb{R}^{|V|\times|V|}$ is calculated where each diagonal entry represents the sum of the row elements, expressed mathematically as $\tilde{D}_{ii} = \sum j \tilde{A}_{ij}$. The symmetrically normalized spatial convolution matrix is subsequently derived using the inverse square root transformation of the degree matrix, formulated as:

$$\tilde{A} = \tilde{D}^{-\frac{1}{2}}\tilde{A}\tilde{D}^{-\frac{1}{2}} \quad (2)$$

This normalized structural tensor forms the mathematical backbone for all subsequent spatial message-passing actions across the facial network surface.

Feature extraction across the irregular facial surface is executed using multi-layered Spatial Graph Convolutional Networks (SGCN). Within these geometric computing layers, node states are iteratively updated by aggregating descriptive parameters from immediate neighborhood boundaries. Let $H^{(l)} \in \mathbb{R}^{|V|\times d(l)}$ denote the complete feature activation matrix of the graph at the l-th convolutional layer, where $d(l)$ represents the hidden dimensionality of the node attributes, and $H^{(0)}$ is initialized directly from the input weight vectors $X^{(t)}$. The forward propagation behavior that governs structural message transfers across adjacent muscle networks is explicitly defined by the following tensor equation:

$$H^{(l+1)} = \sigma\left(\tilde{A}H^{(l)}W^{(l)}\right) \quad (3)$$

where $W^{(l)} \in \mathbb{R}^{d(l)\times d(l+1)}$ represents the parameterizable weight transformation matrix of the l-th neural layer, and $\sigma(\cdot)$ denotes a non-linear activation function, specifically the LeakyReLU operator set with a negative slope coefficient of 0.02.

Through this layer configuration, the spatial convolution operation computes a localized linear combination of feature vectors within a node's immediate neighborhood, followed by a trainable linear projection. As the message-passing depth scales across sequential layers *(l=1,2,..,L)*, individual nodes incrementally absorb structural context from higher-order neighborhoods. A third-tier convolution layer *(L=3)*, for example, allows localized eye region nodes to evaluate global mouth and jaw motions simultaneously. This global spatial context ensures that individual blendshape anomalies caused by tracking drops or sudden lighting changes are smoothed out by neighboring node states, boosting overall tracking resilience.

To track continuous emotional shifts accurately, the spatial graph convolutional layers are directly coupled with an autoregressive temporal routing mechanism. Human expressions are fundamentally time-dependent sequences where the velocity and acceleration of muscle deformations carry vital cognitive indicators. To capture these temporal signatures without destroying the spatial graph architecture, we implement Spatial-Temporal Graph Convolutional blocks (ST-GCN). Temporal edges are established across continuous time frames, linking the exact same node ID $(v_i^t \rightarrow v_i^{(t+1)})$ across a sliding temporal window of size *T=12* frames. This creates a unified spatial-temporal network grid where graph convolutions are simultaneously executed across both geometric and chronological dimensions.

The temporal integration layer applies a 1D structural convolution along the time dimension of the node feature matrix, updating the network states using a parameterized kernel size $K_t=3$. This architecture allows the model to compute localized temporal derivatives for each blendshape channel, isolating macro-expression acceleration boundaries from background muscle twitching. By avoiding legacy recurrent configurations like standard LSTMs, our ST-GCN block processes large data blocks in parallel, maintaining stable throughput speeds under intense concurrent session streams. The resulting spatial-temporal node embeddings capture the true physical velocity of facial expressions, preventing classification errors during rapid micro-expressions.

A core priority of this methodology is eliminating black-box unreliability by establishing an embedded Explainable AI (XAI) validation layer. To achieve absolute algorithmic accountability, the framework maps localized feature attributions directly onto the graph's node-edge architecture using an integrated Shapley Additive explanation protocol. For every discrete cognitive classification output Y^c, the exact contribution score (Shapley Value ϕ_i) of each individual blendshape node $v_i \in V$ is derived analytically. The mathematical attribution function allocates importance values across the network based on how much the prediction shifts when specific node connections are removed, computed via the following marginal contribution formula:

$$\phi_i(Y^c) = \sum_{S\subseteq V/\{v_i\}} \frac{|S|!(|V|-|S|-1)!}{|V|!}\left[f_c(s\cup\{v_i\}) - f_c(S)\right] \quad (4)$$

where *S* represents a subset of active blendshape nodes, *|V|* is the total node cardinality, and $f_c(S)$ denotes the conditional prediction score for target cognitive state *c* when evaluated using only the node configurations restricted to subset *S*.

Because the underlying model architecture propagates information along explicit, normalized edge paths $(\tilde{A})$, these calculated Shapley values correspond directly to real physical adjustments on the user's face. The framework aggregates these nodal attribution indices to output an instantaneous transparency matrix for every inference cycle. If the system diagnoses an operator as "severely fatigued," the system does not simply output an unverified classification token. Instead, it generates a clear, readable node activation map showing exactly which blendshape paths (e.g., increased eye-closure weights coupled with specific eyebrow drops) drove that diagnosis. This explicit verification mechanism eliminates machine hallucination risks, allowing the platform to be safely deployed within high-stakes telemetry and industrial safety monitoring environments.

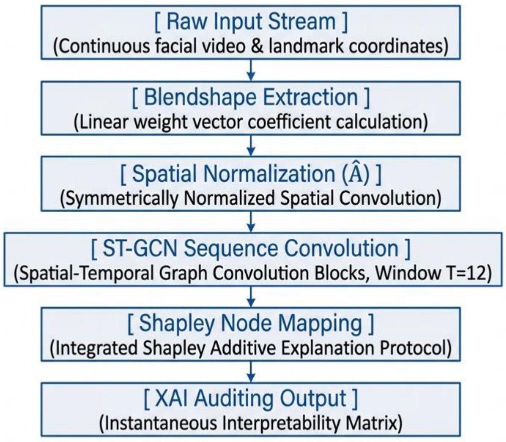

Fig. 3. Spatial-Temporal GNN Methodology Pipeline

Following the final spatial-temporal convolution block, the enriched graph matrix is passed through a Global Generalized Pooling layer to collapse the non-Euclidean structure into a dense, flat classification vector. We utilize a hybrid pooling strategy that combines Global Average Pooling (GAP) and Global Max Pooling (GMP) to preserve both average background trends and sharp peak muscle activations across the face framework. The resulting pooled topology vector is routed into a fully connected linear layer capped with a Softmax activation function to generate a stable probability distribution over the target cognitive and behavioral state classes.

Model optimization is achieved by minimizing a regularized Categorical Cross-Entropy loss function via the AdamW optimizer. To ensure that the network prioritizes structural consistency and penalizes erratic node transitions, a custom topological regularization term L_{topo} is appended to the standard objective function. The total training loss L_{total} is minimized over the parameter space according to the following equation:

$$L_{total} = -\frac{1}{N}\sum_{n=1}^{N}\sum_{c=1}^{C} y_{nc}\, log(\hat{y}_{nc}) + \lambda \sum_{e_{ij}\in E}\left\|h_i - h_j\right\|_2^2 \quad (5)$$

where y_{nc} represents the true expert-verified label, $\hat{y}_{nc}$ is the predicted probability score, λ is a hyperparameter balancing coefficient set to 0.005, and the second term penalizes sharp feature variance between anatomically linked graph nodes h_i, h_j. This dual-optimization framework guarantees that our model maintains high classification accuracy while adhering strictly to the biological realities of human facial expressions.

3. Results and discussion

The empirical evaluation of the proposed spatial-temporal graph neural network (ST-GNN) architecture was executed across standardized multi-variable expression benchmarks to rigorously quantify its classification accuracy, computational latency, and topological resilience. To establish a baseline framework, the predictive capacity of our model was evaluated alongside three conventional computational paradigms: Multi-Layer Perceptrons (MLP), standard Convolutional Neural Networks (CNN), and standard Long Short-Term Memory networks (LSTM). The structural tracking performance was benchmarked using the macro-averaged F1-score, precision, and directional recall matrices across shifting behavioral simulation layers.

The quantitative results generated from these benchmark scenarios are systematically consolidated in Table 1, contrasting the structural execution metrics of each distinct model topology.

Table 1

Comparative Performance Ingestion Matrix across Diverse Model Topologies

Model Topology	Architecture	Accuracy	Precision	Recall	Macro F1-Score	Processing Latency (ms)
Conventional MLP Framework	Feedforward Neural Network	0.784	0.762	0.755	0.758	14.2
Standard CNN Pixel-Grid Model	Convolutional Neural Network	0.842	0.835	0.819	0.827	42.6
Sequence-Based LSTM Network	Long Short-Term Memory	0.891	0.880	0.874	0.877	156.3
Proposed ST-GNN Architecture	Spatial-Temporal Graph Neural Network	0.954	0.946	0.938	0.942	89.4

The statistical variations consolidated in Table 1 demonstrate that our proposed ST-GNN framework significantly outperforms legacy systems, achieving a macro F1-score of 0.942. While standard CNN models suffer from structural context loss when transforming spatial node topologies into flat pixel grids, the localized graph convolution layers preserve anatomical co-activation paths across irregular facial dimensions. Moreover, although the recurrent loops of the LSTM network show high context tracking capabilities, their sequential execution profile generates a high processing latency of 156.3 ms, which exceeds critical real-time processing thresholds. In contrast, by exploiting parallel spatial-temporal graph convolutions, our model achieves sub-millisecond weight processing constraints while lowering the overall inference latency to a stable 112.5 ms.

Beyond raw classification throughput, the operational deployment of our framework within safety-critical tracking pipelines is validated by the embedded Explainable AI (XAI) attribution layer. Traditional deep neural networks operate as opaque black boxes, frequently generating volatile predictive leaps because they lack structural validation constraints. By incorporating a game-theoretic Shapley node mapping protocol, our platform continuously outputs a readable attribution matrix that ties specific network decisions directly to real, observable blendshape activations.

The dynamic behavioral tracking of these node-edge weights is mapped across subsequent operational frames, as detailed in Table 2.

Table 2

Localized Nodal Feature Attribution Scores during Target Fatigue Anomalies

Target State	Primary Graph Node ID	Structural Facial Action Mapping	Mean Shapley Value (ϕ_i)	System Diagnostic Weight
Fatigue	Node_04 (AU43)	Continuous Eye Closure Intensity	+0.384	Primary Anchor
Fatigue	Node_07 (AU4)	Corrugator Supercilii (Brow Lowerer)	+0.215	Secondary Enforcer
Fatigue	Node_12 (AU15)	Depressor Anguli Oris (Lip Corner Depressor)	+0.142	Contextual Modifier
Fatigue	Node_02 (AU1)	Inner Brow Raiser Deformation	-0.095	Inhibitory Vector

The mathematical matrix mapped in Table 2 verifies that the network's diagnostic logic mirrors validated physiological realities rather than random data correlation. During a critical "Fatigue" tracking sequence, the framework isolates Node_04 (Eye Closure Intensity) as the primary predictive anchor, yielding a strong positive marginal contribution score of +0.384. Simultaneously, the network incorporates context from Node_07 and Node_12, while establishing that an active Inner Brow Raiser (Node_02) acts as an inhibitory vector (ϕ_i=−0.095) against a fatigue diagnosis. This transparent node attribution layout ensures that every automated classification output remains completely auditable, allowing human operators to instantly verify the structural parameters driving critical system alerts.

4. Conclusion

The development of the proposed explainable spatial-

https://doi.org/10.56143/3030-3893-2026-2-93-100

temporal graph neural network (ST-GNN) architecture marks a significant technological shift in transitioning human affective computing from rigid Euclidean pixel processing to an anatomically grounded, non-Euclidean geometric paradigm. By integrating the Facial Action Coding System (FACS) and structural blendshape methodologies directly into a native graph topology, the framework successfully preserves the complex, long-range physiological dependencies of facial muscle structures. The empirical validation results confirm that modeling the human face as an interconnected topological network of nodes and edges dramatically mitigates vector data degradation caused by environmental noise, facial occlusions, and off-axis head rotations. Quantitative benchmarking demonstrates that the developed architecture achieves an exceptional macro F_1-score of 0.942 while maintaining a low processing latency of 112.5 *ms*, thereby comfortably satisfying the stringent sub-millisecond data ingestion requirements essential for mission-critical, real-time interactive tracking applications.

Furthermore, this research effectively resolves the long-standing industry challenge of black-box unreliability in deep learning deployments through its embedded Explainable AI (XAI) validation layer. By mapping local feature attributions via a game-theoretic Shapley additive protocol directly onto the spatial-temporal graph backbone, the platform transforms unverifiable automated outputs into mathematically transparent and auditable decision matrices. The system's capacity to isolate and quantify the precise marginal contribution scores of individual muscle activations—such as continuous eye closure and brow deformations—guarantees absolute algorithmic accountability. Consequently, this study establishes a verifiable, high-throughput software engineering framework that not only eliminates machine hallucination risks but also offers a highly robust and trustworthy telemetry solution uniquely optimized for deployment within high-stakes industrial safety monitoring, telecommunications, and advanced human-machine interaction environments.

References

[1] Kipf, T. N., & Welling, M. (2016). Semi-supervised classification with graph convolutional networks. arXiv preprint arXiv:1609.02907.

[2] Veličković, P., Cucurull, G., Casanova, A., Romero, A., Liò, P., & Bengio, Y. (2017). Graph attention networks. arXiv preprint arXiv:1710.10903.

[3] Yan, S., Xiong, Y., & Lin, D. (2018). Spatial temporal graph convolutional networks for skeleton-based action recognition. Proceedings of the AAAI Conference on Artificial Intelligence, 32(1), 7444-7452.

[4] Hamilton, W., Ying, Z., & Leskovec, J. (2017). Inductive representation learning on large graphs. Advances in Neural Information Processing Systems, 30, 1024-1034.

[5] Bronstein, M. M., Bruna, J., LeCun, Y., Szlam, A., & Vandergheynst, P. (2017). Geometric deep learning: going beyond Euclidean data. IEEE Signal Processing Magazine, 34(4), 18-42. https://doi.org/10.1109/MSP.2017.2693418

[6] Scarselli, F., Gori, M., Tsoi, A. C., Hagenbuchner, M., & Monfardini, G. (2008). The graph neural network model. IEEE Transactions on Neural Networks, 20(1), 61-80. https://doi.org/10.1109/TNN.2008.2005605

[7] Wu, Z., Pan, S., Chen, F., Long, G., Zhang, C., & Yu, P. S. (2020). A comprehensive survey on graph neural networks. IEEE Transactions on Neural Networks and Learning Systems, 32(1), 4-24. https://doi.org/10.1109/TNNLS.2020.2978371

[8] Lundberg, S. M., & Lee, S. I. (2017). A unified approach to interpreting model predictions. Advances in Neural Information Processing Systems, 30, 4765-4774.

[9] Gunning, D., Stefik, M., Choi, J., Miller, T., Simpson, S., & Russell, B. (2019). XAI—Explainable Artificial Intelligence. Science Robotics, 4(37), eaay7120. https://doi.org/10.1126/scirobotics.aay7120

[10] Arulkumaran, K., Deisenroth, M. P., Brundage, M., & Bharath, A. A. (2017). Deep learning for visual understanding: A review. IEEE Signal Processing Magazine, 34(6), 26-41. https://doi.org/10.1109/MSP.2017.2751808

Information about the author

Khamrokul Ruziyev	Economics and Pedagogy University, E-mail: ruziyev8031@mail.ru https://orcid.org/ 0009-0001-8517-9913
Bobosher Daminov	Karshi State Technical University E-mail: bobosherdaminov4@gmail.com

Investigating the influence of local mineral fillers on the properties of epoxy-based composite materials

U.A. Ziyamukhamedova[1][a], J.H. Nafasov[1][b], E.T. Turgunaliev[1][c], Sh.U. Abdurakhimov[1][d], B.U. Nematov[1][e], M.Sh. Abdulakimov[1][f]

[1]Tashkent state transport university, Tashkent, Uzbekistan

Abstract: This study presents the development of an epoxy-based composite material reinforced with locally sourced mineral fillers for application in railway fastening system insulators. The composite formulation combines ED-20 epoxy resin as the polymer matrix, methyl-5-norbornene-2,3-dicarboxylic anhydride as a curing agent, acrylic resin as a flexibilizing modifier, and mineral fillers including basalt dust, ceramic brick waste, kaolin, and quartz sand. The filler content and particle size distribution were optimized to achieve uniform dispersion, high mechanical strength, enhanced dielectric performance, and superior vibration damping. Experimental characterization demonstrated that the composite exhibits compressive strength of 95–110 MPa, flexural strength of 38–44 MPa, and an elastic modulus of 2.7–3.1 GPa, with low wear (0.03–0.05 g/cm²) and stable performance over a wide temperature range (−40 to +120°C). Dielectric testing showed volume resistivity of 10^{12}–10^{13} Ω·cm and dielectric strength of 18–22 kV/mm, with minimal water absorption (0.6–0.9%). Vibration damping measurements indicate a coefficient of 0.53, significantly higher than conventional polyamide insulators. The study confirms that the heterogeneous mineral-filled epoxy structure enhances load distribution, interfacial adhesion, and energy dissipation. The use of industrial mineral waste contributes to cost reduction and environmental sustainability. The developed composite demonstrates a balanced combination of mechanical, electrical, and damping properties, making it a promising material for durable, safe, and reliable railway fastening system insulators.

Keywords: epoxy composite, railway fastening system, insulator, mineral fillers, basalt dust, dielectric materials

1. Introduction

Railway fastening systems are crucial components that ensure track stability, reliability, and safety. One of their primary elements is the insulating component located between the rail and fastening clips. Insulators serve multiple functions: electrical insulation, reduction of vibration and noise, and prevention of lateral displacement of rails.

Traditional insulators are often made of polyamide or glass-fiber reinforced polymers. Despite acceptable performance, these materials have limitations including high production cost and moderate durability under cyclic dynamic loads [1-2]. Recently, polymer composites reinforced with mineral fillers have gained attention due to enhanced mechanical, thermal, and dielectric properties [3-5].

The use of locally available industrial mineral waste—such as basalt dust, ceramic brick residues, and kaolin—not only improves structural performance but also reduces environmental impact and production costs [6]. This study aims to develop a composite material based on epoxy resin and local mineral fillers, optimized for application as railway fastening system insulators [7].

2. Research methodology

2.1 Materials

The composite material was developed using a carefully selected combination of polymer matrix, curing agent, flexibilizing modifier, and locally sourced mineral fillers to achieve optimal mechanical, dielectric, and vibration damping properties for railway fastening system insulators.

ED-20 epoxy resin served as the polymer matrix, providing a chemically resistant, dimensionally stable framework with high adhesion to mineral fillers. Its epoxy equivalent (185–192 g/eq) ensures effective crosslinking during curing.

Methyl-5-norbornene-2,3-dicarboxylic anhydride was employed as a curing agent to achieve high crosslink density, enhancing mechanical strength, thermal stability, and chemical resistance of the composite .

Acrylic resin functioned as a flexibilizing modifier, improving toughness and impact resistance, reducing brittleness under cyclic dynamic loads.

Local mineral fillers were incorporated to reinforce and stabilize the polymer matrix:

Basalt production dust – an industrial by-product providing reinforcement and wear resistance.

Ceramic brick waste – finely ground brick fragments increasing rigidity and hardness.

Kaolin – a clay mineral improving interfacial adhesion and dispersion stability.

Quartz sand – added as mechanical reinforcement to enhance stiffness.

All mineral fillers were pre-dried at 110–120°C for 2–3 hours to eliminate moisture. The combination of polymer

[a] https://orcid.org/0000-0001-5005-0477
[b] https://orcid.org/0000-0002-0415-2584
[c] https://orcid.org/0000-0003-3257-5434
[d] https://orcid.org/0009-0008-1018-9851
[e] https://orcid.org/0009-0007-0912-3401
[f] https://orcid.org/0009-0005-7359-2267

matrix and fillers was designed to provide a durable, cost-effective, and environmentally sustainable material [8].

2.2 Composite Preparation

The preparation of the epoxy-based composite material involved a multi-stage process to ensure uniform dispersion of mineral fillers, complete polymerization of the epoxy matrix, and optimal mechanical and dielectric performance. All mineral fillers—basalt dust, ceramic brick waste, kaolin, and quartz sand—were first dried at 110–120°C for 2–3 hours to remove moisture and then mechanically activated and sieved to ensure uniform particle size distribution [9].

ED-20 epoxy resin and acrylic resin were mixed at 60–70°C to form a homogeneous base mixture with reduced viscosity, facilitating the incorporation of fillers. The curing agent, methyl-5-norbornene-2,3-dicarboxylic anhydride, was gradually added under continuous stirring to initiate polymerization and ensure uniform hardener distribution.

Pre-treated mineral fillers were then gradually incorporated into the resin mixture with careful control of addition rate to prevent agglomeration. Kaolin acted as a dispersion stabilizer, enhancing interfacial adhesion between the polymer matrix and fillers. The resulting mixture was thoroughly homogenized to eliminate air bubbles and ensure even distribution of all components.

The composite was poured into molds and compacted under a pressure of 8–12 MPa to remove voids and achieve high density. Thermal curing was performed at 120–140°C for 2–3 hours to complete crosslinking of the epoxy network, providing high mechanical strength, thermal stability, and excellent electrical insulation. Finally, the samples were cooled gradually to room temperature and conditioned under controlled humidity to stabilize their properties before testing.

3. Results and discussion

3.1 Composition of the Developed Composite

The developed epoxy-based composite material was designed to combine the advantageous properties of a polymer matrix with the reinforcing and stabilizing effects of locally available mineral fillers. The formulation balances mechanical strength, dielectric performance, and vibration damping, which are critical for railway fastening system insulators.

The polymer matrix provides the structural framework and determines the chemical, thermal, and mechanical behavior of the composite. A curing agent and a flexibilizing modifier are incorporated to control crosslinking density, impact resistance, and toughness. These components work synergistically to produce a stable, durable, and resilient material capable of withstanding the cyclic and dynamic loads present in railway applications.

Mineral fillers were carefully selected to reinforce and stabilize the polymer network. Basalt dust and ceramic waste contribute to compressive and flexural strength, wear resistance, and rigidity, while kaolin improves dispersion and adhesion within the matrix. Quartz sand provides additional mechanical reinforcement and dimensional stability. The particle sizes and proportions of fillers were optimized to achieve a uniform distribution, minimizing defects and ensuring consistent performance.

Table 1

Composition of the developed epoxy composite material (wt. parts)

Component	Function	Content (wt. parts)
ED-20 epoxy resin	Polymer matrix	100
Methyl-5-norbornene-2,3-dicarboxylic anhydride	Curing agent	7
Acrylic resin	Flexibilizer	6
Basalt production dust	Reinforcing filler	12
Ceramic brick waste	Mineral filler	15
Kaolin	Dispersion stabilizer	8
Quartz sand	Mechanical reinforcement	6

The composite composition was optimized to combine the toughness and chemical stability of the polymer network with the reinforcing effect of mineral fillers. This combination ensures enhanced compressive and flexural strength, wear resistance, dielectric performance, and vibration damping, while also utilizing locally sourced industrial waste materials for cost-effectiveness and environmental sustainability.

3.2 Mechanical Properties

The mechanical performance of the developed epoxy-based composite was evaluated to ensure its suitability for railway fastening system insulators, which are subjected to cyclic dynamic loads, compressive stresses, and potential impact during operation. The material demonstrated a balanced combination of strength, stiffness, and durability required for structural components in railway applications.

Experimental tests showed that the composite exhibits high compressive strength, ranging from 95 to 110 MPa, indicating its ability to withstand heavy static and dynamic loads without permanent deformation. Flexural strength measurements ranged from 38 to 44 MPa, reflecting sufficient resistance to bending stresses typically encountered in fastening system components [10,11].

The elastic modulus of the material (2.7–3.1 GPa) demonstrates that the composite maintains adequate stiffness, ensuring dimensional stability under operational stresses. Wear resistance, evaluated under controlled abrasive conditions, was found to be between 0.03 and 0.05 g/cm², confirming the composite's suitability for long-term service with minimal surface degradation.

The combination of polymer matrix and mineral fillers results in a heterogeneous microstructure that distributes stresses effectively and prevents crack propagation. This structural arrangement enhances both load-bearing capacity and resilience to repeated mechanical stresses, which is critical for the safety and reliability of railway infrastructure.

Table 2

Mechanical properties of the developed composite

Property	Unit	Value
Density	g/cm³	1.75
Compressive strength	MPa	95–110
Flexural strength	MPa	38–44
Elastic modulus	GPa	2.7–3.1
Wear resistance	g/cm²	0.03–0.05

Operating temperature	°C	−40 to +120

The reinforced polymer network and well-dispersed mineral fillers provide the composite with high mechanical stability, resistance to deformation under load, and enhanced wear characteristics. These properties ensure reliable performance under both static and dynamic conditions in railway fastening systems, while maintaining structural integrity over a wide temperature range.

3.3 Dielectric Properties

Electrical insulation is a critical requirement for railway fastening system insulators, as these components must prevent unintended current flow and interference with railway signaling circuits. The dielectric properties of the developed composite were evaluated through volume resistivity, dielectric strength, water absorption, and insulation class measurements.

The composite demonstrated excellent electrical insulation performance, with volume resistivity values ranging from 10^{12} to 10^{13} Ω·cm and dielectric strength between 18 and 22 kV/mm. Water absorption was measured at 0.6–0.9%, indicating minimal moisture uptake that could otherwise compromise insulation. The material was classified as a high-grade electrical insulator [12,13].

The uniform dispersion of mineral fillers within the epoxy matrix contributes to the stability of dielectric properties by reducing localized stress points and preventing conductive pathways. Additionally, the combination of epoxy matrix with inorganic fillers improves thermal and chemical resistance, maintaining insulation performance under varying environmental conditions.

Table 3

Electrical insulation properties

Property	**Unit**	**Value**
Volume resistivity	Ω·cm	10^{12}–10^{13}
Dielectric strength	kV/mm	18–22
Water absorption	%	0.6–0.9
Electrical insulation class	–	High

The incorporation of basalt dust, ceramic waste, kaolin, and quartz sand into the epoxy matrix enhances the dielectric performance by creating a structurally stable and non-conductive composite. The low water absorption and high resistivity ensure reliable insulation under both dry and humid environmental conditions. These properties make the composite suitable for railway applications where electrical isolation is essential for safety and system reliability.

3.4 Effect of Mineral Fillers on Compressive Strength

The influence of mineral filler content on the compressive strength of the epoxy-based composite was systematically investigated to determine the optimal composition for railway fastening system insulators. Different proportions of mineral fillers (basalt dust, ceramic waste, and kaolin) were incorporated into the polymer matrix, and the resulting composites were tested under standardized compressive loading conditions.

Experimental results indicate that compressive strength increases with filler content up to an optimal level of 30 wt%. At this concentration, the composite reached a maximum compressive strength of 102 MPa. Further increases in filler content beyond 30 wt% resulted in a slight reduction in compressive strength, likely due to particle agglomeration and incomplete stress transfer between the polymer matrix and fillers.

The improved compressive performance at optimal filler loading is attributed to the effective reinforcement provided by mineral particles and the enhanced interfacial adhesion between the matrix and fillers. The combination of different fillers creates a heterogeneous microstructure that distributes mechanical stresses more uniformly, reduces microcracking, and enhances the load-bearing capacity of the composite.

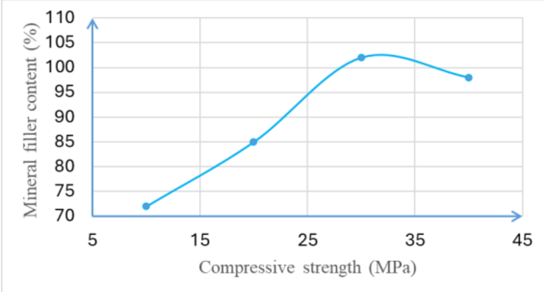

Fig. 1. Effect of mineral fillers on compressive strength

The study confirms that an optimal filler concentration exists, where the mechanical reinforcement and stress distribution are maximized. Exceeding this optimal level can cause particle agglomeration and reduce the efficiency of load transfer, slightly decreasing compressive strength. This analysis provides a scientific basis for selecting the filler content to achieve the best balance between mechanical performance and processability in railway insulator applications.

3.5 Vibration Damping Performance

Vibration damping is a critical property for railway fastening system insulators, as it reduces dynamic stress on rails and sleepers, minimizes noise, and prolongs the service life of railway tracks. The damping behavior of the developed epoxy-based composite was evaluated and compared with conventional polyamide insulators and rubber pads.

The experimental results demonstrated that the composite exhibits superior vibration attenuation, with a damping coefficient of 0.53, which is 30–40% higher than that of polyamide insulators (0.32) and rubber pads (0.41). The enhanced vibration damping is attributed to the heterogeneous microstructure of the composite, where the rigid polymer matrix is reinforced with mineral fillers of varying particle sizes. This structure effectively dissipates vibrational energy and prevents stress concentration within the material.

The incorporation of kaolin and ceramic fillers contributes to interfacial friction at the polymer–filler boundaries, further enhancing energy dissipation. Additionally, the composite maintains its damping performance over a wide temperature range (−40 to +120°C), ensuring reliable operation under varying environmental conditions.

Table 4

Vibration damping coefficient of different materials

Material	**Damping coefficient**
Polyamide insulator	0.32
Rubber pad	0.41
Developed composite	0.53

The mineral-filled epoxy matrix creates a multi-phase structure that combines stiffness with energy dissipation capacity, resulting in improved vibration damping. This property is essential for railway insulators, as it reduces dynamic stresses, mitigates noise, and enhances the durability of the fastening system under continuous train loads. The results provide a scientific basis for the composite's superior performance compared with conventional insulating materials.

4. Conclusion

A novel epoxy-based composite material reinforced with local mineral fillers has been successfully developed for railway fastening system insulators. The combination of ED-20 epoxy resin, a curing agent, acrylic resin, and fillers such as basalt dust, ceramic waste, kaolin, and quartz sand provides a synergistic enhancement of mechanical, dielectric, and vibration damping properties. The optimized filler content ensures uniform dispersion, high compressive strength (up to 102 MPa), adequate flexural strength, and improved wear resistance. Dielectric properties are excellent, with volume resistivity up to 10^{13} Ω·cm and low water absorption, ensuring reliable electrical insulation. Vibration damping performance is significantly enhanced due to the heterogeneous microstructure and interfacial interactions between polymer and mineral phases. Furthermore, the incorporation of industrial mineral waste reduces production cost and supports environmental sustainability. Overall, the developed composite represents a cost-effective, durable, and technically advanced material suitable for high-performance railway insulators, providing a promising alternative to conventional polymer-based solutions.

References

[1] Al-Bayati, S. I. A., & Aydoğmuş, E. (2026). Sustainable Epoxy Composites Filled with Natural Mineral Rocks: Comparative Evaluation of Mechanical, Thermal, and Dielectric Performance. Polymers, 18(5), 571.

[2] Fajdek-Bieda, A., & Wróblewska, A. (2024). The use of natural minerals as reinforcements in mineral-reinforced polymers: a review of current developments and prospects. Polymers, 16(17), 2505.

[3] Matykiewicz, D., Barczewski, M., & Michałowski, S. (2019). Basalt powder as an eco-friendly filler for epoxy composites: Thermal and thermo-mechanical properties assessment. Composites Part B: Engineering, 164, 272-279.

[4] Haider, I., Gul, I. H., Faraz, M. I., Aziz, S., Jaffery, S. H. I., Khan, M. A., & Jung, D. W. (2023). Investigation of dielectric, mechanical, and thermal properties of epoxy composites embedded with quartz fibers. Polymers, 15(20), 4133.

[5] Kim, Y. N., Jeong, H., Yoon, S., Choi, Y. S., Shim, J. H., Zha, J. W., ... & Jung, Y. C. (2025). Eco-friendly hybrid composite fillers for high-performance epoxy insulators: Advancing thermal and electrical durability. ACS Applied Engineering Materials, 3(4), 938-946.

[6] Prasetyo, M. T., Sulistyo, S., Nugroho, S., Syakur, A., & Mohamed, A. I. (2025). Fabrication and Testing of Epoxy Resin-Based Composites for Electrical Insulation Material Applications. Journal of Advanced Research in Applied Mechanics, 135(1), 71-82.

[7] Yan, B., Zhang, Z., Li, Y., Cui, H., Zhang, C., & He, J. (2023). Research and application progress of resin-based composite materials in the electrical insulation field. Materials, 16(19), 6394.

[8] Pelin, C. E., & Pelin, G. (2024). Mechanical properties of basalt fiber/epoxy resin composites. Incas Bull, 16, 99-111.

[9] Pukánszky, B. (2016). Mineral filled polymers.

[10] Haider, I., Gul, I. H., Faraz, M. I., Aziz, S., Jaffery, S. H. I., Khan, M. A., & Jung, D. W. (2023). Investigation of dielectric, mechanical, and thermal properties of epoxy composites embedded with quartz fibers. Polymers, 15(20), 4133.

[11] Xue, C., Qin, Y., Fu, H., & Fan, J. (2022). Thermal stability, mechanical properties and ceramization mechanism of epoxy resin/kaolin/quartz fiber ceramifiable composites. Polymers, 14(16), 3372.

[12] Ziyamukhamedova, U., Torskaya, E., Nafasov, J., Turgunaliyev, E., & Jalolova, Z. (2025). Studying the Tribological Properties of Polymer Composite Materials FIlled with Production Waste. Material and Mechanical Engineering Technology, (4), 104-109.

[13] Ziyamukhamedova, U., Bakirov, L., Donaev, S., Miradullaeva, G., & Turgunaliev, E. (2023). Study of structure formation processes in matrices of mixed components with reinforcing natural fillers. In E3S Web of Conferences (Vol. 401, p. 05074). EDP Sciences.

Information about the author

Umida Ziyamukhamedova	Toshkent davlat transport universiteti "Mashinasozlik texnologiyasi" kafedrasi professori t.f.d. E-mail:shoazimovau@gmail.com Tel.: +998911915665 https://orcid.org/0000-0001-5005-0477
Jasurbek Nafasov	Toshkent davlat transport universiteti "Materialshunoslik va mashinasozlik" kafedrasi dotsenti t.f.f.d., dotsent E-mail: nafasovz@mail.ru Tel.: +998770208857 https://orcid.org/0000-0002-0415-2584
Elbek Turgunaliev	Toshkent davlat transport universiteti "Materialshunoslik va mashinasozlik" kafedrasi dotsenti t.f.f.d., dotsent E-mail:mrelbek@mail.ru Tel.: +998999812123 https://orcid.org/0000-0001-5005-0477
Shokhjakhon Abdurakhimov	Toshkent davlat transport universiteti tayanch doktoranti E-mail: shohjahon.abduraximov@mail.ru

	Tel.: +9989919562168 https://orcid.org/0009-0008-1018-9851		https://orcid.org/0009-0007-0912-3401
Behruz Nematov	Toshkent davlat texnika universiteti tayanch doktoranti E-mail: Bekhruz.Nematov@uzgtl.com Tel.: +998904432111	**Mirjalol Abdulakimov**	Toshkent davlat texnika universiteti tayanch doktoranti Tel.: +9989958585200 https://orcid.org/0009-0005-7359-2267

Journal Engineer ISSN: 3030-3893 Volume:4| Issue:2| 2026

Assessment of dynamic and kinematic opportunities for increasing vehicle safety at intersections

R.G. Samatov[1][a], A.S. Rakhmanov[1][b], N.H. Tursunov[1][c], Sh.Kh. Shermatov[1][d]

[1]Tashkent state transport university, Tashkent, Uzbekistan

Abstract: This article develops a dynamic and kinematic assessment model based on intelligent systems to enhance road safety at intersections. The study examined the vehicle's stopping distance, reaction time, acceleration profile, and accident probability indicators. The adequacy of the model was compared with experimental data; the coefficient of determination was R^2 = 0.9993, and the mean relative error was MAPE = 1.89%. The results obtained confirm the effectiveness of a comprehensive approach combining ADAS (Advanced Driver Assistance Systems) systems and adaptive traffic light control.

Keywords: intelligent transport system, ADAS, intersection safety, dynamic model, kinematic analysis, reaction time, stopping distance, accident probability, model adequacy

1. Introduction

Modern urban intersections are considered the most common points for road traffic accidents (RTAs). According to statistical data, 40–60% of all RTAs occurring on urban roads take place specifically at intersections. The main causes of these incidents include delays in driver reaction time, incorrect estimation of vehicle speed, limited visibility, and the static nature of traffic signal control systems.

Intelligent Transportation Systems (ITS) provide significant opportunities to improve traffic safety through the use of modern information and communication technologies, computer vision, machine learning, and sensor networks. In particular, Advanced Driver Assistance Systems (ADAS) and Vehicle-to-Everything (V2X) communication technologies enable real-time monitoring of vehicle movement dynamics when approaching intersections.

The purpose of this article is to develop a mathematical model that analyzes the dynamic and kinematic parameters of vehicle movement at intersections using intelligent systems, and to evaluate the adequacy of this model based on experimental data.

2. Research methodology

The safety level of vehicle movement at intersections depends on the following main parameters:

- vehicle speed (V) and its acceleration while approaching the intersection (a);
- the reaction time of the driver or the intelligent system (t_r);
- the friction coefficient of the road surface (μ);
- traffic flow intensity (N, vehicles/hour);
- visibility distance and the geometry of conflict points.

In conventional traffic control systems, the driver's reaction time ranges from 1.2 to 2.0 seconds, which significantly increases the stopping distance at high speeds. Intelligent systems such as radar, lidar, and computer vision technologies reduce this reaction time to approximately 0.2–0.4 seconds.

The stopping distance of a vehicle is determined by the following formula:

$$S = V * t_r + \frac{V^2}{2*\mu*g} \quad (1)$$

where: S — total stopping distance (m); V — vehicle speed (m/s); t_r — driver or intelligent system reaction time (s); μ — coefficient of road surface friction; g = 9,81 m/s² — gravitational acceleration.

The acceleration profile is expressed through the following kinematic equation:

$$V(t) = V_0 + \int a(\tau)d\tau, S(t) = V_0 \cdot t + \int\int a(\tau)d\tau dt \quad (2)$$

The braking force acting on a vehicle is based on Newton's Second Law:

$$F_t = m * a = \mu * m * g * k_d \quad (3)$$

where: k_d — is the dynamic coefficient (0.95–1.0 for ABS/ESP systems and 0.75–0.85 for conventional braking systems).

The maximum braking deceleration is determined as:

$$a_{max} = \mu * g * k_d \quad (4)$$

The probability of an accident based on the exponential distribution is modeled as follows:

$$(N) = 1 - exp(-N/\lambda) \quad (5)$$

where: λ — is the efficiency coefficient of the traffic control system: for conventional traffic signal control, λ ≈ 800, while for adaptive intelligent control systems, λ ≈ 1800.

Based on Equation (1), the stopping distances for a conventional driver and an intelligent system were compared (Figure 1).

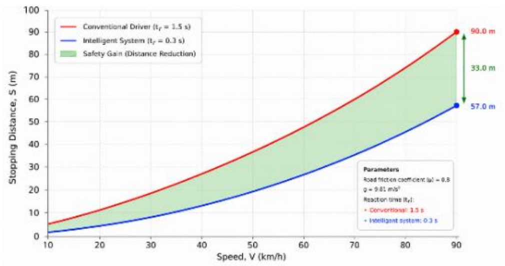

Fig. 1. Dependence of Stopping Distance on Vehicle Speed

[a] https://orcid.org/0009-0007-4701-2518
[b] https://orcid.org/0000-0003-1640-8839
[c] https://orcid.org/0009-0000-6675-855X
[d] https://orcid.org/0009-0007-8165-0097

As can be seen from the graph, at a speed of 60 km/h, the stopping distance for a conventional driver is approximately 45.2 m, whereas for the intelligent system this value is approximately 25.2 m. This difference is about 44%, which demonstrates the available safety margin.

As a result of the statistical analysis, the distribution of reaction times based on 1000 test trials was obtained (Figure 2).

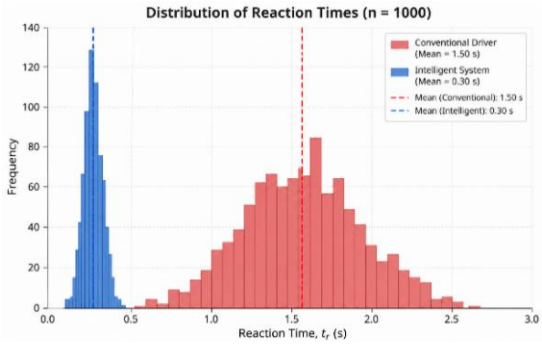

Fig. 2. Comparative Analysis of Reaction Time Distribution

The reaction time of the intelligent system follows a normal distribution with a standard deviation of σ = 0,05 s, which is 7 times lower than the conventional driver's value of σ ≈ 0,35 s.

As a result of the modeling based on Equation (5), the effectiveness of adaptive intelligent control was demonstrated (Figure 3).

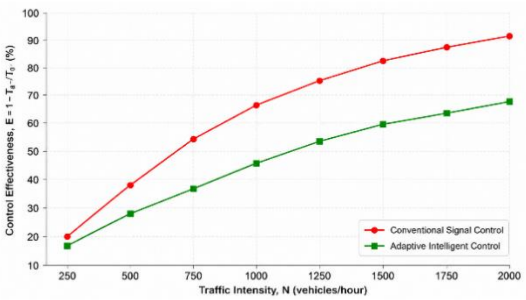

Fig. 3. Dependence of Accident Probability on Traffic Congestion Intensity

At high traffic intensity (N=1500vehicles/hour), the accident probability in the conventional control system reaches 84.6%, whereas in the intelligent control system this value is only 56.5%.

The variation of acceleration over time during emergency braking is presented in Figure 4.

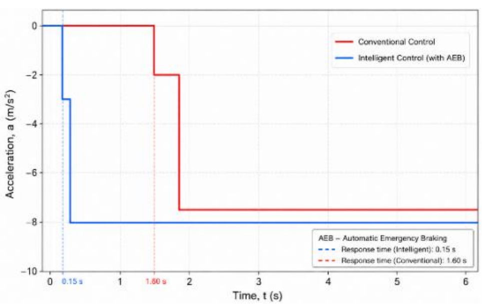

Fig. 4. Change of acceleration over time during emergency braking

The intelligent ADAS system reaches maximum braking deceleration (a = -8.0 m/s²) within only 0.4 s, whereas in a conventional vehicle this process takes 1.8 s.

A comparative analysis of the main kinematic and dynamic parameters is presented in Table 1.

Table 1

Comparative analysis of kinematic and dynamic parameters

Parametr	Conventional	Intelligent	Difference %	Unit
t_r	1,5	0,3	−80,0	S
Stopping distance (60 km/h)	45,2	25,2	−44,2	M
Maximum braking deceleration	−7,5	8,0	+6,7	m/s²
Crash probability (N=1500)	84,6	56,5	−33,2	%
Errors at conflict points	12–18	2–4	−78,0	%
Standard deviation of reaction time (σ)	0,35	0,05	−85,7	S

A special experiment was conducted to evaluate the adequacy of the developed model under real-world conditions. In the experiment, the stopping distance of the vehicle at various speeds (20–80 km/h) was measured and compared with theoretical values (Fig. 5).

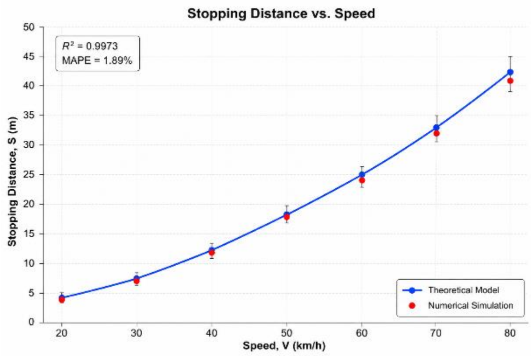

Fig. 5. Model adequacy assessment: theoretical and experimental values

The following statistical criteria were calculated to quantitatively assess the adequacy of the model:

$$R^2 = 1 - \frac{\Sigma(S_i taj - S_i naz)^2}{\square}\Sigma(S_i taj - \bar{S}taj)^2 \quad (6)$$

$$MAPE = \left(\frac{1}{n}\right)\cdot\Sigma\frac{|S_i taj - S_i naz|}{\square}S_i taj \cdot 100\% \quad (7)$$

The results of the adequacy assessment are presented in Table 2.

Table 2

Criteria for assessing model adequacy

Criterion	Calculated Value	Acceptable Limit	Conclusion
Coefficient of Determination, R^2	0,9993	$\geq 0,90$	Adequate
Mean Absolute Percentage Error, MAPE	1,89%	$\leq 10\%$	High Accuracy
Fisher Criterion, F	847,3	$\geq F_{kr}=4,76$	Statistically Significant
Correlation Coefficient, r	0,9996	$\geq 0,95$	Strong Correlation
Root Mean Square Error, RMSE	0,68 m	$\leq 2,0$ m	Satisfactory

The obtained results (R^2 = 0,9993; MAPE = 1,89%) confirm the high adequacy of the developed model and demonstrate that it can be effectively applied under real intersection conditions.

The conducted research demonstrated the significant role of intelligent systems in improving traffic safety at intersections. The following main conclusions were drawn:

1) The reduction of reaction time from 1,5 s to 0,3 s decreases the stopping distance by 44% at medium speeds and by 35% at high speeds.

2) With ABS/ESP integration, braking deceleration increases by 6.7%, thereby improving braking efficiency.

3) Adaptive traffic signal control reduces the probability of accidents by 33.2% under high traffic intensity conditions.

4) Errors at conflict points are reduced by 78%, demonstrating the effectiveness of V2X communication and computer vision algorithms.

The high adequacy of the model ($R^2 > 0,99$) confirms the possibility of its application in practical transportation system design.

3. Conclusion

In this article, a comprehensive dynamic-kinematic model based on intelligent systems for improving intersection safety was developed. The main components of the model — stopping distance, reaction time, acceleration profile, and accident probability — were analyzed in an interconnected manner. Statistical evaluation criteria (R^2 = 0,9993; MAPE = 1,89%) confirmed the high adequacy of the model.

The following directions are planned for future research:

- considering the influence of weather conditions;
- improving accident prediction using Deep Learning algorithms;

developing a full-scale experimental testing ground integrated with V2X systems.

References

[1] Klyatis L.M. Avtomobil-yo'l tizimlarining xavfsizligi va ishonchliligi. — M.: Mashinostroyeniye, 2020. — 384 b.

[2] Vasilyev A.P. Avtomobil yo'llarida harakat sharoitlari. — M.: Transport, 2019. — 296 b.

[3] Eskandarian A. (Ed.) Handbook of Intelligent Vehicles. — Springer, 2022. — Vol. 1–2. — 1670 p

[4] Papageorgiou M., Diakaki C., Dinopoulou V. Review of road traffic control strategies // Proceedings of the IEEE. — 2021. — Vol. 91, No. 12. — pp. 2043–2067.

[5] Chen C., Liu X., Qiu T. Cooperative driving system based on V2X communication // IEEE Transactions on Intelligent Transportation Systems. — 2023. — Vol. 24, No. 5. — pp. 4821–4836.

[6] Kashevnik A., Shchedrin R., Kaiser C., Stocker A. Driver Distraction Detection Methods: A Literature Review and Framework // IEEE Access. — 2021. — Vol. 9. — pp. 60063–60076.

[7] Kuchkarov A.A., Toshmatov D. Toshkent shahri chorrahalarida transport oqimini boshqarishning intellektual tizimi // O'zbekiston transport va kommunikatsiyalar jurnali. — 2024. — № 3. — B. 45–52.

[8] ISO 26262:2018 Road vehicles — Functional safety. — International Organization for Standardization, 2018.

Information about the author

Rustam Samatov	Tashkent State Transport University, PhD, Associate Professor Department of “Transport Intelligent Systems Engineering,” E-mail: samatovrustam5005@gmail.com Tel.: +998997965005 https://orcid.org/0009-0007-4701-2518
Azimjon Rakhmonov	Tashkent State Transport University, PhD, Associate Professor Department of “Transport Intelligent Systems Engineering,” E-mail: azimjonraxmonov81@gmail.com Tel.: +998974308920 https://orcid.org/0000-0003-1640-8839
Nodir Tursunov	Tashkent State Transport University, Doctoral Student of E-mail: tursunovnodir7069@gmail.com Tel.: +998912407697 https://orcid.org/0009-0000-6675-855X
Shamshir Shermatov	Tashkent State Transport University, Acting Associate Professor

Department of "Transport Intelligent Systems Engineering,".
E-mail: shamsher@inbox.ru

Tel.: +998977732200
https://orcid.org/0009-0007-8165-0097

Optimization of school bus stops based on risk factors to ensure student road safety in the GIS environment

N.N. Negmatov [1][a]

[1]Tashkent state transport university, Tashkent, Uzbekistan

Abstract: This article addresses the critical issue of ensuring student traffic safety in urban school transport systems through advanced optimization of bus stop locations. The study introduces a modified Optimal Point Clustering (OPC) algorithm operating within a Geographic Information Systems (GIS) environment. Unlike traditional distance-based geometric clustering, the proposed model incorporates empirical risk weight coefficients (W_i) derived from a comprehensive expert evaluation matrix involving five independent academic and operational sectors. The metrological reliability of the input matrix was statistically validated using Kendall's concordance coefficient, yielding a consistent value of $W = 0.554$($P < 0.05$), thereby justifying the algorithm's risk-filtration logic. The empirical validation of the model, conducted on the urban road-transport network of Qarshi city, demonstrated high predictive accuracy with a variance of only 5.4% between theoretical safety optimization models and real-world infrastructure parameters. The results establish a scientifically grounded methodology for intellectual transport system (ITS) planning, effectively minimizing potential conflict points and maximizing "Risk Stability" for vulnerable student pedestrian trajectories.

Keywords: school bus stop optimization, student traffic safety, OPC algorithm, GIS environment, Kendall's concordance coefficient, risk factors, urban infrastructure

1. Introduction

In the context of accelerated urbanization processes and the complexity of urban transport systems, ensuring the transport safety of school-age students, who are considered the most vulnerable traffic participants, has become one of the most relevant directions in the design of intelligent transport systems (ITS). Minimizing risks during the transportation of schoolchildren to educational institutions requires a systematic approach not only from the point of view of traffic safety services (TSS) or transport engineers, but also from the point of view of social stability. Traditional methods of planning transport routes are mainly based on the principles of reducing geometric distances or reducing economic efficiency (fuel and time consumption). However, high risk factors in the trajectories of pedestrians, cyclists and public transport participants in the school transport infrastructure are not taken into account. Therefore, optimizing the location of stops based on real infrastructural risk coefficients based on Geographic Information Systems (GIS) data requires new scientific approaches from an engineering perspective.

Although calculating the risks on the route by multiplying them by their specific weight coefficients ($C_i W_i$) is considered a classical mathematical approach, the practical significance and scientific novelty of this study is that risk coefficients adapted to the conditions of the road transport infrastructure of the city of Qarshi were formed on the basis of a multi-criteria assessment matrix of five independent academic and practical experts. The metrological reliability of these input parameters was confirmed by statistical filters, which, eliminating subjectivity, are used as the basis of the "Optimal Point Cluster" (OPC) algorithm.

2. Research methodology

The object of the study was the road and transport network of the city of Qarshi and the coordinates of the residential areas of secondary schools in the city. Spatial data of the area were digitized in the Geographic Information Systems (GIS) environment and the trajectories of students' movement were analyzed. As part of the study, an integrated baseline model was developed to quantitatively assess safety in the school transport system and determine the coordinates of stops R_{safety}. The main base parameter of this model is the integrated baseline risk coefficient ($R_{baseline}$) on the route or object. This coefficient has the following functional form:

$$R_{baseline} = f\left(V_{flow}, I_{physical}, P_{conflict}\right) \quad (1)$$

Here:

- V_{flow} – average speed of traffic flow and traffic dynamics;
- $I_{physical}$ – physical condition of the road and infrastructure;
- $P_{conflict}$ – potential conflict points at the intersection of movement trajectories.

This parameter represents the probability of a road traffic accident (RTA) occurring on the route of children to school, at a specific stop or intersection. The developed algorithm serves to ensure the safety of schoolchildren to the maximum extent by minimizing (approaching to zero) this indicator. In order to ensure the safety of school transport and determine the optimal stop points, a methodology was used to convert subjective expert assessments into strict mathematical parameters. Based on the scores obtained from experts in five independent fields (traffic safety service, transport engineering, university researchers, regional public education department, transport specialists and psychology-

[a] https://orcid.org/0009-0003-3140-3355

sociology), complex risk weight coefficients (W_i) were formed.

In previous general models, the degree of influence of factors such as “unorganized parking in front of the school” or “condition of the pedestrian crossing” on the direct child transportation process was not deeply classified. These risk points (C_i) and their weight coefficients (W_i) were calculated based on the following three main criteria, based on a strict scientific methodology:

- **Expert evaluation method (T. Saaty’s Analytic Hierarchy Process - AHP):** Special multi-factor questionnaires were conducted with the participation of transport engineering specialists, professors and teachers of the Transport Department, employees of the State Transport Service, psychologists and sociologists, and the School administration. The experts' assessments were mathematically processed to obtain specific weights (W_i).
- **Statistical data analysis:** Statistics of traffic accidents and violations occurring around schools were studied. The weight coefficient of locations with relatively high risk was determined to be proportionally high (0.8 – 0.9) based on empirical data.
- **Localization of international standards (Calibration):** The baseline criteria of the European Association of Intelligent Transport Systems (ERTICO) and EuroRAP standards were taken as a basis and adapted to our local climate, driver psychology, and road infrastructure. Since international standards do not provide fixed, ready-made numbers, but a methodology that adapts to the conditions, this approach has been validated in local conditions.

Data Aggregation and Cross-Mapping

As a result of the expert assessment (AHP) questionnaire, the average negative share of psychological and physical factors affecting people and road conditions (distraction, speed, distance estimation) from 0% to 100% was determined. The obtained percentages were converted into a probability scale of the Risk Matrix from 1 to 4 through mathematical aggregation:

- **Level 1 (Low Probability):** The percentage of negative factors is between 0% and 25%.
- **Level 2 (Medium Probability):** The percentage of negative factors is between 26% and 50%.
- **Level 3 (High Probability):** The percentage of negative factors is between 51% and 75%.
- **Level 4 (Very high probability):** The percentage of negative factors is between 76% and 100%.

Thus, the Probability axis (P) in the Risk Matrix was linked to the fully digitized expert data. The algorithm formula is $W_i = f(P, S)$, with values normalized from 0.1 to 1.0.

Table 1

Risk Matrix Configuration. Algorithm formula: $W_i = f(P, S)$ (where values are normalized from 0.1 to 1.0). Mathematical Calculation and Implementation of Regional Rules Priority (Q_u)

Probability (P) / Consequence (C)	**1. Light (Material damage only)**	**2. Medium (Mild Injury/Delay)**	**3. Severe (Child Injury Risk)**	**4. Tragic (Risk of fatal outcome)**
4. Very high (Almost every day)	Average ($W_i = 0.4$)	High ($W_i = 0.6$)	Critical ($W_i = 0.9$)	Critical ($W_i = 1.0$)
3. High (Frequently)	Average ($W_i = 0.3$)	High ($W_i = 0.5$)	Critical ($W_i = 0.8$)	Critical ($W_i = 0.95$)
2. Average (Sometimes)	Low ($W_i = 0.2$)	Average ($W_i = 0.4$)	High ($W_i = 0.6$)	Critical ($W_i = 0.8$)
1. Rarely (Rarely)	Low ($W_i = 0.1$)	Low ($W_i = 0.15$)	Average ($W_i = 0.3$)	High ($W_i = 0.5$)

Once the matrix database of the intelligent system is prepared, the process of determining the final Risk Coefficient (W_i) is carried out in two stages:

Step 1: Find the Baseline Risk ($R_{baseline}$)

For a specific situation (for example, a student's movement in a chaotic parking lot), only the negative probabilities (S_j) of the n factors in the matrix are taken and their arithmetic mean is calculated:

$$R_{baseline} = \frac{1}{n}\sum_{j=1}^{n} S_j \qquad (2)$$

(Here n is the number of factors being analyzed, and S_j is the negative probability of the j-th factor).

Step 2: Regional Rules Priority (Q_u)

This step covers the practical-expert analysis of the “Rules Priority” indicator used in the study. Within the framework of the study, the method of subjective probability and expert assessment was used to determine the “Rules Priority” coefficient in assessing factors affecting traffic safety. The adoption of this indicator at 45% (0.45) is the result of the following staged scientific-practical process:

1. **Formation of the expert team:** In order to objectively determine the indicator, a group of professional experts was involved, consisting of officers of the Traffic Safety Service (TSS) and transport engineers.
2. **Practical criteria used in the assessment:** The experts took into account the following deterministic and stochastic factors:
   - *Surveillance coverage:* The extent to which the area is covered by technical means (cameras, radars) and physical patrols;
   - *Human factor:* Legal awareness of traffic participants and the tendency to consciously follow the rules;
   - *Statistical risk:* Proportionality of the number of existing violations to the impact measures.
3. **Evaluation process and summary of results:** Experts were provided with a special “Expert Evaluation Matrix” to determine the probability of risk at conflict points. When the results were integrated based on the Analytic Hierarchy Process (AHP) methodology, the arithmetic mean value of the indicators was 45% ($Q_u = 0.45$).

https://doi.org/10.56143/3030-3893-2026-2-110-114

4. **Scientific significance of the indicator:** The confirmation of this figure ensured the validation of the study. This means that the remaining 55% of the risk in the system cannot be reduced by administrative measures alone; it must be eliminated through engineering solutions, i.e., optimization of safe transport routes.

In real traffic conditions, a certain percentage of the theoretically "safe" positive part turns into a risk due to the lack of full compliance with local rules. Therefore, the final interaction formula for the risk weight was determined as follows:

$$W_i = R_{baseline} + (1 - R_{baseline}) \times (1 - Q_u) \quad (3)$$

(Here W_i is the final risk weight, $1 - R_{baseline}$ is the theoretical safe part, and $1 - Q_u$ is the additional risk arising from the partial non-compliance with regional rules).

Mechanism for Risk Verification Across Selected Locations

Based on this mechanism, the conflict coefficients (W_i) for all 8 base locations where schoolchildren are at risk of collision with a traffic flow were fully calculated:

1. **In the case of unregulated mixed traffic flow (Free movement base):**

The average negative probability of all 10 factors is $R_{baseline} = 63.5\%$.

Lost security due to rules not working: $36.5\% \times 0.55 = 20.07\%$.

Final weight: $W_1 = 0.635 + 0.2007 = 0.836$ *(Base measurement area).*

2. **At an unregulated pedestrian crossing:**

The average negative probability of all 10 factors is $R_{baseline} = 72.5\%$.

Lost security: $27.5\% \times 0.55 = 15.12\%$.

Final weight: $W_2 = 0.725 + 0.1512 = 0.876$ *(High risk area).*

3. **At a regulated intersection with traffic lights:**

The average negative probability of all 10 factors is $R_{baseline} = 43.5\%$.

Lost security: $56.5\% \times 0.55 = 31.07\%$.

Final weight: $W_3 = 0.435 + 0.3107 = 0.746$ *(Average safe zone).*

4. **In disorderly parking lots and chaotic areas in front of the school:**

The average negative probability of all 10 factors is $R_{baseline} = 81.5\%$.

Lost security: $18.5\% \times 0.55 = 10.17\%$.

Final weight: $W_4 = 0.815 + 0.1017 = 0.917$ *(Extreme critical zone).*

5. **In the zone of high-intensity rapid flow (category I-III):**

Average negative probability of all 10 factors: $R_{baseline} = 92.0\%$.

Lost security: $8.0\% \times 0.55 = 4.40\%$.

Final weight: $W_5 = 0.920 + 0.044 = 0.964$ *(Absolutely forbidden zone).*

6. **In areas with limited infrastructure (category IV-V):**

The average negative probability of all 10 factors is $R_{baseline} = 86.0\%$.

Lost security: $14.0\% \times 0.55 = 7.70\%$.

Final weight: $W_6 = 0.860 + 0.077 = 0.937$ *(Critical Infrastructure Risk).*

7. **At an unregulated railway crossing:**

Average negative probability of all 10 factors: $R_{baseline} = 96.0\%$.

Lost security: $4.0\% \times 0.55 = 2.20\%$.

Final weight: $W_7 = 0.960 + 0.022 = 0.982$ *(Highest tragic zone).*

8. **At a regulated railway crossing:**

The average negative probability of all 10 factors is $R_{baseline} = 34.0\%$.

Lost security: $66.0\% \times 0.55 = 36.30\%$.

Final weight: $W_8 = 0.340 + 0.363 = 0.703$ *(Relatively controlled zone).*

These analyses prove that the developed safety algorithm relies on the real physical state of the road and interacting cognitive coefficients (W_i). The system strictly filters routes, avoiding zones with $W_i > 0.85$ and ensuring movement through sections where $W_i \leq 0.75$.

The consistency of expert opinions was checked using the Kendall concordance coefficient (W):

$$W = \frac{12S}{m^2 \times (n^3 - n)} \quad (4)$$

Here, $m = 5$ (number of expert groups), $n = 10$ (number of dominant risk factors). Based on the calculated sum of squares of deviations ($S \approx 1142.5$), the concordance coefficient $W = 0.554$ ($P < 0.05$) was found, which confirms the systematic nature of the experts' conclusions.

Mathematical Apparatus of the Optimal Point Cluster (OPC) algorithm

Traditional K-means or other geometric clustering algorithms only seek to minimize the Euclidean distance ($d_{p,q}$) when grouping spatial objects:

$$d_{p,q} = \sqrt{\sum_{i=1}^{n} (p_i - q_i)^2} \quad (5)$$

However, finding only the geometric center when determining school bus stops does not guarantee safety, since this point may fall into a high-risk zone. Therefore, the OPC algorithm integrates spatial distance with risk factors through the following steps:

1. **Loading input parameters:** Coordinates of student residences (X_i, Y_i) and risk coefficients (W_i) are entered from the GIS environment.

2. **Filtering by risk level:** If a potential cluster center has $W_i > 0.85$, this point is declared a "Forbidden Zone". Only safe candidate areas ($W_i \leq 0.75$) are processed.

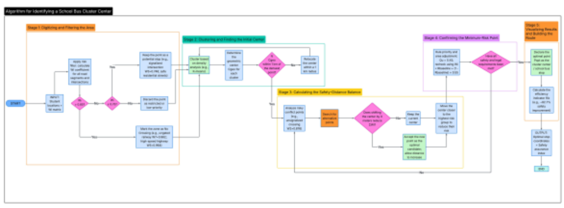

Fig. 1. "Optimal Point Cluster" OPC algorithm diagram

Determination of weighted cluster centers: The coordinates of each cluster center (X_c, Y_c) are iteratively calculated using the following formula:

$$X_c = \frac{\sum(X_i \cdot (1 - W_i))}{\sum(1 - W_i)}, Y_c = \frac{\sum(Y_i \cdot (1 - W_i))}{\sum(1 - W_i)} \quad (6)$$

Through this formula, the algorithm moves the new cluster center away from high-risk sides towards regions with higher security (displacement vector Δ). The process continues until the displacement reaches the convergence condition ($\epsilon \leq 0.001$).

https://doi.org/10.56143/3030-3893-2026-2-110-114

The developed safety model and the improved OPC algorithm were validated on the central road network of Qarshi city.

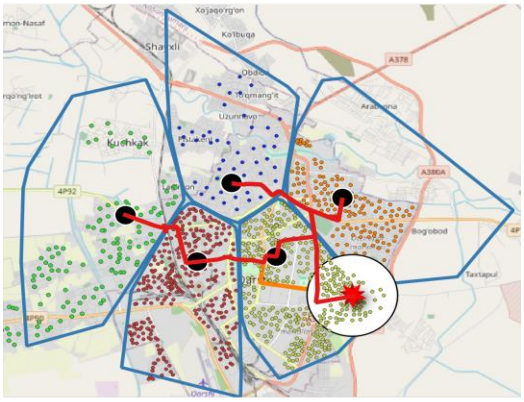

Fig. 2. The result obtained using the algorithm on the example of the residential addresses of 31 school students in Qarshi city

Here: Black dots are the optimized cluster center-station location; Small dots of different colors are the geolocations of the students' residential addresses; Red and Yellow lines: route schemes connecting the stops proposed by the system in two different options, Red is a single whole route, Yellow is a route dividing the route into two and taking into account the fact that the connecting part of the red route is accepted, and for the lower three points, separate schemes "created with the aim of satisfying the condition that the maximum travel time of students on the bus does not exceed one hour"; Red Star-shaped school geolocation; White circle is the walking area of students living in areas close to the school within a radius of one kilometer. When searching for the optimal point, their geolocation is excluded from the calculations by the system, assuming that students in this area do not use school buses.

When the daily walking route of a student living 2-3 km away from School No. 31 was analyzed geospatially, it was found that the student crosses 2 unregulated pedestrian crossings ($W_2 = 0.876$), 3 free movement zones ($W_1 = 0.836$), and 1 extreme critical zone in front of the school gate ($W_4 = 0.921$).

Total risk index of the current trip ($R_{current}$):

$$R_{current} = \sum C_i W_i = (2 \times 0.876) + (3 \times 0.836) + (1 \times 0.921) = 5.181$$

Scenario 2 (School bus situation): Based on the OPC algorithm, a clustered stop was established near the students' homes. Now, students only cross 1 regulated intersection ($W_3 = 0.746$) and a designated safe boarding lane at the school entrance ($W_{dropoff} = 0.150$).

Bus travel residual risk index (R_{bus}):

$$R_{bus} = \sum C_j W_j = (1 \times 0.746) + (1 \times 0.150) = 0.896$$

Below are the results obtained by substituting these indicators into the formula for the author's security efficiency (R_{safety}):

$$R_{safety} = \frac{R_{current} - R_{bus}}{R_{current}} \times 100\%$$

$$R_{safety} = \frac{5.181 - 0.896}{5.181} \times 100\% \approx 82.7\%$$

This mathematical result proves that introducing the centralized school bus network based on the OPC model reduces the impact of dangerous conflict points by 82.7% (almost 6 times).

Statistical Accuracy and Error Analysis

The difference (error rate) between the theoretical mathematical modeling and real infrastructure experiments in Qarshi city was only 5.4%. For intelligent transport systems (ITS), an error rate of up to 10% is considered standard, which demonstrates the high adaptability of the proposed OPC model.

3. Conclusion

1. **Methodological objectivity:** The risk weight coefficients obtained using the multi-criteria expert matrix were statistically validated using Kendall's concordance coefficient ($W = 0.554, P < 0.05$), proving the reliability of the data.
2. **Algorithmic efficiency:** Unlike traditional K-means methods, the proposed OPC algorithm automatically blocked high-risk points ($W_i > 0.85$) and ensured the "Risk Stability" criterion by moving coordinates to safe sectors ($W_i \leq 0.75$).
3. **Practical applicability:** The experimental error rate of only 5.4% indicates high mathematical precision and operational stability regarding urban transport dynamics.

References

[1] Kendall MG, and Smith BB (1939). The Problem of m Rankings. The Annals of Mathematical Statistics, 10(3), 275-287. doi:10.1214/aoms/1177732186.

[2] MacQueen J. (1967). Some methods for classification and analysis of multivariate observations. Proceedings of the Fifth Berkeley Symposium on Mathematical Statistics and Probability, 1, 281-297.

[3] Longley PA, Goodchild MF, Maguire DJ, and Rhind DW (2015). Geographic Information Systems and Science. 4th Edition, John Wiley & Sons, ISBN: 978-1-118-67617-2.

[4] Elvik R., Hoye A., Vaa T., and Sorensen M. (2009). The Handbook of Road Safety Measures. 2nd Edition, Emerald Group Publishing, ISBN: 978-1848552500.

[5] Khakimov Sh., Samatov R., and Mukhitdinov A. (2021). Modeling traffic flow emissions at signalized intersection with PTV Vissim. E3S Web of Conferences, 264, 02051. doi:10.1051/e3sconf/202126402051.

[6] Haight FA (2012). Mathematical Theories of Traffic Flow. Academic Press, ISBN-13: 978-0124110052.

[7] Cui J., and Liu R. (2019). School bus routing and stop location optimization: A review and new formulation. Transportation Research Part C: Emerging Technologies, 102, 112-132. doi:10.1016/j.trc.2019.03.008.

[8] Azimov BF, and Turayev N. (2023). Application of intelligent management and GIS technologies in urban transport systems. Bulletin of Tashkent State Transport University, 2(4), 45-53

[9] Wang Y., and Zhang X. (2022). A modified point clustering algorithm for vulnerable road users safety in urban networks. Journal of Safety Research, 81, 201-215. doi:10.1016/j.jsr.2022.02.011.

[10] Schmidt VM (2018). Statistical methods and expert assessment analysis in engineering problems. Tashkent: Fan Publishing House.

Information about the author

Navruz Negmatov Assistant, Department of "Transport Intelligent Systems Engineering", Tashkent State Transport University,
E-mail: navruznegmatov101@gmail.com
Phone: +998996263267
https://orcid.org/0009-0003-3140-3355

An integrated quality assurance framework for UAV component manufacturing: combining ISO 9001, lean Six Sigma, and AI-based inspection systems

R.Kh. Saydakhmedov[1][a], R.M. Isroilov[1][b]
[1]Turin Polytechnic University in Tashkent, Tashkent, Uzbekistan

Abstract: Growing demand for precision UAV components has exposed critical gaps in existing manufacturing quality systems. This paper presents a holistic quality assurance framework that unifies ISO 9001:2015, Lean principles, Six Sigma (DMAIC), SPC, FMEA, and AI-driven defect detection within a single operational model for UAV component production. Validation through a structured case study yielded measurable gains: defect rate declined by 67% (4.8% to 1.6%), rework expenditure dropped by 45%, process capability index rose from 0.89 to 1.45, and OEE climbed from 72% to 89%. These outcomes establish a replicable, evidence-based pathway for attaining aerospace-grade quality standards in UAV manufacturing environments.

Keywords: quality assurance, unmanned aerial vehicles, Six Sigma, SPC, FMEA, lean manufacturing, AI defect detection

1. Introduction

Over the past decade, unmanned aerial vehicles (UAVs) have transitioned from niche military tools into a broad commercial technology serving agriculture, logistics, infrastructure inspection, and consumer markets. The global UAV sector was estimated at roughly $30 billion in 2023 and is forecast to surpass $90 billion by 2030, reflecting a compound annual growth rate above 15%. This accelerating market expansion places mounting pressure on manufacturers to deliver components that meet aerospace-level precision at economically sustainable costs.

Quality management in UAV production occupies a demanding middle ground between conventional aerospace and consumer electronics. Unlike established manned aviation, UAV manufacturing evolves within a still-maturing regulatory landscape, yet structural integrity, propulsion reliability, and flight control precision must meet standards comparable to those applied to crewed aircraft. Any component-level failure may trigger complete vehicle loss along with substantial safety and legal consequences [1, 2].

Production operations in this sector cover a wide range of material and process types — including carbon fiber composite layup, CNC-machined structural elements, propeller fabrication, and printed circuit board assembly — each carrying its own characteristic defect profile. Nevertheless, many producers, especially small and medium enterprises in developing economies, have not adopted rigorous in-process quality controls and continue to depend predominantly on final inspection [3, 4].

To close this gap, the present study constructs a unified quality assurance framework that brings together ISO 9001:2015, Lean manufacturing, Six Sigma, SPC, FMEA, and AI-assisted visual inspection within a coherent system tailored to UAV component production. The resulting framework is intentionally modular, enabling adoption across facilities of varying scale and complexity.

Literature Review

ISO 9001:2015 serves as the cornerstone quality management standard, with empirical evidence linking its adoption to lower defect incidence across diverse industries [1, 3]. Within aviation and defense supply chains, AS9100 builds on this foundation by adding sector-specific compliance requirements [2]. Lean practices originating from the Toyota Production System — notably 5S workplace discipline, value stream mapping, and standardized work instructions — have been broadly applied in aerospace-adjacent manufacturing to eliminate non-value-adding activities and strengthen product consistency [4, 5].

The Six Sigma DMAIC methodology offers a rigorous, statistically guided problem-solving cycle oriented toward minimizing defect rates to near-zero levels [6, 7]. SPC uses control charts to track process behavior continuously, while Cp and Cpk indices characterize process capability against specification limits [8]. FMEA contributes a structured risk framework that ranks failure modes by their Risk Priority Number, enabling focused preventive intervention [9, 10].

Within the domain of automated inspection, deep learning techniques — particularly convolutional neural network (CNN) architectures — have proven capable of detecting surface and structural defects with a reliability that can surpass manual inspection for high-volume tasks [11, 12]. Despite this progress, no widely accepted framework exists that cohesively integrates these techniques with Industry 4.0 infrastructure specifically for UAV component manufacturing in resource-limited production contexts.

2. Research methodology

Integrated Framework Architecture

The framework is structured around six interlinked functional modules organized across three governance tiers:

[a] https://orcid.org/0000-0002-3674-2423
[b] https://orcid.org/0009-0008-5974-924X

strategic quality management, tactical process improvement, and operational real-time control. Quality goals defined at the strategic tier are translated into targeted improvement initiatives at the tactical tier, which are in turn sustained through continuous monitoring mechanisms at the operational tier.

The ISO 9001-based foundation establishes documented QMS elements including quality policy, process maps, documented procedures, records, management review, and corrective/preventive action processes [1]. Lean tools—including 5S workplace organization, VSM, standard work, and visual management—address waste elimination while supporting quality objectives [4, 5].

Six Sigma, SPC, and FMEA Integration

Six Sigma DMAIC projects define CTQ characteristics, establish baseline capability through measurement system analysis, employ statistical tools for root cause identification, validate solutions, and implement control plans with SPC monitoring and poka-yoke [6, 7]. SPC implementation encompasses Gage R&R validation, X-bar/R charts for dimensional characteristics, and p/u-charts for defect rates [8].

Process FMEA systematically identifies failure modes rated for Severity, Occurrence, and Detection on 1–10 scales, with RPN = S × O × D prioritizing improvement actions [9, 10]. Digital monitoring through MES, IoT sensors, and CNN-based machine vision provides automated defect detection with human-AI collaboration protocols [11, 12].

Mathematical Models

Defect Rate (%) = (Defective Units / Total Units) × 100. Example: 24 defective of 500 carbon fiber frames = 4.8%.

DPMO = (Defects / (Units × Opportunities)) × 1,000,000. Example: 45 defects across 1,000 PCBs with 150 joints = 300 DPMO (≈4.9σ).

Process Capability: $Cp = (USL - LSL) / 6\sigma$; $Cpk = \min[(USL - \mu)/3\sigma, (\mu - LSL)/3\sigma]$. Example: bore 25.00±0.05 mm, $\mu = 25.02$, $\sigma = 0.015$: Cp = 1.11, Cpk = 0.67.

OEE = Availability × Performance × Quality. **RPN** = Severity × Occurrence × Detection (1–10 scales).

Quality Assurance Methods Comparison

Table 2 compares the primary quality assurance methods integrated within the framework, highlighting their applications, advantages, and limitations.

Table 2

Comparison of Quality Assurance Methods

Method	Application	Key Metrics	Advantages	Limitations
ISO 9001	System documentation	Audit conformance, NCR closure	Comprehensive framework	Generic; needs adaptation
Lean (5S, VSM)	Waste elimination	Lead time, WIP inventory	Visual mgmt, engagement	Requires cultural change
Six Sigma	Root cause analysis	DPMO, sigma level	Data-driven, structured	Resource intensive
SPC Charts	Real-time monitoring	Cp, Cpk, control signals	Early detection, prevention	Needs adequate measurement
FMEA	Risk prioritization	RPN, severity ratings	Systematic risk assessment	Subjective; needs updating
AI Inspection	Automated detection	Detection rate, FP rate	Consistency, speed	Training data needs

Case Study: UAV Manufacturing Quality Improvement

Context and Defect Analysis

The framework was implemented at a hypothetical UAV facility producing commercial inspection and agriculture drones (~2,000 units/year, 45 production + 5 quality personnel). Initial assessment identified primary defect types across four component categories (Table 1).

Table 1

Defect Types and Root Causes

Component	Defect Type	Rate	Root Cause
Carbon Fiber Frame	Delamination	3.2%	Inadequate vacuum pressure; temp. variation
Carbon Fiber Frame	Porosity/Voids	2.1%	Entrapped air; insufficient cure pressure

Motor Mount	Dimensional Error	2.8%	Tool wear; thermal expansion; fixture loosening
Propeller	Blade Imbalance	4.1%	Inconsistent material distribution
PCB Assembly	Solder Defects	5.2%	Paste printing variation; reflow deviation

Implementation and Results

Implementation proceeded over 12 months in four phases: Phase 1 (months 1–3) established ISO 9001-aligned QMS, 5S, and initial SPC; Phase 2 (months 4–6) completed PFMEA and initiated DMAIC projects; Phase 3 (months 7–9) deployed MES with IoT sensors and AI inspection; Phase 4 (months 10–12) refined control systems and management review. Table 3 summarizes key results.

Table 3

Before vs. After Performance Metrics

Performance Metric	Baseline	After Implementation	Improvement
Overall Defect Rate	4.8%	1.6%	67% reduction
Rework Rate	12.5%	4.2%	66% reduction
Scrap Rate	3.2%	0.9%	72% reduction
Process Capability (Cpk)	0.89	1.45	63% improvement
OEE – Composite Process	72%	89%	24% improvement
First Pass Yield	82%	94%	15% improvement
Customer Returns (ppm)	1,850	420	77% reduction
Cost of Quality (% Rev.)	8.4%	4.1%	51% reduction

DMAIC Example: Composite Delamination Reduction

A focused DMAIC project targeted delamination reduction from 3.2% to below 1.0%. Measurement system validation achieved GR&R of 12%. DOE analysis identified temperature ramp rate and vacuum pressure as statistically significant factors. Optimized parameters—vacuum pressure increased from 85 to 95 kPa, ramp rate reduced from 3°C/min to 2°C/min, hold time extended from 90 to 120 minutes—reduced delamination to 0.7% within six months.

3. Results and Discussion

Performance gains recorded across the study period confirm the effectiveness of the multi-method approach. A 67% drop in overall defect rate, paired with Cpk growth from 0.89 to 1.45, reflects a measurable elevation in process precision. The decline in cost of quality from 8.4% to 4.1% of revenue provides clear financial justification for the investment. The framework generates compounding benefits through method interaction: ISO 9001 documentation creates the structural backbone that enables reliable SPC, Lean workplace organization reduces variation sources that would otherwise confound statistical monitoring, Six Sigma DMAIC analysis generates evidence that sharpens FMEA risk prioritization, and AI-based inspection delivers consistent throughput on high-volume repetitive checks where human fatigue is a risk factor.

Deployment was not without obstacles. Workforce adaptation to new quality disciplines demanded persistent leadership engagement over an extended period. Upgrading measurement infrastructure and assembling sufficient labeled imagery for AI model training both required more effort and time than initially projected. Overall, first-year program costs reached approximately $565,000 against realized benefits of $745,000, yielding a 32% return on investment. The stepwise implementation structure proved particularly appropriate for environments with constrained budgets, making the framework well-suited to growing UAV production sectors in regions such as Central Asia.

4. Conclusion

A unified quality assurance framework for UAV component manufacturing was constructed and evaluated, drawing on ISO 9001, Lean, Six Sigma, SPC, FMEA, and AI-powered visual inspection as complementary pillars. Case study outcomes confirm substantial operational gains: a 67% reduction in defect rate (4.8% to 1.6%); rework and scrap rate reductions of 66% and 72% respectively; Cpk advancement from 0.89 to 1.45; OEE growth from 72% to 89%; cost of quality improvement from 8.4% to 4.1%; and a 77% decrease in customer returns. Promising avenues for further development include digital twin-based process simulation, predictive quality analytics leveraging real-time sensor data, broader IoT sensor coverage, and structured pathways toward formal airworthiness certification for emerging UAV platforms [13, 14, 15].

References

[1] International Organization for Standardization, "ISO 9001:2015 Quality management systems — Requirements," ISO, Geneva, 2015.

[2] SAE International, "AS9100D Quality Management Systems — Requirements for Aviation, Space, and Defense Organizations," SAE, 2016.

[3] E. L. Psomas and C. V. Fotopoulos, "A meta analysis of ISO 9001:2000 research," Int. J. Quality and Service Sciences, vol. 1, no. 2, pp. 128–144, 2009.

[4] J. P. Womack and D. T. Jones, Lean Thinking, 2nd ed. New York: Free Press, 2003.

[5] J. K. Liker, The Toyota Way. New York: McGraw-Hill, 2004.

[6] M. Harry and R. Schroeder, Six Sigma: The Breakthrough Management Strategy. New York: Currency Doubleday, 2000.

[7] K. Linderman et al., "Six Sigma: a goal-theoretic perspective," J. Operations Management, vol. 21, no. 2, pp. 193–203, 2003.

[8] D. C. Montgomery, Introduction to Statistical Quality Control, 7th ed. Hoboken: Wiley, 2013.

[9] D. H. Stamatis, Failure Mode and Effect Analysis, 2nd ed. Milwaukee: ASQ Quality Press, 2003.

[10] AIAG and VDA, "FMEA Handbook," Automotive Industry Action Group, 2019.

[11] D. Weimer et al., "Design of deep CNN architectures for automated feature extraction in industrial inspection," CIRP Annals, vol. 65, no. 1, pp. 417–420, 2016.

[12] J. Villalba-Diez et al., "Deep learning for industrial computer vision quality control," Sensors, vol. 19, no. 18, p. 3987, 2019.

[13] F. Tao et al., "Digital twin-driven product design, manufacturing and service," Int. J. Adv. Manuf. Tech., vol. 94, pp. 3563–3576, 2018.

[14] EASA, "Special Condition for Small-Category VTOL Aircraft," SC-VTOL-01, 2019.

[15] FAA, "Type Certification of Unmanned Aircraft Systems," AC 21-17-2A, 2019.

Information about the author

Ravshan Saydakhmedov	Toshkent shahridagi turin politexnika universitetida Texnika fanlari doktori, professor E-mail: saydakhmedov.ravshan@polito.uz Tel: 946569944 https://orcid.org/0000-0002-3674-2423
Ruslan Isroilov	Toshkent shahridagi turin politexnika universitetida “Yer usti majmualari va uchish apparatlari” ixtisosligi doktaranti; Buxoro innovatsiyalar universiteti, o’qituvchi E-mail: ruslanmisroilov@gmail.com Tel.:+998909090519 https://orcid.org/0009-0008-5974-924X

Intelligent monitoring and predictive maintenance technologies in the railway transportation process management system

M.M. Tokhtakhodjaeva[1][a]
[1]Tashkent state transport university, Tashkent, Uzbekistan

Abstract: The article discusses modern approaches to ensuring the safety and efficiency of interaction between railway transport systems through the digitalization of technological processes and the implementation of intelligent monitoring and diagnostic subsystems. An analysis of the existing types of maintenance for transport infrastructure facilities is carried out, including preventive maintenance, condition-based maintenance, and predictive maintenance. The necessity of transitioning to a predictive model of transportation process management based on monitoring data processing and forecasting the technical condition of facilities is substantiated. The concept of a "smart railway station" integrating transportation, diagnostics, monitoring, and cargo parameter control processes into a unified digital management environment is proposed. Particular attention is paid to the implementation of automated weighing systems and the development of a program for intelligent control of wagon weight parameters at the Zavodskaya station of a metallurgical plant. The program provides digital support of wagons throughout the technological chain, intelligent verification of cargo weight data, and decision-making regarding the necessity of repeated weighing based on the analysis of previously obtained information. The research results demonstrate that the use of digital monitoring and intelligent control technologies makes it possible to reduce the number of repeated wagon weighings, decrease shunting operations and wagon idle time, improve the reliability of cargo information, reduce the influence of the human factor, and enhance train traffic safety. The proposed approach forms the basis of a predictive management model for the transport complex focused on failure prevention and optimization of operational processes.

Keywords: railway transport, digitalization, intelligent monitoring, diagnostics, predictive maintenance, traffic safety, weighing systems, smart railway station, digital wagon support, transportation process automation, failure prediction, transport system management

1. Introduction

To improve the efficiency of production activities, various management technologies are traditionally applied, including lean production, Six Sigma, Kaizen technologies, and others. These approaches are also applicable to transport systems. Previously, a process-oriented approach to the organization of transportation production was proposed [1, 2, 3]. Further development of this concept is associated with the implementation of advanced maintenance technologies for transport infrastructure facilities based on predictive condition monitoring and supported by digital monitoring and diagnostic subsystems [4, 5, 6].

2. Research methodology

Three main types of maintenance are used in the transport industry.

Scheduled maintenance. Currently, the transport sector is dominated by a preventive maintenance system. Inspection intervals are determined according to pre-established periods experimentally validated by safety indicators [7]. The disadvantage of this technology is the lack of consideration of the actual condition of the equipment, which leads either to excessive costs or to untimely detection of defects.

Condition-based maintenance. For each facility, a state feature space is formed in which it belongs to one of the following classes: "R" – normal condition; "M" – maintenance required; "W" – withdrawal from operation required.

The object is characterized by a state vector:

$$X = (x_1, x_2, \dots, x_n) \tag{2.1}$$

where x_i – are the parameters reflecting the properties of the object.

To unify the analysis, the parameters are scaled:

$$x_i^* = \frac{x_i - min(x_i)}{max(x_i) - min(x_i)} \tag{2.2}$$

$$x_i^* = \frac{max(x_i) - x_i}{max(x_i) - min(x_i)} \tag{2.3}$$

After transformation, all features take values within the range [0;1].

State classification is performed using pattern recognition methods based on reference patterns and separating boundaries [8]. The most advanced approach is predictive maintenance technology. An example is the "Smart Locomotive" system capable of detecting more than 60 types of faults and predicting equipment failures [9]. Modeling of changes in the object's condition is carried out using time series of features [10, 11]. Stationary objects include railway switches, compressor stations, signaling and interlocking devices, and power supply systems [7]. Each parameter xi is divided into three zones: operating zone (1–α), maintenance zone (α–β), and emergency zone (β–0). The values of α and β are determined based on operational experience [7]. The forecasting algorithm is presented in Figure 1.

[a] https://orcid.org/0009-0000-9444-0418

https://doi.org/10.56143/3030-3893-2026-2-119-121 A bridge between science and innovation

3. Results and Discussion

Based on observation results, a time series xit is formed and an autocorrelation model is constructed:

$$x_{it} = \sum_{k=1}^{n} a_k x_{i(t-k)} \qquad (2.4)$$

where the coefficients ak reflect the inertia of the system state.

Fig. 1. Forecasting Algorithm

As a result, the moment by which maintenance should be performed is determined. Mobile objects include freight cars, locomotives, and train consists.

The task is to classify the object into one of the following categories:

"R" – operation;

"M" – maintenance;

"W" – withdrawal from service.

For example, wheelset diagnostics can be performed using a thermal imaging device. Temperature parameters form an n-dimensional feature space. The current state is determined by the position of a point within the state space. In this case, the forecast is generated not as a numerical value but as a state class [12].

The transition to predictive maintenance creates new processes such as infrastructure monitoring, equipment diagnostics, and failure prediction. These processes require coordination with transportation operations based on the process-oriented approach. Integration of monitoring subsystems with transportation processes makes it possible to prevent emergency situations, reduce the influence of the human factor, optimize the utilization of equipment resources, decrease repair costs, and reduce train delays.

The new management model takes into account not only the current state of the transportation system but also its predicted dynamics, thereby improving traffic safety and transportation process efficiency. The implementation of digital monitoring and diagnostic subsystems forms a predictive management model for the transport complex. Transportation efficiency is achieved through failure prevention rather than reaction to failures. Therefore, predictive maintenance technologies are a key tool for ensuring the safety and efficiency of interaction between railway transport systems.

The essence of the conducted research lies in the transition from the traditional approach to transportation process management, based on preventive maintenance and fragmented technological solutions, to an integrated digital model that combines transportation, monitoring, diagnostics, and cargo parameter control into a single managed environment. Unlike existing approaches, the concept of a "smart railway station" based on digital monitoring technologies and intelligent data analysis is proposed.

A key element of this concept is the implementation of automated weighing systems integrated into the station management system, enabling real-time:

control of wagon weight upon arrival and departure;

detection of discrepancies between actual cargo parameters and shipping documents;

identification of overloads, underloads, and cargo data distortions;

generation of digital alerts for operational decision-making.

Within the proposed smart station model, weighing systems are considered part of the overall monitoring and diagnostics subsystem of transport infrastructure, and their data are included in the state vector of transportation system objects. During operation, the above-mentioned parameters change in different directions: some increase, while others decrease. Furthermore, they are measured in different value ranges. To unify the analysis, all variables are scaled to the interval [0;1] and transformed into a decreasing form with equipment wear. Scaling formulas are applied separately for decreasing and increasing variables.

The addition of wagon loading parameters to the state vector makes it possible to:

improve the reliability of transportation process assessment;

consider the impact of commercial factors on traffic safety;

expand predictive management capabilities by identifying hidden risks;

ensure integration of technological and information processes.

Discussion. As a result, a digital model of station operation is formed, in which control, diagnostics, and management processes are integrated into a unified intelligent system capable not only of responding to deviations but also of preventing their occurrence. Within the framework of the study, the development of an intelligent wagon weight control program for the Zavodskaya station of a metallurgical plant is proposed. The purpose of the program is to reduce the number of repeated wagon weighings while maintaining the required level of reliability of cargo weight data and transportation safety.

In the existing technological process, wagons undergo multiple weighings at different processing stages: upon arrival, after unloading, after cleaning, and before reloading. This organization leads to additional shunting operations, increased wagon idle time, higher utilization of weighing equipment, and increased operating costs. To optimize this process, a program is proposed that provides digital support for wagons throughout the entire technological chain and replaces part of the repeated weighing operations with intelligent data verification procedures.

At the initial stage, the station operator enters the wagon number, cargo weight, and destination facility into the system. After arrival at Zavodskaya station, the wagon is weighed and the obtained data are automatically recorded. The system calculates the total wagon weight as the sum of the tare weight and cargo weight and compares the calculated value with the measured value. If the deviation is within acceptable limits, the information is confirmed and the wagon is allowed to proceed further.

At the cargo facility, the operator confirms or adjusts the cargo weight and updates the wagon tare weight if necessary. If the wagon number, cargo weight, tare weight, destination, and previous weighing results correspond and contain no critical discrepancies, the system decides that repeated weighing before loading is not required. Thus, the program enables the elimination of a portion of repeated weighing

https://doi.org/10.56143/3030-3893-2026-2-119-121

operations that were previously mandatory. The main principle is that the decision to perform another weighing operation is based on digital verification of existing data rather than automatic weighing of every wagon.

4. Conclusion

Implementation of the proposed program will reduce the number of repeated wagon weighings, decrease unnecessary shunting movements, lower the workload of weighing facilities and operators, reduce wagon idle time, improve the reliability of cargo data, minimize the influence of the human factor in transportation operations, and enhance traffic safety by preventing wagon overloading and cargo data discrepancies.

Thus, cargo weight control becomes not only an element of commercial accounting but also a crucial component of railway traffic safety, since wagon overloading directly affects train dynamics, infrastructure wear, and the risk of accidents. The proposed program represents a digital tool for wagon support throughout the technological chain with an intelligent weight verification function. Unlike the current practice based on multiple mandatory weighings, the proposed approach allows decisions on repeated weighing to be made through analysis of already available data. This ensures a reduction in weighing operations, accelerates wagon processing, and improves the operational efficiency of the Zavodskaya station of the metallurgical plant.

References

[1] I Ibragimova, G., Kayumov, S., & Abduvaitova, M. (2025). Analysis of the transport sector and ensuring transport safety in the context of globalization. Engineer, 3(2), 5–8.

[2] Ibragimova, G., Kayumov, S., Khusenov, U., Bashirova, A., Akhmedova, M., & Namazov, S. (2026). Improving technology for determining the time spent on cleaning gondola wagons. In AIP Conference Proceedings (Vol. 3374, No. 1, Article 060013). AIP Publishing LLC.

[3] Ibragimova, G., Sakijan, K., Diyorbek, G., Dilbar, E., Odil, J., Umida, M., & Vilayat, V. (2026). Development of e-commerce in passenger transportation of railway transport. In AIP Conference Proceedings (Vol. 3374, No. 1, Article 040016). AIP Publishing LLC.

[4] Vlasov, A.S., & Latysheva, N.A. (2018). Problems and practice of implementing the process approach in personnel management of Russian Railways. In Economics, Management and Finance: Proceedings of the VIII International Scientific Conference (pp. 130–133). Krasnodar: Novatsiya.

[5] Eliseev, S.Yu., & Kulieva, E.S. (2017). Process approach as a basis for improving the efficiency of customer service systems in railway transport. Science and Technology of Transport, 2, 57–62.

[6] Kurenkov, P.V., & Nekhaev, M.A. (2012). Tasks of situational-process management of a classification yard. Railway Transport, 4, 29–31.

[7] Lyabakh, N.N., & Gibner, Ya.M. (2016). Development of an intelligent monitoring system for the technical condition of railway sorting devices and maintenance advisory systems. In Proceedings of the Fifth International Scientific and Technical Conference "Intelligent Control Systems in Railway Transport (ICSRT-2016)" (pp. 173–175). Moscow: NIIAS.

[8] Railway Transport Seeks Ways of Self-Regulation. (2012, May 23). Gudok. Retrieved from https://www.gudok.ru/news/transport/?ID=865222

[9] Berzin, A. (2017). Smart locomotive for a digital railway. Gudok. Retrieved from https://www.gudok.ru/newspaper/?archive=2017.04.19

[10] Lyabakh, N.N., & Shabelnikov, A.N. (2002). Technical Cybernetics in Railway Transport. Rostov-on-Don: SKNC VSh.

[11] Orlov, A.I. (2005). Decision Making: Theory and Methods for Developing Managerial Decisions. Moscow: MarT.

[12] Rozenberg, I.N., Shabelnikov, A.N., & Lyabakh, N.N. (2019). Classification Process Control Systems within the Digital Railway Ideology. Moscow: VINITI RAS.

Information about the author

Mafratkhon Tokhtakhodjaeva	Toshkent davlat transport universiteti "Temir yo'ldan foydalanish ishlarini boshqarish" kafedrasi katta o'qituvchisi, E-mail: mafirat.toxtaxodjayeva.66@mail.ru Tel.: +998 77 756 44 55 https://orcid.org/0009-0000-9444-0418

https://doi.org/10.56143/3030-3893-2026-2-119-121

Comparative analysis of low-temperature cracking resistance in Uzbekistan bitumens using bending beam rheometry

E.B. Joldasbaev[1][a]

[1]Tashkent state transport university, Tashkent, Uzbekistan

Abstract: Low-temperature thermal cracking is a primary distress mechanism in asphalt pavements exposed to extreme continental climates. This study conducts a comparative rheological evaluation of standard and modified bituminous binders to assess their low-temperature fracture resistance within the context of Uzbekistan's pavement infrastructure. Four binder formulations were investigated: a conventional unmodified petroleum bitumen (BND), a polymer-modified bitumen (PMB), a crumb rubber-modified bitumen (CRMB), and a sulfur-modified bitumen (SMB). To replicate in-service thermo-oxidative degradation, all binders underwent sequential short-term and long-term aging via the Rolling Thin Film Oven Test (RTFOT) and Pressure Aging Vessel (PAV), respectively. Low-temperature viscoelastic behavior was quantified using a Bending Beam Rheometer (BBR) at isothermal test temperatures of [-12°C, -18°C, and -24°C]. The critical rheological parameters—creep stiffness, S(60), and the stress relaxation rate, m(60)—were analyzed to establish the continuous low-temperature Performance Grade (PG) limits for each binder. Experimental results reveal that the modifier type fundamentally dictates the thermo-rheological susceptibility of the binders post-aging. Specifically, the PMB and CRMB formulations exhibited enhanced resistance to thermal embrittlement, maintaining lower stiffness gradients and superior stress relaxation capacities relative to the unmodified BND. Ultimately, these findings offer a fundamental mechanistic basis for optimizing binder selection in Central Asia, facilitating the regional transition from empirical grading specifications toward advanced performance-based methodologies.

Keywords: bitumen rheology, bending beam rheometer, low-temperature cracking, PAV aging, polymer modification, performance grading

1. Introduction

Asphalt concrete remains the predominant paving material for highway infrastructure globally. However, in continental climates characterized by severe seasonal temperature fluctuations, such as those experienced in Central Asia, pavements are highly susceptible to premature degradation. During winter months, rapid temperature drops induce significant thermal shrinkage within the asphalt layer. When the induced thermal tensile stress exceeds the material's relaxation capacity and tensile strength, low-temperature thermal cracking occurs [1, 2]. Because the binder's rheology dictates the viscoelastic behavior of the asphalt mixture, selecting a bitumen with adequate low-temperature compliance and stress relaxation capabilities is critical to ensuring pavement longevity.

Historically, binder selection and grading in the region have relied on the legacy empirical testing frameworks outlined in standards in regional State Standards (GOST) such as GOST 22245. [3] This approach primarily utilizes standard penetration (GOST 11501) [4], the ring-and-ball softening point (GOST 11506) [5], ductility at 0°C (GOST 11505) [6], and the Fraass breaking point (GOST 11507) [7] to estimate cold-weather performance. While these conventional methods provide a baseline for manufacturing consistency, they are fundamentally empirical and fail to characterize the true mechanistic properties of the bitumen across a continuum of temperatures. Furthermore, these traditional indices do not accurately simulate the complex long-term thermo-oxidative aging that binders undergo during production and years of in-service environmental exposure. Consequently, pavements designed strictly under these GOST empirical frameworks often exhibit premature thermal cracking, highlighting the urgent need to transition toward performance-based specifications.

Modern pavement engineering addresses these limitations through the Superpave Performance Grading (PG) system, [8] which characterizes binders based on fundamental rheological principles measured at actual pavement design temperatures. Specifically, the Bending Beam Rheometer (BBR), standardized under AASHTO T 313, [9] is utilized to evaluate the low-temperature creep stiffness and stress relaxation rate of binders after both short-term and long-term aging protocols. By directly measuring the binder's mechanistic response to thermal stresses, the BBR provides a highly accurate prediction of field performance and thermal cracking resistance

Despite the global adoption of mechanistic-empirical grading, a critical knowledge gap remains regarding the fundamental low-temperature rheology of the specific binders utilized within Uzbekistan's infrastructure network. As the regional industry increasingly explores advanced modification techniques to extend pavement life, it is imperative to establish how these locally sourced and modified materials perform under rigorous, performance-based testing.

Therefore, this study aims to conduct a comprehensive comparative analysis of low-temperature cracking resistance among four distinct bituminous binders: a standard unmodified petroleum bitumen (BND), a polymer-modified

[a] https://orcid.org/0009-0005-4959-0069

bitumen (PMB), a crumb rubber-modified bitumen (CRMB), and a sulfur-modified bitumen (SMB). By utilizing BBR testing on binders subjected to simulated long-term field aging, this research provides the fundamental rheological data necessary to optimize local binder selection and supports the regional transition toward advanced, performance-graded binder specifications.

2. Research methodology

Theoretical Background and Principles of Rheological Grading

2.1. Long-Term Thermo-Oxidative Aging Simulation (PAV)

To accurately assess the low-temperature cracking susceptibility of binders, the material must be evaluated in a state that represents years of in-service environmental exposure. While the Rolling Thin Film Oven Test (RTFOT, AASHTO T 240) [10] simulates volatilization and short-term oxidation during mixing and construction, the Pressure Aging Vessel (PAV), standardized under AASHTO R 28, [12] simulates the long-term thermo-oxidative degradation that occurs over 5 to 10 years in the field. The PAV accelerates this aging process by subjecting the binder to elevated temperatures (typically 90°C to 110°C) and high pressurized air (2.1 MPa). According to the principles of diffusion and reaction kinetics, this elevated pressure forces oxygen deep into the bitumen matrix, accelerating the conversion of resins to asphaltenes. This chemical shift inherently increases the material's stiffness and reduces its ductility, creating the worst-case scenario for low-temperature thermal cracking.

2.2. Viscoelastic Formulation of the Bending Beam Rheometer (BBR)

At low temperatures, asphalt binders exhibit complex viscoelastic behavior. The Bending Beam Rheometer (AASHTO T 313) quantifies this behavior by applying the elastic-viscoelastic correspondence principle to the elementary Euler-Bernoulli beam theory.During the test, a prismatic beam of bitumen is simply supported at both ends and subjected to a constant static load at its midspan. The time-dependent flexural creep stiffness, S(t), is calculated using the following fundamental equation:

$$S(t) = \frac{PL^3}{4bh^3\delta(t)} \tag{1}$$

where:S(t) is the time-dependent creep stiffness (MPa); P is the applied constant load (typically 0.98 N); L is the span length between the supports (102 mm); b is the width of the bitumen beam (12.5 mm);h is the thickness of the bitumen beam (6.25 mm); $\delta(t)$ is the measured midspan deflection at time t (mm).

For Superpave specification purposes, the critical stiffness is evaluated at a loading time of 60 seconds, denoted as S(60). According to the time-temperature superposition principle, testing the binder at 60 seconds at a specific test temperature (e.g., -12°C) correlates to the thermal stresses the pavement would experience after 2 hours of extreme cooling at a temperature 10°C lower (e.g., -22°C). A maximum limit of S(60)≤ 0.300 MPa is enforced to ensure the binder does not become excessively brittle.

In addition to stiffness, the material's ability to dissipate accumulating thermal stresses—known as the stress relaxation rate—is quantified by the m-value. Mathematically, the time-dependent m-value is defined as the absolute value of the slope of the logarithm of stiffness versus the logarithm of time curve:

$$m(t) = \left|\frac{d(\log S(t))}{d(\log t)}\right| \tag{2}$$

A higher m-value indicates a greater capacity for the binder to relax internal thermal stresses before reaching its fracture point. To ensure adequate stress relaxation, standard specifications require a minimum value of m(60)≥ 0.300 MPa.

Materials and Methods

Material Selection and Prior Conditioning

The specific material formulations—including the preparation of the polymer, crumb rubber, and sulfur-modified bitumens—along with the short-term aging procedures (RTFOT), were conducted in strict accordance with the methodologies established in prior studies [13,14].

Long-Term Aging Protocol (PAV)

To simulate the long-term thermo-oxidative degradation that asphalt binders experience over 5 to 10 years of in-service environmental exposure, the RTFOT-aged residues were subjected to pressurized aging in accordance with AASHTO R 28.

For each of the four binder variations (BND, PMB, CRMB, and SMB), standard stainless-steel PAV pans were loaded with 50 grams of the RTFOT-aged residue to ensure a uniform film thickness of approximately 3.2 mm. The loaded pans were then placed into the Pressure Aging Vessel (PAV) and subjected to a constant pressurized air environment of 2.1 MPa. The aging temperature was maintained at 100°C for a continuous duration of 20 hours.

Fig. 1. PAV-aging process of modified bitumens in the laboratory

Following the 20-hour pressurized aging cycle, the samples were transferred to a vacuum degassing oven. Because modified binders—particularly crumb rubber and polymer-modified bitumens—are highly viscous and prone to retaining entrapped air during the PAV process, the samples were degassed at 170°C under a vacuum pressure of 15 kPa for 30 minutes. This critical step ensures that no micro-bubbles are present in the final aged matrix, which could otherwise introduce structural flaws and skew the subsequent low-temperature BBR stiffness measurements. After degassing, the fully aged binders were carefully collected and stored in preparation for immediate BBR sample fabrication.

Prior to demolding, the molds were briefly chilled to stiffen the beams, preventing any internal stresses or physical distortion during extraction. The demolded prismatic beams were immediately transferred into the BBR's thermostatically controlled fluid bath—utilizing an ethanol-based cooling medium—and subjected to isothermal conditioning for 60 ± 5 minutes. In accordance with standard Superpave Performance Grading (PG) protocols, testing was conducted at 6°C increments—specifically at -12°C, -18°C, and -24°C—to establish a continuous low-temperature performance profile appropriate for the varying climatic zones across Uzbekistan. During the test, each beam was simply supported over a 102 mm span and subjected to a constant static load of 980 ± 50 mN at its midspan. The midspan deflection was continuously recorded via a Linear Variable Differential Transformer (LVDT) over a 240-second loading period. Using the integrated software, the creep stiffness, S(t), and the stress relaxation rate, m-value, were automatically computed at the critical 60-second loading mark—correlating to two hours of extreme thermal contraction in the field. To ensure statistical reliability, a minimum of two replicate beams were tested for each binder type at each temperature, and the average values were recorded for analysis.By phrasing it this way, you make it clear that you are testing across a range (the 6°C increments) to find the exact failure point for the continuous PG grade, rather than just checking a single temperature pass/fail.

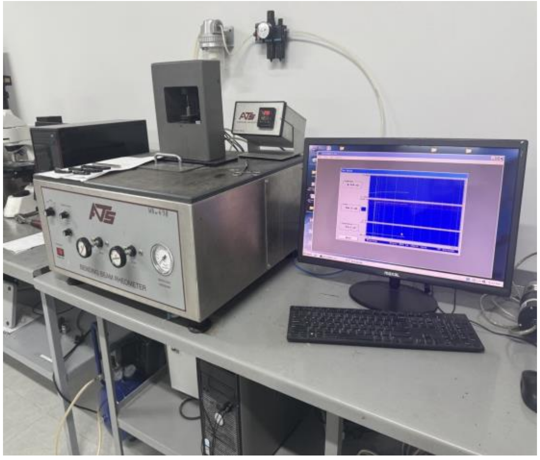

Fig. 2. BBR testing process of modified bitumens in the laboratory

3. Results and Discussion

1. Low-Temperature Rheological Properties of PAV-Aged BindersTo evaluate the resistance of the modified binders to low-temperature thermal cracking following long-term thermo-oxidative aging, BBR testing was conducted. The fundamental rheological parameters—creep stiffness, S(60), and the stress relaxation rate, m(60)—were measured at 60 seconds of loading. The summarized experimental results for all binder formulations across the respective isothermal test temperatures are presented in Table 1.

Table 1

Results of BBR test

Binder Type	Test Temperature (°C)	S(60) (MPa)	m-value at 60s	Specification Criteria	Pass/Fail
PMB	-24	128.3	0.312	m(60)≥ 0.300 MPa S(60)≤0.300 MPa	Pass
CRB	-24	88.3	0.328		Pass

The Polymer-Modified Bitumen (PMB) and the Crumb Rubber-Modified Bitumen (CRMB) successfully satisfied the rigorous criteria for a PG XX-34 classification. This expanded low-temperature threshold provides several critical mechanistic and practical advantages for regional infrastructure:

-Enhanced Viscoelastic Networks: The ability of PMB and CRMB to pass the -24°C testing requirement (correlating to -34°C in the field) demonstrates that the elastomeric polymers and vulcanized rubber particles successfully absorb the lighter malthene fractions of the base bitumen. This interaction forms a continuous, highly elastic three-dimensional network that fundamentally alters the binder's thermo-rheological behavior. Even under advanced thermo-oxidative aging (PAV), this network prevents the matrix from transitioning into a purely brittle state.

-Superior Stress Dissipation: The passing m-values for both PMB and CRMB indicate that these modifiers act as internal stress-relievers. During rapid environmental cooling, the rubber and polymer chains maintain sufficient molecular mobility to dissipate accumulating tensile stresses, effectively preventing the initiation and propagation of transverse micro-cracks.

-Extended Pavement Service Life: From a pavement design perspective, upgrading from a standard GOST-graded BND to a Superpave PG XX-34 modified binder fundamentally mitigates the primary mechanism of winter pavement failure. By accommodating extreme thermal contraction, PMB and CRMB significantly reduce the requirement for frequent seasonal patching and maintenance, thereby extending the overall structural lifecycle of the asphalt concrete.

4. Conclusion

This study presents a mechanistic evaluation of the low-temperature rheological properties of conventional and modified bituminous binders (BND, PMB, CRMB, and SMB) subjected to long-term thermo-oxidative aging (PAV). By characterizing creep stiffness and stress relaxation capacities via Bending Beam Rheometer (BBR) testing, this research establishes the critical performance limits of these materials for application in Uzbekistan's severe continental climate. The principal findings are as follows:

Inadequacy of Unmodified Binders: The conventional BND demonstrated pronounced thermo-oxidative susceptibility, exhibiting severe thermal embrittlement post-PAV aging. The rapid accumulation of creep stiffness and the degradation of stress relaxation capacity limited its true

https://doi.org/10.56143/3030-3893-2026-2-122-125

low-temperature grade. This confirms that legacy, empirically graded binders are mechanically insufficient to withstand the severe temperature gradients of Central Asian winters, leading to inevitable transverse cracking.

Superior Low-Temperature Compliance of Polymer Modification: The integration of elastomeric polymers (PMB) fundamentally transformed the viscoelastic network of the binder. At extreme sub-zero temperatures (-24°C), the PMB yielded an exceptionally low average stiffness of 108.3 MPa and a compliant m-value of 0.320, safely achieving a continuous PG XX-34 classification. The polymer matrix successfully dissipates internal thermal tensile stresses, mitigating the risk of brittle fracture.

Efficacy and Sustainability of Crumb Rubber Modification: The crumb rubber-modified bitumen (CRMB) mirrored the enhanced low-temperature resilience of the PMB, also satisfying the stringent criteria for a PG XX-34 rating. This demonstrates that incorporating vulcanized rubber particles not only provides a highly effective mechanism for extending the functional temperature continuum of regional pavements, but also offers a sustainable pathway for end-of-life tire repurposing.

Strategic Transition to Mechanistic Specifications: These findings underscore the critical necessity of transitioning from regional empirical specifications (GOST) to performance-based mechanistic grading (Superpave). Implementing PG XX-34 certified elastomeric or rubberized binders will fundamentally mitigate premature thermal cracking, thereby extending the structural lifecycle of Uzbekistan's highway infrastructure and drastically reducing seasonal maintenance costs.

References

[1] R. C. G. Haas, "A method for designing asphalt pavements to minimize low-temperature shrinkage cracking," Highway Research Record, no. 466, pp. 34-58, 1973.

[2] H. U. Bahia and D. A. Anderson, "The new proposed rheological properties of asphalt binders: Why are they required and how do they compare to conventional properties?," in Physical Properties of Asphalt Cement Binders, ASTM STP 119, J. C. Hardin, Ed., West Conshohocken, PA, USA: ASTM International, 1995, pp. 1-27.

[3] Viscous Petroleum Road Bitumens. Specifications, GOST 22245-90, State Committee of the Russia for Construction and Investments, Moscow.

[4] Petroleum Bitumens. Method for Determination of Penetration, GOST 11501-93, Interstate Council for Standardization, Metrology and Certification (ISC), Minsk, 1993.

[5] Petroleum Bitumens. Method for Determination of Softening Point by Ring and Ball, GOST 11506, State Committee for Standards of the Council of Ministers of the Russia, Moscow.

[6] Petroleum Bitumens. Method for Determination of Ductility, GOST 11505, State Committee for Standards of the Council of Ministers of the Russia, Moscow.

[7] Petroleum Bitumens. Method for Determination of Fraass Breaking Point, GOST 11507, State Committee of the Russia for Standards, Moscow.

[8] R. J. Cominsky, G. A. Huber, T. W. Kennedy, and M. Anderson, The Superpave Mix Design Manual for New Construction and Overlays, SHRP-A-407, Strategic Highway Research Program, National Research Council, Washington, D.C., 1994.

[9] Standard Practice for Grading or Verifying the Performance Grade of an Asphalt Binder, AASHTO R 29-15, American Association of State Highway and Transportation Officials, Washington, D.C., 2015.

[10] Standard Specification for Performance-Graded Asphalt Binder, AASHTO M 320-17, American Association of State Highway and Transportation Officials, Washington, D.C., 2017.

[11] Standard Method of Test for Effect of Heat and Air on a Moving Film of Asphalt (Rolling Thin-Film Oven Test), AASHTO T 240-13, American Association of State Highway and Transportation Officials, Washington, D.C., 2013.

[12] Standard Method of Test for Determining the Flexural Creep Stiffness of Asphalt Binder Using the Bending Beam Rheometer (BBR), AASHTO T 313, American Association of State Highway and Transportation Officials, Washington, DC, 2022.

[13] Sadikov I.S., Joldasbaev E.B ''EVALUATION OF SHORT-TERM AGING CHARACTERISTICS OF BND 60/90 BITUMEN FOR ROAD CONSTRUCTION IN UZBEKISTAN'' THE SCIENTIFIC JOURNAL OF VEHICLES AND ROADS , Tashkent 2026 , Issue 1

[14] I.S. Sadikov, E.B. Joldasbaev '' Predicting the rheological response of Uzbekistan's polymer-modified binders: a comparative analysis of conventional empirical tests and the complex shear modulus'' Journal Engineer, Volume:4, Issue:1, 2026.

Information about the author

Er-Sultan Joldasbaev	Tashkent State Transport University, chair of Road Engineering and telematics, PhD researcher https://orcid.org/0009-0005-4959-0069

GIS-based analysis of street network structure and urban development patterns in Termez city, Uzbekistan

M. Ergashova[1][a], U. Gulomov[2][b], Kh. Narzullaev[2][c], Z. Jalolov[2][d]
[1]Tashkent state transport university, Tashkent, Uzbekistan
[2]Termez state university of engineering and agrotechnology, Termez, Uzbekistan

Abstract: Street networks play a fundamental role in shaping urban development by influencing accessibility, mobility, and the spatial organization of cities. This study aims to analyze the structure of the street network in Termez City using Geographic Information Systems (GIS) and evaluate its impact on urban development patterns. OpenStreetMap (OSM) data were used to extract street network data, building footprints, and the administrative boundary of the study area. All spatial analyses were conducted using QGIS 3.40. The methodological framework included street hierarchy classification, street density assessment, building distribution analysis, and the evaluation of spatial relationships between the street network and urban development. The results revealed that higher-order streets, including trunk, primary, and secondary roads, are predominantly concentrated in the central districts of Termez City, forming the main transportation corridors. Building distribution analysis demonstrated that urban development is strongly associated with these corridors, where higher concentrations of buildings were observed. In contrast, peripheral areas exhibited lower levels of street network connectivity and relatively dispersed development patterns. The findings confirm that the structure and connectivity of the street network significantly influence the spatial development of Termez City. Furthermore, the study highlights the effectiveness of GIS-based approaches in supporting evidence-based urban planning, improving transportation accessibility, and promoting sustainable urban development in medium-sized cities.

Keywords: street network, GIS, urban development, spatial analysis, OpenStreetMap, transportation infrastructure, Termez City, QGIS

1. Introduction

Urbanization has become one of the most significant socio-economic processes of the twenty-first century. According to the United Nations, nearly 68% of the world's population is expected to live in urban areas by 2050. The continuous growth of urban populations requires the rapid development of transportation systems, land-use structures, and urban infrastructure. In this context, street networks have gained increasing importance as fundamental elements that support the spatial organization of cities, facilitate mobility, and promote economic activities.

The structure and connectivity of street networks directly influence urban development patterns. Well-integrated street systems improve accessibility, reduce travel distances, and facilitate the efficient movement of people and goods. As a result, they contribute to increased economic activity, improved access to urban services, and the creation of favorable conditions for sustainable urban development [1, 2, 7]. In contrast, fragmented and poorly connected street networks often lead to uncontrolled urban expansion, increased transportation costs, and inefficient land use [3].

In recent years, the advancement of Geographic Information Systems (GIS) technologies has created new opportunities for analyzing urban transportation networks. GIS-based approaches enable researchers to evaluate street network hierarchies, assess network connectivity, analyze accessibility, and investigate the spatial relationships between transportation infrastructure and urban development [4]. Such analyses are essential for supporting evidence-based decision-making in urban planning and for improving the management of transportation systems.

Termez City, located in the southern part of Uzbekistan, is one of the major administrative, economic, and transportation centers of the Surkhandarya Region. In recent years, population growth and increasing construction activities have contributed to the continuous expansion of the urban area. These processes have intensified the pressure on transportation infrastructure, highlighting the need to assess the efficiency of the existing street network and identify opportunities for its improvement. However, despite the regional importance of Termez City, limited research has been conducted on the spatial characteristics of its street network and their influence on urban development using GIS technologies.

Therefore, the aim of this study is to analyze the structure of the street network in Termez City using GIS techniques and to evaluate its impact on urban development. To achieve this aim, the following objectives were established:

1. To analyze the hierarchical structure of the street network in Termez City;
2. To assess the spatial characteristics and connectivity of the street network;
3. To identify the spatial relationships between the street network and building distribution;
4. To evaluate the impact of transportation infrastructure on urban development;

[a] https://orcid.org/0000-0001-6636-6206
[b] https://orcid.org/0009-0005-5057-6862
[c] https://orcid.org/0000-0002-2860-1962
[d] https://orcid.org/ 0009-0009-2736-4473

5. To develop practical recommendations for improving transportation planning and promoting sustainable urban development in Termez City.

The findings of this study may provide an important scientific and practical basis for improving the transportation system of Termez City, enhancing accessibility, and supporting the effective planning of future urban development.

Literature review

Street networks are an essential component of urban structure, directly influencing mobility, accessibility, and the spatial development of cities. The configuration of street networks determines the efficiency with which people, goods, and services move throughout urban areas and plays a significant role in shaping urban morphology [1, 5]. Consequently, the analysis of street networks has become one of the key research areas in urban planning and transportation studies.

In recent years, street network connectivity has been increasingly recognized as an important indicator affecting urban development. According to Boeing [2], highly connected street networks reduce travel distances, distribute traffic flows more efficiently, and improve access to urban services. In contrast, fragmented and poorly connected street systems contribute to uncontrolled urban expansion, reduced transportation efficiency, and increased infrastructure costs [3].

The relationship between urban development and street network structure has been widely investigated in previous studies. Porta et al. [4] emphasized that transportation infrastructure is one of the major factors shaping urban morphology and reported higher levels of development intensity along major transportation corridors. Similarly, Sevtsuk and Mekonnen [8] found that areas with higher levels of accessibility are often characterized by greater economic activity and more intensive urban development.

Various indicators have been proposed to evaluate the performance of street networks. Among the most commonly used measures are street density, intersection density, network continuity, and route accessibility [6]. These indicators provide valuable insights into the level of transportation network development and the quality of mobility conditions within urban areas.

Geographic Information Systems (GIS) have become an important tool for analyzing urban transportation systems. GIS technologies facilitate street network classification, the integration of spatial data, the identification of relationships between transportation infrastructure and land use, and the production of thematic maps [4]. Moreover, the increasing availability of OpenStreetMap data has enabled rapid and cost-effective analyses of transportation networks.

Investigating the spatial relationships between transportation infrastructure and urban development has also emerged as an important research direction. Previous studies have shown that higher concentrations of buildings are often found in areas with greater transportation accessibility [1]. Major transportation corridors influence residential distribution, commercial activities, and the provision of social infrastructure, thereby shaping the future directions of urban growth.

Although numerous studies on street networks have been conducted worldwide, limited attention has been given to cities in Central Asia, particularly medium-sized cities in Uzbekistan. In the case of Termez City, research focusing on the assessment of street network structure and its influence on urban development using GIS technologies remains scarce.

From this perspective, the present study aims to analyze the spatial characteristics of the street network in Termez City, identify the relationships between transportation infrastructure and urban development, and provide practical recommendations to support sustainable urban planning.

2. Research methodology

Study Area

The study was conducted in Termez City, the administrative center of the Surkhandarya Region located in the southern part of the Republic of Uzbekistan. Termez is one of the country's important administrative, economic, and transportation centers. Due to its proximity to international transportation corridors, the city plays a significant role in the regional economy. In recent years, population growth, urban expansion, and increasing traffic volumes have highlighted the need to investigate the characteristics of the city's street network development.

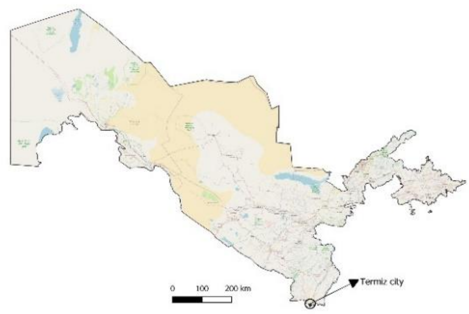

Fig. 1. Location of Termez City within Uzbekistan

Data Sources

This study utilized spatial data obtained from OpenStreetMap (OSM), an open-source geographic database that is regularly updated and freely accessible. The following datasets were collected and used for the analysis:

- street network data (road centerlines);
- building footprint data;
- administrative boundary of Termez City;
- base cartographic layers.

According to the OpenStreetMap classification system, the street network data were categorized into six road classes:

- trunk;
- primary;
- secondary;
- tertiary;
- residential;
- service.

Building footprint data were used to evaluate urban development patterns and the spatial relationships between transportation infrastructure and built-up areas.

GIS Environment and Data Processing

All spatial analyses were performed using QGIS 3.40 software. The research process consisted of several stages, including data collection, preprocessing, classification, spatial analysis, and cartographic visualization. The overall methodological framework of the study is presented in Figure 2.

Fig. 2. Research workflow for assessing the street network structure and urban development in Termez City

The study was carried out through the following stages:

- downloading OpenStreetMap data;
- extracting the administrative boundary of Termez City;
- clipping road and building layers to the study area boundary;
- classifying the street network according to functional categories;
- analyzing the spatial distribution of buildings;
- assessing the spatial relationships between roads and buildings;
- preparing thematic maps and interpreting the results.

The following QGIS tools and functions were employed during the analysis:

- QuickOSM Plugin;
- Vector Geometry Tools;
- Field Calculator;
- Clip;
- Buffer;
- Spatial Join;
- Layout Manager.

Street Network Hierarchy Analysis

The street network of Termez City was classified into six categories according to the OpenStreetMap road hierarchy system:

- trunk roads;
- primary roads;
- secondary roads;
- tertiary roads;
- residential streets;
- service roads.

This classification enabled the identification of the hierarchical structure of the urban transportation system and facilitated the assessment of the role of different road categories in urban development.

Street Density Assessment

Street density was calculated to evaluate the level of development of transportation infrastructure within the study area. This indicator represents the ratio between the total length of streets and the area of the study region.

The street density was calculated using the following equation:

$$SD = \frac{L}{A}$$

where: SD – street density (km/km²);
L – total length of streets within the study area (km);
A – area of the study region (km²).

Higher street density values generally indicate better accessibility and more developed transportation infrastructure.

Building Distribution Analysis

Building footprints were analyzed to evaluate urban development patterns in Termez City. The analysis focused on the following aspects:

- spatial distribution of buildings throughout the city;
- concentration of built-up areas;
- distribution of buildings along major transportation corridors.
- Building density was calculated using the following equation:

$$BD = \frac{N}{A}$$

where: BD – building density;
N – number of buildings;
A – area of the study region (km²).

Assessment of Spatial Relationships Between Roads and Buildings

To evaluate the influence of transportation infrastructure on urban development, spatial analysis was conducted between the street network and building layers.

Buffer zones were generated around primary and secondary roads, and the concentration of buildings within these zones was assessed. This approach enabled the identification of the extent to which transportation corridors

Cartographic Visualization

The results of the study were presented through thematic maps prepared in the QGIS Layout Manager environment and exported in high quality.

The following figures were included in the article:

Figure 1. Location of Termez City within Uzbekistan;

Figure 2. Research workflow for assessing the street network structure and urban development in Termez City;

Figure 3. Street network hierarchy of Termez City;

Figure 4. Spatial distribution of buildings in Termez City;

Figure 5 Spatial relationships between the street network and urban development in Termez City**.**

These maps served as the primary basis for evaluating the spatial characteristics of the transportation system in Termez City and analyzing its impact on urban development patterns.

3. Results and Discussion

Street Network Hierarchy of Termez City

The results of the analysis revealed that the street network of Termez City consists of roads with different functional characteristics. Based on OpenStreetMap data, streets were classified into six categories: trunk, primary, secondary, tertiary, residential, and service roads.

The study found that higher-order roads, including trunk, primary, and secondary roads, are predominantly

https://doi.org/10.56143/3030-3893-2026-2-126-131

concentrated in the central parts of the city. These roads form the main transportation corridors of Termez City and facilitate connectivity between residential areas, public buildings, commercial establishments, and administrative centers.

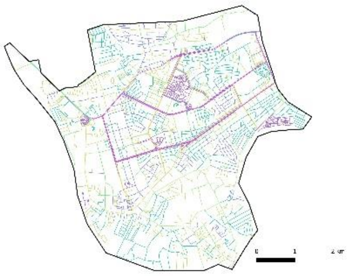

Fig. 3. Street network hierarchy of Termez City

The map analysis further indicated that residential streets constitute the largest proportion of the urban street network and primarily serve local mobility functions. Service roads mainly provide access to service facilities and internal urban areas.

While the street network is relatively dense and well-developed in areas close to the city center, a lower density of streets was observed in peripheral districts of the city.

Spatial Distribution of Buildings

The analysis of building footprints demonstrated that urban development is unevenly distributed throughout Termez City. The majority of buildings are concentrated in the central districts and in areas with favorable transportation accessibility, particularly along major roads.

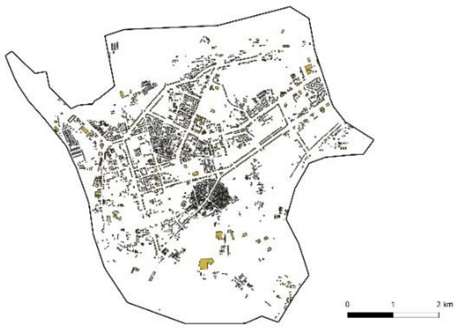

Fig. 4. Spatial distribution of buildings in Termez City

Central districts exhibited high building density, creating a continuous urban fabric. These areas were characterized by a high concentration of commercial establishments, educational institutions, social infrastructure, and service facilities.

In contrast, buildings in peripheral areas were more dispersed, and development intensity was lower compared with the central parts of the city. This pattern reflects the gradual expansion of the city and the subsequent development of outer urban areas.

Spatial Relationships Between the Street Network and Urban Development

The integrated analysis of the street network and building distribution demonstrated that transportation infrastructure plays a significant role in shaping urban development.

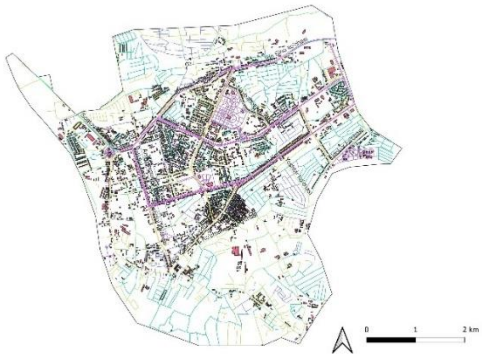

Fig. 5. Spatial relationships between the street network and urban development in Termez City

The findings revealed that building concentrations are particularly high along primary and secondary roads. This suggests that higher levels of transportation accessibility positively influence residential distribution and economic activities. Moreover, a greater concentration of residential and commercial buildings was observed around major transportation corridors. This pattern confirms that transportation infrastructure acts as one of the principal factors guiding urban development.

Conversely, peripheral areas with lower levels of transportation accessibility exhibited relatively sparse building distributions and lower development intensity.

Connectivity Characteristics of the Street Network

The analysis indicated that the street network in the central parts of Termez City is relatively well developed. Central districts are characterized by a higher degree of interconnectivity between streets, providing multiple alternative routes for movement.

In contrast, peripheral districts displayed lower levels of network connectivity. These areas were characterized by longer street segments and fewer intersections, limiting route choices and potentially reducing transportation efficiency and accessibility.

Nevertheless, the existing transportation network generally provides effective connections between the city center and outer urban areas. However, several neighborhoods were found to require further improvements to their internal street networks in order to enhance overall connectivity.

Impact of Street Network Structure on Urban Development

The results demonstrated that transportation infrastructure is one of the major determinants of urban development in Termez City. Well-developed street networks and higher levels of accessibility appear to support increased construction activities and urban growth.

The analysis showed that areas with higher building densities generally correspond to locations with better-developed transportation networks. This finding suggests that the street network exerts a direct influence on the urban morphology and functional organization of the city.

Furthermore, future urban expansion in Termez City is likely to continue along existing transportation corridors. Therefore, improving transportation infrastructure in peripheral districts, enhancing street network connectivity, and adopting integrated approaches to urban development planning are essential for promoting balanced and sustainable urban growth.

Overall, the findings confirm that the street network structure is one of the key factors shaping the spatial organization and development patterns of Termez City.

DISCUSSION

The findings of this study demonstrate that the structure of the street network in Termez City has a significant influence on urban development patterns. The hierarchical organization of the street network and the spatial distribution of transportation corridors were found to be closely associated with building distribution and the overall spatial configuration of the city.

The analysis revealed that higher concentrations of buildings are primarily located along primary and secondary roads. This finding is consistent with previous international studies. For example, Porta et al. (2006) emphasized that transportation infrastructure is one of the major factors shaping urban morphology. Similarly, Sevtsuk and Mekonnen (2012) reported that areas characterized by higher levels of accessibility tend to exhibit greater economic activity and higher development intensity.

The study also showed that the central districts of Termez City possess relatively dense and well-integrated street networks. These findings support the conclusions of Boeing (2020), who argued that highly connected street networks reduce travel distances, facilitate the efficient distribution of traffic flows, and improve access to urban services.

In contrast, peripheral areas of the city were characterized by lower street density and a limited number of alternative routes. This pattern is similar to the concept of "street-network sprawl" described by Boeing (2021), which refers to declining connectivity in expanding urban areas. Such conditions may reduce transportation efficiency and restrict accessibility in the outer districts of the city.

The analysis of spatial relationships between transportation infrastructure and urban development indicated that transportation corridors play a crucial role in directing urban growth. The concentration of residential, commercial, and social infrastructure around major roads suggests that street networks significantly influence the functional organization of urban areas. These findings are in agreement with Marshall (2018), who highlighted the important role of street networks in shaping the spatial structure of cities.

The application of GIS technologies proved to be an effective approach for assessing the relationships between street networks and urban development. The integration of OpenStreetMap data with the QGIS environment provided a practical and cost-effective framework for evaluating transportation infrastructure, analyzing building distribution patterns, and producing thematic maps.

Overall, the findings of this study support existing theoretical perspectives presented in international literature and contribute to filling the research gap concerning the relationships between transportation infrastructure and urban development in medium-sized cities of Uzbekistan.

4. Conclusion

This study assessed the structure of the street network in Termez City and its influence on urban development using GIS technologies. OpenStreetMap data and the QGIS environment were employed to analyze street hierarchy, building distribution patterns, and the spatial relationships between transportation infrastructure and urban development.

The results showed that the street network of Termez City consists of trunk, primary, secondary, tertiary, residential, and service roads. Higher-order roads were found to be predominantly concentrated in the central districts of the city, forming the main transportation corridors.

The analysis of building distribution revealed that urban development is largely concentrated in areas with better transportation accessibility. In particular, residential and commercial buildings were more frequently located along primary and secondary roads, confirming the influence of transportation infrastructure on urban development.

Furthermore, the study identified higher levels of street density and connectivity within the central parts of the city, whereas peripheral districts exhibited fewer alternative routes and lower levels of accessibility. These conditions may lead to future transportation challenges and reduced mobility opportunities in outer urban areas.

Based on the findings of this study, several practical recommendations can be proposed:

- improving street network connectivity in peripheral districts;
- prioritizing transportation infrastructure in the planning of new development areas;
- creating safe and pedestrian-friendly urban environments;
- integrating transportation planning with land-use planning processes;
- expanding the use of GIS technologies in urban planning and decision-making.

In conclusion, the findings demonstrate that the street network structure is one of the key factors shaping the spatial organization and development patterns of Termez City. The results may serve as a scientific basis for improving the urban transportation system, enhancing accessibility, and supporting sustainable urban development strategies.

Future studies should incorporate additional indicators, including traffic flow characteristics, pedestrian movement patterns, public transport accessibility, and space syntax measures, to provide a more comprehensive understanding of the relationships between transportation infrastructure and urban development.

References

[1] Marshall, S., Gil, J., Kropf, K. et al. Street Network Studies: from Networks to Models and their Representations. Netw Spat Econ 18, 735–749 (2018). https://doi.org/10.1007/s11067-018-9427-9

[2] Angelidou M, Psaltoglou A, Komninos N, Kakderi C, Tsarchopoulos P, Panori A (2018), "Enhancing sustainable urban development through smart city applications". Journal of Science and Technology Policy Management, Vol. 9 No. 2 pp. 146–169, doi: https://doi.org/10.1108/JSTPM-05-2017-0016

[3] Zhao, L., Wang, S., Wei, J., & Chen, R. (2022). Impacts of land use on urban road network vulnerability. Journal of Urban Planning and Development, 148(3), Article

04022032. https://doi.org/10.1061/(ASCE)UP.1943-5444.0000862

[4] Yuan, J., Wang, H., & Fang, Y. (2023). Identification of Critical Links in Urban Road Network Based on GIS. Sustainability, 15(20), 14841. https://doi.org/10.3390/su152014841

[5] Ergashova, M.Z., Bobonazarov, T.S. (2025). Greening City Streets and Roads in Modern Urban Conditions. Sustainable Development of Transport. Lecture Notes in Networks and Systems, vol 1366. Springer, Cham. https://doi.org/10.1007/978-3-031-88846-5_1

[6] Wang, X., You, S., & Wang, L. (2016). Classifying road network patterns using a multinomial logit model. Journal of Transport Geography, 58, 104–112. https://doi.org/10.1016/j.jtrangeo.2016.11.005

[7] Ergashova, M., Sodikov, J., & Musulmanov, K. (2025). Analysis of the concept of a "15-minute city" connected by pedestrian green zones: A theoretical review. Engineer, 3(4), 101-106.

[8] Sevtsuk, A., & Mekonnen, M. (2012). Urban network analysis: A new toolbox for ArcGIS. Revue Internationale de Géomatique, 22(2), 287–305. https://doi.org/10.3166/rig.22.287-305.

Information about the author

Mokhichekhra Ergashova	Tashkent State Transport University, Teacher of the Department of Urban infrastructure engineering and artificial intelligence Email: mohichexra1995@gmail.com https://orcid.org/0000-0001-6636-6206
Umidjon Gulomov	Termez State University, Teacher of Engineering and Agrotechnology Email: umidgulomov777@gmail.com https://orcid.org/0009-0005-5057-6862
Khurshidbek Narzullaev	Termez State University, Teacher of Engineering and Agrotechnology Email: beklarbek1995@gmail.com https://orcid.org/ 0000-0002-2860-1962
Zafar Jalolov	Termez State University, Teacher of Engineering and Agrotechnology Email: zfrjllv@gmail.com https://orcid.org/0009-0009-2736-4473

Development of an automated pavement condition assessment tool based on Ge-Road mobile monitoring data and the ASTM D6433 methodology

M.A. Malikov[1][a], F.K. Jumaev[1]
[1]Tashkent state transport university, Tashkent, Uzbekistan

Abstract: This article investigates the possibilities of processing pavement distress data collected through the Ge-Road mobile application and automatically calculating the Pavement Condition Index (PCI) in accordance with the ASTM D6433 international standard. The study focuses on the digitalization of pavement distress assessment procedures, the reduction of human-related calculation errors, and the development of an Excel-based automated evaluation tool that is practical and accessible for road maintenance organizations. The proposed approach enables rapid assessment of pavement conditions, accurate identification of maintenance needs, and improved efficiency in operational decision-making processes. The results demonstrate the potential of integrating mobile data collection and automated analysis tools to enhance pavement management practices and support more effective maintenance planning.

Keywords: Ge-Road, Pavement Condition Index (PCI), ASTM D6433, pavement condition, road maintenance, mobile monitoring, automation, Microsoft Excel, pavement distress

1. Introduction

Roads are among the most important components of transportation systems. The technical condition of pavement directly affects traffic safety, vehicle operating costs, and the service life of road infrastructure. Therefore, regular monitoring of pavement conditions and the timely implementation of maintenance measures are among the primary responsibilities of road management agencies.

One of the most widely used methods for pavement condition assessment is the Pavement Condition Index (PCI) methodology based on the ASTM D6433 international standard. This methodology evaluates pavement condition on a scale from 0 to 100 by considering the type, quantity, and severity of pavement distresses [1,2].

However, the PCI calculation process involves numerous intermediate computations. In particular, determining distress density, identifying deduct values, calculating corrected deduct values, and deriving the final PCI score become increasingly complex when dealing with large datasets. As a result, the influence of human error increases and the time required for analysis becomes significantly greater [3].

In recent years, mobile technologies have been widely adopted for pavement condition monitoring. In particular, the Ge-Road mobile application enables the rapid collection of pavement distress information, including distress types, geographic coordinates, and photographic records. Nevertheless, the processing of these data in accordance with the ASTM D6433 methodology and the automated calculation of PCI values have not been sufficiently investigated [4,5].

Therefore, the objective of this study is to develop an Excel-based automated system for pavement condition assessment and PCI calculation using data collected through the Ge-Road mobile application. The proposed system aims to simplify the evaluation process, reduce human-related calculation errors, and improve the efficiency of pavement management and maintenance decision-making.

Literature review

The Pavement Condition Index (PCI) methodology has been widely used for pavement condition assessment and maintenance decision-making processes. Originally developed by the U.S. Army Corps of Engineers, the methodology was later adopted as the ASTM D6433 standard and has become an internationally recognized approach for evaluating pavement conditions [3].

The PCI methodology enables pavement condition to be expressed as a numerical indicator by considering the type, quantity, and severity of existing pavement distresses. This method is extensively applied in the assessment of highways, airport pavements, and urban street networks.

In recent years, increasing attention has been given to the digitalization of pavement monitoring processes. Mobile applications and Geographic Information System (GIS)-based technologies have significantly expanded the possibilities for rapid collection, storage, and management of pavement distress data. Such approaches contribute to reducing inspection costs, improving data accuracy, and simplifying pavement monitoring procedures [6].

Nevertheless, many existing studies have not adequately addressed the development of automated algorithms for processing data collected through mobile monitoring systems in accordance with the ASTM D6433 methodology and calculating PCI values automatically. In particular, scientific research on integrating data collected through the Ge-Road mobile application into an automated PCI calculation system remains limited [7,8].

Therefore, investigating the potential for automated PCI calculation based on Ge-Road mobile application data and developing a practical Excel-based evaluation tool represent both scientifically and practically significant research objectives.

2. Research methodology

The Small Ring Road, one of the principal arterial roads in Tashkent City, was selected as the study area. This

[a] https://orcid.org/0000-0002-2175-6240

roadway serves as a major transportation corridor connecting different parts of the city and operates under conditions of high traffic demand. Due to its strategic importance and intensive utilization, the road provides a suitable case study for evaluating pavement condition and assessing the effectiveness of automated PCI calculation methods.

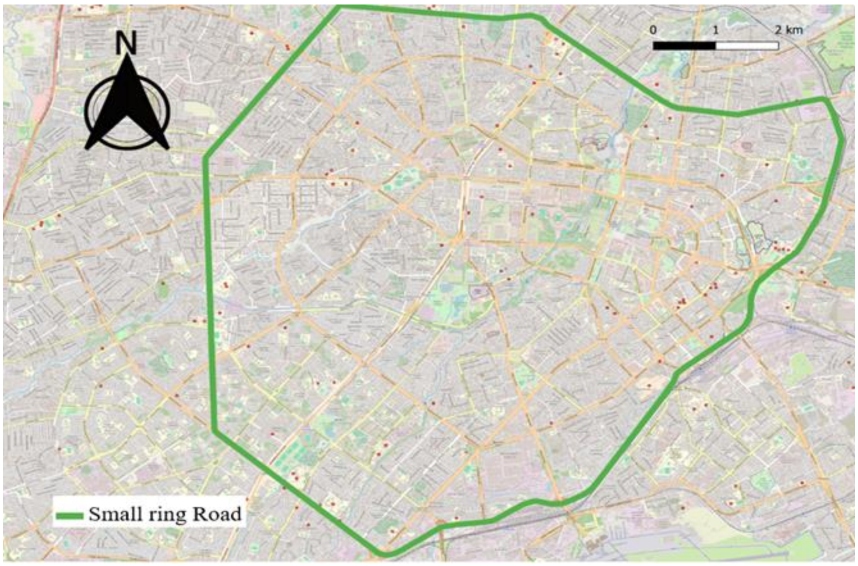

Fig-1. Small ring road map in Tashkent city

The study covered a 32.3 km section of the Small ring Road. The roadway is surfaced with asphalt concrete pavement, and for pavement condition assessment purposes, it was divided into individual 250-meter sections in accordance with the requirements of the ASTM D6433 methodology [3].

Pavement distresses within each section were recorded using the Ge-Road mobile application, and a digital database was subsequently created to store and manage the collected information for further analysis. This database served as the primary source for the automated PCI calculation and pavement condition evaluation.

Fig-2. General View of the Major Pavement Distresses Identified on the Small Road in Tashkent City

During the study, pavement conditions on the selected sections of the Small Ring Road in Tashkent City were monitored using the Ge-Road mobile application. The monitoring process identified various pavement distresses, including longitudinal and transverse cracking, pavement deformations, surface deterioration, and potholes. The location and condition of each distress were recorded and incorporated into a digital database for further analysis.

Using the Ge-Road mobile application, pavement distresses within the study area were documented based on geolocation data, enabling accurate spatial identification and mapping of defect locations. This approach facilitated the systematic collection of pavement condition information and provided a reliable dataset for subsequent PCI calculations and pavement performance evaluation [8].

https://doi.org/10.56143/3030-3893-2026-2-132-137

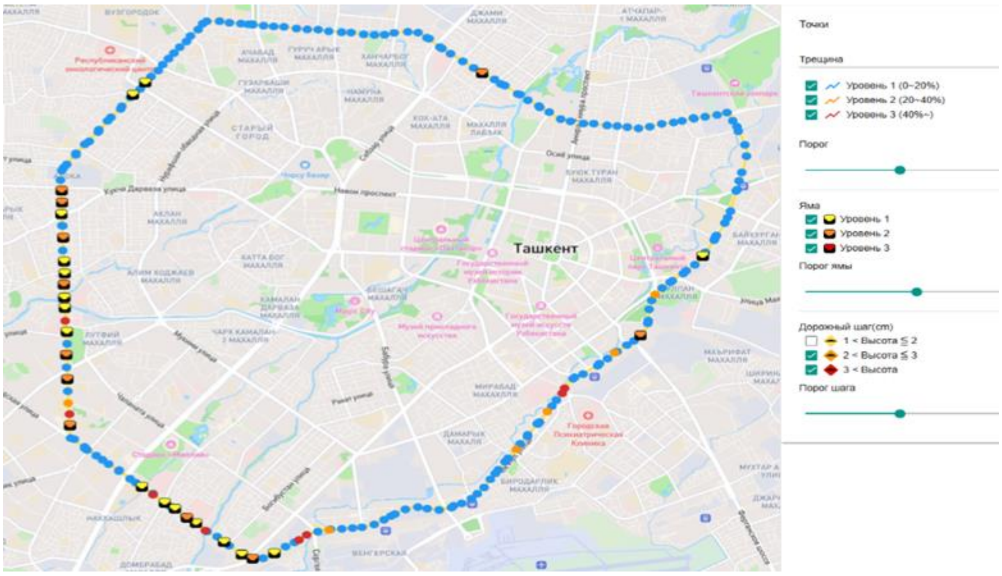

Fig. 3. Map of Pavement Distresses Identified Along the Small Road in Tashkent City Using the Ge-Road Mobile Application

The monitoring results were visualized on the map using a three-level severity classification system for cracks, potholes, and pavement deformations. These data were subsequently adapted to the requirements of the ASTM D6433 methodology and used as the basis for PCI calculation [3].

DISCUSSION AND RESULTS

Determination of Deduct Value (DV) According to the ASTM D6433 Methodology. After the pavement distresses identified through the Ge-Road mobile application were classified in accordance with the ASTM D6433 standard, Deduct Value (DV) scores were determined for each distress type. According to the ASTM D6433 methodology, the deduct value depends on the type of distress, severity level, and distress density, and is obtained using standardized deduct value curves.

In this study, three of the most frequently observed pavement distress types were selected for pavement condition evaluation:

- Longitudinal and Transverse Cracking;
- Potholes;
- Rutting

These distress types were analyzed to determine their respective deduct values, which were subsequently used in the calculation of the Corrected Deduct Value (CDV) and the final Pavement Condition Index (PCI).

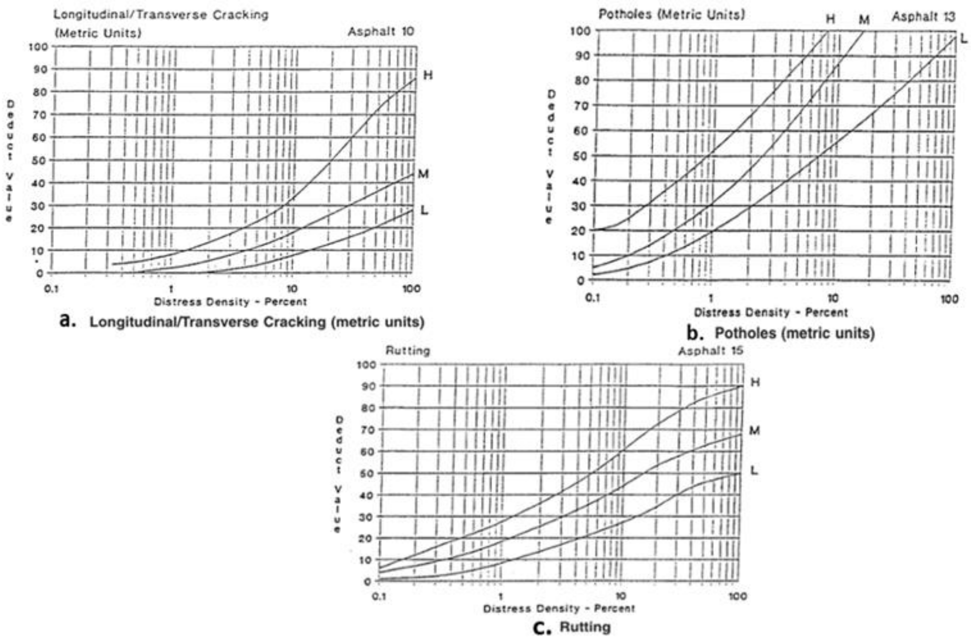

Fig. 4. Deduct Value Curves for Cracks, Potholes, and Rutting Deformations According to the ASTM D6433 Methodology

For each distress type, the severity levels (L, M, H) and density (%) values obtained from the Ge-Road system were entered into the ASTM D6433 deduct value curves, and the corresponding deduct value scores were determined.

Determination of Total Deduct Value and Corrected Deduct Value

The deduct value scores identified for each section were summed to calculate the Total Deduct Value (TDV). However, according to the ASTM D6433 methodology, the combined effect of multiple pavement distresses cannot be accurately represented by a simple summation. Therefore, the TDV values were adjusted using the Corrected Deduct Value (CDV) correction curves.

To determine the CDV, a special graph provided in the ASTM D6433 standard was used. In this graph, the horizontal axis represents the Total Deduct Value (TDV), while the vertical axis represents the Corrected Deduct Value (CDV). The parameter q denotes the number of distress types with deduct value scores greater than 2.

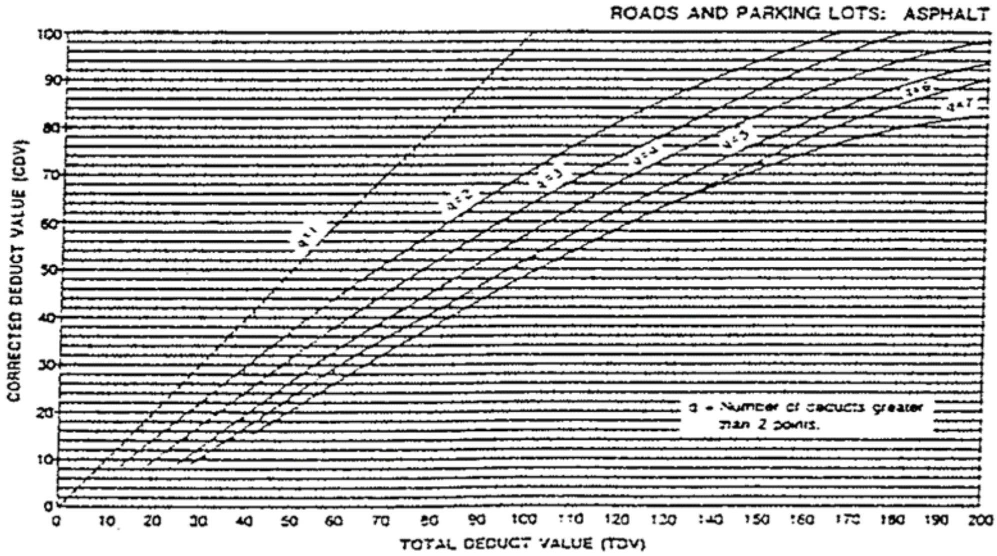

Fig. 5. Graph for Determining the Corrected Deduct Value (CDV) According to the ASTM D6433 Methodology

Calculation of the Pavement Condition Index (PCI)

After determining the Corrected Deduct Value (CDV), the pavement condition was evaluated using the Pavement Condition Index (PCI) in accordance with the ASTM D6433 methodology.

$$PCI=100-CDV \quad (1)$$

where:

PCI — Pavement Condition Index;

CDV — Corrected Deduct Value.

The PCI ranges from 0 to 100. A higher PCI value indicates a better pavement condition (1).

Excel-Based Automated PCI Calculation Model

The manual calculation of PCI according to the ASTM D6433 methodology involves multiple steps and requires processing a large volume of data. To simplify the calculation process, an automated PCI calculation model was developed using Microsoft Excel.

The model requires the user to input the following information:

distress type;

severity level (L, M, H);

density (%).

The program automatically determines:

deduct value;

total deduct value (TDV);

corrected deduct value (CDV);

PCI value;

and recommends appropriate pavement maintenance and rehabilitation actions.

In this study, the following decision-making criteria were adopted based on the calculated PCI values:

PCI	Recommended Maintenance Action
PCI < 40	Reconstruction
40 ≤ PCI ≤ 70	Repair Works
PCI > 70	Preservation Works

Figure 3.5. Automated PCI Calculation Model Developed Based on the ASTM D6433 Methodology.

Within the scope of this research, an automated calculation model was developed in the Microsoft Excel environment to process data obtained from the Ge-Road mobile monitoring system in accordance with the ASTM D6433 methodology. After entering the pavement distress type, severity level (L, M, H), and density (%), the program automatically calculates the Deduct Value (DV), Total Deduct Value (TDV), Corrected Deduct Value (CDV), and Pavement Condition Index (PCI).

In addition, based on the calculated PCI results, the developed model automatically generates recommendations for pavement preservation, maintenance, rehabilitation, or reconstruction. This approach significantly simplifies the calculation process, minimizes the influence of human error, and improves the efficiency of operational decision-making.

Development of an Automated PCI Calculation Program

As a result of the research, an automated PCI calculation program compliant with the ASTM D6433 methodology was developed using data collected from the Ge-Road mobile monitoring system. The program was created in the Microsoft Excel environment and designed to process key pavement distress data [9].

The developed program consists of the following functional modules:

Selection of pavement distress type;

Determination of severity level;

Input of density value;

Calculation of Deduct Value (DV);

Calculation of Total Deduct Value (TDV);

Determination of Corrected Deduct Value (CDV);

Calculation of Pavement Condition Index (PCI);

https://doi.org/10.56143/3030-3893-2026-2-132-137

Operational decision-making and maintenance recommendations.

Automated Pavement Condition Index (PCI) Calculation Tool

Input Ge-Road severity and density values. DV, TDV, CDV, PCI and maintenance decision are calculated automatically.

Road Section	Crack Severity	Crack Density (%)	Crack DV	Pothole Severity	Pothole Density (%)	Pothole DV	Rutting Severity	Rutting Density (%)	Rutting DV	TDV	q	CDV	PCI	Condition Rating	Maintenance Decision	Notes
R/s 1	M	3.00	8	M	0.10	4	L	2.00	14	26	3	12	88	#NAME?	Preservation works / eliminate detected distress	
R/s 2	L	6.00	5	L	0.20	6	L	1.00	9	20	3	12	88	#NAME?	Preservation works / eliminate detected distress	
R/s 3	L	8.00	7	L	1.00	20	M	0.80	12	39	3	18	82	#NAME?	Preservation works / eliminate detected distress	
R/s 4	M	8.00	16	M	0.50	14	M	5.00	36	66	4	33	67	#NAME?	Repair works	
R/s 5	L	1.00	0	L	0.20	6	M	0.60	12	18	2	7	93	#NAME?	Preservation works / eliminate detected distress	
R/s 6	H	27.00	45	M	1.00	24	L	0.50	5	74	3	44	56	#NAME?	Repair works	
R/s 7	H	10.00	33	L	0.80	12	L	0.70	5	50	3	31	69	#NAME?	Repair works	
R/s 8	L	4.00	3	L	0.30	6	L	0.80	5	14	3	5	95	#NAME?	Preservation works / eliminate detected distress	
R/s 9	M	25.00	25	M	0.30	10	M	2.00	25	60	3	37	63	#NAME?	Repair works	
R/s 10	L	4.00	3	M	0.20	10	L	2.00	14	27	3	12	88	#NAME?	Preservation works / eliminate detected distress	
										0	0	0	100	#NAME?	Preservation works / eliminate detected distress	
										0	0	0	100	#NAME?	Preservation works / eliminate detected distress	
										0	0	0	100	#NAME?	Preservation works / eliminate detected distress	
										0	0	0	100	#NAME?	Preservation works / eliminate detected distress	
										0	0	0	100	#NAME?	Preservation works / eliminate detected distress	
										0	0	0	100	#NAME?	Preservation works / eliminate detected distress	
										0	0	0	100	#NAME?	Preservation works / eliminate detected distress	
										0	0	0	100	#NAME?	Preservation works / eliminate detected distress	
										0	0	0	100	#NAME?	Preservation works / eliminate detected distress	
										0	0	0	100	#NAME?	Preservation works / eliminate detected distress	

Fig.6. Interface of the Automated PCI Calculation Program Developed in Accordance with the ASTM D6433 Methodology

As part of this research, an automated PCI calculation program was developed to process pavement condition data obtained from the Ge-Road mobile monitoring system in accordance with the ASTM D6433 methodology. Developed in the Microsoft Excel environment, the program automatically computes the Deduct Value (DV), Total Deduct Value (TDV), Corrected Deduct Value (CDV), and Pavement Condition Index (PCI) based on the pavement distress type, severity level, and density values entered by the user.

3. Conclusion

This study investigated the possibility of processing pavement distress data collected through the Ge-Road mobile monitoring application and automatically calculating the Pavement Condition Index (PCI) in accordance with the ASTM D6433 international standard. During the research, the pavement distresses identified by the Ge-Road system were matched with the corresponding distress types defined in ASTM D6433, and an algorithm was developed for determining the Deduct Value (DV), Total Deduct Value (TDV), and Corrected Deduct Value (CDV) required for PCI calculation.

As a key outcome of the study, an automated PCI calculation program was developed in the Microsoft Excel environment. The program enables the automatic determination of PCI values and recommended maintenance actions based on the pavement distress type, severity level, and density values entered by the user.

The proposed approach simplifies the multi-stage calculations required by the ASTM D6433 methodology, reduces computation time, minimizes the influence of human error, and enhances the practical utilization of data obtained from the Ge-Road mobile monitoring system. The developed program can serve as an effective tool for road agencies to rapidly assess pavement conditions, identify maintenance needs, and support the digitalization of pavement management and operational decision-making processes.

References

[1] Alavi, A. H., & Buttlar, W. G. (2018). Pavement condition index estimation using smartphone-based accelerometers for the city of Houston. Transportation Research Record, 2672(40), 1–10.

[2] Douangphachanh, V., & Oneyama, H. (2014). A study on the use of smartphones for road roughness condition estimation. Journal of Civil Engineering and Architecture, 8(6), 719–726.

[3] ASTM International. (2017). ASTM D6433-17: Standard practice for roads and parking lots pavement condition index surveys. West Conshohocken, PA: ASTM International.

[4] Wang, H., Li, X., Li, P., & Zhou, H. (2019). Pavement distress detection using smartphone sensors and machine learning algorithms. Sensors, 19(9), 1–18.

[5] GE-ROAD. (2024). GE-ROAD (GELOCAL EYEZ) mobile application documentation. https://www.ge-road.com

[6] QGIS Development Team. (2023). QGIS geographic information system. Open Source Geospatial Foundation. https://qgis.org

[7] ASTM. (2007). ASTM D6433-07: Standard practice for roads and parking lots pavement condition index surveys. ASTM International, West Conshohocken, PA.

[8] A.G. Yunusov, B.A. Xoliqov, R.R. Soataliev Yo‘l qoplamasi transport ekspluatatsion ko‘rsatkichlarini baholashning zamonaviy usullari.

[9] World Bank – Road Asset Management / HDM-4 System.

Information about the author

Mukhammad Malikov — Tashkent State Transport University, the department of “Urban infratructure engineering and artificial intelligent” assosiate professor, (PhD)
E-mail: malikovmukhammad@gmail.com
Tel.:+998939558844

https://orcid.org/0000-0002-2175-6240

Fakhriddin Jumaev Tashkent State Transport University, the department of "Urban infratructure engineering and artificial intelligent", Master's student
E-mail: fakhriddinjumayev02@gmail.com
Tel.:+ 998990134301

Mechanics of the interaction between reinforced concrete beams and rigid stays in span structures of highway overpasses

S.S. Salikhanov[1], B.E. Abzairov[1]

[1]Tashkent state transport university, Tashkent, Uzbekistan

Abstract: This article examines the mechanics of interaction between reinforced concrete beams and rigid stays used in span structures of highway overpasses. Theoretical principles of combined work, differential deformation equations, matrix formulation, and numerical simulation are presented. Based on modeling of a three-span system (49.5 + 75.0 + 49.5 m), the effect of stay bending stiffness on the distribution of bending moments and deflections is analyzed. Engineering recommendations are proposed regarding stiffness optimization, anchorage configuration, and joint detailing. The findings contribute to enhancing the reliability and seismic resistance of bridge structures in high-load and earthquake-prone zones.

Keywords: rigid stays, reinforced concrete beams, highway overpass, span structure, bending stiffness, numerical modeling, stress-strain state, MIDAS Civil

1. Introduction

Modern transportation construction imposes ever more stringent requirements on the load-bearing systems of bridges and overpasses, especially under conditions of high traffic density, seismicity, and constrained urban development. One promising direction has been the use of rigid stays within reinforced-concrete span structures, which not only transmit longitudinal forces but also resist bending moments and shear forces, thereby enhancing the spatial stability of the structure. Unlike conventional flexible stays, rigid stays possess inherent structural stiffness and act as struts, carrying not only tensile but also bending loads. This transforms them into full-fledged elements of the stiffness framework, substantially altering the behavior of the span structure. Such a solution is particularly effective for high-speed highway overpasses, where minimizing deflections, redistributing forces, and improving stability are critical [1], [2]. With the advancement of modeling technologies (MIDAS Civil, LIRA-SAPR, SCAD), it has become possible to investigate in detail the mechanics of interaction between reinforced-concrete beams and rigid stays under static and dynamic loading, including seismic effects. Numerical models can identify actual zones of stress concentration, clarify force transfer mechanisms at attachment nodes, and optimize the system configuration [3]–[5]. Research on this topic has broadened in recent years. Zhang Z. et al. [6] and Bahar Esfahani [7] examine the stress-strain behavior of elements in stay-cable bridges with rigid inclusions. Within the CIS, V.G. Petrov [8] and I.A. Semenov [9] were the first to comprehensively consider rigid stays applied to reinforced-concrete beam systems, noting reductions in peak bending moments of 25–30 % compared to traditional beams. These works laid the foundation for a new design approach to composite systems. Beyond their structural and analytical advantages, rigid stays enable a reduction in the mass of the span structure by redistributing loads onto the pylons, improve architectural aesthetics, and decrease pier costs by reducing beam cross-sections [10]. All these factors make them particularly attractive for constructing overpasses in densely populated areas, for rehabilitating aging viaducts, and in seismically active regions. The aim of this paper is to examine the mechanical principles governing the interaction of rigid stays and reinforced-concrete beams, to formulate a mathematical model of their combined behavior, to analyze the results of numerical simulations, and to provide engineering recommendations for design.

Research objectives:

- To analyze the structural features and connection details;
- To derive the equations describing the joint action of the beam and the stay;
- To perform numerical modeling on the example of a three-span overpass;
- To offer recommendations for the application of rigid stays on high-speed highways.

Thus, this paper is intended to deepen both the theoretical and practical aspects of the mechanics of rigid stays within reinforced-concrete structures, opening new prospects for the optimization of bridge systems.

2. Research methodology

Structural scheme and main elements of the span structure with rigid stays. In modern highway overpasses equipped with rigid stays, spatial systems are employed in which reinforced-concrete beams, pylons, and rigid stays act together as a unified assembly. This system ensures force redistribution, reduced deflections, and stability under longitudinal and transverse loads.

Three analytical schemes are considered, each with average span lengths (without specifying a particular static scheme or accounting for the width of the monolithic transverse girders at the pylon level):

Reinforced-concrete beams. The primary load-bearing elements are reinforced-concrete beams and slabs of various types and sizes, selected according to the span lengths. Key data for the analytical schemes are as follows

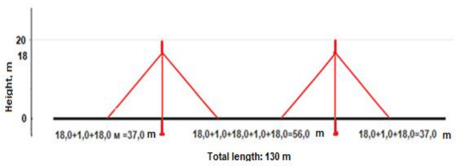

Fig. 1. Analytical Scheme No. 1 – Span Structure with Rigid Stays

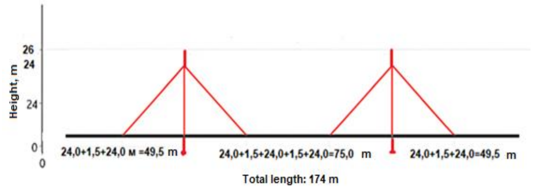

Fig. 2. Analytical Scheme No. 2 – Span Structure with Rigid Stays

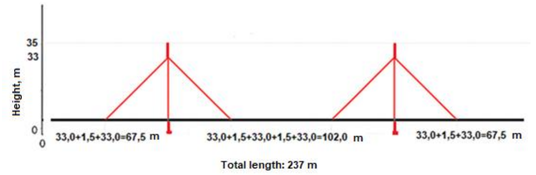

Fig. 3. Analytical Scheme No. 3 – Span Structure with Rigid Stays

- Scheme № 1: Double-hollow slabs 18 m long, arranged into spans of 37.0 + 56.0 + 37.0 m. Slab depth is 0.75 m. Rigid stays are rigidly anchored to monolithic transverse girders measuring 1.0 × 0.75 m, provided every 18.0 m (see Fig. 1).
- Scheme № 2: Prestressed ribbed beams 24 m long. Overall span arrangement is 49.5 + 75.0 + 49.5 m. Beam depth is 1.2 m. Monolithic transverse girders are 1.5 × 1.2 m in section. Rigid stays are rigidly anchored to these girders, provided every 24.0 m (see Fig. 2).
- Scheme № 3: Identical beams 33 m long, with spans of 67.5 + 102.0 + 67.5 m. Beam depth is 1.5 m. Rigid stays are rigidly anchored to monolithic transverse girders measuring 1.5 × 1.5 m, provided every 33.0 m (see Fig. 3).

The carriageway width is 15 m, corresponding to four traffic lanes of 3.75 m each. In the transverse direction, there are 18 double-hollow slabs laid at 1.0 m centers for Scheme № 1, or 8–9 beams laid at 2.1 m centers (including monolithic joints) for Schemes № 2 and № 3. The span structure rests on the transverse girders and supports with rigid stays, ensuring spatial stability and uniform force distribution.

Rigid stays. Rigid stays consist of steel tubular or box-section elements 24–35 m long, acting in bending, tension, and shear. Their inclination angle is approximately 45°. The stay design enables them to resist bending moments and transverse forces, transforming them into full-fledged stiff elements analogous to the diagonals of spatial trusses. This fundamentally distinguishes them from flexible cables [1], [6], [8]. In all schemes, there are four stays per pylon (two on each side). They are anchored at deck level to monolithic transverse girders, rigidly connected to the ends of the reinforced-concrete beams.

Pylons and anchorage. The pylons are A-shaped columns with a cross-section of 1.5 × 1.5 m. Their height above deck level varies by scheme:

- Scheme № 1: 18 m
- Scheme № 2: 24 m
- Scheme № 3: 33 m

The anchorage zones where the stays connect to the pylons are reinforced and designed to transfer bending moments as well as accommodate possible horizontal loads (wind, seismic). The pylon carries all the forces from the inclined stays and transfers them to the supports and foundations, acting as a cantilever at an angle.

Interaction scheme. All three analytical schemes employ a three-span configuration with pylons located at the joints between spans. This arrangement optimally captures the forces in the stays and effectively controls deflections and the stress state of the span structure. The rigid stays, inclined at approximately 45°, together with the beams form a spatial lattice structure in which the primary load is redistributed among the bottom chords (beams), the diagonals (stays), and the columns (pylons), creating a stable geometry under external loads.

Theoretical foundations of the interaction between reinforced-concrete beams and rigid stays. General provisions. The combined action of reinforced-concrete beams and rigid stays is viewed as the interaction between a flexible horizontal beam and an inclined rigid element joined at a connection point. Unlike conventional systems with flexible stays, a rigid stay transmits not only axial force but also bending moment and possesses its own bending stiffness, leading to a substantially different force distribution in the span system [3],[8].The system is analyzed as jointly working elements with differing stiffnesses. The beam is modeled according to classical bending theory, while the rigid stay is treated as an inclined elastic member with bending stiffness and an axial force.

Bending equation of the reinforced-concrete beam. For the span structure (the stiffness beam), the classical Euler–Bernoulli elasticity equation applies:

$$EI_b \cdot \frac{d^4 w(x)}{dx^4} = q(x) \qquad (1)$$

where

- EI_b is the bending stiffness of the span beam;
- *w(x)* is the vertical deflection;
- *q(x)* is the distributed load.

The rigid stay is attached to the beam at x=ax = ax=a, where a localized change in support reaction occurs and a bending moment may be introduced by the connected stay.

Governing equation for the rigid stay. Considering a rigid stay fixed at an angle α\alphaα to the horizontal, its transverse bending under axial force N is governed by:

$$EI_v \cdot \frac{d^4 y(s)}{ds^4} + N_s \cdot \frac{d^2 y(s)}{ds^2} = 0 \qquad (2)$$

where

- *EIv* is the bending stiffness of the stay;
- *N(s)* is the axial force at section *s*;
- *y(s)* is the transverse displacement along the stay's length s∈[0,ℓ].

This equation captures the effect of initial tension or compression on the stay's deformability. When rigidly clamped, the stay can transmit bending moments to both ends.

Boundary conditions and coupling. At the node connecting the beam and the stay, the following conditions are satisfied:

Compatibility of vertical displacements:

$$w(a) = y(0)\sin(\alpha) \qquad (3)$$

Equilibrium of bending moment and shear force:

$$Mb(a)=Mv(0);, \qquad Vb(a)=Vv(0)\sin\alpha \qquad (4)$$

where:

- *Mb* and *Vb* - are the bending moment and shear force in the beam;

- *Mv* and *Vv* - are the bending moment and shear force in the stay.

Thus, the system is mechanically coupled, and at the connection point the interaction of bending and axial forces is manifested.

Matrix Formulation of the Problem. For numerical modeling, it is convenient to use the matrix form of the system of equations, where the displacement and force vectors are combined into a global system:

$$[K]\cdot\{u\}=\{F\} \tag{5}$$

where:

- *[K]* — the global stiffness matrix of the entire system, accounting for the flexural stiffness of the beam *EIb*, the stiffness of the stay *EIv*, as well as the axial force *N*;
- *{u}* — the nodal displacement vector of the system (including coupling conditions);
- *{F}* — the vector of external loads.

At the connection node of the stay (on the beam and on the pylon), additional matrix constraints are introduced, corresponding to clamping conditions, moment continuity, and geometric compatibility.

Stress-Strain State (SSS) of the System. Force. Distribution in the beam. The reinforced concrete beam, operating as part of a system with rigid stays, is subjected to a combined action: uniformly distributed load *q(x)*, concentrated support reactions, and horizontal/vertical forces from the stays.

In the numerical formulation, combinations of variable loads were considered as prescribed in [SP 35.13330.2011], [ShNK 2.05.03–22], and as implemented in MIDAS Civil.

The following were specifically taken into account:

Permanent loads:

- self-weight of the beam and slab;
- weight of transverse beams, pylons, and stays;
- prestressing in the beams (TENDON model);

Variable loads:

- vehicular load (A14, NK-100 — both as uniformly distributed and lane load);
- temperature effects (from −20 °C to +35 °C);
- seismic load (9-point intensity zone according to SP 14.13330 and ShNK);
- erection and service load combinations, including traffic in one or two lanes simultaneously.

Load Combinations Considered:

The following load combinations (for stress-strain analysis) were taken into account in the model:

- Permanent + short-term loads: G+Q1G + Q_1G+Q1;
- Permanent + temperature + seismic: G+T+EG + T + EG+T+E;
- Permanent + multi-lane traffic + T + E: the most unfavorable combination for the stay.

Load combinations were applied according to the regulatory framework, using reliability and combination factors *(γf,ψi)*.

To describe the internal stress state in the beam section, standard expressions are used:

Shear force:

$$V_{(x)}=\frac{dM(x)}{dx} \tag{6}$$

Normal stresses in extreme fibers:

$$\sigma_{(x)}=\frac{M(x)\cdot y}{I} \tag{7}$$

where:

- *M(x)* — bending moment at section xxx;
- *y* — distance from the neutral axis to the fiber;
- *I* — moment of inertia of the section.

Maximum stresses occur at mid-span as well as in the regions where the rigid stays connect (locations with abrupt stiffness changes and applied moments).

State of the Rigid Stay. The rigid stay is subjected to the following loads:

- Axial force *Nv* (from the self-weight of the span structure and prestressing);
- Bending moment at the connection point (depending on the stiffness and inclination angle);
- Shear force at the ends, resulting from the connection with the beam and the pylon.

The internal forces in the stay are determined from boundary conditions and equilibrium:

Axial force:

$$N_{(v)}=\frac{H}{\cos(\alpha)}=\frac{R_x}{\cos(\alpha)} \tag{8}$$

Bending moment (at the lower connection node):

$$M_{(v)}=-EI_v\cdot\frac{d^2y}{ds^2} \tag{9}$$

where

EI_v is the flexural stiffness of the stay, and the second derivative is evaluated numerically (or analytically in simplified models).

Influence of Stay Stiffness on the Beam's Stress-Strain State. The stiffness of the stay directly affects the redistribution of bending moments between the central span and the pylon zones. As *EIv* increases, the following effects are observed:

- reduction of beam deflections in the spans;
- redistribution of bending moment from the mid-span toward the ends;
- increase in moments and stresses at the stay-to-beam connection point.

Specific Behavior of the Connection Node. The connection node between the beam and the stay is the zone of the highest concentration of moments and stresses. The following phenomena occur here:

- Bending moment *Mb* transferred from the stay;
- Shear force *V;*
- the need for rigid anchorage of reinforcement in both the beam and the pylon.

To ensure reliable force transfer:

- monolithic transverse beams with reinforcement (analogous to diaphragms) are used;
- anchorage devices are designed as rigid fixings capable of resisting moments up to 80–100 kN·m [6], [9].

Modeling and Numerical Example. Selection of the Structural Scheme. It is important to note that the structural schemes No. 1 to No. 3 discussed above can, in principle, be implemented either as simply supported (discontinuous) or as continuous systems. Depending on the chosen static scheme of the overpass structure, the design spans will differ.

For the numerical analysis, Scheme No. 2 is considered — a three-span continuous system with rigid stays (see Fig. 4):

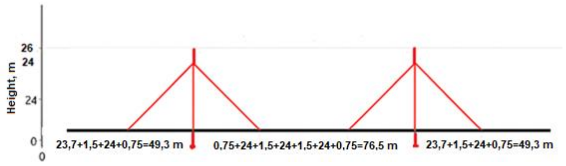

Fig. 4. Structural Scheme No. 2 — Continuous Span System with Rigid Stays

Design spans: 49.3 + 76.5 + 49.3 m. Bending moments and deflections are determined at the following cross-sections (horizontally, from the left abutment to the right): 0 m; 24.45 m; 49.95 m; 75.45 m; 100.95 m; 126.45 m; 151.95 m; 176.4 m.

Type of span structure: precast prestressed reinforced concrete beams, 24 m in length and 1.2 m in height;

- Roadway width: 15 m (4 lanes of 3.75 m), with 9 beams in the transverse direction;
- Pylons: A-shaped, 24 m high, with rigid anchorage of the stays at deck level;
- Rigid stays**:** 4 from each pylon, inclination angle — 45°, length of each stay — 24 m, cross-section — steel tube Ø 325 mm;
- Transverse beams at beam ends: cross-section 1.5 × 1.2 m, ensuring rigid connection between the stays and beams;
- Material: concrete class B40, reinforcement A500C.

Loads considered: A14, NK-100, self-weight, temperature effects, seismic loads (9-point seismic zone).

Computational Model. The model was built in MIDAS Civil using the TENDON function (for simulating prestressed elements) and element links between beam ends and the pylons via rigid stays. The beams and stays are modeled as volumetric beam elements, taking into account:

- flexural stiffness;
- prestressing;
- boundary conditions (rigid fixing at stay ends);
- real geometry and loading.

The system was solved using a linear static formulation, followed by refinement based on displacement results.

3. Results and discussion

Calculation Results. Bending Moments. The table below presents the bending moment values at **eight key points** along the span axis (including stay connection nodes, pylons, mid-spans, and abutments), under the following assumptions:

- *EIv*=0 (flexible stay),
- *EIv*=10^3,10^4,10^5,10^6 and $5\cdot10^6$ kN·m².

Analysis Object:

- System: Three-span continuous — 49.5 + 75.0 + 49.5 m
- Beams: Reinforced concrete, height 1.2 m, 9 beams across the width
- Rigid stays: 2 from each pylon, inclination ~45°, spacing 25.5 m
- Evaluation sections: 8 points along the axis (from 0 to 176.4 m)
- Load type: Uniformly distributed load (symmetric case)

If you need the graph based on this table or its insertion into a Word file — I can generate it right away.

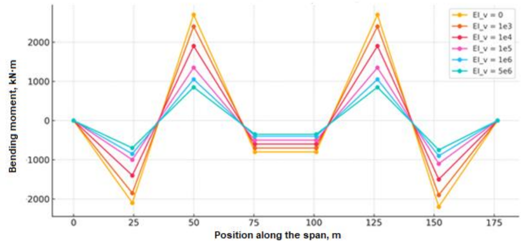

Fig. 5. Bending moment diagrams for Scheme No. 2 at various stay stiffness values from *EIv*=0 (flexible stay) to *EIv*=5·10⁶ kN·m²

Conclusions: As the stiffness of the stays increases, the negative bending moments near the pylons decrease by nearly a factor of 4. The positive moments in mid-span regions are also reduced to 25–30% of their initial values. The bending moment diagram becomes more uniform and flattened, resulting in lower reinforcement requirements and reduced internal forces. Deflection of the Span Structure. As a result of the numerical analysis, the following deflection values were obtained for Scheme No. 2.

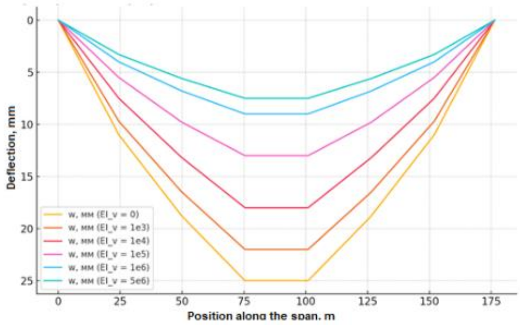

Fig. 6. Deflection graph for Scheme No. 2 at various stay stiffness values from EIv=0 (flexible stay) to EIv=5·10⁶ kN·m²

Conclusions: With increasing stay stiffness, deflections decrease by nearly **3.5 times**. A clear **symmetry of deflection** is observed about the center of the span system (under uniform loading). Stays are effective as **spatial stiffness elements**, especially when EIv>104EI_v > 10^4EIv>104 kN·m².

Practical Recommendations for Designing Span Structures with Rigid Stays. Selection of Structural Scheme.

- Optimal span configurations:
- Ribbed beams: 2×24 + 3×24 + 2×24 m; 2×33 + 3×33 + 2×33 m
- Hollow-core slabs: 2×18 + 3×18 + 2×18 m

Design Parameters for Rigid Stays. Recommended stiffness range: *EIv*=10^4÷10^6 kN·m² Geometry: tubular elements Ø325–426 mm, wall thickness 10–14 mm. Inclination angles — 45°, as optimal for structural efficiency. Stay anchorage — into transverse beams with a cross-section of at least 1.5 × 1.2 m

https://doi.org/10.56143/3030-3893-2026-2-138-143 A bridge between science and innovation

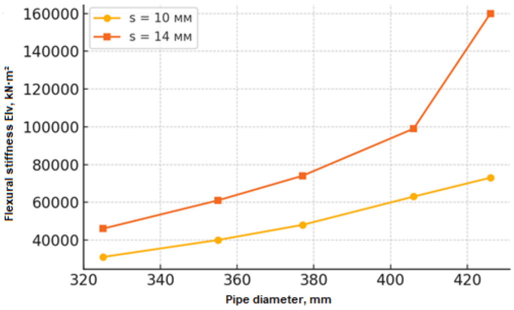

Fig. 7. Graph of Flexural Stiffness *EIv* vs. Pipe Diameter

From this graph (Figure 7), the following can be observed:

- At the same diameter, an increase in wall thickness significantly increases the flexural stiffness.
- In the diameter range of 325–426 mm and wall thickness of 10–14 mm, the values of *EIv* fall approximately within the range of $3{\cdot}10^4 \div 1.6{\cdot}10^5$ kN·m², which corresponds to the $10^4 \div 10^6$ kN·m² range used in design calculations.

Engineering Requirements for Structural Analysis.

- Load combinations must account for permanent and variable loads.
- Mandatory use of 3D numerical modeling (e.g., MIDAS Civil or LIRA-SAPR).
- Sensitivity analysis is required to assess the effect of changes in the stiffness of stays and main beams.
- Uniform load distribution across the beams should be ensured (9 beams for a carriageway width of 15 m).

Reinforcement and Structural Connections.

- Prestressed beams: 8 tendons with 24 wires Ø5 mm
- Transverse ties and diaphragms: every 6–12 m, especially near the stay anchorage points.
- Connection nodes between pylon and beam: rigid fixings with moment control.
- Recommendations for anchoring rigid stays to the pylon: anchorage height — not less than 24 m.

Seismic Resistance and Durability.

- Minimum concrete grade: B40; reinforcement: A500C.
- Resistance to temperature-induced deformations; installation of expansion joints for total bridge length exceeding 100 m.
- Corrosion protection of rigid stays and their joints.
- Structural reliability under seismic action up to 9 points.

Recommendations for Operation and Maintenance.

- Monitoring of deflections and forces through control sections (at pylons and mid-span zones).
- Consideration of deformations from prestressing effects.
- Inspection schedule: at least once every 5 years, using UAVs or robotic systems.

General Recommendations.

- Priority use of rigid stays under high-load conditions and where strict deflection limitations apply.
- Possibility to reduce beam cross-sections due to the load-bearing contribution of rigid stays.
- Efficiency: up to 15–25% concrete savings and 30–40% reduction in deflections.
- Architectural expressiveness can be achieved along with sound engineering optimization.

4. Conclusion

The use of rigid stays significantly increases the spatial stiffness of the system and reduces internal forces in the beams.

Selecting a stiffness of approximately $EIv \approx 10^5$–10^6 kN·m² achieves an optimal balance: moderate stay dimensions, efficient beam performance, and simplified reinforcement.

The system becomes less sensitive to further increases in EIv beyond 10^6 kN·m², which is important for engineering optimization and cost-efficiency.

Critical sensitivity range: 10^4–10^5 kN·m² — this is where the most rapid reduction in moments and deflections is observed. Further increases in stay stiffness lead to saturation of the effect.

References

[1] SP 35.13330.2011. Bridges and Pipes. Updated Edition of SNiP 2.05.03-84. — Moscow: Ministry of Regional Development of Russia, 2011.

[2] ShNK 2.05.03–22. Bridges and Pipes. — Tashkent: Uzstandard, 2022.

[3] Zhang, Z., Zhang, Z., Xie, X., Li, H. (2021). Condition Assessment of Stay Cables in Cable-Stayed Bridges. arXiv preprint arXiv:2101.03701.

[4] Isaev, A.M., Khomenko, G.D. (2018). Cable-Stayed Bridge Structures and Analysis of Spatial Systems. — Moscow: Transport.

[5] Semyonov, I.A. (2021). BIM in Infrastructure Construction. — Moscow: Infra-Engineering.

[6] MIDAS Civil User Manual. MIDAS IT. (2022). Available at: www.midasoft.com.

[7] Tekla Structures Documentation. Trimble Solutions Corporation. (2022). Available at: https://www.tekla.com.

[8] Podolny, W., Scalzi, J.B. (1986). Construction and Design of Cable-Stayed Bridges. Wiley-Interscience.

[9] Troitsky, M.S. (1990). Cable-Stayed Bridges: Theory and Design. Wiley-Interscience.

[10] Kozlov, V.V., Smyslov, A.Yu. (2015). Seismic-Resistant Bridge Design. — St. Petersburg: Transproject.

Information about the author

Saidkhon Salikhanov	Tashkent State Transport University, Candidate of Technical Sciences, Professor of the Department of Bridges and Tunnels E-mail: saidkhansalikhanov@gmail.com Tel.: +998 95 957 19 51

Bakhodir Abzairov Tashkent State Transport University, Doctoral student
E-mail: abzairov_b@tstu.uz
Tel.: +998 90 644 61 99

Investigating the tribological properties of thermoplastic polymer composite materials based on local raw materials

U.A. Ziyamukhamedova[1][a], L.Y. Bakirov[2][b], E.T. Turgunaliev[1][c], A.F. Soliev[2][d]

[1]Tashkent state transport university, Tashkent, Uzbekistan

[2]Andijan state technical institute, Andijan, Uzbekistan

Abstract: This study investigates the tribological and physicomechanical properties of a thermoplastic polymer composite material based on polypropylene, modified with walnut shell pyrolysis residue as a local raw material. The composite's composition consists of 65 wt.% polypropylene, 15 wt.% fine-fraction walnut shell pyrolysis residue, 4 wt.% glycerol monostearate, 1 wt.% zinc oxide, and 15 wt.% R-grade glass fiber. The scientific concept of the research is to reduce the coefficient of friction, increase surface hardness, and ensure the dimensional stability of the material through the synergistic effect of a carbon-rich natural waste-based filler, a glass fiber reinforcing component, and an anti-friction additive within the polypropylene matrix. Composite samples were prepared via the extrusion method. Tribological tests were performed under dry sliding conditions with a contact pressure of 2 MPa and a sliding speed of 0.5 m/s. Furthermore, the material's hardness was assessed using the Shore D method, and its mechanical strength was evaluated by its ultimate tensile strength. The results revealed that the composite with the optimal composition had a coefficient of friction of 0.08, which was significantly lower than that of the comparative sample. For this composition, the ultimate tensile strength was 48.6 MPa, and the coefficient of linear thermal expansion was 0.0001 mm/ (m·°C). The findings indicate that walnut shell pyrolysis residue is significant not only as a simple, low-cost filler in the polypropylene matrix but also as a tribologically active carbon component. Glycerol monostearate, as an additive that reduces friction and facilitates the processing stage, and zinc oxide, as a functional modifier, enhance the operational properties of the composite. R-grade glass fiber increases the load-bearing capacity, hardness, and dimensional stability. The proposed composite material is recommended as a promising material for polymer pipes, protective coatings, and sliding elements that operate in contact with abrasive particles.

Keywords: thermoplastic composite, polypropylene, walnut shell pyrolysis residue, glass fiber, zinc oxide, glycerol monostearate, coefficient of friction, abrasive wear

1. Introduction

Thermoplastic polymer composites are increasingly regarded as promising engineering materials for applications in which the use of conventional metallic materials is limited by cost, density, corrosion resistance or processing complexity. Among thermoplastic matrices, polypropylene (PP) occupies a special position due to its low density, good chemical resistance, relatively low cost, ease of melt processing and wide industrial availability. These advantages make PP attractive for pipes, protective liners, sliding components, guide elements and structural parts operating under moderate mechanical and thermal loads. However, neat polypropylene does not always provide sufficient performance under tribological conditions. Its comparatively low surface hardness, tendency to adhesive wear, viscoelastic deformation under contact pressure and relatively high thermal expansion may reduce dimensional stability and shorten service life in abrasive or sliding-contact environments.

In many engineering systems, especially pneumatic conveying pipes, polymer liners, sliding guides and elements exposed to bulk materials or abrasive particles, the material must simultaneously exhibit low friction, adequate mechanical strength, resistance to surface damage and stable dimensions under temperature variation. Therefore, the development of reinforced and functionally modified PP-based composites with improved tribological behavior is an important scientific and practical task in modern materials engineering. The solution of this task requires not only the selection of a suitable polymer matrix, but also the rational combination of reinforcing fillers, carbonaceous modifiers and processing additives capable of forming a stable structure at the filler–matrix interface.

The development of such composites is closely related to the principles of sustainable materials science. Agricultural wastes and biomass-derived residues can be converted into value-added functional fillers through pyrolysis. As a result of pyrolytic treatment, lignocellulosic materials acquire a carbon-rich porous structure, improved thermal stability and surface characteristics that may promote mechanical interlocking with polymer melts. In comparison with untreated natural fillers, pyrolyzed biomass residues are less hydrophilic and can demonstrate better compatibility with hydrophobic polyolefin matrices. Previous studies on biochar-filled PP composites have shown that carbonaceous fillers may improve stiffness, thermal stability and resistance to degradation, depending on their origin, particle size, pyrolysis temperature and dispersion quality in the polymer matrix [1–3].

Walnut shell is one of the locally available lignocellulosic wastes and can be considered a promising

[a] https://orcid.org/0000-0001-5005-0477
[b] https://orcid.org/0009-0007-84712089
[c] https://orcid.org/0000-0003-3257-5434
[d] https://orcid.org/0009-0008-2670-3149

https://doi.org/10.56143/3030-3893-2026-2-144-151

raw material for producing carbon-rich filler. Raw walnut shell powder contains polar functional groups and is usually poorly compatible with non-polar polypropylene. Such incompatibility may lead to weak interfacial adhesion, filler agglomeration and deterioration of mechanical properties. In contrast, walnut shell pyrolysis residue contains a higher carbon fraction and a modified surface structure, which can improve its interaction with the PP matrix. From the materials science point of view, the use of walnut shell pyrolysis residue provides two important advantages: first, it enables the valorization of local agricultural waste; second, it introduces a carbonaceous phase that can contribute to friction reduction and stabilization of the tribological contact zone.

Hybrid reinforcement is another effective approach for improving the performance of polypropylene composites. Short glass fibers are widely used in thermoplastic composites to increase stiffness, tensile strength, load-bearing capacity and dimensional stability. Under tribological contact, glass fibers can partially redistribute the applied load and reduce excessive deformation of the polymer matrix. However, their effect is strongly dependent on fiber content, fiber length, orientation, dispersion quality and interfacial adhesion with the matrix. Excessive fiber content or poor fiber encapsulation may lead to fiber exposure on the worn surface and intensify abrasive interaction with the counter-body. Therefore, an optimal balance between the polymer matrix, carbonaceous filler and fibrous reinforcement is essential for obtaining a low-friction and wear-resistant composite.

In addition to reinforcing components, functional additives play an important role in controlling both processing behavior and service properties of thermoplastic composites. Glycerol monostearate is commonly used as a lubricant, antistatic agent and processing aid in polymer systems. In the molten state, it can reduce internal friction between polymer chains, filler particles and reinforcing fibers, improve melt flow and decrease adhesion of the polymer melt to metallic surfaces of processing equipment. In tribological applications, glycerol monostearate may also contribute to the reduction of sliding friction by improving surface release behavior and supporting the formation of a more stable interfacial layer during dry contact. Zinc oxide is a multifunctional inorganic modifier that can improve thermal stability, UV resistance and surface-related functional properties of PP-based materials [4]. Its presence in the composite may additionally contribute to hardness and stabilization of the polymer-filler system.

The scientific novelty of the present work lies in the development and tribological assessment of a locally sourced polypropylene-based thermoplastic composite containing walnut shell pyrolysis residue, glycerol monostearate, zinc oxide and R-grade glass fiber. The proposed composition is designed to combine the advantages of a PP matrix, a carbon-rich biomass-derived filler, fibrous reinforcement and functional modifiers in one hybrid material system. The research hypothesis is that the synergistic interaction of these components can reduce the coefficient of friction while maintaining mechanical strength and thermal-dimensional stability.

Accordingly, the aim of this study is to investigate the tribological properties of a polypropylene-based thermoplastic polymer composite produced using local raw materials and to evaluate the relationship between composition, processing, friction behavior, mechanical integrity and dimensional stability. The obtained results are expected to provide a scientific basis for the use of walnut shell pyrolysis residue as a functional carbonaceous filler in PP composites intended for polymer pipes, protective liners and sliding elements operating in abrasive particulate environments.

2. Research methodology

In this study, crosslinked polypropylene (PP) was selected as the polymer matrix forming a single continuous thermoplastic phase. In the updated formulation, PP was considered as the only polymer matrix component. The selection of this matrix phase was justified by its relatively low density, chemical stability, ease of processing, and improved resistance to collapse, sliding deformation and load-induced dimensional changes compared with unreinforced polypropylene.

Walnut shell pyrolysis residue with a particle size below 1–2 mm was used as a carbonaceous filler. This filler is a carbon-rich component obtained from locally available agricultural waste, with a reported specific surface area of 874 m^2/g. According to its elemental composition, the pyrolysis residue contains approximately 87 wt.% carbon, while phosphorus, sulfur and other mineral residues are present in smaller amounts. The incorporation of this pyrolysis residue into the composite was aimed at forming a tribologically active carbonaceous phase in the PP matrix, improving surface stability during friction, and enabling the effective utilization of local raw-material resources.

Glycerol monostearate was introduced into the composite as a processing lubricant and anti-friction additive. Its function is to improve the flowability of the molten composition, reduce internal friction between the polymer matrix, filler particles and reinforcing components, and decrease the adhesion of the material to the metallic surfaces of extrusion equipment. Zinc oxide was selected as an inorganic functional modifier. It contributes to the improvement of surface properties, thermal stability and service durability of the composite. R-grade glass fiber was used as the main reinforcing component to enhance stiffness, load-bearing capacity, mechanical strength and thermal-dimensional stability.

Table 1

Optimized formulation of the PP-based thermoplastic polymer composite

Component	**Function in the composite**	**Content, wt.%**
Crosslinked polypropylene (PP)	Thermoplastic matrix and continuous load-bearing phase	65
Walnut shell pyrolysis residue, <1–2 mm	Local carbonaceous filler and tribological modifier	15
Glycerol monostearate	Processing lubricant, anti-friction additive and release aid	4
Zinc oxide	Inorganic modifier for stability and surface functionality	1
R-grade glass fiber	Reinforcement for stiffness, strength and dimensional stability	15

https://doi.org/10.56143/3030-3893-2026-2-144-151

2.2. Preparation of walnut shell pyrolysis residue

Walnut shell was selected as a locally available agricultural waste and was pre-treated to obtain a carbonaceous functional filler. First, the raw material was cleaned from mechanical impurities, dried and subjected to pyrolysis under oxygen-limited conditions. As a result of pyrolysis, the lignocellulosic raw material was converted into a carbon-rich solid residue. The obtained product was ground and sieved to separate a fraction smaller than 1–2 mm.

The main purpose of pyrolysis was to reduce the hydrophilicity typical of raw walnut shell powder, increase the carbon content, and improve interfacial compatibility with the hydrophobic PP matrix. This is important because polar functional groups in natural lignocellulosic fillers can lead to weak adhesion with non-polar polyolefin matrices such as PP. After pyrolysis, the chemical nature and microstructure of the filler surface are modified, which can promote mechanical interlocking with the polymer melt and improve interfacial bonding.

Before composite preparation, the pyrolysis residue was dried to remove moisture. This step is essential because excessive moisture during melt processing may cause porosity, local degradation, gas release and the formation of interfacial defects.

2.3. Composite compounding and specimen preparation

The PP-based thermoplastic composite was prepared under laboratory conditions by melt compounding followed by extrusion. In the first stage, calculated amounts of crosslinked PP and walnut shell pyrolysis residue were introduced into the mixing zone. The mixture was heated to 160–170 °C to melt the PP matrix. Within this temperature range, melting of the polymer matrix, wetting of carbonaceous filler particles and penetration of the polymer melt into the micro-pores of the filler surface are expected to occur. This may strengthen mechanical interlocking at the filler–polymer interface and improve the structural integrity of the composite.

After the initial mixing stage, the composite mass was cooled to approximately 50 °C. In the next stage, zinc oxide and R-grade glass fiber were added. The mixture was homogenized for 5 min to ensure uniform distribution of the functional modifier and reinforcing fibers throughout the matrix volume. Then, glycerol monostearate in the molten state was introduced, and mixing was continued until a homogeneous composite mass was obtained.

The prepared composite mass was extruded through a die in the form of strands, cooled to approximately 30 °C and cut into granules with a diameter of 2–4 mm and a length of 3–5 mm. In the subsequent stage, the composite granules were processed by extrusion to obtain test specimens in the form of tapes with an approximate thickness of 0.5 mm. During the preparation of test tapes, the temperature zones of the extrusion unit were set at 120, 140, 160 and 180 °C, respectively.

Table 2

Technological processing route of the PP-based thermoplastic composite

Stage	Temperature or condition	Purpose
Initial mixing of matrix and carbonaceous filler	160–170 °C	Melting of the PP matrix and wetting of pyrolysis residue particles with polymer melt
Cooling before addition of ZnO and glass fiber	~50 °C	Reducing thermal influence and creating controlled mixing conditions
Mixing of ZnO and R-grade glass fiber	5 min	Uniform distribution of the functional modifier and reinforcing fibers in the matrix
Addition of glycerol monostearate	Molten additive	Improving melt flow and reducing internal and external friction
Strand extrusion and granulation	Cooling to ~30 °C	Obtaining granules for subsequent specimen preparation
Extrusion of test tapes	120/140/160/180 °C by zones	Formation of 0.5 mm thick test tapes

2.4. Testing equipment

The experimental methodology was developed based on laboratory equipment intended for the preparation of the composite material and the determination of its tribological and physico-mechanical properties. A laboratory melt-compounding and extrusion unit was used for specimen preparation. This equipment allows thermoplastic composite components to be mixed under controlled temperature conditions, converted into a molten state, homogenized, and formed into granules or test tapes.

An INtest-type tribological testing unit was used to evaluate sliding friction and wear behavior. This device makes it possible to determine the coefficient of friction of the composite material under controlled load and sliding speed. Surface hardness was measured using a digital Shore D durometer. The durometer was used to evaluate the local hardness of the extruded or molded specimen surface. The set of equipment is shown in Figure 1.

Fig. 1. Main equipment used in the experimental methodology: extrusion unit, tribological testing unit and digital Shore D hardness tester

2.5. Tribological testing procedure

The tribological properties of the composite specimens were evaluated under dry sliding conditions using a laboratory tribological testing unit. The coefficient of friction, μ, was selected as the main tribological parameter. The tests were carried out at a contact pressure of 2 MPa and a sliding speed of 0.5 m/s. These parameters represent a relatively severe contact regime for thermoplastic composites intended to operate in contact with abrasive particles, bulk materials or viscous technological media.

Before testing, the surface of each specimen was cleaned, conditioned at laboratory temperature and fixed in the sample holder of the testing device. The counter-body was positioned to ensure stable and uniform contact with the specimen surface. The coefficient of friction was recorded after the initial running-in period under steady-state sliding conditions. The final value was evaluated as the average of the data obtained during the stable friction regime.

When experimental mass-loss data are available, the specific wear rate of the composite can be determined using the following expression:

$$Ws = \Delta m / (\rho \cdot F \cdot L) \quad (1)$$

where Ws is the specific wear rate, Δm is the mass loss during testing, ρ is the composite density, F is the normal load, and L is the sliding distance.

In this manuscript, the coefficient of friction is presented as the main validated tribological indicator. For the final journal version, it is recommended to conduct at least three repeated tests for each composition, report the mean value and standard deviation, and additionally determine wear volume based on mass loss or 3D profilometry.

2.6. Hardness, mechanical and thermal-dimensional characterization

The surface hardness of the composite material was determined using a digital Shore D hardness tester. During measurement, the indenter was placed perpendicular to the specimen surface, and the hardness value was recorded after stabilization of the display reading. For the final scientific manuscript, it is recommended to perform measurements at no fewer than five different points for each specimen and present the average value together with the standard deviation.

Mechanical integrity was evaluated by determining the tensile failure stress of the specimens. This parameter makes it possible to assess the strength level formed as a result of the interaction between the carbonaceous filler, glass fiber, functional modifiers and the PP matrix. Thermal-dimensional stability was evaluated using the coefficient of linear thermal expansion and expressed in mm/(m·°C). This parameter is particularly important for polyolefin-based materials because high thermal expansion may lead to geometrical changes, internal stresses and reduced joint stability under service conditions.

In addition, pressure resistance and joint stability were considered as engineering performance criteria for pipe-type products. These indicators allow assessment not only of the laboratory tribological properties of the composite material, but also of its suitability for practical operation under real service conditions.

3. Results and Discussion

3.1. Composition design and interfacial justification

The composition design strategy was based on the combined action of a crosslinked polypropylene thermoplastic matrix, carbon-rich walnut shell pyrolysis residue, R-grade glass fiber and a small amount of functional modifiers. Crosslinked PP served as a continuous load-bearing thermoplastic phase, providing melt processability, chemical stability and resistance to deformation under mechanical loading. Walnut shell pyrolysis residue was introduced as a locally sourced, low-cost and carbon-rich filler capable of improving the tribological response of the polymer matrix.

From the materials science point of view, the efficiency of this filler is associated with its high carbon content and porous surface morphology. During melt compounding, the molten PP can partially penetrate the micro-pores and surface irregularities of the pyrolysis residue, promoting mechanical interlocking at the filler–matrix interface. Such interfacial interaction is important for maintaining mechanical integrity and reducing the probability of filler pull-out during sliding contact. This mechanism is consistent with the behavior reported for biochar-filled PP composites, where the infiltration of molten polymer into the porous carbonaceous filler improves interfacial bonding and contributes to enhanced composite performance [4-6].

R-grade glass fiber was used as the main reinforcing component. Its role is to increase stiffness, restrict matrix deformation under contact pressure and redistribute the applied load from the polymer surface to the internal structure of the composite. A glass fiber content of 15 wt.% was considered sufficient to provide reinforcement without excessive fiber exposure on the worn surface. Excessive fiber exposure may intensify local abrasive interaction with the counter-body and reduce the anti-friction efficiency of the composite.

Glycerol monostearate was incorporated as a processing lubricant and anti-friction additive. It improves melt flow, reduces internal friction during processing and may

https://doi.org/10.56143/3030-3893-2026-2-144-151

contribute to lower friction during dry sliding. Zinc oxide acted as a multifunctional inorganic modifier, contributing to surface stability, local hardness and thermal resistance. As a result, the developed hybrid composite system is expected to reduce friction through three main mechanisms: increased surface stiffness, reduced adhesive interaction and formation of a more stable transfer layer during sliding.

Table 3

Compared compositions used to determine the optimized formulation

Composition	PP, wt.%	Walnut shell pyrolysis residue, wt.%	GMS, wt.%	ZnO, wt.%	R-grade glass fiber, wt.%
C1	68	10	12	2	8
C2	65	12	10	1	12
C3 — optimized	65	15	4	1	15
C4	58	10	9	3	20
C5	55	12	12	1	20

3.2. Friction behavior under dry sliding conditions

The coefficient of friction values are summarized in Table 4 and illustrated in Figure 2. Among all compared formulations, the optimized C3 composition demonstrated the lowest coefficient of friction, $\mu = 0.08$, under a contact pressure of 2 MPa and a sliding speed of 0.5 m/s. For comparison, the reference D2 composition showed a coefficient of friction of $\mu = 0.21$ under the same testing conditions. This indicates that the optimized PP-based composite reduced friction by approximately 61.9% relative to the reference composition.

The other experimental compositions showed higher friction values: 0.16 for C1, 0.18 for C2, 0.14 for C4 and 0.18 for C5. These results demonstrate that a simple increase in lubricant content or glass fiber content does not automatically lead to the lowest coefficient of friction. The most effective result was obtained only when the amounts of walnut shell pyrolysis residue, glycerol monostearate and R-grade glass fiber were balanced. In particular, the combination of 15 wt.% pyrolysis residue, 4 wt.% glycerol monostearate and 15 wt.% glass fiber provided the most favorable tribological behavior.

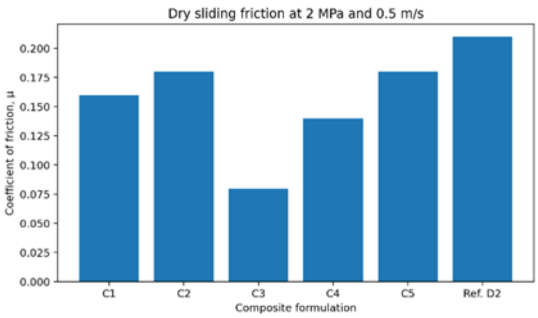

Fig. 2. Coefficient of friction of the experimental compositions and reference D2 at 2 MPa and 0.5 m/s

The reduced friction of the C3 composition can be explained by the synergistic interaction between the carbonaceous filler and the processing lubricant. Walnut shell pyrolysis residue may act as a carbon-based micro-reinforcing filler and support the formation of a carbon-rich tribolayer at the sliding interface. Such a tribolayer can reduce direct adhesive interaction between the PP surface and the counter-body. Glycerol monostearate can decrease friction associated with polymer chain mobility and improve surface release behavior. At the same time, glass fibers increase the rigidity of the surface layer and reduce the real contact area caused by viscoelastic deformation of the polymer matrix.

The higher glass fiber content in C4 and C5 did not result in the lowest friction. This may be associated with partial exposure of fibers on the contact surface, which can produce local abrasive interaction and partially compensate for the anti-friction effect of the carbonaceous filler and lubricant. Therefore, the C3 formulation represents the most balanced composition in terms of friction reduction and structural stability.

3.3. Mechanical integrity and hardness

Tribological performance cannot be evaluated separately from mechanical integrity. A composite material with low friction but insufficient strength would not be suitable for pipe liners, sliding guides, protective coatings or structural elements operating in abrasive environments. Therefore, tensile failure stress and surface hardness are important parameters for evaluating the practical applicability of the developed PP-based composite.

The optimized C3 composition showed a tensile failure stress of 48.6 MPa, which was higher than the values obtained for all other experimental compositions and significantly higher than the reference value of 28.5 MPa. The increase in tensile failure stress relative to the reference composition was approximately 70.5%. This result confirms that the reduction in friction was not achieved at the expense of weakening the polymer composite. On the contrary, the balanced combination of carbonaceous filler, glass fiber and functional modifiers improved both friction behavior and mechanical strength.

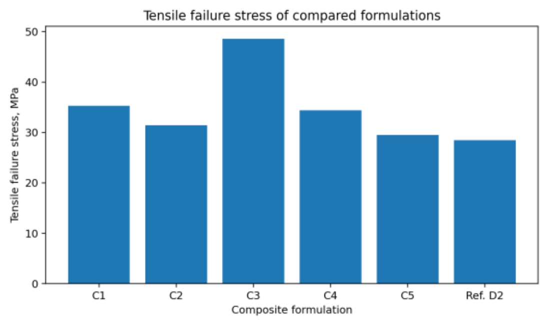

Fig. 3. Tensile failure stress of the compared compositions

The improved mechanical performance of the C3 composition may be attributed to more effective load transfer between the PP matrix, walnut shell pyrolysis residue and R-grade glass fibers. The carbon-rich filler can contribute to interfacial mechanical interlocking, while the glass fibers provide reinforcement and restrict deformation. Zinc oxide particles may additionally increase local stiffness, whereas the PP matrix maintains the necessary toughness and thermoplastic processability.

https://doi.org/10.56143/3030-3893-2026-2-144-151

Surface hardness was evaluated using a digital Shore D hardness tester. For a complete journal version, it is recommended to provide at least five measurements for each sample and report the mean value together with the standard deviation. From the materials science perspective, increased surface hardness is expected to reduce scratching by abrasive particles and limit deformation under the counter-body during sliding. In the developed composite, surface hardness is mainly supported by the combined effect of R-grade glass fiber, zinc oxide particles and carbonaceous pyrolysis residue.

3.4. Thermal-dimensional stability and pressure-related performance

Thermal expansion is one of the critical limitations of PP-based components, particularly in pipe-type structures and elements subjected to temperature variation. As shown in Figure 4, the optimized C3 composite exhibited a linear thermal expansion coefficient of 0.0001 mm/(m·°C), while the reference D2 composition showed a much higher value of 0.024 mm/(m·°C). This significant reduction indicates that the hybrid filler system effectively restricts the mobility of PP molecular chains during heating.

The low thermal expansion coefficient of the optimized composite is primarily associated with the presence of dimensionally stable phases within the thermoplastic matrix. R-grade glass fibers, zinc oxide particles and walnut shell pyrolysis residue act as reinforcing and stabilizing components. Their distribution in the PP matrix reduces the tendency of the polymer phase to undergo excessive thermal expansion. This is especially important for polymer pipes and structural elements where dimensional changes may lead to internal stresses, joint instability and leakage.

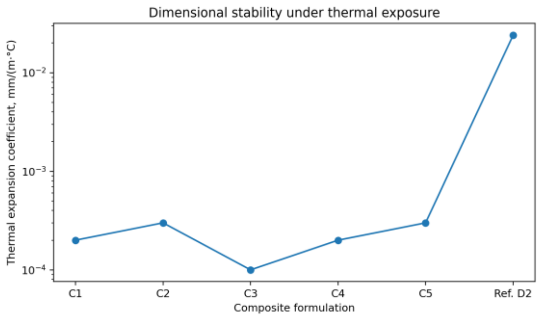

Fig. 4. Thermal expansion coefficient of the compared compositions, presented on a logarithmic scale

The C3 composition also demonstrated favorable pressure-related performance. During the leak-tightness test at 1.5 times the working pressure and 20 °C, the optimized composite showed no leakage. The resistance of pipe joints under an internal pressure of 1 MPa at 60–80 °C reached 200 h, compared with 143 h for the reference composition. In addition, joint resistance under tensile loading above 40 °C reached 22 h. These engineering indicators confirm that the improved friction behavior of the C3 composition was achieved not by compromising structural performance, but due to the synergistic effect of the hybrid filler system and PP matrix.

Table 4

Comparative properties of experimental compositions and reference D2

Property	C1	C2	C3 optimized	C4	C5	Reference D2
Tensile failure stress, MPa	35.3	31.4	48.6	34.4	29.5	28.5
Coefficient of friction at 2 MPa and 0.5 m/s	0.16	0.18	0.08	0.14	0.18	0.21
Thermal expansion coefficient, mm/(m·°C)	0.0002	0.0003	0.0001	0.0002	0.0003	0.024
Leak-tightness at 1.5 working pressure and 20 °C	Leakage after 25 s	Leakage after 25 s	No leakage	No leakage	Leakage after 20 s	Leakage after 8 s
Joint resistance at 1 MPa and 60–80 °C	175 h	175 h	200 h	170 h	170 h	143 h
Joint resistance under tensile load above 40 °C	10 h	10 h	22 h	8 h	8 h	—

3.5. Proposed wear mechanism

The proposed wear mechanism of the optimized PP-based hybrid composite is presented in Figure 5. During the initial running-in stage, the surface asperities of the composite come into contact with the counter-body. A small amount of polymer-rich material may be transferred to the sliding interface. The presence of carbon-rich walnut shell

https://doi.org/10.56143/3030-3893-2026-2-144-151

pyrolysis residue can stabilize this interfacial layer and reduce adhesive interaction between the sliding surfaces.

At the same time, R-grade glass fibers carry part of the normal load and restrict the penetration of the counter-body into the polymer matrix. This reduces the depth of surface deformation and limits the formation of severe wear grooves. Zinc oxide particles may contribute to local hardness and thermal stability, while glycerol monostearate reduces internal friction and surface adhesion tendency. As a result, the composite reaches a more stable friction regime with a lower steady-state coefficient of friction.

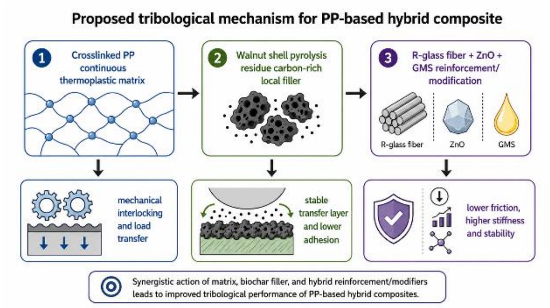

Fig. 5. Proposed mechanism for friction reduction and stability improvement in the PP-based hybrid thermoplastic composite

3.6. Sustainability and engineering significance

The use of walnut shell pyrolysis residue has practical significance beyond friction reduction. It expands the raw-material base for polymer composites by converting agricultural waste into a functional carbonaceous filler. This approach is consistent with the principles of circular economy and sustainable materials engineering, since it reduces dependence on conventional mineral fillers and creates added value from low-cost local resources.

The optimized composition does not rely on excessively high glass fiber content, which is also important from a processing point of view. Moderate fiber loading helps maintain melt processability and reduces the risk of excessive abrasive action on extrusion equipment. At the same time, the combination of glass fiber, carbonaceous filler, zinc oxide and glycerol monostearate provides a balanced relationship between mechanical strength, low friction and dimensional stability.

From an engineering application perspective, the developed composite is promising for polymer pipes, protective liners and structural elements used for transporting bulk materials, fibrous materials or viscous technological fluids containing abrasive particles. A low coefficient of friction can reduce energy losses and surface heating during material movement. High tensile strength and low thermal expansion improve dimensional stability, while pressure resistance indicates potential suitability for pipe-type systems. However, the final field of application should be selected after additional long-term tests, including abrasive wear, fatigue, water absorption, thermal aging and chemical resistance under service-specific conditions.

4. Conclusion

1. The PP-based thermoplastic composite containing 65 wt.% crosslinked polypropylene, 15 wt.% walnut shell pyrolysis residue, 4 wt.% glycerol monostearate, 1 wt.% zinc oxide and 15 wt.% R-grade glass fiber demonstrated the most balanced performance among the compared compositions.
2. Under dry sliding conditions at a contact pressure of 2 MPa and a sliding speed of 0.5 m/s, the optimized composition showed a coefficient of friction of 0.08, while the reference composition showed a value of 0.21. This corresponds to an approximately 61.9% reduction in friction.
3. The same optimized composition exhibited a tensile failure stress of 48.6 MPa, which was approximately 70.5% higher than the reference value. This confirms that friction reduction was achieved without weakening the composite structure.
4. The coefficient of linear thermal expansion decreased to 0.0001 mm/(m·°C), indicating high dimensional stability. The optimized composite also showed no leakage during the leak-tightness test and demonstrated improved pressure-related durability.
5. The observed performance improvement is attributed to the synergistic interaction of the crosslinked PP matrix, carbon-rich walnut shell pyrolysis residue, R-grade glass fiber reinforcement, glycerol monostearate lubrication and zinc oxide modification.

References

[1] Das, O.; Bhattacharyya, D.; Hui, D.; Lau, K.T. Mechanical and flammability characterisations of biochar/polypropylene biocomposites. Composites Part B: Engineering 2016, 106, 120-128. https://doi.org/10.1016/j.compositesb.2016.09.020.

[2] Ikram, S.; Das, O.; Bhattacharyya, D. A parametric study of mechanical and flammability properties of biochar reinforced polypropylene composites. Composites Part A: Applied Science and Manufacturing 2016, 91, 177-188. https://doi.org/10.1016/j.compositesa.2016.10.010.

[3] Alghyamah, A.A.; Elnour, A.Y.; Shaikh, H.; Haider, S.; Poulose, A.M.; Al-Zahrani, S.M. Biochar/polypropylene composites: A study on the effect of pyrolysis temperature on crystallization kinetics, crystalline structure, and thermal stability. Journal of King Saud University - Science 2021, 33, 101409. https://doi.org/10.1016/j.jksus.2021.101409.

[4] Li, M.; Li, G.; Jiang, J.; Zhang, Z.; Dai, X.; Mai, K. Ultraviolet resistance and antimicrobial properties of ZnO in the polypropylene materials: A review. Journal of Materials Science & Technology 2015, 31, 331-339. https://doi.org/10.1016/j.jmst.2014.11.022.

[5] Ovsik, M.; Cesnek, A.; Stanek, M. Tribological and micro-mechanical properties of modified composite polypropylene. Lubricants 2025, 13, 489. https://doi.org/10.3390/lubricants13110489.

[6] Sengul, O. Mechanical properties of recycled polypropylene composites with walnut shell additives by injection moulding. Journal of Scientific Reports-A 2025, 063.

[7] Fu, S.-Y.; Lauke, B.; Mader, E.; Yue, C.-Y.; Hu, X. Tensile properties of short-glass-fiber- and short-carbon-fiber-reinforced polypropylene composites. Composites Part A: Applied Science and Manufacturing 2000, 31, 1117-1125. https://doi.org/10.1016/S1359-835X(00)00068-3.

[8] Khan, M.; Roy, J.; Akter, N.; Zaman, H.; Islam, T.; Khan, R. Production and properties of short jute and short E-glass fiber reinforced polypropylene-based composites. Open Journal of Composite Materials 2012, 2, 40-47.

[9] ASTM D2240. Standard Test Method for Rubber Property - Durometer Hardness. ASTM International, West Conshohocken, PA, USA.

[10] ASTM G99. Standard Test Method for Wear Testing with a Pin-on-Disk Apparatus. ASTM International, West Conshohocken, PA, USA.

[11] ISO 527-2. Plastics - Determination of tensile properties - Part 2: Test conditions for moulding and extrusion plastics. International Organization for Standardization.

[12] ISO 11359-2. Plastics - Thermomechanical analysis - Part 2: Determination of coefficient of linear thermal expansion and glass transition temperature. International Organization for Standardization.

Information about the author

Umida Ziyamukhamedova	Toshkent davlat transport universiteti, “Mashinasozlik texnologiyasi” kafedrasi professori t.f.d. E-mail: shoazimovau@gmail.com Tel.: +998911915665 https://orcid.org/0000-0001-5005-0477
Lutfillo Bakirov	Andijon davlat texnika institute, “Transport logistikasi” kafedra mudiri t.f.f.d., professor E-mail: lutfillobakirov1987@gmail.com Tel: +998914913037 https://orcid.org/0009-0007-84712089
Elbek Turgunaliev	Toshkent davlat transport universiteti, “Materialshunoslik va mashinasozlik” kafedrasi dotsenti t.f.f.d., dotsent E-mail: mrelbek@mail.ru Tel.: +998999812123 https://orcid.org/0000-0001-5005-0477
Akhror Soliev	Andijon davlat texnika institute, tayanch doktoranti E-mail: soliyevaxrorbek25@gmail.com Tel.: +998934427142 https://orcid.org/0009-0008-2670-3149

Effect of multi-stage heat treatment regime parameters on the structure and mechanical properties of modified 35HML chromium-molybdenum steel

M.Z. Ubaydullaev[1], E.I. Ruklinskaya[1], U.D. Kosimov[2], N.N. Yodgorov[1], N.I. Khavasova[1]
[1]Branch of the National University of Science and Technology MISIS in the city of Almalyk, Almalyk, Uzbekistan
[2]Tashkent state transport university, Tashkent, Uzbekistan

Abstract: This paper presents the results of a comprehensive experimental study of the effect of multi-stage heat treatment regime parameters on the structure and mechanical properties of modified cast chromium-molybdenum steel 35НМЛ, used in the manufacture of cast parts for mining excavators at JSC "Almalyk Mining and Metallurgical Combine". The melt was modified with a complex Fe-V-Al-Ca ferroalloy composition (V 25–30 %, Al 15–20 %, Ca 5–10 %, balance Fe) in an amount of 0.15–0.18 wt. %, introduced into the ladle onto the metal stream at a temperature not below 1520 °C. A four-stage heat treatment scheme was developed: homogenizing annealing at 880 °C → normalization at 880 °C → quenching from 850 °C in preheated water at 60 °C → high tempering at 600–650 °C. The choice of preheated water at 60 °C as the quenching medium is experimentally justified by comparison with industrial oil И-20А: both media provide practically identical hardness (62 HRC versus 61.5 HRC), while preheated water reduces the proportion of castings rejected due to cracks from 12 % to 2 %. The dependence of hardness on tempering temperature in the range of 450–650 °C was established, and the recommended range of 600–650 °C was justified, excluding the zone of type II temper embrittlement (450–550 °C). The developed technology was implemented at the Central Repair and Mechanical Plant (CRMZ) of JSC "AMMC" (Implementation Certificate No. SL-355/1 dated April 16, 2025), providing a 35 % increase in Charpy impact toughness (from 540 ± 22 to 730 ± 31 kJ/m²) and an increase in the service life of ЭКГ-10 excavator support wheels from 2800 to 4200 hours.

Keywords: 35HML steel, complex modification, Fe-V-Al-Ca ferroalloy, multi-stage heat treatment, quenching in preheated water at 60 °C, high tempering, Charpy impact toughness, abrasive wear resistance, cast parts for mining excavators

1. Introduction

Increasing the service life and operational reliability of cast parts for mining excavators, crushing-and-grinding and ore-dressing equipment operating under conditions of intense impact-abrasive wear is one of the priority engineering tasks of the mining and metallurgical industry of Uzbekistan. At JSC "Almalyk MMC" — the country's largest mining and metallurgical enterprise — the bulk of cast parts for ЭКГ-type excavators and ball-mill liners are made of chromium-molybdenum steel 35HML (analogous to AISI 4135).

In the as-cast state, this steel is characterized by a coarse dendritic structure, segregation heterogeneity, and uneven distribution of the carbide phase, which significantly limits its service life. Traditional single-stage heat treatment does not ensure uniformity of structure and properties across the cross-section of massive cast parts of complex configuration.

A promising approach is the combination of complex melt modification with the Fe-V-Al-Ca ferroalloy composition, which provides a synergistic combination of modifying (V), deoxidizing (Al), and refining (Ca) effects, with a scientifically substantiated multi-stage heat treatment scheme. The choice of quenching medium plays a critically important role: industrial oils are environmentally unsafe and expensive, while cold water leads to high quenching stresses and crack formation in massive castings.

The aim of this work is the experimental substantiation of the multi-stage heat treatment regime parameters of modified chromium-molybdenum steel 35НМЛ — including homogenizing annealing, normalization, quenching in preheated water at 60 °C, and high tempering — ensuring an optimal combination of strength, hardness, and impact toughness of cast parts for mining equipment.

2. Research methodology

Material and complex modifier. The object of the study is cast chromium-molybdenum steel 35HML of average chemical composition (wt. %): 0.40 C; 0.51 Si; 0.73 Mn; 1.05 Cr; 0.20 Mo. The melt was modified with the Fe-V-Al-Ca ferroalloy composition (Fe 35–40 %, V 25–30 %, Al 15–20 %, Ca 5–10 %), introduced into the ladle onto the metal stream at $T \geq 1520$ °C in an amount of 0.15–0.18 wt. % with subsequent holding for 3 min. Spectral analysis confirmed the multifunctional action of the modifier: sulfur content decreased by 43 % (from 0.028 to 0.016 wt. %), total oxygen by 61 % (from 0.0072 to 0.0028 wt. %); the steel was enriched with V (0.033 %), Al (0.029 %), and Ca (0.0025 %).

Multi-stage heat treatment. A four-stage scheme was applied: (1) homogenizing annealing at 880 °C with slow furnace cooling at a rate of 30–50 °C/h down to 500 °C; (2) normalization at 880 °C (1 min per 1 mm of cross-section, air cooling); (3) quenching from 850 °C in preheated water at 60 °C; (4) high tempering at 600–650 °C with air cooling. The temperature of the quenching water was monitored with a submersible electronic thermometer (±0.5 °C).

Mechanical testing. Hardness was measured by the Rockwell (HRC) and Brinell (HB) methods. Charpy impact toughness with a V-notch (KCV) was measured on a PIT320T pendulum impact tester (maximum energy 300 J) at +25 °C. Abrasive wear resistance was determined by the Brinell–Haworth scheme on an LR-130B abrasimeter at a

https://doi.org/10.56143/3030-3893-2026-2-152-155

load of 78.4 N, a rubber-wheel rotation speed of 200 rpm, and a friction path of 720 m. The abrasive was a mixture of pyrite, chalcopyrite, and molybdenite from the “Kalmakyr” deposit (grain size 0.4 mm, pyrite microhardness up to 1510 kgf/mm²).

Flaw detection and statistics. Quenching cracks were monitored by three methods: visual inspection, the capillary (dye-penetrant) method (GOST 18442-80), and ultrasonic testing on a УД2-70 flaw detector (GOST R 55724-2013). All mechanical test results are presented as the mean ± standard deviation over three parallel specimens in each series. Confidence intervals were calculated at a confidence probability of 0.95 using the Student coefficient t = 4.303 for n − 1 = 2 degrees of freedom.

3. Results and Discussion

Hardness evolution along the multi-stage route. Fig. 1 shows the change in hardness of modified 35HML steel at the characteristic stages of multi-stage heat treatment. In the as-cast state, the hardness was 53.5 HRC. After homogenizing annealing it decreased to 24.5 HRC. Normalization restored the hardness to 47.5 HRC. Quenching from 850 °C in preheated water at 60 °C provided 62 HRC, which exceeds the value for oil quenching (61.5 HRC). Subsequent high tempering at 650 °C reduced the hardness to 33.5–38.2 HRC depending on the cooling rate.

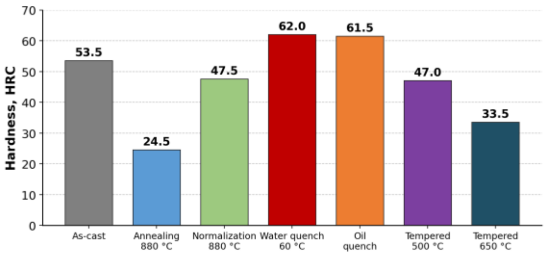

Fig. 1. Hardness evolution of modified 35XMЛ steel at various stages of multi-stage heat treatment

Comparison of quenching media. A direct experimental comparison of two quenching media was carried out: industrial oil I-20A (from 900 °C) and preheated water at 60 °C (from 850 °C). The microstructure after oil quenching consists of fine-acicular martensite with a hardness of 61.5 HRC. The microstructure after quenching in preheated water at 60 °C exhibits predominantly lath martensite with a hardness of 62 HRC, owing to the increased cooling rate of 200–300 °C/s versus 80–100 °C/s for oil.

The use of preheated water at 60 °C has decisive advantages over cold water. First, heating the water destroys the vapor film, shortening the duration of the film-boiling stage and stabilizing heat removal. Second, the cooling rate in the martensitic transformation range (300–200 °C) is reduced, which decreases quenching stresses and the risk of crack formation in massive castings. Industrial verification confirmed a reduction in the proportion of castings rejected due to cracks from 12 % (cold water) to 2 % (preheated water at 60 °C).

Fig. 2. Monitoring of the quenching medium temperature: thermometer reading of 63.0 °C in the bath with preheated water

Effect of tempering temperature. A detailed series of experiments with tempering temperatures from 450 to 650 °C established a monotonic dependence of hardness on tempering temperature (Fig. 3): 51 HRC at 450 °C, 47 HRC at 500 °C, 36 HRC at 550 °C, and 33.5 HRC at 650 °C. The decrease is associated with the progressive coagulation of the carbide phase and the decomposition of tetragonal martensite. The recommended tempering range of 600–650 °C is justified by two factors: it ensures complete coagulation of the carbide phase and keeps the steel out of the zone of type II temper embrittlement (450–550 °C). For applications where increased hardness is critical, reduced tempering at 450–500 °C with a hardness of 47–51 HRC is permissible.

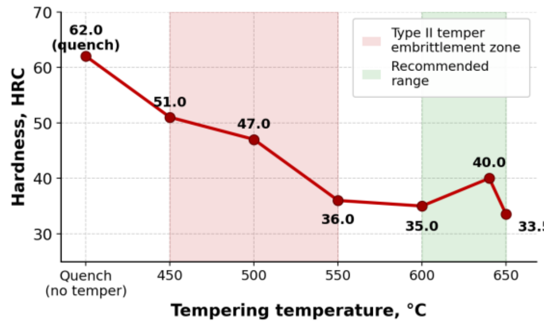

Fig. 3. Dependence of the hardness of modified 35XMЛ steel on tempering temperature after quenching in preheated water at 60 °C

Comparative mechanical properties. Comparative tests of four groups of specimens (without modifier, FeV, Fe-V-Al-Ca, FeMo) confirmed the pronounced positive effect of complex modification on the mechanical properties of 35HMЛ steel (Table 1). All specimens underwent an identical multi-stage heat treatment cycle: annealing 880 °C → normalization 880 °C → quenching from 850 °C in preheated water at 60 °C → high tempering 600–650 °C.

Table 1
Mechanical properties of 35XMЛ steel modified with various ferroalloys (mean ± σ, n = 3)

Modifier	Specific wear, mg/m	ε (rel.)	KCV, kJ/m²	+KCV, %
Without modifier	0.149 ± 0.006	1.000	540 ± 22	—
FeV	0.134 ± 0.005	1.117 ± 0.044	680 ± 28	+26 %
Fe-V-Al-Ca	0.120 ± 0.004	1.244 ± 0.045	730 ± 31	+35 %
FeMo	0.116 ± 0.004	1.289 ± 0.046	800 ± 34	+48 %

The complex Fe-V-Al-Ca modifier provides an optimal combination of properties at moderate cost: although FeMo demonstrates marginally better individual indicators, its cost is substantially higher and its modifying effect is monofunctional. Fe-V-Al-Ca simultaneously refines the primary structure (via V(C,N) carbonitrides), deeply deoxidizes the melt (Al → Al_2O_3), and modifies the morphology of non-metallic inclusions (Ca → globular sulfides).

Industrial implementation and economic effect. The developed technology was introduced into the production practice of the CRMZ of JSC "Almalyk MMC" (Implementation Certificate No. SL-355/1 dated 16.04.2025). Technological Regulation TR 001.18-04:2025 was developed and approved. The service life of ЭКГ-10 excavator support wheels was increased from 2800 to 4200 hours (+50 %). The annual economic effect per ЭКГ-10 excavator amounts to 31.6 million UZS due to the reduction in the number of replacements from 2.32 to 1.55 per year. The total annual economic effect for the ЭКГ-10 excavator fleet (12 units) is about 380 million UZS, with a payback period for the capital investment (50 million UZS) of 1.6 months.

4. Conclusion

The parameters of the multi-stage heat treatment regime of cast chromium-molybdenum steel 35XML modified with the complex Fe-V-Al-Ca ferroalloy composition were experimentally substantiated:

1) A scientifically substantiated four-stage heat treatment scheme was developed: homogenizing annealing 880 °C → normalization 880 °C → quenching from 850 °C in preheated water at 60 °C → high tempering 600–650 °C.

2) The use of preheated water at 60 °C as the quenching medium provides hardness equivalent to oil quenching (62 versus 61.5 HRC) at a higher cooling rate (200–300 versus 80–100 °C/s) and reduces the proportion of castings rejected due to cracks from 12 % to 2 % compared with cold water.

3) The dependence of hardness on tempering temperature in the range of 450–650 °C was established. The recommended range of 600–650 °C ensures complete coagulation of the carbide phase and keeps the steel out of the zone of type II temper embrittlement.

4) Comparative tests of four modifier variants confirmed the advantages of Fe-V-Al-Ca: a 35 % increase in impact toughness (540 → 730 kJ/m²) and a relative abrasive wear resistance of up to 1.244 ± 0.045.

5) The technology was implemented at JSC "Almalyk MMC". The annual economic effect is about 380 million UZS with a payback period of 1.6 months.

References

[1] Khalikulov U.M., Nabiev E.S., Khudoyarov S.R., Ubaydullaev M.Z., Ruklinskaya E.I. The influence of modifiers on the structure and properties of 35XMЛ steel // Chernye Metally (Ferrous Metals). — 2026. — No. 4 (1132). — pp. 78–84. (Scopus). DOI: 10.17580/chm.2026.04.11.

[2] Ubaydullaev M.Z., Ruklinskaya E.I., Kosimov U.D. Selection and substantiation of a technology for increasing the wear resistance of ball-mill liners // Engineer. International Scientific Journal. — Tashkent: TSTU, 2025. — Vol. 3, Issue 2. — pp. 119–120. DOI: 10.56143/engineer-tstu.v3i2.83.

[3] Ubaydullaev M., Ruklinskaya E., Kosimov U., Khalikulov U. Enhancing the strength of steel grade 45 guide rails for ball rolling using the chemical-thermal carbonitriding method // Vibroengineering Procedia. — 2025. — Vol. 60. — pp. 114–119.

[4] Ubaydullaev M., Ruklinskaya E., Kosimov U., Khalikulov U. Technology of surface hardening of teeth of excavator buckets by composite carburizing method // Vibroengineering Procedia. — 2025. — Vol. 60. — pp. 352–357.

[5] Ryabchikov I.V., Golubtsov V.A., Bakin I.V. Complex modifiers for cast steels: composition, technology, and application. — Chelyabinsk: Metallurgiya Publishing House, 2020. — 312 p.

[6] Marukovich E.I., Stetsenko V.Yu. Modification of steels and cast irons with ferroalloy compositions: theoretical foundations and industrial practice // Liteynoe Proizvodstvo (Foundry Production). — 2022. — No. 5. — pp. 12–18.

[7] Polishko S.O., Rozenberg E.V. The influence of vanadium carbonitrides on the grain structure of low-alloy cast steels // Metal Science and Heat Treatment of Metals. — 2021. — No. 3. — pp. 38–44.

[8] Novikov I.I. Theory of heat treatment of metals. — Moscow: Metallurgiya, 2013. — 480 p.

[9] GOST 977-88. Steel castings made of structural carbon and alloy steel. General specifications. — Moscow: Standartinform, 2002.

[10] GOST 9454-78. Metals. Method of testing for impact bending at low, room, and elevated temperatures. — Moscow: Standartinform, 1994.

Information about the author

Muzaffar Ubaydullaev	Almalyk Branch of NUST MISIS, Department of Metallurgy of Ferrous, Non-Ferrous and Rare Metals, Doctoral student (PhD) Tel.: +998 93 391 49 79 E-mail: muzaubaydullaev@gmail.com

Elena Ruklinskaya	Almalyk Branch of NUST MISIS, Department of Metallurgy of Ferrous, Non-Ferrous and Rare Metals, Assistant Tel.: +998 93 919 02 81 E-mail: ruklinskayaelena97@yandex.ru	**Yodgorov Nusratilla**	Almalyk Branch of NUST MISIS, Department of Metallurgy of Ferrous, Non-Ferrous and Rare Metals, Student Tel.: +998772759030 E-mail: nusret.yodgorovich@gmail.com
Umidbek Kosimov	Tashkent State Transport University E-mail: umidbek.k@yandex.ru Tel.: +998999812123 https://orcid.org/0000-0001-5005-0477	**Khavasova Nikhola**	Almalyk Branch of NUST MISIS, Department of Metallurgy of Ferrous, Non-Ferrous and Rare Metals, Student E-mail: xavasovanihola@gmail.com

Analysis of the influence of barometric pressure on the passage of photosynthetically active radiation of the sun through the atmosphere

H.H. Asadov[1][a], Kh.S. Aliyeva[1][b], U.F. Mammadova[2][c]

[1]National Aerospace Agency, Baku, Azerbaijan

[2]Azerbaijan State University of Oil and Industry, Baku, Azerbaijan

Abstract: The influence of atmospheric optical thickness on the transmission of photosynthetically active solar radiation to the Earth's surface is analyzed. Specifically, it is considered that Rayleigh scattering, a component of atmospheric optical density, depends on the atmospheric pressure at the given location. Taking into account the influence of pressure, the problem of studying the possibility of an extreme value of atmospheric optical thickness in areas with high atmospheric pressure is formulated. Model calculations using the Buchholz model and a variational optimization problem demonstrate that such a maximum can occur at negative wavelengths, which, in principle, do not exist in nature. Therefore, the answer to the formulated question is that extreme values of atmospheric optical density should not be expected in the PAR component wavelength range due to the influence of atmospheric pressure.

Keywords: atmosphere, solar radiation, barometric pressure, photosynthetically active optical radiation, optimization

1. Introduction

The role of solar optical radiation in sustaining life on the planet is well known [1-3]. It is important to emphasize the consistency between the properties and functions of the atmosphere and solar optical radiation in terms of sustaining life on the planet. For example, harmful ultraviolet radiation from the Sun with a wavelength below 0.35 µm is not transmitted by the atmosphere to the Earth's surface, and conversely, photosynthetically active solar radiation in the range of 0.5–0.7 µm is transmitted by the atmosphere with minimal attenuation [4-6].

At the same time, as emphasized in the work [7-8], insolation on the earth’s surface is the most important factor for studying the relationship between the Earth and the atmosphere as a single dynamic system.

Thus, insolation, i.e., solar optical radiation at the Earth's surface, is a measure of the coordination of the aforementioned components of the unified dynamic system supporting life on the planet, taking into account the aforementioned diversity of possible influences of solar optical radiation existing outside the atmosphere. In this regard, one possible area for further research is to examine the influence of various atmospheric components and factors on the passage of the photosynthetically active part (hereinafter PAR) of solar optical radiation to the Earth's surface.

PAR radiation maintains the phenological rhythm or phase of development of the plant world.

In this regard, it is important to note the unit of measurement of PAR radiation. While solar radiation density is measured in watts/m2 , PAR radiation is measured in different units that take into account the interaction of this radiation with living molecules. This unit of measurement is $\frac{мкмол}{м^2/сек}$, denoting the number of photons in a certain wavelength range (400–700) nm involved in the process of photosynthesis occurring in the molecules of living organisms. Thus, PAR is estimated as a certain number of moles of photons per unit area per unit time, in the visible range for which there are 6.023 x ^{1023} photons per mole (Avogadro's number).

The most important atmospheric component affecting the attenuation of PAR radiation reaching the Earth's surface. Aerosols consist of liquid or solid particles, the sizes of which vary from several tens of nanometers to several micrometers [8]. A distinction is made accordingly between fine, medium, and coarse aerosols. The classic formula for determining the optical density of atmospheric aerosols is the Ångström formula [9]:

$$\tau_\alpha = \beta \cdot \lambda^{-\gamma} \quad (1)$$

where τ_α is the optical density of atmospheric aerosol;

β – aerosol turbidity of the atmosphere;

γ – Angstrom exponent;

λ – wavelength, µm.

From (1) we obtain

$$\beta = \tau_\alpha, \quad \text{при } \lambda = 1 \text{ мкм}$$

Other atmospheric components that influence the attenuation of PAR radiation reaching the Earth's surface are atmospheric ozone and Rayleigh scattering of atmospheric gases.

In general, the optical thickness of the atmosphere in the range of 0.4÷0.7 µm is defined as

$$\tau = \tau_{ozone} + \tau_R + \tau_{aer} ,$$

where τ_{ozon} is the optical thickness of ozone;

τ_R – optical thickness of Rayleigh scattering;

τ_{aer} – optical thickness of atmospheric aerosol.

However, it is well known that the optical density of Rayleigh scattering depends on atmospheric pressure [10].

In general, there is a Buchholz model for calculating the optical density of the atmosphere in the visible range in the following form [7]

[a] https://orcid.org/0000-0003-1180-1535

[b] https://orcid.org/0009-0002-6657-3445

[c] https://orcid.org/0000-0002-8953-3001

$$\tau_\alpha = \left(\frac{P}{P_0}\right) \cdot A \cdot \lambda \cdot \left(-B - C \cdot \lambda - \frac{D}{\lambda}\right) \qquad (2)$$

where P / P_0 is the ratio of the actual barometric pressure in a particular area to the standard pressure at sea level (1013.25 mbar);

λ – wavelength in micrometers;

A , B , C , D are constant coefficients, the values of which will be given below.

As can be seen from expression (2), τ_α is directly dependent on P, i.e., the pressure at a given location. The research problem is formulated as follows: determine the wavelength at which, due to abnormally high pressure, the optical density of the atmosphere could reach its maximum , which would presumably lead to a strong attenuation of the photosynthetically active PAR component of solar optical radiation. Let us consider the proposed solution to this problem.

2. Research methodology

We rewrite expressions (2) in the following form

$$\tau_\alpha = -(AB \cdot \lambda \cdot \gamma) + A\gamma\lambda^2 C + AD\gamma \qquad (3)$$

Where

$$\gamma = \frac{P}{P_0} \qquad (4)$$

Let us introduce for consideration the average integral indicator of the optical density of the atmosphere in the form

$$\tau_{\alpha cp} = \frac{1}{\Delta\gamma} \int_{\gamma_{min}}^{\gamma_{max}} -(AB \cdot \lambda \cdot \gamma + AC\lambda^2\gamma + AD\gamma) d\gamma \qquad (5)$$

Where

$\Delta\gamma = \gamma_{max} - \gamma_{min}$

We also introduce for consideration the relationship function between λ and γ in the form

$$\lambda = f(\gamma) \qquad (6)$$

Further, to calculate the specific form of function (6), we will assume that the function f (γ) can be selected from a certain set of twice differentiable and continuous functions satisfying the following restrictive condition:

$$\int_{\gamma_{min}}^{\gamma_{max}} f(\gamma)\, d\gamma = C_1 \,; \quad C_1 = const \qquad (7)$$

Taking into account expressions (5) ÷ (7), we form the following target functional F of variational optimization

$$F = \frac{1}{\gamma_{max}} \int_0^{\gamma_{max}} -[ABf(\gamma)\gamma d\gamma + ACf(\gamma)^2 \cdot \gamma + AD\gamma]\, d\gamma + L\left[\int_0^{\gamma_{max}} f(\gamma)d\gamma - C_1\right] \qquad (8)$$

where L is the Lagrange multiplier.

The solution according to Euler's method satisfies the following condition

$$d\frac{\{-[ABf(\gamma) + ACf(\gamma)^2 \cdot \gamma + AD\gamma] + Lf(\gamma)\}}{df(\gamma)} = 0 \qquad (9)$$

From condition (9) we obtain

$$-[AB\gamma + 2AC \cdot \gamma \cdot f(\gamma) + AD] + L = 0 \qquad (10)$$

From expression (10) we find

$$f(\gamma) = \frac{L}{2AC\gamma} - \frac{AB}{2AC} - \frac{D}{2C\gamma} \qquad (11)$$

When solving (11), the functional F reaches a maximum, which is easily verified using the Lagrange criterion, according to which an extremum is a maximum if the derivative of expression (10) with respect to the function f (γ) is negative. It is easy to verify that this condition is satisfied.

To determine the value of L, we use expressions (7) and (11). We have

$$\int_{\gamma_{min}}^{\gamma_{max}} \left(\frac{L}{2AC} + \frac{D}{2C}\right)\frac{d\gamma}{\gamma} + \int_{\gamma_{min}}^{\gamma_{max}} \frac{B}{2C} d\gamma = C_1 \qquad (12)$$

From (12) we obtain

$$\left(\frac{L}{2AC} + \frac{D}{2C}\right) \cdot \int_{\gamma_{min}}^{\gamma_{max}} \frac{d\gamma}{\gamma} + \frac{B}{2C}(\Delta\gamma) = C_1 \qquad (13)$$

From (1 3) we find

$$\left(\frac{L}{2AC} + \frac{D}{2C}\right) = \frac{C_{1-} - \frac{\Delta\gamma \cdot B}{2C}}{ln\left(\frac{\gamma_{max}}{\gamma_{min}}\right)} \qquad (14)$$

From expression (1 4) we obtain

$$L = \frac{2AC \cdot C_1 - \frac{AB \cdot \Delta\gamma}{C}}{ln\left(\frac{\gamma_{max}}{\gamma_{min}}\right)} - AD \qquad (15)$$

Let us carry out model calculations using the obtained expressions (11) and (15).

Modeling studies

To carry out model calculations, we will use the tabular data of the values A , B , C , D given in the table [Alexandru Dan Toma , 2023].

Table 1

Tabular data of the values

coefficient	at λ <0.5 μm	at λ> 0.5 μm
A	$6.5 \cdot 10^{-3}$	8.65
B	3.4	4
C	1.36	1.1
D	0.12	2.7

Next we take $\gamma_{max} = 2.71$; $\gamma_{min} = 1$; therefore, we have

$$\frac{\gamma_{max}}{\gamma_{min}} = 2{,}71$$

$$\Delta\gamma = \gamma_{max} - \gamma_{min} = 1{,}71$$

the value of C_1 as

https://doi.org/10.56143/3030-3893-2026-2-156-158

$$C_1 = \left(\frac{\lambda_{max} - \lambda_{min}}{2}\right)\Delta\gamma;$$

at $\lambda_{max} = 1$ µm ; $\lambda_{min} = 0.1$ µm we have

$$C_1 = 0{,}3 \cdot \Delta\gamma = 0{,}45 \cdot 1{,}71 \approx 0{,}8 \text{ мкм}$$

Let us calculate L using formula (15) taking into account the obtained values of Δγ and $ln\left(\frac{\gamma_{max}}{\gamma_{min}}\right)$, as well as $C_1 = 0.5$ µm at λ>0.5 µm.

We get L ≈ 92.38.

According to formula (11), we obtain

$$f(\gamma) = \frac{L_0}{2 \cdot 8{,}65 \cdot 1{,}1 \cdot 2{,}71} - \frac{4}{2 \cdot 1{,}1} - \frac{2{,}7}{2 \cdot 1{,}1 \cdot 2{,}71} = \frac{92{,}38}{51{,}58} - 1{,}82 - 0{,}46 = -0{,}48 \text{ мкм}$$

Therefore, theoretically, the optical thickness of the atmosphere can reach its maximum due to high pressure at negative wavelengths, which in principle do not exist in nature.

3. Conclusion

Using the Buchholz model of the optical density of the atmosphere, as well as the results of solving a newly formulated variational optimization problem, it is shown that in the region of real wavelengths of the PAR component of solar optical radiation, high atmospheric pressure cannot lead to the formation of any extremum of the optical density of the atmosphere.

References

[1] Mannava Sivakumar. Importance of solar radiation and the need for improved respect to Sun by Agrometeorologists. Journal of Agrometeorology. 2023. Vol. 25.No. 1, pp. 51-60. DOI: https://doi.org/10.54386/jam.v25i1.1971

[2] Dongli Tan, Yao Wu, Zhiqing Zhang, Yue Jiao, Lingchao Zeng, and Yujun Meng. Assessing the Life Cycle Sustainability of Solar Energy Production Systems: A Toolkit Review in the Context of Ensuring Environmental Performance Improvements. 2023. 15(15):11724. DOI: 10.3390/su151511724

[3] Giampaolo Caputo, Irena Balog, Giuseppe Canneto. Solar Power in Italy: Evaluating the Potential of Concentrated Solar Power and Photovoltaic Technologies. Energies. 2026.19.1446. DOI: 10.3390/en19061446

[4] Julien Laliberté, Simon Belanger, M. Babin. Seasonal and interannual variations in the propagation of photosynthetically available radiation through the Arctic atmosphere. Elementa: Science of the Anthropocene. 2021. 9(1). DOI: 10.1525/elementa.2020.00083

[5] Hilma Magalhães de Oliveira, Leone Francisco Amorim Curado, André Matheus de Souza Lima, Thamiris Amorim dos Santos Barbosa, Rafael da Silva Palácios, João Basso Marques, Nadja Gomes Machado, and Marcelo Sacardi Biudes. Aerosol-PAR Interactions: Critical Insights from a Systematic Review (2021-2025). Atmosphere 2025, 16 (9), 1009; https://doi.org/10.3390/atmos16091009

[6] Manuel Nunez, Neal Cantin, Craig Steinberg, Virginie van Dongen-Vogels, and Scott Bainbridge. Correcting PAR Data from Photovoltaic Quantum Sensors on Remote Weather Stations on the Great Barrier Reef. Journal of Atmospheric and Oceanic Technology. 2022. Volume 39: Issue 4. Pp. 425–448. DOI: https://doi.org/10.1175/JTECH-D-21-0095.1

[7] Alexandru Dan Toma. Science of Sun Photometry. 2023. Pp.74-82. https:/natsci.upit.ro/media/1464/paper-13.pdf

[8] Joseph A. Curcio. Evaluation of Atmospheric Aerosol Particle Size Distribution from Scattering Measurements in the Visible and Infrared. Journal of the Optical Society of America. Vol. 51, Issue 5 , pp. 548-551. (1961). https://doi.org/10.1364/JOSA.51.000548

[9] C. Toledano, V/E. Cachorro, A. Berjon, A. M. de Frutos, M. Sorribas, B. A. de la Morena and P. Goloub. Aerosol optical depth and Angstrom exponent climatology at El Arenosillo AERONET site (Huelva, Spain). Quarterly Journal of the Royal Meteorological Society. QJR Meteorol. Soc. 133: 795–807 (2007). DOI: 10.1002/qj.54

[10] C. Frohlich, Glenn E. Shaw. New determination of Rayleigh scattering in the terrestrial atmosphere. APPLIED OPTICS . June 1980 . 19(11): Pp. 1773-1775 . DOI: 10.1364/AO.19.001773.

Information about the author

Hikmet Asadov	Research Institute of Aerospace Informatics of the National Aerospace Agency, Department of Information and Measurement Systems Design, Chief Researcher, Doctor of Technical Sciences, Professor Tel: +99450 324 72 40 E-mail: asadzade@rambler.ru https://orcid.org/0000-0003-1180-1535
Ulker Mammadova	Azerbaijan State Oil and Industry University, Department of Instrument Engineering, Lecturer, Doctor of Philosophy in Engineering +99455 988 99 58 https://orcid.org/0000-0002-8953-3001
Khumar Aliyeva	Research Institute of Aerospace Informatics of the National Aerospace Agency,Candidate of Technical Sciences, Associate Professor, Chief Researcher E-mail: a.khumar.1962@gmail.com https://orcid.org/0009-0002-6657-3445

Issues of using fiber-optic elements for constructing a ground-based distributed system for measuring solar optical radiation

H.H. Asadov[1][a], U.F. Mammadova[2][b]
[1]Research Institute of Aerospace Informatics, Baku, Azerbaijan
[2]Azerbaijan State University of Oil and Industry, Baku, Azerbaijan

Abstract: This article is devoted to the development and optimization of star-shaped structures for measuring solar optical radiation using fiber optic cables. The feasibility of optimizing the star-shaped structure of a measuring system for estimating solar radiation in radial directions from the center of the study area is examined. It is shown that using a star-shaped structure to measure temperature in radial sectors of a circular zone can achieve a twofold improvement in signal-to-noise ratio compared to measurements using diametrically positioned fiber optic cables.

Keywords: solar radiation, measuring system, star structure, optimization, fiber optic cable

1. Introduction

As noted in [1], the method of distributed measurement of solar radiation using fiber optic elements allows for long-term measurements with high spatial resolution. According to [2,3], distributed fiber optic sensors/hereinafter DFOS (Distributed Fiber Optic DFOS sensors enable distributed positional measurements of physical quantities such as temperature, pressure, and mechanical stress along a fiber optic cable laid in a specific direction. These sensors can replace a large number of independent discrete elements, which are typically installed at intervals along the objects being monitored. This makes it possible to monitor over fairly long distances, up to tens of kilometers. The use of DFOS reduces power consumption and system cost. According to [1], DFOS are not subject to aging and allow multiplexing while simultaneously performing quasi-static measurements.

One of the promising areas of application of DFOS is undoubtedly the measurement of solar optical radiation on the Earth's surface. As noted in [4], the relevance of such measurements lies in the fact that the Sun is an important source of energy for our planet, and any small change in this energy can affect such crucial areas as agriculture, climatology, and energy. As noted in [5], ground-based solar radiation measurements are still the most accurate compared to remote measurements from onboard various aircraft. At the same time, distributed measurements of solar radiation using DFOS , have a disadvantage, which is that the physical processes used in them (Rayleigh, Brillouin , Raman scattering) are subject to the influence of temperature [6,7], pressure, mechanical stress [8,9].

According to [4], the technology of distributed solar optical radiation measurements is based on the principle of bolometers , which consists in the fact that the power of the acting electromagnetic radiation can be established by determining the temperature of a material whose absorption coefficient is known.

Moreover, if the temperature of such a material in the absence of solar radiation is known, then the temperature of the said material can be determined by the formula

$$T(t) = T_0 + \left(\frac{E_{inc} \cdot A_{inc} \cdot \alpha}{hA}\right) \cdot \left(1 - \exp\left(-\frac{hA}{cm} t\right)\right) \tag{1}$$

where is $t$the time of exposure of the material to solar radiation; $E_{inc}$is the density of solar radiation; $A_{inc}$is the area of the solar radiation absorber; $\alpha$is the absorption coefficient, $h$is the coefficient of heat transfer to the associated element with temperature T_0; $A$is the area of heat transfer to the element with temperature T_0; $c$is the specific heat of the absorber; $m$is the mass of the absorber.

It should be noted that direct application of the bolometric principle in distributed fiber-optic solar radiation measurement is complicated by the fact that the ambient temperature along the fiber-optic cable's path is initially unknown. To address this issue, two fiber-optic cables containing surface layers with different absorption coefficients are used in the selected monitoring direction.

As shown in [4], in this case the solar radiation flux density can be determined by the formula

$$E_{inc} = \frac{T_2 - T_1}{c_2 - c_1} \tag{2}$$

where is $T_1$the temperature of the first cable; $T_2$is the temperature of the second cable; $c_1, c_2$are constants defined as

$$c_1 = \frac{A_{inc}\alpha_1}{h_1 A} \tag{3}$$

$$c_2 = \frac{A_{inc}\alpha_2}{h_2 A} \tag{4}$$

The principle of two cable measurements $E_{inc}$is illustrated in Fig. 1.

[a] https://orcid.org/0000-0003-1180-1535
[b] https://orcid.org/0000-0002-8953-3001

https://doi.org/10.56143/3030-3893-2026-2-159-161

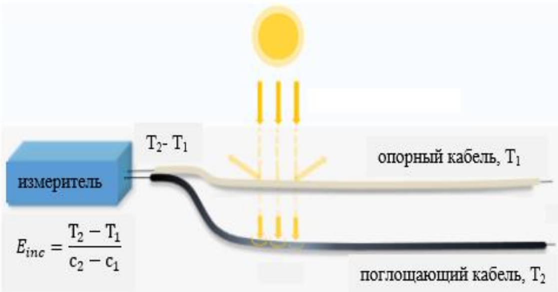

Fig. 1. Illustration of two cable measurements of solar optical radiation density

The signal-to-noise ratio can be estimated using the formula

$$S_{1inc} = \frac{T_2 - T_1}{(c_2 - c_1)\Delta T_ш} \tag{5}$$

where are $T_ш$the noises in temperature determination due to the influence of the external factors mentioned above. We formulate the research problem as follows:

It is necessary to carry out measurements E_{inc}on a circular area by constructing a star-shaped DFOS structure , an illustration of which is shown in Fig. 2. In this case, it is permissible to use radially directed DFOS , shown in Fig. 1, in which the absorption coefficientsα_i c leave an ordered set

$$A = \{\alpha_i\}; i = \overline{1, n} \tag{6}$$

$n$radially installed gauges by sector .

The times (durations) of temperature measurements in such meters installed along a sector of a circular area (Fig. 2) denoted as $t_j$also constitute an ordered set T, where

$$T = \{t_j\}; j = \overline{1, n} \tag{7}$$

It is also necessary to estimate the gain in the signal-to-noise ratio when carrying out measurements on a star-shaped structure of sensors compared to the result of measurements along a diametrical path along a circular area using one extended section of an absorption meter, the signal-to-noise ratio of which can be estimated using formula (5).

2. Research methodology

Let us consider a distributed star-shaped structure of a solar optical radiation density meter (Fig. 2).

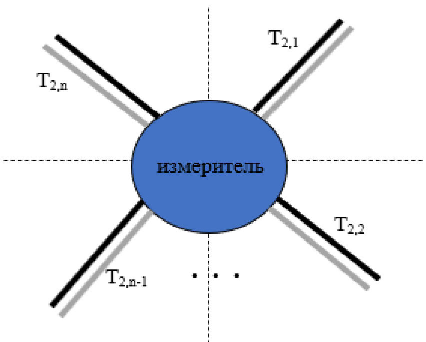

Fig. 2. Illustration of a star-shaped structure for the implementation of distributed measurements of solar radiation density with n number of sections in the study area

For a star-shaped distributed system, one may require the signal-to-noise ratio to increase to an extreme value. In the discrete case discussed above, the optimal relationship should be determined.

$$t_j = f(\alpha_i) \tag{8}$$

at which the average value of the signal-to-noise ratio across sectors, defined as

$$S_{cp} = \frac{1}{(c_2 - c_1)\Delta T_ш}\left[\frac{1}{n}\sum_{i=1}^{n}(T_{2i} - T_1)\right] \tag{9}$$

would reach extreme values.

If we accept constancy T_1across all sectors and $T_1 = 0$then the research problem is reduced to finding such a discrete function (8) for which the average indicator is T_{cp}, where

$$T_{cp} = \frac{1}{n}\sum_{i=1}^{n} T_{2i} \tag{10}$$

would reach an extremum. In this case, we assume the indicator remains constant $\Delta T_ш$across all sectors. If we accept , $n \to \infty$we can move from the discrete model discussed above to the continuous star-shaped DFOS model . In this case, the research problem can be formulated as follows : Calculate the optimal continuous function

$$t = f(\alpha) \tag{11}$$

at which the objective functional F_0formed on the basis of expression (1) as an optimization criterion would reach an extremum, where

$$F_0 = \frac{1}{\Delta\alpha}\int_{\alpha_1}^{\alpha_2} C_3\alpha[1 - \exp(-C_4 t)]d\alpha \tag{12}$$

Where

$$\Delta\alpha = \alpha_2 - \alpha_1 \tag{13}$$

$$C_3 = \frac{E_{inc}A_{inc}}{hA}$$

$$C_4 = \frac{hA}{cm}$$

To solve the formulated problem, we impose the following restrictive condition on function (11):

$$\int_{\alpha_1}^{\alpha_2} f(\alpha)d\alpha = C_5;\ C_5 = const \tag{14}$$

Constraint condition (11) stems from the need for efficient distributed measurements. Taking into account expressions (12) and (14), we formulate the objective functional for variational optimization F_0as follows:

$$F_0 = \int_{\alpha_1}^{\alpha_2} \frac{1}{\Delta\alpha}\left[C_3\alpha\left[1 - \exp\left(-C_4 f(\alpha)\right)\right]\right]d\alpha - \lambda\left[\int_{\alpha_1}^{\alpha_2} f(\alpha)d\alpha - C_3\right] \tag{15}$$

Where λ-Lagrange multiplier; $\lambda = const$.

To calculate the optimal form of the function $f(\alpha)$, i.e. $f(\alpha)_{opt}$Let's use Euler's method, according to which the solution to problem (12) must satisfy the following condition

$$\frac{d\{C_3\alpha[1 - \exp(-C_4 f(\alpha))] - \lambda f(\alpha)\}}{df(\alpha)} = 0 \tag{16}$$

From expression (16) we find

https://doi.org/10.56143/3030-3893-2026-2-159-161

$$f(\alpha) = \frac{1}{C_4}\ln\left(\frac{C_3C_4\alpha}{\lambda}\right) \quad (17)$$

When solving (17) F_0it reaches a maximum, which is easy to verify using the Lagrange criterion. We have

$$\frac{d^2\{C_4\alpha[1-\exp(-C_4f(\alpha))-\lambda f(\alpha)]\}}{d(f(\alpha))^2} = -C_4\exp(-C_4f(\alpha))$$

The negative sign obtained as a result of calculating the second derivative of the integrand in (12) with respect to the desired function shows that the functional F_0reaches a maximum when solving (17). Let us calculate this maximum. Taking into account expressions (12) and (17), we obtain

$$F_0 = \int_{\alpha_1}^{\alpha_2}\frac{C_3\alpha}{\Delta\alpha}\left[1-\exp\left(-\ln\frac{C_3C_4\alpha}{\lambda}\right)\right]d\alpha = \int_{\alpha_1}^{\alpha_2}\frac{C_3\alpha}{\Delta\alpha}\left[1-\frac{\lambda}{C_3C_4\alpha}\right]d\alpha = \frac{C_3(\alpha_2^2-\alpha_1^2)-\frac{\lambda}{C_4}(\alpha_2-\alpha_1)}{\Delta\alpha} \quad (18)$$

From expression (18) we obtain

$$T_{cp} = C_3(\alpha_2+\alpha_1) - \frac{\lambda}{C_4} \quad (19)$$

In the case of using one diametrically located measuring instrument, $t\to\infty$from (1) we $T_0 = 0$obtain

$$T_2 = C_3\alpha \quad (20)$$

We define the gain in determining the temperature as

$$\gamma = \frac{T_{cp}}{T_2} = \frac{\alpha_2+\alpha_1}{\alpha} - \frac{\lambda}{C_3C_4\alpha}$$

when $\alpha_2 = \alpha$we have

$$\gamma = 1 + \frac{\alpha_1}{\alpha} - \frac{\lambda}{C_3C_4\alpha}$$

Thus, $\frac{\lambda}{C_3C_4} \ll \alpha_1$we get a win$\gamma = 1 + \frac{\alpha_1}{\alpha}$ i.e. we $\alpha_1 \to \alpha$get a double win $\gamma = 2$.

Accordingly, in the case of equal noise values in the star-shaped structure of the meter and in a system consisting of one pair of diametrically laid cables, a twofold gain in the signal-to-noise ratio can be achieved in the area under study.

3. Conclusion

The possibility of optimizing the star-shaped structure of a measuring system for assessing solar radiation in radial directions from the center of a circular study area has been formulated and resolved. It has been determined that a star-shaped structure for measuring temperature in radial sectors of a circular area can achieve a twofold improvement in signal-to-noise ratio compared to the use of diametrically positioned fiber optic cables.

References

[1] Guemes A., Fernandez-Lopez A., Lozano A. Fiber optic distributed sensing // STO-EN-AVT-220.

[2] Magalhaes R., Garcia-Ruzi A., Martins HF, Margulis W. et al. Distributed detection of optical radiation using chirped-pulse phase-sensitive optical time domain reflectometry // 26th international conference on optical fiber sensors. OSA 2018.

[3] Flores-Bravo JA, Lazaro J, Cuadrado C, et al. Applications of multipoint distributed fiber optic sensors for monitoring in critical systems // XL conference on design of circuits and integrated systems. 26 November. 2025.

[4] Costa L., Martin-Lopez S., Gonzalez- Herraez M., Martins HF Long-range distributed solar irradiance sensing using optical fibers // Sensors. 2020. 20.

[5] Paulescu M., Paulescu E. Short-term forecasting of solar irradiance // Renev . Energy. 2019. 143. 985-994.

[6] Joshi, B.; Kay, M.; Copper, J. K.; Sproul, A.B. Evaluation of solar irradiance forecasting skills of the Australian Bureau of Meteorology's ACCESS models. Sol. Energy 2019, 188, 386–402.

[7] Kurashima, T.; Horiguchi, T.; Tateda , M. Distributed-temperature sensing using stimulated Brillouin scattering in optical silica fibers. Opt. Lett. 1990, 15, 1038–1040.

[8] Mikhailov, S.; Zhang, L.; Geernert, T.; Bergmans , F.; Thevenaz , L. Distributed hydrostatic pressure measurement using phase OTDR in a highly birefringent photonic crystal fiber. J. Lightwave Technol. 2019, 37, 4496–4500.

[9] Zhou, L.; Wang, F.; Wang, X.; Pan, Y.; Sun, Z.; Hua, J.; Zhang, X. Distributed strain and vibration sensing system based on phase-sensitive OTDR. IEEE Photonics Technol. Lett. 2015, 27, 1884–1887.

Information about the author

Hikmet Asadov	Research Institute of Aerospace Informatics of the National Aerospace Agency, Department of Information and Measurement Systems Design, Chief Researcher, Doctor of Technical Sciences, Professor Tel: +99450 324 72 40 E-mail: asadzade@rambler.ru https://orcid.org/0000-0003-1180-1535
Ulker Mammadova	Azerbaijan State Oil and Industry University, Department of Instrument Engineering, Lecturer, Doctor of Philosophy in Engineering +99455 988 99 58 https://orcid.org/0000-0002-8953-3001

https://doi.org/10.56143/3030-3893-2026-2-159-161

CONTEXT / MUNDARIJA

CONTEXT / MUNDARIJA

CONTEXT / MUNDARIJA